Fall 2016

Development of chemically active metal oxide composite nanofiber filters for water treatment

Katherine E. Greenstein
University of Iowa

DEVELOPMENT OF CHEMICALLY ACTIVE METAL OXIDE COMPOSITE NANOFIBER FILTERS FOR WATER TREATMENT

by

Katherine E. Greenstein

A thesis submitted in partial fulfillment
of the requirements for the Doctor of
Philosophy degree in Civil and Environmental Engineering
in the Graduate College of
The University of Iowa

December 2016

Thesis Supervisors: Associate Professor David M. Cwiertny
Professor Emeritus Gene F. Parkin

Graduate College
The University of Iowa
Iowa City, Iowa

CERTIFICATE OF APPROVAL

_____

PH.D. THESIS

_____

This is to certify that the Ph.D. thesis of

Katherine E. Greenstein

has been approved by the Examining Committee
for the thesis requirement for the Doctor of Philosophy
degree in Civil and Environmental Engineering at the December 2016
graduation.

Thesis Committee: _____
David M. Cwiertny, Thesis Supervisor

_____
Gene F. Parkin, Thesis Supervisor

_____
Sarah C. Larsen

_____
Syed Mubeen

_____
Michelle M. Scherer

To my family, for their endless love and support.

ACKNOWLEDGMENTS

I would like to thank a great many folks, without whom I would not have successfully completed my doctorate…

David Cwiertny, my advisor. Thank you for actively recruiting me to come to the University of Iowa (a great opportunity for me) and for your encouragement, guidance, and patience throughout my pursuit of a doctorate. Your mentorship ensured my professional development and made completing my dissertation (in an extremely timely fashion) possible.

Gene Parkin, my co-advisor. Thank you for your guidance and words of wisdom throughout my time in graduate school. Thank you for listening to my research issues and supporting my efforts at a work-life balance. I truly count you among the "nano-heads" of our field.

My labmates throughout graduate school – Rebekah Oulton, Danmeng Shuai, Shen Qu, Caylyn Lanzl, Jason Haase, Kyle Nelson, Kathy Peter, Jiajie Qian, Brandon Jennings, Nick Pflug, Matt Nagorzanski, and Bailey Kelsay. It was a pleasure working with you, and I learned something from each and every one of you!

Our collaborators at University of California Riverside, Michael Nalbandian and Nosang Myung, who contributed to this work. Marty St. Clair and Susan Noreuil at Coe College, as well as Brian Hanft and Sophia Walsh with Cerro Gordo Department of Public Health, who made much of this work possible. Thank you for your indispensable assistance!

My funding sources, the University of Iowa Presidential Research Fellowship, Donald E. Bently Professorship, Ballard Seashore Fellowship, and the U.S. EPA STAR grant (no. R835177).

My friends and family, for supporting me throughout the tricky journey that is graduate school. Mom and Dad, thank you for always pushing me to keep going (and for the extra emotional support during the last month of writing my dissertation). Ann, thank you for always being "Ann."

Edgard Verdugo, my husband and best friend. Thank you for your unconditional love and endless assistance. You made this experience exceed my wildest dreams.

ABSTRACT

Small drinking water systems, often financially and resource-limited, face unprecedented challenges due to the current diversity and ubiquity of water pollutants. Well-characterized inorganic legacy pollutants, including arsenic, copper, hexavalent chromium, and lead, remain persistent in drinking water systems. In addition, emerging organic contaminants, like endocrine disrupting compounds and pharmaceuticals, are largely uncharacterized but prevalent in the environment and water supplies, calling into question what levels of these relatively new contaminants are truly safe in drinking water. Point-of-use (POU) and point-of-entry (POE) water treatment devices, installed at a specific tap or at the water entry point to a single facility, respectively, are necessary to ensure safe drinking water in contexts where centralized water treatment is not available or cannot adapt to meet new regulatory standards. While existing POU and POE technologies, including reverse osmosis and packed bed media filters, are effective for removing contaminants, installation costs, energy demands, and spatial footprints of these systems can inhibit their implementation. There is a need for new POU and POE technologies that remove a diversity of water contaminants while maintaining a small application footprint.

Nanotechnology, referring to technology using material with at least one dimension or feature less than 100 nm in length, is ideal for meeting this need in drinking water treatment. With high surface area-to-volume ratios, nano-enabled treatment technologies exhibit enhanced reactivity with less material, keeping overall footprint relatively small. Specifically, electrospinning, a process in which a polymer precursor solution is electrified

to produce a cohesive sheet of nanofibers, can be used to easily synthesize chemically active nanofiber filters for water treatment applications.

In this study, we develop electrospun nanofiber filters that harness nano-scaled hematite (Fe_2O_3) for sorption of inorganic contaminants (e.g., As, Pb) and nano-scaled titanium dioxide (TiO_2) for use with ultraviolet (UV) and visible light as an advanced oxidation process (AOP) for removal of emerging organic contaminants (e.g., benzotriazole, carbamazepine, DEET). Most importantly, we strive to optimize both reactivity and material strength to develop cohesive, durable filtration platforms that overcome barriers to use of nanomaterials in water treatment (e.g., concerns over leaching of nanoparticles deployed as suspensions).

Herein, we first demonstrate reactivity optimization of pure (though brittle) TiO_2 nanofiber photocatalysts by noble metal catalyst (Au) surface loading. Additionally, we optimize polymer-Fe_2O_3 composite nanofibers for reactivity while maintaining material flexibility by coating the doped polymer with additional Fe_2O_3 surfaces available for metal/metalloid uptake. Finally, we apply reactivity optimization and strategies to maintain material strength in the development of carbon/TiO_2 nanofiber composites used for (photo)chemical filtration of water containing emerging organic contaminants. Ultimately, we find that nanofiber composites exhibit substantial reactivity and structural integrity in water treatment platforms. Outcomes of this work contribute to making nanomaterials, which have been studied for decades but have yet to be commercially employed for water treatment, practical for chemically active water filtration.

PUBLIC ABSTRACT

A variety of pollutants, from a metals like lead and arsenic to the herbicide atrazine, challenge water quality across the United States. Point-of-use (POU) and point-of-entry (POE) water treatment devices, installed at a specific tap or at the water entry point to a single facility, respectively, can ensure safe drinking water when water treatment facilities are not available or cannot meet new regulatory standards. Nanomaterials, referring to materials with at least one dimension or feature less than 100 nm in length, are ideal for removing many water pollutants due to their high reactivity and small footprint. Specifically, electrospinning, a process in which a solution is electrified to produce a flexible sheet of nanofibers, can be used to easily make nanofiber filters for water treatment applications. In this study, we develop electrospun nanofiber filters that use the iron oxide hematite (Fe_2O_3) to remove metals (e.g., Pb) and titanium dioxide (TiO_2) for use with ultraviolet (UV) to remove organic pollutants (e.g., herbicides, pharmaceuticals). Most importantly, we strive to balance both reactivity (efficiency at removing pollutants) and material strength (flexibility, durability) to develop resilient water filters that overcome barriers to use of nanomaterials in water treatment (e.g., concerns over release of nanomaterials into treated water). This work brings reactive nanomaterials, which have been studied for decades but have yet to be used for commercial water treatment, closer to actual application as water filters.

TABLE OF CONTENTS

LIST OF TABLES

LIST OF FIGURES

CHAPTER 1: INTRODUCTION

1.1. Diversity of pollutants challenging drinking water quality

Despite the promotion of safe drinking water standards on a national scale put forth by the Safe Drinking Water Act (SDWA), the quality of drinking water in the United States remains persistently challenged by water contaminants in three primary ways: (i) naturally-occurring or anthropogenic contamination of water supplies, (ii) failure of wastewater treatment plants (WWTPs) and water treatment plants (WTPs) to remove contaminants, and (iii) generation or release of contaminants resulting from WTPs and drinking water distribution systems. “Legacy” pollutants, so called due to their historical origin, established toxicity, and current persistence as pollutants in the environment [1], include both organic compounds (e.g., polychlorinated biphenyls, PCBs and dichlorodiphenyltrichloroethane, DDT) and inorganic compounds (e.g., lead, Pb, hexavalent chromium, Cr(VI), and arsenic, As). These pollutants are regulated by the U.S. Environmental Protection Agency (EPA) under the SDWA. This means that for each pollutant, there is an enforceable maximum contaminant level (MCL) that establishes the maximum concentration allowed in drinking water provided to the public. “Contaminants of emerging concern” (CECs), also termed “emerging organic contaminants” (EOCs), include organic contaminants with often uncharacterized health risks [1–5]. While EOCs have been detected in drinking water, these contaminants are currently unregulated due to their relatively recent emergence and/or detection and the limited information available about their toxicity.

1.1.1. Inorganic legacy pollutants in drinking water

Heavy metals and metalloids, legacy pollutants that have presented long-term challenges to water quality, include arsenic (As), hexavalent chromium [Cr(VI)], copper (Cu), and lead (Pb). While Cu is predominantly toxic to aquatic organisms [6,7], As, Cr(VI), and Pb are especially toxic to humans, with both acute and chronic health effects. Although legacy pollutants like As, Cu, Pb, and Cr(VI) have been studied and characterized throughout the years [7–16], heavy metals and metalloids remain prevalent in water sources and drinking water. Acid-base and redox (oxidation/reduction) chemistry impact mobility, bioavailability, and toxicity of these inorganic pollutants.

A potent carcinogen, As has a MCL of 10 parts per billion (ppb) (i.e., 10 μg/L) as established in 2001; prior to 2001, the MCL had been 50 ppb [17], which attests to the evolving understanding of risks associated with legacy pollutants. This metalloid, which can naturally occur in groundwater, is typically known for causing blackfoot disease and skin lesions [8]. Even at levels below the current MCL, As can impede early stage growth in humans [18]. As a carcinogen, As consumption through drinking water can result in tumor growth in skin and internal organs [8]. Soluble As is present in water as oxyanions, As(III) (arsenite, AsO_3^{3-}) and the more oxidized As(V) (arsenate, AsO_4^{3-}) species. Depending on pH, these species can be present in water as protonated or deprotonated forms. As(III) is both more mobile in the environment and toxic than As(V) [19]. The greater toxicity of As(III) is related to its interactions with sulfur and generation of reactive oxygen species (ROS) [9]. Notably, conditions that are acidic and oxidizing can result in large releases of As into water from sediment [20]. A recent survey of groundwater wells in the state of Iowa found As in 48% of samples (**Figure 1-1**) [21]. Additionally, a recent study estimated levels of As in exceedance of the MCL in many groundwater wells in the

Central Valley of California [22]. Other regions of the United States are afflicted with the same issue [10].

Cr(VI), another carcinogen, can cause kidney and liver damage as well as gastrointestinal tract irritation and stomach ulcers [14]. Although its MCL of 100 ppb refers to total Cr [both Cr(III) and Cr(VI)], Cr(III) is relatively harmless while Cr(VI) is much more bioavailable, acutely toxic, and chronically toxic [15]. As a result, the California Department of Public Health (CDPH) has set a Cr(VI) MCL of 10 ppb [23]. Cr(III) present in water can be oxidized during drinking water treatment processes like chlorination [16], which results in direct input of Cr(VI) into distribution systems. Cr(VI) can also enter water supplies from industrial discharge, as Cr is commonly used to inhibit corrosion [24]. Depending on pH, Cr(VI) is typically present in water as oxyanions $HCrO_4^-$ or CrO_4^{2-}. Cr(VI) has recently been detected in the tap water of 31 cities in the United States [25].

Pb is a neurotoxin with serious implications for health of children; with no truly "safe" level for drinking water, it can impair neurological functions [12]. The main source of Pb is water distribution system pipes, joints, and solder. Corrosion can cause the release of this Pb, and thus many drinking water distributors add corrosion inhibitors, like ortho-phosphate, to water before it enters distribution systems. The EPA has set a maximum contaminant level goal (MCLG) for Pb of zero, though the EPA's enforceable Lead and Copper Rule sets an action level of 15 ppb for Pb; above this level, action must be taken to control corrosion of pipes in distribution systems [26]. However, poor understanding of Pb chemistry has resulted in water treatment decisions that cause the metal to continue to plague water quality; this has been seen in Washington, D.C. during 2001-2004, when the change from free chlorine to chloramines for disinfection caused corrosion leading to Pb

release [27], and now in Flint, Michigan, when the change to a corrosive water supply caused corrosive Pb release [28]. Pb can be present in water in soluble and particulate forms. Depending on pH and constituents in water, it can take the form of Pb^{2+}, Pb-hydroxide complexes [e.g., $PbOH^{+}$, $Pb(OH)_2$ (aq)], and lead carbonate [e.g., $PbCO_3$ (aq)] complexes [13,29]. Alkalinity can increase the solubility of Pb [11].

Cu, like Pb, is released through corrosion in distribution systems [26], but is far less toxic than its counterpart. The Lead and Copper Rule action level for Cu is 1.3 ppm, likewise used as an indicator of corrosion occurring in water distribution systems. While high doses of Cu (greater than 2 ppm) can be associated with nausea, lower levels do not appear to have acute or chronic toxic effects in humans [30]. Cu^{2+} is the predominant species present below pH 7, with limited solubility above pH 7.2 as $Cu(OH)_2$ dominates. However, alkalinity can increase the solubility of Cu in water [11]. Cu is of concern because it is associated with corrosion and it is toxic to algae and fish [6,7].

1.1.2. Organic pollutants: "emerging" today, "legacy" tomorrow?

At one time, even notorious legacy pollutants like DDT and PCBs were "emerging" contaminants. The characterization of their risks and subsequent regulation in drinking water transitioned them from EOCs to legacy pollutants. Many unregulated contaminants expected or detected in drinking water are reviewed by the EPA through the Contaminant Candidate List (CCL). The EPA publishes the CCL every 5 years, as mandated by the SDWA. The EPA then must determine whether five or more contaminants on the CCL should be regulated according to the SDWA based on whether the contaminant in question (i) is likely to adversely affect human health, (ii) is present or is expected to be present in public water systems at levels and with frequency causing concern for public health, and (iii) if regulated, would serve as a "meaningful opportunity for health risk reductions for

persons served by public water systems" [31]. As intermediate steps, the EPA can set health advisories, which are non-enforceable, for chemicals of health concern as well as require monitoring of unregulated contaminants under the Unregulated Contaminant Monitoring Rule (UCMR) to collect data needed to support establishing regulation under the SDWA. Examples of chemicals currently undergoing this review process are perfluorooctanoic acid (PFOA) and perfluorooctane sulfonate (PFOS), perfluoroalkyl substances historically used as flame retardants and in the manufacture of products resistant to grease, stains, or water. Though these chemicals were mostly phased out of use in the 2000s, contamination of soils and groundwater (e.g., near firefighting training facilities) [32,33] has led to persistence in water. A health advisory level of 70 parts per trillion (ppt, or ng/L) has been recommended for total PFOA and PFOS based on their health effects, including their carcinogenicity and adverse impacts on fetuses during pregnancy and breastfed babies. These chemicals continue to be under study and review by the EPA to determine if they should have an enforceable MCL in drinking water. An additional chemical under federal review (on the CCL and monitored under the UCMR) is N-nitrosodimethylamine (NDMA), a disinfection byproduct that can be released by WWTPs. However, California does have a notification level (NL) of 10 ppb and a Public Health Goal (PHG) of 3 ppb for NDMA in drinking water, likely spurred by high concentrations of NDMA found in Sacramento groundwater from rocket fuel production (~150 ppb) [34]. While EPA regulations predominantly result from perceived human health risks, organic contaminants can also present ecosystem risks likely to become problems prior to occurrence of human health effects, as historically seen with eggshell thinning and subsequent bird population endangerment as result of DDT introduced into the environment in the 1940s and 1950s [35].

1.1.3. Emerging organic contaminants in drinking water

EOCs are more and more frequently being detected in water and wastewater samples, and their health and ecological effects are typically negative or unknown, especially as relates to human health [3,4]. This evolving class of organic micropollutants includes pharmaceuticals and personal care products (PPCPs), endocrine disrupting compounds (EDCs), and pesticides, all of which are ubiquitous in water and may have serious implications for drinking water treatment [2,3,5,36]. These EOCs are designed to be bioactive and illicit biological responses (therapeutic effects from PPCPs and EDCs, and death from pesticides), and thus even at trace levels could be able to alter biological function in exposed organisms – even in humans, despite typically being well below the therapeutic dose [37]. Primary sources of EOCs are excretion and discharge in wastewater, agricultural runoff, and hospital effluent [3]. Especially high concentrations of pharmaceuticals (mg/L levels) have been detected globally in wastewater from production of the compounds [38]. If determined hazardous to human health, these contaminants present a heightened risk to water quality because many are recalcitrant to conventional water and wastewater treatment processes, as shown in **Figure 1-2** [3,36]. Evolving regulations for organic micropollutants in drinking water require development and implementation of new technologies to ensure their successful removal prior to water consumption.

EOCs are generally unregulated, though many are on the EPA CCL and under review, as previously discussed for PFOA/PFOS and NDMA. The overall process of making EOCs regulated is a struggle. Even in cases where health data clearly point to a problem and occurrence in drinking water (e.g., as with PFOA/PFOS), the nature and volume of data required to support regulation development places responsibility on the

EPA and researchers to unequivocally prove that chemicals harm human health [39] (rather than presuming a new chemical may be hazardous, and placing responsibility on chemical producers to indisputably prove a chemical does not harm human health, or on WWTPs or WTPs to remove new, relatively uncharacterized chemicals). A commonly encountered class of PPCPs is antibiotics; a consequence of their prevalence in the environment involves increased threat of the development of antibiotic resistance in bacteria [40]. EDCs, some of which represent a subset of PPCPs, include both endogenous hormones (e.g., 17β-estradiol) and synthetic steroids like 17β-trenbolone, which is used widely in animal agriculture. While hormones like 17β-estradiol can lead to the feminization of fish, even at ng/L concentrations [41], steroids like 17β-trenbolone can lead to the masculinization of fish [42], with both EDCs causing reproductive problems and declines in fish populations. While some pesticides and herbicides are very well-researched species (e.g., atrazine), but no less important from a water quality standpoint due to their persistence, there remain several classes of pesticides and herbicides for which environmental occurrence, fate and risk data is limited (e.g., neonicotinoid insecticides and herbicide safeners). Neonicotinoids, implicated in declining populations of pollinating insects [43], have only recently been explored as pollutants present in aquatic ecosystems across the United States [44,45]. Likewise, herbicide safeners, used to protect desirable crops from herbicides, are bioactive and can impact ecosystems despite being largely termed “inert” for decades [46]. In both cases, the chemicals were used by industry and released into the environment before long-term implications were considered, resulting in the widespread presence of these contaminants in the environment with (i) relatively little understanding of their impacts on

ecosystems and human health and (ii) no associated regulatory standards requiring their removal from water during wastewater or water treatment at present.

1.2. Small water treatment systems

Already limited in their financial resources and operational capacity, small communities struggle to maintain water treatment systems compliant with regulations and adaptable to future needs [47,48]. Compliance with the SDWA is complicated, in part, by the diversity of chemical constituents typically encountered in source waters for small public water systems (PWS). PWS, systems that serve 25 people or more or have at least 15 service line connections, must comply with all drinking water standards set by the EPA [49]. However, even smaller water systems remain unregulated. From EOCs to legacy pollutants, the responsibility for having water tested and implementing water treatment falls upon individuals using and drinking the unregulated water.

As a case study, in rural Iowa, which encompasses 40% of the state's population [50], most utilize privately owned (and thus unregulated) groundwater wells. A recent survey [21] found these wells to be compromised by organic and inorganic contaminants. The herbicide atrazine, which is often present at levels in violation of maximum contaminant levels (MCLs) in small PWS [47], was found in 8% of samples (40 out of 429) with mean and maximum concentrations of 0.104 μg/L and 0.5 μg/L, respectively. Arsenic (As) was detected in 48% of samples, with 40 instances (out of 473) exceeding its MCL of 0.01 mg/L (**Figure 1-1**). Source water quality problems are not isolated to groundwater; PWS in Iowa using surface water are subject not only to agrochemicals (like neonicotinoids) [45] but also other constituents of emerging concern including pharmaceuticals and hormones [51].

1.3. Treatment technologies for diverse water qualities encountered by small water systems

Due to the decentralized nature of small water systems (in contrast with centralized water systems that have a conventional water treatment plant and distribution system), point-of-use (POU) and point-of-entry (POE) are often the best alternatives for treating water. POU devices treat water for consumption (and are typically only installed at one tap), while POE devices treat water entering a single facility (e.g., a single home or school) [52]. POE and POU devices often employ adsorptive media or reverse osmosis (RO). However, the spatial footprint required for adsorptive media (i.e., deployed in relatively large packed bed filters) and the energy requirement of RO (which operates at high pressure) can be prohibitive for some small water systems. Additionally, both RO and sorptive media filtration result in waste streams that necessitate special disposal. RO produces a concentrated brine, and sorption processes result in media coated with large quantities of contaminants (e.g., granular iron oxide sorbents covered by sorbed As).

With conventional water treatment processes failing to remove many EOCs [36] and introducing contaminants (like Pb) through distribution systems [27], decentralized water treatment like POU and POE treatment, in addition to improved wastewater treatment, is the best line of defense for removal of contaminants of concern for human health.

1.3.1. Sorption and advanced oxidation processes in water treatment

In water treatment, advanced oxidation processes (AOPs) are processes in which hydroxyl radicals (·OH), a type of reactive oxygen species (ROS) that proves to be the strongest oxidant in water, are generated that can chemically oxidize nearly all aqueous contaminants [53]. AOPs are ideal for removing EOCs from water, due to the resultant

non-specific oxidation of all organics present and elimination of bioactivity associated with PPCP occurrence [40,54]. AOPs that can be used for oxidation of EOCs in water include ultraviolet light (UV) with ozone (O_3) (UV/O_3), UV with hydrogen peroxide (H_2O_2) (UV/H_2O_2), and UV with titanium dioxide (TiO_2) (UV/TiO_2) [53]. Processes with UV are beneficial because UV can simultaneously be applied for disinfection in water treatment; disinfection can also be achieved directly by AOPs [55].

Sorption is a process commonly utilized for water treatment. Referring to uptake of contaminants by media, sorption can remove organic and inorganic pollutants from water. Notable sorbents currently used for water treatment include granular activated carbon (GAC) and granular ferric hydroxide (GFH®, Evoqua). GAC has been demonstrated to remove both organic contaminants [ranging from EOCs to established disinfection byproducts (DBPs)] [56] and inorganic contaminants (including As and Pb) [57]. GFH® is approved as a best-available technology (BAT) for As removal by the EPA, but has also been demonstrated to remove other contaminants like copper and phosphate. Both GAC and GFH® employ large internal surface areas for sorption, in turn requiring relatively long contact times with water and thus large packed bed reactor systems. Such design parameters can inhibit deployment of GAC and GFH® in POU and POE treatment devices.

1.4. Novel metal oxide nano-scaled treatment technologies

Nanotechnology is technology development on the scale of 1-100 nm, creating structures with novel properties and functions arising from their molecular-level nature [58]. The promise of nanotechnology-integrated water treatment is the ability to optimize process efficiency via unique material properties exhibited within the nano-domain while simultaneously reducing the footprint of engineered systems. Nevertheless, environmental

engineers have been hesitant to embrace nano-engineered materials, primarily due to concerns over possible adverse effects upon their incidental release into the environment [59]. As such, there remain a wealth of unrealized opportunities for safe, responsible applications of engineered nanomaterials in water treatment.

Such nanotechnology-enabled treatment solutions are ideal for small PWS, as they exhibit high reactivity with a small footprint. The high surface area-to-volume ratio of nanomaterials makes them particularly attractive for adsorption and redox processes targeting dissolved chemical constituents [60,61]. For example, highly reactive nano-engineered materials represent ideal building blocks for multi-functional materials capable of performing several treatment operations simultaneously over short spatial dimensions. If synthesized in sufficient quantities and designed sustainably, multi-functional nanostructures represent an innovative approach for the simultaneous treatment of undesirable constituents in water via operations and principles (e.g., filtration, chemical oxidation, adsorption, and disinfection) long exploited by water quality engineers.

1.4.1. TiO_2 as a nano-scaled photocatalyst for advanced oxidation

Titanium dioxide (TiO_2) is a metal oxide semiconductor that serves as a photocatalyst. TiO_2 can oxidize or reduce organic pollutants for water treatment when exposed to ultraviolet (UV) light [62]. On the nanoscale, the reactivity of TiO_2 is affected by surface area-to-volume ratio, doping with other elements, and structural phase composition of the TiO_2 [63–67]. TiO_2 has not been implemented for actual water treatment; however, practical demonstrations of TiO_2 span several years and include membrane filters, solar reactors, and magnetic TiO_2 nanoparticles [68–70]. Several challenges of TiO_2 as a heterogeneous photocatalyst must be overcome for applied use in water treatment, including potential for leaching, aqueous stability, toxicity of the released

photocatalyst, and fouling of the material [71–74]. However, UV/TiO_2 has vast potential for water treatment because if immobilized, TiO_2 can eliminate the need to generate or store and dose chemicals (like O_3 and H_2O_2) as part of water treatment. This benefit extends to the deployment of UV/TiO_2 as an AOP in POU/POE water treatment; a filter with TiO_2 used in conjunction with UV light (with UV already utilized in POU devices [52]) would require minimal training and operational knowledge, making it ideal for POU/POE applications.

1.4.2. Hematite as a nano-scaled iron oxide sorbent for metal/metalloid uptake

Hematite (α-Fe_2O_3) is a metal oxide semiconductor that serves as a sorbent. This iron oxide can sorb heavy metals and metalloids (e.g., As) [75,76] as well as ions (e.g., phosphate) [77]. While iron-based materials are employed in water treatment (e.g., Evoqua granular ferric hydroxide, GFH®, for As sorption), hematite nanomaterials face the same barriers for applied use in water treatment that TiO_2 nanomaterials do [78].

1.4.3. Electrospinning

Electrospinning (**Figure 1-3**) has emerged as an innovative approach for the synthesis of ultra-long nanofibers with controlled diameter (from nm to μm) and composition while using a simple apparatus operated at room-temperature [79–81]. Electrospinning allows the high-yield production of nanoengineered materials in a format, nanofiber mats, that has the potential to be robust and stable under a variety of conditions [81]. Most notably, nanofiber mats are promising tools for filtration; they possess a larger surface area-to-volume ratio than conventional filters, and tend to exhibit lower degrees of pressure drop [81].

Initially developed for polymers, metal oxide nanofibers can now be synthesized by electrospinning sol-gel precursors with or without polymer hosts, followed by

calcination in air [79]. While electrospun nanofibers have found numerous applications in catalysis, sensing, medicine, and energy [82], their use in water treatment has grown slowly. Limited work to date has focused primarily on the application of polymeric nanofibers via direct filtration and incorporation into membrane bioreactors [83–86]. Current demonstrated uses of metal oxide nanofiber mats for water treatment applications either rely on dispersion via sonication of the nanofibers followed by filtration onto another substrate [87,88] or on formulations of the metal oxide nanofibers (e.g., TiO_2) that have relatively lower reactivity [89,90]. In studies to date, maintaining material strength remains a challenge while optimizing reactivity of metal oxide materials, as apparent with the reactive but brittle electrospun TiO_2 and Fe_2O_3 nanofibers shown in **Figure 1-4**.

1.5. Study objectives and hypotheses

Nanomaterials, particularly titanium dioxide (TiO_2) and hematite (α-Fe_2O_3), have exhibited great potential in water treatment due to their unique and tunable structural, physical, and chemical properties. Although decades of research have demonstrated the use of these nano-scaled metal oxides for water treatment applications as photocatalysts and adsorbents, true application in the field of water treatment remains limited due to practical challenges associated with nanomaterial use. Pure metal oxide nanofibers are brittle and ill-suited for water treatment (**Figure 1-4**), despite their significant reactivity toward contaminants. This work demonstrates the application of electrospun metal oxide nanofibers for use as chemically active filtration materials in water treatment, incorporating the concurrent requisites of robustness and optimal reactivity.

Specific objectives include the following:

- Via electrospinning, tailor nanofiber properties to optimize the reactivity of TiO_2 as a photocatalyst for chemical oxidation.
- Synthesize and characterize free-standing hematite filters using electrospun polymer-based nanofiber mats, and optimize reactivity in a flow-through filtration system by assessing performance (e.g., pollutant removal efficiencies).
- Synthesize and characterize free-standing TiO_2 filters using electrospun carbon-based nanofiber mats, and optimize reactivity in a cross-flow filtration system by assessing performance (e.g., permeate flux and pollutant removal efficiencies).

The hypothesis driving the first objective is that characteristics including diameter, grain size, dopant levels, and crystal structure could be tailored during synthesis to optimize nanofiber reactivity toward organic micropollutants. Hypotheses driving the second and third objectives are that optimized nanofibers could outperform conventional approaches utilizing similar operational principles across a range of performance metrics including active filtration lifetime, constituent removal capacity, and regeneration ability.

The research herein contributes to the transition of nanomaterials from benchtop demonstration to application in the field of water treatment. This work established formulations of TiO_2 and hematite nanofiber filters that have enhanced reactivity and are easily synthesized.

1.6. Overview and thesis organization

This thesis contains three chapters of research completing objectives and testing aforementioned hypotheses. Chapter 2, the first research chapter (a version of which was published in *ES&T* [91]), describes the optimization of TiO_2 nanofibers as photocatalysts for oxidation of EOCs. Crystalline phase (anatase versus rutile), nanofiber diameter, and

grain size are tuned to enhance photoreactivity of TiO_2. Additionally, Au nanoparticles are examined as catalysts for further increasing reactivity of TiO_2. Finally, the efficacy of TiO_2 nanofibers, Au/TiO_2 nanofiber composites, and commercially-available Aeroxide® P25 (TiO_2 nanoparticles) are compared across a suite of organic micropollutants and water qualities in batch.

The second research chapter, Chapter 3, demonstrates polymer/hematite (Fe_2O_3) composite nanofiber filters and Fe_2O_3-polymer/Fe_2O_3 core-shell nanofiber filters for removal of heavy metal and metalloid contaminants from water via sorption. Nanofiber filters are studied in batch and flow-through systems for removal of As(V), Cu(II), Cr(VI), and Pb(II) across different pH values, pollutant concentrations, and water qualities.

Chapter 4, the final research chapter, explores carbon/TiO_2 composite nanofiber filters for removal of EOCs in cross-flow filtration with UV light. Nanofiber filters are optimized by tuning thickness of the filter, mass of TiO_2 loaded in nanofibers, and phase and size of TiO_2 nanoparticles incorporated into nanofibers. Different flow rates are also assessed for cross-flow and dead-end applications. Filters are ultimately tested for removal of a suite of organic micropollutants in cross-flow filtration.

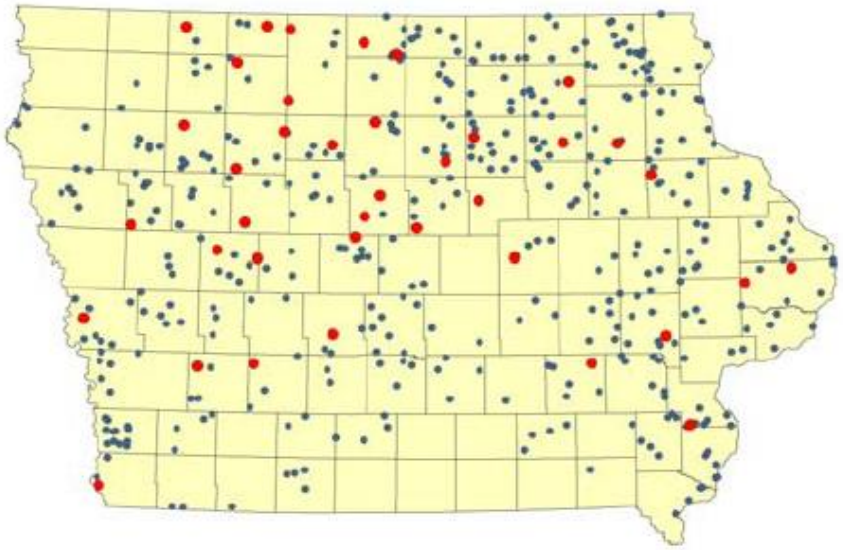

Figure 1-1. Instances of As occurrence in well water in rural Iowa communities [21]. Large red dots indicate ≥ 0.01 mg/L (the EPA MCL). Small blue dots indicate 0.001-0.009 mg/L [21].

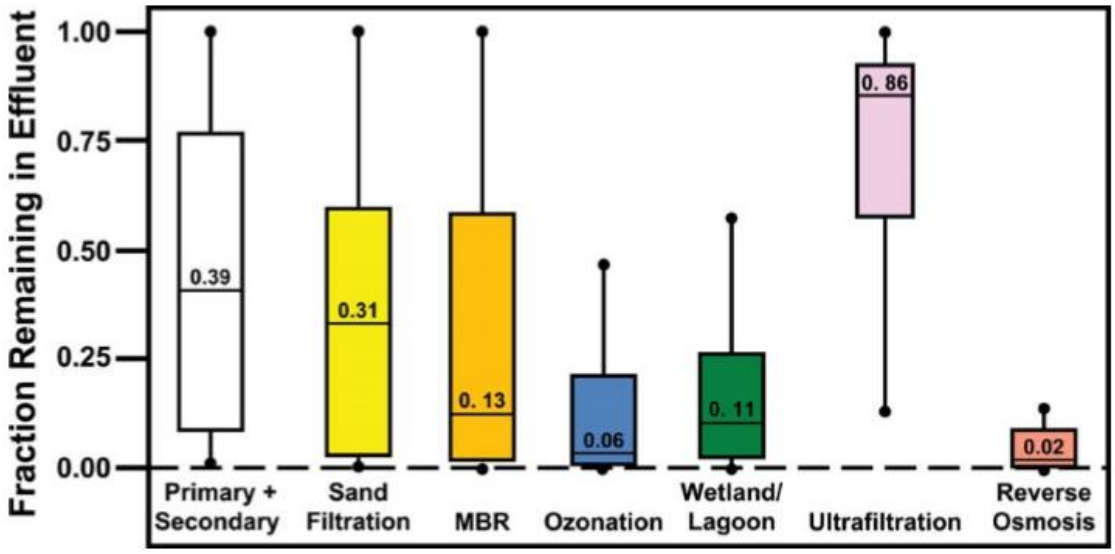

Figure 1-2. A box plot showing removal efficiencies of PPCPs for different wastewater treatment processes [36]. In each box, the solid line displays the median (50th percentile). Maxima and minima display 90th and 10th percentiles for fraction remaining in effluent; boxes extend from 25th to 75th percentiles.

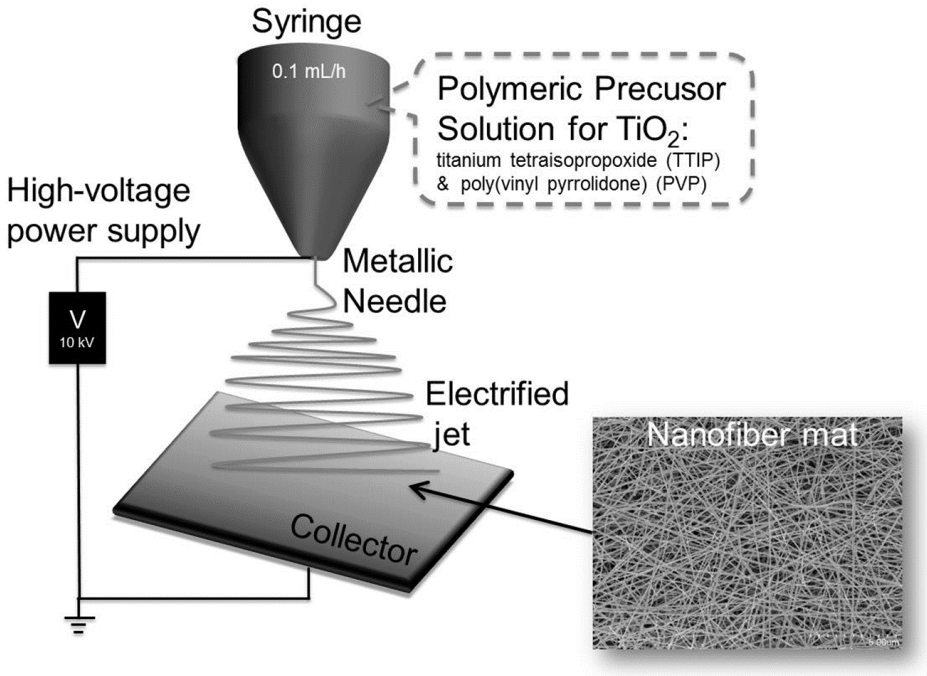

Figure 1-3. An electrospinning setup consists of a high-voltage power supply, spinneret (metallic needle), collector (e.g. Al foil, Si wafer, or metallic drum), and syringe pump. Polymer-based sol-gels are used as electrospinning solutions (e.g. Ti-doped polymer sol-gel for synthesis of TiO_2 nanofibers). Inset shows SEM image of electrospun nanofibers.

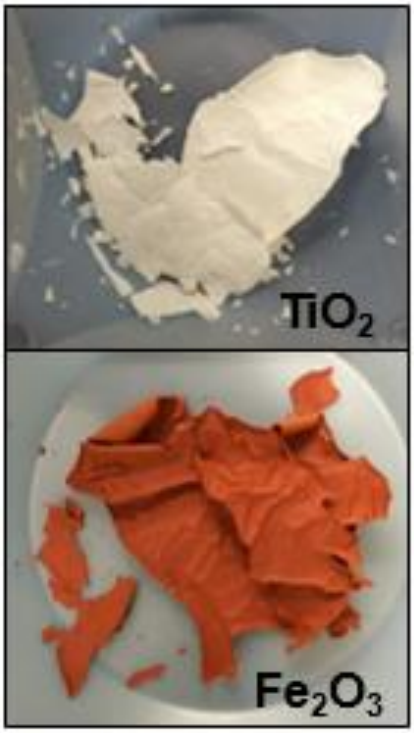

Figure 1-4. Pure electrospun TiO_2 and Fe_2O_3 nanofibers after calcination in air. These nanofibers are extremely brittle and poorly-suited for practical water treatment applications.

CHAPTER 2: TAILORED SYNTHESIS OF PHOTOACTIVE TITANIUM DIOXIDE NANOFIBERS AND GOLD/TITANIUM DIOXIDE NANOFIBER COMPOSITES: STRUCTURE AND REACTIVITY OPTIMIZATION FOR WATER TREATMENT APPLICATIONS[1]

2.1. Abstract

Here, titanium dioxide (TiO_2) nanofibers with tailored structure and composition were synthesized by electrospinning to optimize photocatalytic treatment efficiency. Nanofibers of controlled diameter (30-210 nm), crystal structure (anatase, rutile, mixed phases) and grain size (20-50 nm) were developed along with composite nanofibers with either surface-deposited or bulk-integrated gold (Au) nanoparticle co-catalysts. Their reactivity was then examined in batch suspensions toward model (phenol) and emerging (pharmaceuticals, personal care products) pollutants across various water qualities. Optimized TiO_2 nanofibers meet or exceed the performance of traditional nanoparticulate photocatalysts (e.g., Aeroxide® P25) with the greatest reactivity enhancements arising from (i) decreasing diameter (i.e., increasing surface area); (ii) mixed phase composition [74/26 (±0.5) % anatase/rutile]; and (iii) small amounts (1.5 wt.%) of surface-deposited, more so than bulk-integrated, Au nanoparticles. Surface Au deposition consistently enhanced photoactivity by 5- to 10-fold across our micropollutant suite independent of their solution concentration, behavior that we attribute to higher photocatalytic efficiency from improved charge separation. However, the practical value of Au/TiO_2 nanofibers was

[1] A version of this chapter has been published: Nalbandian, M. J., Greenstein, K. E., Shuai, D., Zhang, M., Choa, Y., Parkin, G.F., Myung, N.V., and Cwiertny, D. M., *Tailored Synthesis of Photoactive TiO_2 Nanofibers and Au/TiO_2 Nanofiber Composites: Structure and Reactivity Optimization for Water Treatment Applications*. *Environ. Sci. Technol.*, 2015, **49**(3), p. 1654–1663.

limited by their greater degree of inhibition by solution phase radical scavengers and higher rate of reactivity loss from surface fouling in non-idealized matrices (e.g., partially treated surface water). Ultimately, unmodified TiO_2 nanofibers appear most promising for use as reactive filtration materials because their performance was less influenced by water quality, although future efforts must increase the strength of TiO_2 nanofiber mats to realize such applications.

2.2. Introduction

Engineered nanomaterials have immense, but as yet largely unrealized, potential for water treatment applications. Reactive nanomaterials have been demonstrated as high surface area adsorbents, (photo)catalysts, and antimicrobial or antifouling agents [92], often times with enhanced reactivity relative to larger or bulk materials. Nanotechnologies also hold the promise of being deployed across a range of treatment platforms, either as stand-alone technologies, integrated into conventional operations, or as point-of-use devices to polish tap water [93]. Harnessing these novel technologies may one day lessen society's reliance on centralized treatment systems while decreasing material and energy consumption associated with traditional water resource management [93].

Titanium dioxide (TiO_2) photocatalysts are among the most mature nanomaterial-enabled technologies from the perspective of fundamental research, having been extensively investigated as an alternative advanced oxidation process (AOP) [94–97]. Nevertheless, many well-recognized challenges hinder TiO_2 application in water treatment. Their inherent reactivity is relatively low compared to other AOPs (e.g., UV/ozone) [98] and they rely on high energy light (UVA; $\lambda < 390$ nm) that comprises only 5% of the solar spectrum. There are also a multitude of practical hurdles including the design,

modeling and scale-up needed for full-scale treatment plants [99–101]. Further, amid concerns over the environmental release of engineered nanomaterials [102–105], a major design consideration is mitigating TiO_2 loss or leaching into the treated water supply [106] even though nanoparticle immobilization on a support can adversely impact reactivity by sacrificing available surface sites [107]. Suspension instability may also be limiting if TiO_2 nanoparticle aggregation decreases reactive surface area [108,109]. Finally, in complex water matrices, scavengers of photogenerated reactive oxygen species (e.g., hydroxyl radical scavenging carbonate and natural organic matter) and surface fouling can limit treatment efficiency [110,111].

In light of these challenges, researchers have recently turned to electrospinning [112–117] as an innovative and scalable route for the synthesis of ultra-long TiO_2 nanofibers in a platform, a permeable two-dimensional nanofiber network, that is analogous to reactive filtration materials constructed from TiO_2 nanoparticles. However, while many studies have demonstrated the synthesis and photocatalytic activity of such nanofibers, relatively little work has been geared toward optimizing their structure, morphology and composition to improve performance in simulated water treatment. A major benefit of electrospinning is that the synthesis process is highly tunable, allowing nanofiber properties including diameter, grain size, phase composition and the integration of co-catalysts to be readily optimized for a targeted application [118,119]. Nevertheless, details on how the interplay of these variables influences the reactivity of TiO_2 nanofibers toward recalcitrant organic micropollutants (i.e., the typical target of AOPs), especially in aquatic matrices relevant to technology implementation, require further consideration. Instead, a number of studies [115,120–124] to date have utilized model pollutants (e.g.,

dyes) in highly idealized experimental systems that leave the practical utility of electrospun TiO_2 nanofibers very much in question.

Preliminary work for this study centered on the optimization of electrospun TiO_2 nanofibers for degradation of phenol by tuning diameter, grain size, and phase composition. Decreasing polymer concentration in sol-gel, from 15 to 12 wt.%, and increasing applied voltage, from 8 to 12 kV, during synthesis decreased average diameter of TiO_2 nanofibers, as shown in histograms in **Figure 2-1a**. Different phases of TiO_2, including pure anatase, mixtures of anatase/rutile, and pure rutile, were achieved by annealing electrospun nanofibers at different temperatures, ranging from 500 to 800°C (**Figure 2-1b**). Annealing temperature likewise impacted grain size (**Figure 2-2**). These materials were tested for degradation of phenol as a measure of reactivity. Ultimately, the most reactive TiO_2 nanofibers were those with narrow (30 nm) diameter (and thus having largest surface area to volume ratio) and mixed phase composition [74/26 (±0.5)% anatase/rutile] (**Figures 2-3, 2-4**), a phase ratio comparable to that of commercial P25 [125].

In this study, we use electrospinning to synthesize TiO_2 nanofibers with tailored structure and composition, and compare the performance of optimal nanofiber formulations to commercial nanoparticle photocatalysts across a range of treatment targets and water qualities. Using electrospinning, we obtained desired TiO_2 nanofiber properties (e.g., diameter, crystal structure, grain size) through previously explored synthesis parameters (e.g., applied voltage, annealing temperature). Nanofiber composition was also varied through fabrication of Au/TiO_2 composites because Au nanoparticle co-catalysts can potentially enhance reactivity not only by promoting charge separation akin to other noble metals (e.g., Pt) but also by surface plasmon resonance effects [115,126–128].

Properties of synthesized nanofibers and composites were obtained from microscopy and spectroscopy and then correlated with metrics of their photocatalytic activity toward a suite of model (phenol) and emerging (DEET, atrazine, sulfamethoxazole, and carbamazepine) organic micropollutants. Their longevity in matrices representative of drinking water treatment was also evaluated.

This work aims to establish the material properties of TiO_2 nanofibers and nanofiber composites most influential on photocatalytic activity and how the performance (i.e., reactivity and longevity) of optimal nanofiber formulations compares to traditional nanoparticle photocatalysts (e.g., Aeroxide® P25) in a treatment setting. Ultimately, outcomes of this work are the first step toward the development of nanofiber-enabled technologies with the potential for multi-functional chemical (e.g., oxidation) and physical (e.g., filtration) treatment of impaired water supplies.

2.3. Experimental methods

2.3.1. Reagents

All chemicals were reagent grade or better and used as received. The synthesis of the TiO_2 nanofibers involved titanium tetraisopropoxide (TTIP) (Sigma Aldrich, 97%), ethanol (Fisher Scientific, anhydrous), acetic acid (Fisher Scientific, glacial 99.7%) and polyvinylpyrrolidone (PVP) (Sigma Aldrich, MW: 1,300,000 g/mol). Gold(III) chloride trihydrate (Sigma-Aldrich, 49+% Au basis) and urea (Fisher Scientific, 99+%) were used to prepare Au/TiO_2 nanofiber composites.

A buffer solution prepared from 5 mM potassium phosphate monobasic (Fisher Scientific, 99.3%) with pH adjusted to 7 was used in all photoreactivity experiments. Aeroxide® P25 (Acros Organics) was used as a commercially available TiO_2 photocatalyst

for treatment efficiency comparison. Phenol (Sigma-Aldrich, 99+%), atrazine (Sigma-Aldrich, 98.8%), carbamazepine (Sigma-Aldrich, 98+%), N,N-Diethyl-meta-toluamide (DEET) (Sigma-Aldrich, 97.6%), and sulfamethoxazole (Sigma-Aldrich, 99+%) were used as organic micropollutants in photoactivity studies. Potassium nitrate (Fisher Scientific, 99.9%), humic acid sodium salt (Aldrich), magnesium chloride (Fisher Scientific, 99.4%), calcium chloride dihydrate (Fisher Scientific, 74.3%), sodium hydrosulfide hydrate (Acros Organics, 67+%), and isopropanol (Fisher Scientific, 70%v/v) were used as foulants and inhibitors in photoactivity studies. The eluents for HPLC analyses of micropollutants contained sodium acetate (Sigma Aldrich, anhydrous), potassium phosphate monobasic (Fisher Scientific, 99.3%), acetonitrile (ACN) (Fisher Scientific, 99.9%), and methanol (Fisher Scientific, 99.9%). All solutions were prepared in deionized (DI) water (Millipore, Milli-Q).

2.3.2. Synthesis of electrospun TiO_2 nanofibers

The synthesis of TiO_2 nanofibers began with the preparation of two separate solutions, the titanium precursor solution containing titanium tetraisopropoxide (TTIP) and the polymer solution containing polyvinylpyrrolidone (PVP). A designated amount of PVP (12 wt.% in the overall sol-gel) and 4.5 mL of ethanol were combined in a 50 mL glass beaker and stirred with a magnetic stirrer at a rate of 300 rpm for at least 2 hours, ensuring that all of the PVP had dissolved. Additionally, 1.68 mL of TTIP, 3 mL of ethanol and 3 mL of acetic acid were combined in a 50 mL glass beaker and stirred at a rate of 300 rpm for 10 minutes. After both solutions dissolved completely, they were mixed together for an hour, creating the desired electrospinning solution. We note that during creation of Au-embedded composite nanofibers, precursor metal salts were integrated into this electrospinning solution at the desired levels based upon wt.%.

For the electrospinning process, a 12 mL syringe was filled with the solution and loaded onto a Braun Perfusor syringe driver. Using polyethylene tubing, the syringe was attached to a stand retrofitted with a metallic syringe adapter and 25 gauge plastic needle tip from NanoNC (Korea). The stand was set 10 cm away from an aluminum foil-covered rotating drum, purchased from SPG Co., Ltd. (Korea), which acted as the grounded collector. The metal adapter was connected to an Acopian (Easton, PA) high-voltage power supply controlled by a computer via National Instrument Labview program. An applied voltage of 10 kV was utilized. As the solution slowly progressed through the system at a flow rate of 0.3 mL/hr, it became electrified as it reached the metal adaptor, forming a distorted conical shape, known as a Taylor cone due to the solution overcoming its naturally high surface tension. The tip of the cone expelled an electrified jet of fibers, forming a fibrous mesh on the grounded collector.

After 3 hours (a typical synthesis duration), the electrospinning was ceased and the Al foil coated with the nanofibers was removed and inserted into a drying oven (Yamato DVS 402) at 60 °C overnight. After this low heating, the nanofiber mat (typically 0.13 x 0.28 m^2) was peeled off and placed into a ceramic bowl for annealing in a box furnace (Thermolyne; Thermo Scientific). The furnace was heated to the desired temperature from room temperature at a rate of 3 °C/min, maintained at the desired temperature for 3 h, and cooled down to room temperature. An annealing temperature of 650 °C was used to control the relative abundance of possible crystal phases and to remove polymer. Such phase tuning was motivated by Aeroxide® P25 (hereafter simply P25), a mixed phase TiO_2 photocatalyst with anatase (70-80%) and rutile (20-30%) [107,129] that is frequently reported to outperform pure phases in reactivity studies [107,129–131]. Further, grain size,

which also was tuned by annealing temperature, provides a means to control crystallinity, which strongly influences the recombination rate of photogenerated holes and electrons. After annealing, typically 20-25 mg of nanofibers were produced.

2.3.3. Synthesis of composite TiO_2 nanofibers

Au/TiO_2 composites were synthesized either by (i) embedding Au nanoparticles in TiO_2 nanofibers using a one-pot synthesis or (ii) loading Au nanoparticles onto the surface of TiO_2 nanofibers using a post-synthesis chemical precipitation method. Au embedded TiO_2 nanofibers were prepared by incorporation of Au(III) chloride trihydrate into the precursor solution at loadings between 1-10 wt.% [132]. Alternatively, Au nanoparticles were loaded onto the nanofiber surface after electrospinning and annealing. For comparison, P25 nanoparticles with surface-deposited Au nanoparticles were also prepared.

2.3.4. Surface deposition of Au

Au nanoparticles were deposited onto the TiO_2 nanofiber surface via reductive precipitation with urea, resulting in Au contents between 0.25 and 10 wt.% (assuming complete deposition). Based on previous work [133], a suspension (1 g/L) of TiO_2 nanofibers was dispersed via sonication (Bransonic Ultrasonic Cleaner Model 1510), and then the desired amount of Au precursor solution (i.e., gold(III) chloride trihydrate) and urea solution were added and thoroughly mixed at 80 ºC for 4 hours in a thermomixer (HLC by DITABIS Model MKR 13). The molar concentration ratio between urea and Au was at least 100, and it facilitated Au deposition by increasing solution pH to 8 after thermal decomposition of urea. Au/TiO_2 nanofibers were separated from solution by centrifugation at 14,000 rpm (16,900 g) for 10 minutes, washed with DI water and centrifuged (a process repeated three times), dried at 100 ºC overnight in an oven (Fisher Scientific Isotemp Oven

Model 750G), and subsequently annealed at 300 ºC for 4 hours in air in a tube furnace (MTI OTF-1200X-80).

2.3.5. Details of photocatalyst material and optical characterization

Nanofiber diameter, as well as Au nanoparticle size and distribution in composites, was examined by scanning electron microscopy (SEM) and transmission electron microscopy (TEM) with energy dispersive X-ray spectroscopy (EDX). Nanofiber crystal phase and average grain size were determined by X-ray diffraction (XRD). Surface composition was examined with X-ray photoelectron spectroscopy (XPS).

Nanofiber diameter and Au nanoparticle size were examined with a Phillips XL30 FEG scanning electron microscope (SEM). For SEM, samples were prepared by placing approximately a 0.5 cm x 0.5 cm area of nanofibers onto a SEM sample holder. SEM imaging of n = 100 nanofibers yielded average diameters (with standard deviation) that were used to create sizing histograms. Transmission electron microscopy (TEM) with energy dispersive X-ray spectroscopy (EDX) (JEOL JEM 2100F field emission transmission electron microscope) was also used to explore the spatial distribution and estimate the size of Au nanoparticles on TiO_2 nanofibers.

Crystal phase and average grain size were determined by a Bruker D8 Advance X-ray diffractometer (XRD). XRD samples were prepared by depositing a 1 x 1 cm^2 area of nanofibers onto a glass slide. Samples were analyzed from 20° to 80° for the Bragg angle with an interval of 0.03°. Using XRD analysis, the crystal structure, crystal orientation, and average grain size were determined. The motivation for crystal phase tuning is that Aeroxide®, a mixed phase TiO_2 with an anatase to rutile ratio of 70-80:20-30 [107,129], outperforms both pure phases in reactivity studies [130]. Moreover, grain size tuning represents a means to control crystallinity, which strongly influences the recombination

rate of photogenerated holes and electrons. Using the XRD spectra data, the rutile percent composition was calculated by means of equation 2-1 [134]:

$$R(\%) = \frac{0.79\left(\frac{IR}{IA}\right)}{1+\left(0.79\left(\frac{IR}{IA}\right)\right)} \tag{2-1}$$

where *IR* is the intensity of the rutile peak (1 1 0) at 2θ = 27.5° and *IA* is the intensity of the anatase peak (1 0 1) at 2θ = 25.4°. The average grain size was calculated by the Scherrer-Debye equation, as seen in equation 2-2 [134]:

$$D = \frac{k\lambda}{Bcos\theta} \tag{2-2}$$

where *D* is the average grain size in nm, *k* is the shape factor constant (0.9), λ is the wavelength used by XRD (0.154 nm), *B* is the broadening of the diffraction line measured by the full width at half maximum of the peak and θ is the Bragg angle of the peak from the XRD spectrum.

Extinction and absorption coefficients were determined with the Thermo Scientific Evolution 300 UV-Vis spectrophotometer and the Praying Mantis diffuse reflectance infrared Fourier transform spectroscopy (DRIFTS) accessory. The specific extinction coefficients (L/cm·g) were calculated using the absorbance measured for 0.1 g/L suspensions of material by UV-vis spectrophotometer with equation 2-3:

$$\varepsilon_\lambda = \frac{2.303A}{d*C_{cat}} \tag{2-3}$$

where ε_λ is the specific extinction coefficient (L/cm·g), A is the measured absorbance, *d* is the cell path length (cm), and C_{cat} is the mass concentration of the catalyst (g/L) [135]. General extinction coefficients (cm^{-1}) were determined by multiplying specific extinction coefficients by mass concentration of catalyst. Optical thicknesses (τ, unitless) of the 0.1 g/L suspensions were determined using equation 2-4:

$$\tau = \varepsilon_\lambda * d * C_{cat} \quad (2\text{-}4)$$

The extinction coefficient is equal to the absorption coefficient, K, plus the scattering coefficient, S [136,137]. From DRIFTS on the dry materials and Kubelka-Munk calculations, ratios of the coefficients (K/S values) were determined. Using extinction coefficients and K/S values, absorption coefficients and scattering coefficients were algebraically determined. Specific extinction coefficients, absorption coefficients, scattering coefficients, and optical thicknesses for materials are given in **Figure 2-5**.

The surface-chemical composition of Au/TiO_2 nanofibers reacted in UIWTP sedimentation basin effluent was investigated using a custom-designed Kratos Axis Ultra X-ray photoelectron spectroscopy (XPS) system equipped with a monochromatic Al Kα X-ray source. An extensive description of this system can be found elsewhere [138,139]. For XPS, Au/TiO_2 nanofiber samples were collected from 0.1 g/L suspensions after reaction (immediate and 24 h aging in sedimentation basin effluent). Samples were immobilized on a 13 mm polyvinylidene difluoride (PVDF) filter, and samples were washed extensively with DI water (~40 mL) prior to analysis. PVDF filters were mounted on Cu stubs for analysis. XPS was used to collect full spectrum survey scans, as well as to examine O 1s, C 1s, Ti 2p, and Au 4f regions.

2.3.6. Photocatalysis experiments

Reactivity experiments were conducted in batch systems using a commercially available 1000 W Xenon arc lamp (Newport Corporation) equipped with a 305 nm long-pass filter to better simulate the wavelengths of light available at earth's surface. For the 1000 W Xenon arc lamp, the light was first passed through a water filter to remove infrared (IR) radiation, reflected off a 90° full reflectance beam turning mirror, and then passed

through a long-pass filter with cut-on wavelength of 305 nm to better simulate the wavelengths of light available at earth's surface. More details of this system can be found elsewhere [140].

Lamp irradiance at wavelengths of 250 nm and greater was measured with a spectroradiometer (ILT950) at reactor height. Photon fluence (photons/cm^2·s) was then calculated at each wavelength using equation 2-5:

$$\frac{dN_{p\lambda}}{dt} = P_\lambda \lambda * 5.03 * 10^{15} \quad (2\text{-}5)$$

where P_λ is the irradiance at a given wavelength (W/cm^2), λ is wavelength (nm), and 5.03x10^{15} is a factor incorporating Planck's constant and the speed of light [141]. Photon fluence for each wavelength was plotted versus wavelength, and the curve was integrated from 305 nm to 400 nm to determine photon fluence over the range of absorbable photons for the TiO_2 materials in reactions. This fluence was 6.13x10^{15} photons/cm^2·s. For all reactions, time can be multiplied by photon fluence to analyze kinetics in terms of photon fluence.

Reactivity studies were conducted within a jacketed photoreactor with catalyst suspensions (0.005-0.1 g/L) that were well mixed (with magnetic stir bar and stir plate), prepared at pH 7 (5 mM phosphate buffer) and maintained at 25 °C with a recirculating water bath. The majority of experiments were conducted at 0.1 g/L, at which optical properties (e.g., optical thickness, specific extinction coefficient, scattering coefficient and absorption coefficient) for photocatalyst suspensions were quantified as previously described. This loading was sufficient to produce optical thicknesses (τ) recommended for optimal photon absorption efficiency [136].

Reactivity of TiO_2 nanofibers, nanofiber composites (Au/TiO_2) and P25 nanoparticles was explored toward a suite of organic targets over a range of initial concentrations (5-100 μM). Experiments to optimize diameter, grain size and Au loading of TiO_2 nanofibers employed phenol. Once an optimal nanofiber formulation was identified, additional reactivity studies were conducted with a set of organic micropollutants, *N,N*-Diethyl-meta-toluamide (DEET), atrazine, carbamazepine and sulfamethoxazole, known to be recalcitrant to traditional treatment processes [142]. First, suspensions of 1 g/L TiO_2 nanofibers were prepared in DI water and dispersed via sonication (Bransonic Ultrasonic Cleaner Model 1510) for 5 hours. Suspended TiO_2 nanomaterials and a given target pollutant (phenol, atrazine, carbamazepine, DEET, or sulfamethoxazole) were added to 5 mM phosphate buffer adjusted to pH 7 in a jacketed reactor, having a total reaction volume of 15 mL. The reactor had a diameter of 3.7 cm and starting depth of solution of 1.5 cm. The surface of the solution was centered 18 cm below the lamp, which had a beam width of 4.8 cm. The solution was stirred for 20 minutes in the dark in order to ensure solution homogeneity, after which a 700 μL sample was taken to quantify the initial pollutant concentration. There was no indication of sorption of any pollutants onto the nanofibers based on comparison of this initial concentration with measurements made in control reactors without nanofibers. The reactor was then irradiated (typically for 60 minutes), during which aliquots were withdrawn periodically to measure change in aqueous phase concentration of the pollutant target. Samples were centrifuged at 10,000 rpm (8,600 g) for 8 min in the dark to allow extraction of the supernatant. The supernatant was transferred to a 1.5 mL amber autosampler vial for subsequent analysis

via high performance liquid chromatography with photodiode array detector (1200 Series Agilent HPLC-DAD).

To explore the influence of water quality on performance, particularly matrices representative of water treatment systems, the reactivity of optimal nanofibers toward DEET was explored in water samples collected from the University of Iowa Water Treatment Plant (UIWTP). The UIWTP treats a surface water source (the Iowa River) with a process train of coagulation/ flocculation, sedimentation, softening, chlorination and filtration. Samples were collected after filtration (simulating photocatalytic treatment as a final polishing step for drinking water) and after sedimentation (simulating photocatalytic treatment applications in dirtier matrices). Following the general set-up described above, TiO_2 or Au/TiO_2 nanomaterials and DEET (the target in all real water systems) were added to either sedimentation basin effluent or clearwell effluent from the University of Iowa Water Treatment Plant. For longevity studies, TiO_2 nanomaterials were added to sedimentation basin effluent or clearwell effluent and these mixtures were magnetically stirred in the dark for 24 hours. DEET was added to the reactor 20 minutes before irradiation to ensure solution homogeneity, and again, there was no evidence of sorption in any system. According to analyses conducted by the UIWTP, the sedimentation basin effluent had alkalinity of 224 mg/L, pH of 7.4, and turbidity of 0.9 NTU. The clearwell effluent had alkalinity of 40 mg/L, pH of 9.5, and turbidity of 0.07 NTU.

Complementary experiments with the model radical scavenger isopropanol [140] and individual components of UIWTP water samples provided insights into constituents most influential on photocatalyst performance. Constituents investigated included carbonate ($\leq$ 5 mM $NaHCO_3$), organic matter ($\leq$ 5 mg/L Aldrich humic acid sodium salt),

hardness (≤ 50 mM $CaCl_2$ or $MgCl_2$), nitrate (≤ 5 mg-N/L as KNO_3) and reduced sulfur (≤ 100 μM NaHS), with concentration ranges chosen to span those of natural waters.

2.3.7. HPLC analytical details

The 1200 Series Agilent HPLC-DAD was equipped with an Eclipse XDB-C18 column (4.6 × 50 mm, 1.8 μm particle size). The HPLC method of analysis for phenol was based on previous work and employed a mobile phase of 65:35 1 mM sodium acetate: ACN at pH 3, a flow rate of 0.75 mL/min, an injection volume of 20 μL and a 254 nm detection wavelength [143]. The HPLC method of analysis for atrazine was based on previous work and employed a mobile phase of 50:50 DI water: ACN, a flow rate of 1 mL/min, an injection volume of 100 μL and a 223 nm detection wavelength [144]. The HPLC method of analysis for carbamazepine was based on previous work and had a mobile phase of 55:45 DI water: ACN, a flow rate of 1 mL/min, an injection volume of 25 μL, and a 213 nm detection wavelength [145]. For DEET, the HPLC method of analysis employed a 60:40 5 mM potassium phosphate monobasic: ACN (all adjusted to pH 3), a flow rate of 1 mL/min, an injection volume of 100 μL, and a 220 nm detection wavelength. The HPLC method of analysis for sulfamethoxazole had a mobile phase of 70:30 5 mM potassium phosphate monobasic adjusted to pH 5: methanol, a flow rate of 1 mL/min, an injection volume of 20 μL, and a 268 nm detection wavelength.

2.4. Results and discussion

2.4.1. Influence of Au co-catalysts on photocatalytic activity

For Au embedded TiO_2 nanofiber composites, representative SEM images and pictures are shown in **Figure 2-6a and 2-6b**. These materials were synthesized by addition of up to 10 wt.% Au(III) chloride trihydrate (relative to TiO_2) to the electrospinning

solution and using the d = 60 nm protocol (PVP 12 wt.%, voltage 10 kV) with subsequent annealing at either 500 or 650 °C for 3 h. Embedded composites were blue in color, and elemental mapping (**Figure 2-6c**) indicated the Au nanoparticles (~5-10 nm) were uniformly distributed and primarily embedded within the TiO_2 nanofibers. Alternatively, reductive deposition with urea (**Figure 2-7**) produced composites with relatively uniformly, albeit sparsely, distributed Au nanoparticles (~2-5 nm) on the TiO_2 nanofiber surface. Surface-loaded Au/TiO_2 composites, prepared across a range of Au concentrations (up to 10 wt.% relative to TiO_2), were pink in color, matching the typical appearance of Au nanoparticles in aqueous solution.

In subsequent reactivity studies with phenol **(Figure 2-8**), Au embedded nanofibers exhibited a slight reactivity enhancement (~2-fold) at a loading of 2 wt.%, but no positive effect on photoactivity was observed at any other level explored. In fact, although not entirely understood, the highest Au loading considered (10 wt.%) actually inhibited photoactivity relative to unmodified TiO_2 nanofibers, while their reactivity was further diminished when annealed at higher temperatures (e.g., 500 °C vs. 650 °C). In contrast, surface-loaded Au composites exhibited significantly enhanced photoactivity, particularly at low Au contents (i.e., 0.25-5 wt.%; nominal values assuming complete surface deposition during synthesis). The optimal Au surface loading of 1.5 wt.% was nearly 7-fold more reactive than unmodified TiO_2 nanofibers. Thus, while not as convenient as the one-pot synthesis used for Au embedded nanofibers, surface deposited composites are the superior alternative from the standpoint of reactivity. We note that at higher surface Au contents (5 and 10 wt.%), reactivity decreased and eventually became inhibited relative to bare TiO_2 nanofibers, though not to the extent seen with embedded Au. The clear maximum

in reactivity at 1.5 wt.% likely implies that an optimal size of deposited Au nanoparticles is achieved at this loading, a property known to influence the performance of nanoparticulate Au as a co-catalyst [146].

2.4.2. Comparison of nanofiber reactivity relative to commercial nanoparticle photocatalysts

Using TiO_2 nanofibers (d = 60 nm) and Au/TiO_2 composites (1.5 wt.% of surface Au on d = 60 nm nanofibers), additional experiments compared their reactivity relative to P25, a traditional nanoparticle catalyst, and an Au modified P25 (Au/P25) prepared using the same surface deposition process with urea (**Figure 2-7d**). We note that we used d = 60 nm nanofibers in these studies (rather than most reactive d = 30 nm materials) because they were more reliably synthesized in large quantities (i.e., using longer electrospinning times) needed for these comparative studies. Concentration versus time plots for phenol and DEET are shown in **Figure 2-9,** which shows pollutant conversion both as a function of time and fluence in irradiated photocatalyst suspensions. These profiles and corresponding k_{obs} values (**Table 2-1**) reveal the general reactivity trend of Au/TiO_2 nanofibers ≈ Au/P25 >> P25 > TiO_2 nanofibers. Because this trend was developed with 60 nm diameter nanofibers, we expect that the relative reactivity of nanofibers and P25 may change with smaller diameter, higher surface area nanofibers (see **Figure 2-4a**).

This trend holds across a range of system variables including photocatalyst suspension loading (from 0.005 – 0.1 g/L; **Figure 2-10** and **Table 2-2**), and the initial concentration (**Figure 2-11a**) and type of pollutant target (**Figure 2-11b**). For example, **Figure 2-11a** shows k_{obs} values for phenol transformation across a range of initial phenol concentrations. Consistent with prior reports with phenol [147–150], k_{obs} values from all

systems decreased monotonically over the range of concentration explored (5-100 μM). This behavior was also observed for DEET (**Figure 2-12**) and is often interpreted as evidence of reactive surface sites becoming saturated at high pollutant concentrations. Nevertheless, changes in k_{obs} for unmodified TiO_2 nanofibers mirrored those of P25 across all phenol levels, while the reactivity of both Au-modified composites was statistically equivalent and roughly 6-fold greater than their unmodified counterparts. Similarly, **Figure 2-11b** compares k_{obs} values for each photocatalyst type for atrazine, carbamazepine, DEET, and sulfamethoxazole degradation at a fixed initial micropollutant concentration of 20 μM. As with phenol, reactivity was comparable between TiO_2 nanofibers and P25, while the addition of surface Au at 1.5 wt.% increased k_{obs} values by roughly one order of magnitude (ranging from 6- to 13-fold for Au/TiO_2 nanofiber composites**)** across the suite.

Converging lines of evidence, therefore, suggest that TiO_2 nanofibers and Au-modified nanofiber composites exhibit reactivity near equivalent to that expected from more traditional nanoparticle catalysts. Not surprisingly, measured bandgaps were essentially identical for P25 and TiO_2 nanofibers (3.19 and 3.21 eV, respectively), while identical bandgap shifts were observed upon Au modification of P25 and TiO_2 nanofiber surfaces (2.79 eV for both). Accordingly, measured absorption coefficient profiles (as a function of wavelength) were comparable for TiO_2 nanofibers and P25, as well as for both types of Au-modified photocatalysts (**Figure 2-5**), consistent with observed similarities in the macroscopic measures (e.g., k_{obs} values) of their photocatalytic reactivity.

We propose the superior performance of Au-modified materials primarily results from improved charge separation. While Au nanoparticles may also enhance the response of TiO_2 to visible light through local surface plasmon resonance (LSPR) [126,127],

photooxidation experiments under visible light (using a long-pass optical filter for λ >400 nm) resulted in negligible pollutant (phenol and DEET) degradation over the timescales typical under UV plus visible light (>305 nm). Because proximity of Au nanoparticles is critical for promoting LSPR effects of supported Au nanoparticles [151–153], this lack of visible light activity is likely due to the low spatial density of Au nanoparticles on the TiO_2 nanofiber surface (see **Figure 2-7**). The most likely mechanism of enhancement, therefore, is the ability of Au nanoparticles to act as sinks for photogenerated conduction band electrons, thereby improving charge separation and promoting charge migration to the catalyst surface [154–156].

Comparable molecular-level processes also appear responsible for pollutant transformation in all photocatalyst systems. Experiments with DEET in the presence of the model radical scavenger isopropanol (IPA) inhibited reactivity of all materials, suggesting radical involvement in transformation reactions (**Figure 2-13a**). However, while k_{obs} values decreased with increasing IPA concentration for all photocatalysts, Au-modified materials were consistently more sensitive to inhibition (e.g., 1 mM isopropanol reduced k_{obs} values by 90% in Au-modified photocatalyst systems, while only a 70% reduction was observed for unmodified materials). The greater degree of inhibition for Au-modified relative to unmodified TiO_2 photocatalysts may reflect differences in the nature and/or distribution (e.g., near-surface versus bulk solution) of reactive radicals present in each system.

Additional mechanistic insights into pollutant transformation were obtained through transformation product yields, which were identical across all photocatalyst systems (**Figure 2-14**) and development of reactivity cross correlations [157,158] that

compared k_{obs} values from each TiO_2 system to published [159–161] second-order rate coefficients for micropollutant reaction with hydroxyl radical (k_{OH} values), the presumptive oxidizing agent based upon results with IPA. For TiO_2 nanofibers a linear relationship between log(k_{obs}) and log(k_{OH}) was observed (**Figure 2-13b**), implying that the rate of reaction with hydroxyl radical ($^{\bullet}OH$), either in bulk solution or at the surface, governs the overall rate of pollutant transformation in nanofiber systems. Interestingly, P25 produced k_{obs} values that were essentially independent of corresponding micropollutant k_{OH} values (**Figure 2-13c**). Thus, while $^{\bullet}OH$ may still be the reactive entity, there are likely other steps in the sequence of pollutant transformation (e.g., surface adsorption or product desorption) that are rate-limiting in our P25 systems. Positive, albeit weaker, correlations between log(k_{obs}) and log(k_{OH}) were also observed for both Au/TiO_2 and Au/P25 (**Figure 2-15**), a notable observation for Au/P25 given the absence of such a correlation for unamended P25.

2.4.3. Performance comparison in matrices representative of water treatment

In effluent from the UIWTP sedimentation basin (collected prior to softening, chlorination and filtration) (**Figure 2-16a**), Au/TiO_2 nanofibers exhibited a near-immediate, more than 20-fold loss in reactivity toward DEET relative to model water (phosphate buffer) systems. This ultimately resulted in Au/TiO_2 nanofibers exhibiting less reactivity than was observed for unmodified TiO_2 nanofibers, whose reactivity only decreased by a factor of 3 when dispersed in sedimentation basin effluent. The greater, near immediate inhibition of Au/TiO_2 reactivity is consistent with expectations from our IPA results, suggesting that radical inhibitors present in the water sample (e.g., carbonate or organic matter) are likely responsible for most of this activity loss. Notably, the extent of reactivity loss increased over time for Au-modified materials; after 24 h of catalyst mixing

(i.e., "aging") in sedimentation basin effluent, Au/TiO_2 nanofibers were nearly unreactive toward DEET over the timescales considered. In contrast, TiO_2 nanofibers exhibited essentially equivalent reactivity over this aging period. Thus, in addition to their greater susceptibility to inhibition by radical scavengers, reactivity loss over time suggests the Au surface is also more prone to fouling. This behavior was also observed for Au-modified P25 in natural water samples (**Figure 2-17**).

Analogous behavior was observed in clearwell effluent (i.e., finished water; **Figure 2-16b**). Even in this cleaner matrix, Au/TiO_2 nanofibers exhibited more than a 10-fold immediate loss in reactivity relative to model water systems. Reactivity loss continued after 24 h of aging, although the extent (2-fold) was not as pronounced as in sedimentation basin effluent. In contrast, the reactivity of unmodified TiO_2 nanofibers in clearwell effluent was comparable to that in model water systems, regardless of the extent of their aging. In fact, performance of unmodified TiO_2 nanofibers was nearly independent of water quality in UIWTP samples, with only modest differences in k_{obs} values for DEET transformation measured in either clearwell effluent or sedimentation basin effluent (**Table 2-3**).

Experiments with individual, model constituents likely encountered in natural water samples provided limited insight as to the agent likely responsible for the reactivity loss of Au/TiO_2 over time in UIWTP samples (**Figure 2-18**). While a few components produced some near-immediate reactivity loss (i.e., $CaCl_2$, $MgCl_2$ and NaHS), additional reactivity loss over 24 h of Au/TiO_2 aging was only observed at the highest concentration of $MgCl_2$ explored (50 mM, which is well beyond environmental relevance) and the decrease in reactivity was not nearly enough to account for that observed in sedimentation basin effluent.

Given the inability of model systems to mimic the extent of reactivity loss over time for Au/TiO_2, we hypothesize that dissolved organic matter in the UIWTP samples is most likely responsible for fouling. Given the complexity of natural organic matter, it is unlikely that the surrogate used in these experiments (Aldrich humic acid) accurately reflects the diverse nature of organic matter present in Iowa River water, which is impacted by both agricultural runoff and domestic wastewater effluent. Further, XPS characterization of Au/TiO_2 samples over 24 h of aging in sedimentation basin effluent only revealed changes in the O and C regions, while all other relevant regions (e.g., Ti, Au) remain unchanged. Finally, we note that in a limited number of attempts to react aged Au/TiO_2 materials over longer periods of irradiation, a small amount of reactivity could be restored to passivated Au/TiO_2 after extended light exposure, which we believe suggests a passivating agent susceptible to oxidative breakdown over time. While the exact nature of organic matter foulant remains unclear, evidence suggests that the performance of Au-modified photocatalysts will be more sensitive to water quality characteristics.

2.5. Conclusion

Growing interest in nanotechnology has led to significant advances in material synthesis, which in turn has produced a plethora of uniquely structured nanomaterials often touted as next-generation water treatment options. However, although there is little doubt as to the significant promise nanomaterials possess for water treatment applications, it is often unclear whether innovative, highly tailored nanostructures can ever be viable alternatives in practice.

We have attempted to bridge the existing gap between fundamentals and practice for electrospun TiO_2 nanofibers, a promising synthesis route given the high degree of

tailoring it affords to nanomaterial structure and composition. We demonstrate that the photocatalytic performance of TiO_2 nanofibers is governed by the same material, physical, chemical and optical properties established for traditional nanoparticle TiO_2 photocatalysts (e.g., P25). Accordingly, electrospun nanofibers are perhaps an ideal focal point for future technology development based on the advantages this approach provides, specifically the ability to fabricate nanomaterials with tunable properties that can be integrated into treatment as a reactive nanofiber networks, mats or coatings.

Our work provides the best strategies for optimizing nanofiber reactivity in such applications. Most notably, the practical value of Au nanoparticles as a co-catalyst must be carefully considered due to their greater propensity for inhibition by radical scavengers and fouling, even in relatively clean matrices such as the finished product water from the UIWTP. Au-modified materials appear best applied to high purity matrices after extensive pretreatment (e.g., high pressure membranes). Perhaps, therefore, materials like the Au/TiO_2 nanofibers can find value in select cases as an alternative AOP as a final polishing step for drinking water, particularly when targeting recalcitrant dissolved constituents only prone to degradation by $^{\bullet}OH$.

A far more versatile technology may be unmodified TiO_2 nanofibers, which showed reactivity that was relatively invariant to water quality in UIWTP samples. Despite their lower inherent reactivity relative to Au/TiO_2 in model systems, the unmodified materials exhibited better longevity and a lower propensity for inhibition and fouling herein. Thus, more sustained gains in reactivity might be attained simply by fabricating nanofibers with the largest available specific surface area (i.e., smallest diameter) or through reactors designed to maximize contact time between illuminated nanofibers and target pollutants.

We acknowledge, however, that their performance needs to be explored over longer timescales and in flow through systems more representative of their intended application platform.

A critical design consideration that merits immediate attention is material robustness; although smaller diameter nanofibers will be best from a reactivity standpoint, they may compromise material strength, promoting mechanical failure of electrospun mats that may promote nanofiber release. Future work, including work in subsequent chapters, must aim to identify optimal materials at the interface of reactivity and strength. For example, while the TiO_2 nanofiber mats we have synthesized (**Figure 2-19**) can be picked up and gently manipulated, they exhibit limited mechanical strength and are prone to fracture. In fact, we were not able to quantify mechanical properties of optimal TiO_2 mats because they routinely fractured during preparation of samples for stress-strain analysis using a standard load cell. Nanofiber composites, particularly those utilizing carbon nanotubes, may be promising in this regard for increasing material strength. Another promising approach is the hydrothermal treatment of TiO_2 nanofiber mats; although this treatment considerably alters nanofiber structure, it produces a stronger mat that may be more robust for treatment applications (**Figure 2-20**). We anticipate, however, that synthetic approaches intended to increase material strength will undoubtedly influence, perhaps negatively, reactivity. Thus, going forward, an appropriate balance between material reactivity and strength must be found to fulfill the promise of TiO_2 nanofiber mats as a reliable water treatment technology.

Table 2-1. Representative k_{obs} values for DEET and phenol transformation in photocatalytic systems considered herein. Values are provided both in terms of time and fluence, and correspond to data contained in **Figure 2-9**. Experimental conditions: pH 7, 0.1 g/L photocatalyst, 20 μM of initial DEET or phenol.

DEET	k_{obs} (min^{-1})	k_{obs} ($cm^2/10^{18}$ photons)
P25	1.1 (± 0.1) x 10^{-1}	2.9 (± 0.4) x 10^{-1}
TiO_2 NFs	6.4 (± 0.5) x 10^{-2}	1.7 (0.1) x 10^{-1}
Au/P25	5.1 (± 0.1) x 10^{-1}	1.37 (± 0.03)
Au/TiO_2 NFs	6.7 (± 0.2) x 10^{-1}	1.83 (± 0.05)
Phenol	k_{obs} (min^{-1})	k_{obs} ($cm^2/10^{18}$ photons)
P25	1.5 (± 0.1) x 10^{-1}	4.0 (± 0.4) x 10^{-1}
TiO_2 NFs	7.2 (± 0.4) x 10^{-2}	2.0 (± 0.1) x 10^{-1}
Au/P25	9.4 (± 0.5) x 10^{-1}	2.6 (± 0.1)
Au/TiO_2 NFs	6.52 (± 0.04) x 10^{-1}	1.77 (± 0.01)

Table 2-2. Values of k_{obs} for DEET transformation as a function of photocatalyst suspension loading (in g/L). Values are provided both in terms of time and fluence, and correspond to data contained in **Figure 2-10**. Experimental conditions: pH 7, 0.005-0.1 g/L photocatalyst, 20 μM of initial DEET.

	k_{obs} (min^{-1})			k_{obs} ($cm^2/10^{18}$ photons)		
Solids Loading	0.005 g/L	0.01 g/L	0.1 g/L	0.005 g/L	0.01 g/L	0.1 g/L
P25	1.5 (± 0.2) x 10^{-2}	7.4 (± 0.6) x 10^{-2}	2.0 (± 0.1) x 10^{-1}	4.2 (± 0.5) x 10^{-2}	2.0 (± 0.2) x 10^{-1}	5.3 (± 0.4) x 10^{-1}
TiO_2 NFs	3.9 (± 0.6) x 10^{-3}	1.2 (± 0.2) x 10^{-2}	7.6 (± 0.5) x 10^{-2}	1.1 (± 0.2) x 10^{-2}	3.3 (± 0.5) x 10^{-2}	2.1 (± 0.1) x 10^{-1}
Au/P25	7.0 (± 0.3) x 10^{-2}	1.47 (± 0.08) x 10^{-1}	9 (± 2) x 10^{-1}	1.90 (± 0.08) x 10^{-1}	4.0 (± 0.2) x 10^{-1}	2.4 (± 0.5)
Au/TiO_2 NFs	4.27 (± 0.05) x 10^{-2}	1.29 (± 0.03) x 10^{-1}	6.5 (± 0.2) x 10^{-1}	1.16 (± 0.01) x 10^{-1}	3.51 (0.07) x 10^{-1}	1.76 (± 0.04)

Table 2-3. Values of k_{obs} for DEET (20 µM) in phosphate buffer (PB), clearwell effluent (CW), clearwell effluent, clearwell effluent after mixing for 24 hours with nanomaterials (CW-24), sedimentation basin effluent (SB), and sedimentation basin effluent after mixing for 24 hours with nanomaterials (SB-24). Values are provided for 1.5 wt.% Au/P25, 1.5 wt.% Au/TiO_2 nanofibers, P25, and TiO_2 nanofibers. Values correspond to data show in **Figure 2-16** and in **Figure 2-17**.

	k_{obs} (min^{-1})				
	PB	**CW**	**CW-24**	**SB**	**SB-24**
Au/P25	6.8 (± 0.6) x 10^{-1}	1.6 (± 0.1) x 10^{-1}	6.9 (± 0.4) x 10^{-2}	2.7 (± 0.4) x 10^{-2}	7 (± 1) x 10^{-3}
Au/TiO_2 NF	8 (± 4) x 10^{-1}	6.2 (± 0.4) x 10^{-2}	3.3 (± 0.4) x 10^{-2}	3.4 (± 0.2) x 10^{-2}	9 (± 5) x 10^{-4}
P25	1.22 (± 0.04) x 10^{-1}	1.04 (± 0.08) x 10^{-1}	1.5 (± 0.1) x 10^{-1}	4.86 (± 0.09) x 10^{-2}	4.3 (± 0.5) x 10^{-2}
TiO_2 NF	1.26 (± 0.08) x 10^{-1}	4.8 (± 0.1) x 10^{-2}	2.9 (± 0.2) x 10^{-2}	3.93 (± 0.09) x 10^{-2}	4.0 (± 0.9) x 10^{-2}

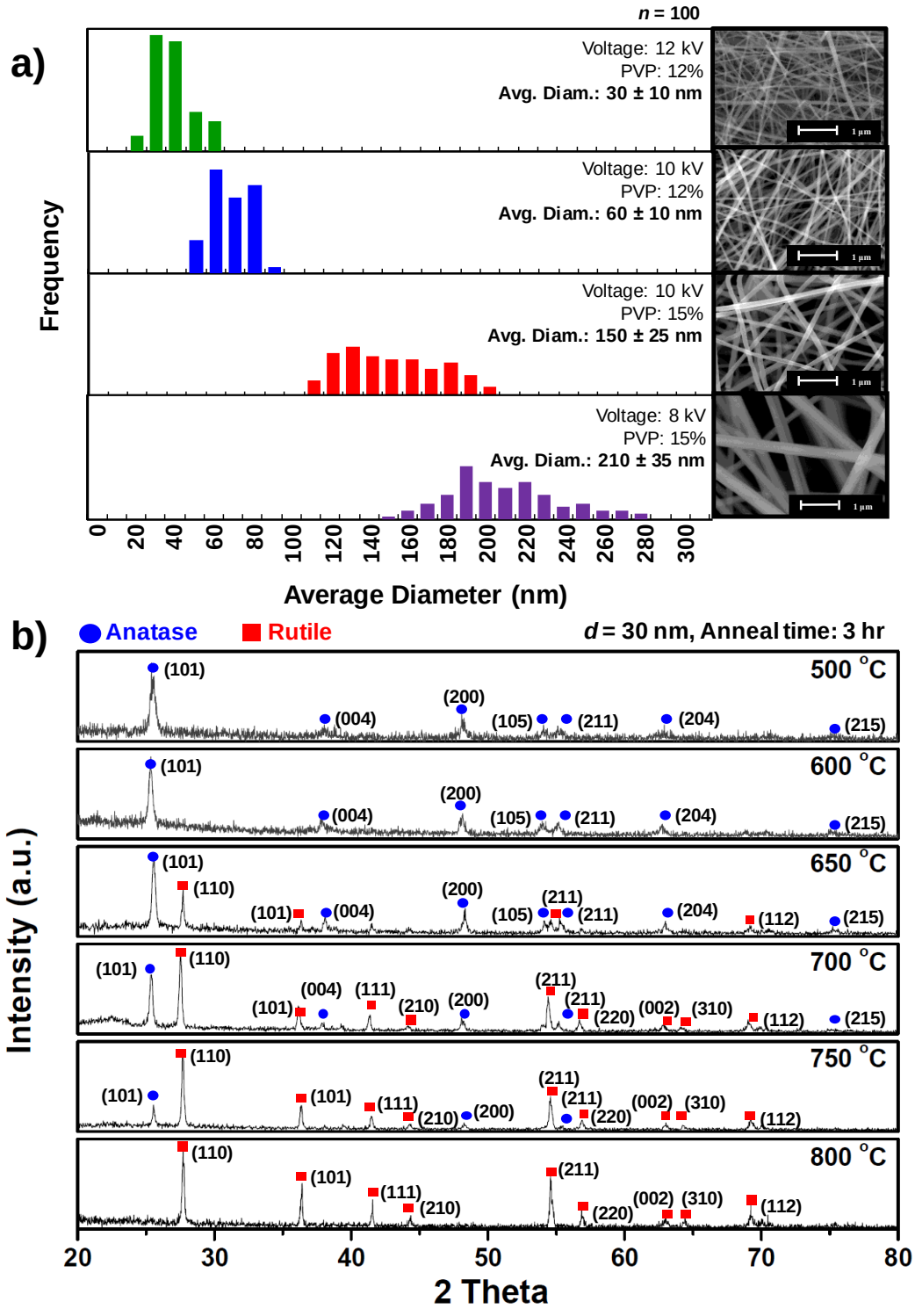

Figure 2-1. (a) Histogram of TiO_2 nanofiber diameter (average and standard deviation from n = 100 fibers) with associated SEM images. (b) XRD pattern of synthesized TiO_2 nanofibers (d = 30 nm) as a function of annealing temperature [91].

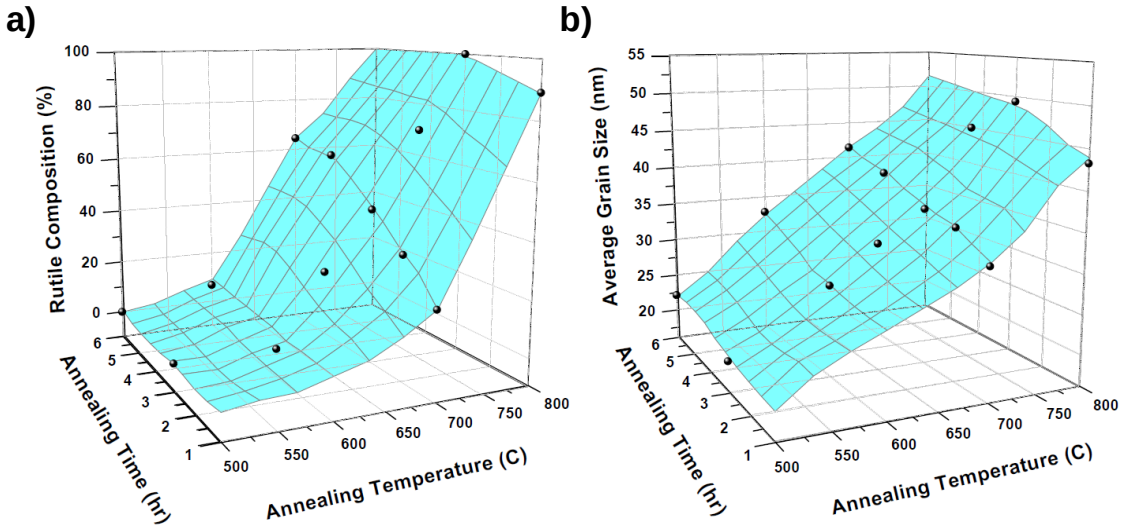

Figure 2-2. 3D surface plots of TiO_2 nanofiber (a) rutile content and (b) average grain size as a function of annealing temperature (500-800 °C) and annealing time (1-6 hours) for nanofibers with average diameter of 30 nm [91].

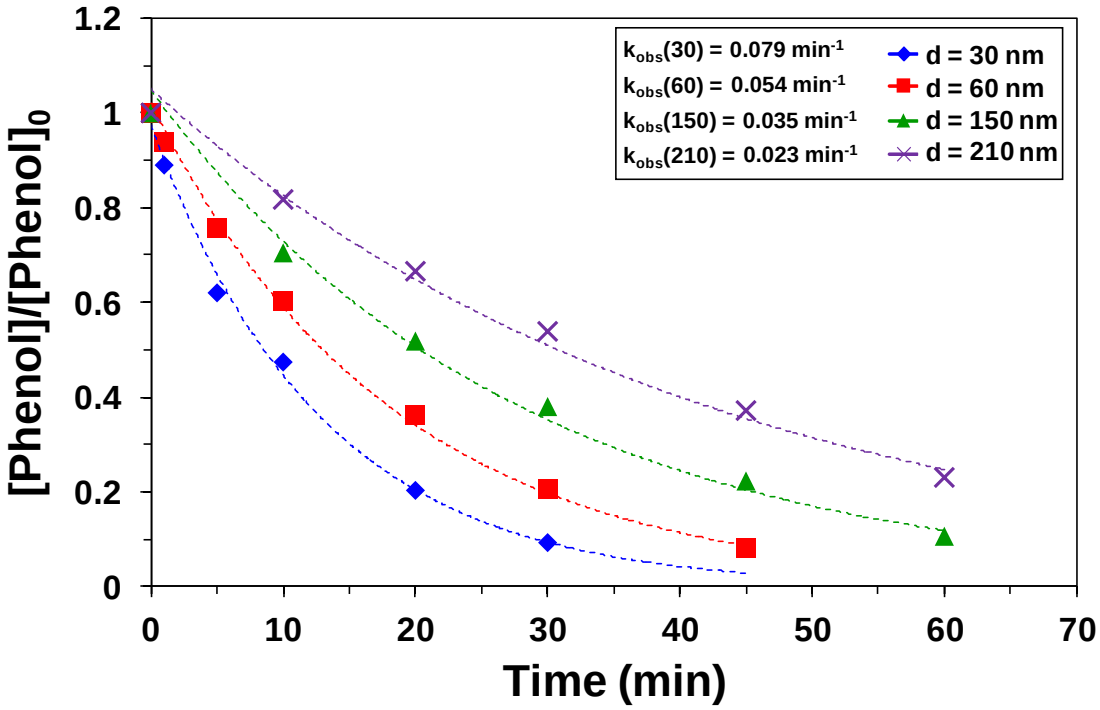

Figure 2-3. Representative concentration versus time profiles for phenol decay in irradiated suspensions of TiO_2 nanofibers. Phenol removal follows exponential decay and was described by a pseudo-first-order kinetic model (results of regression analysis are shown). Experimental conditions: pH 7, 0.1 g/L TiO_2 nanofibers (annealed at 500 °C for 3 h), initial phenol concentration of 100 μM [91].

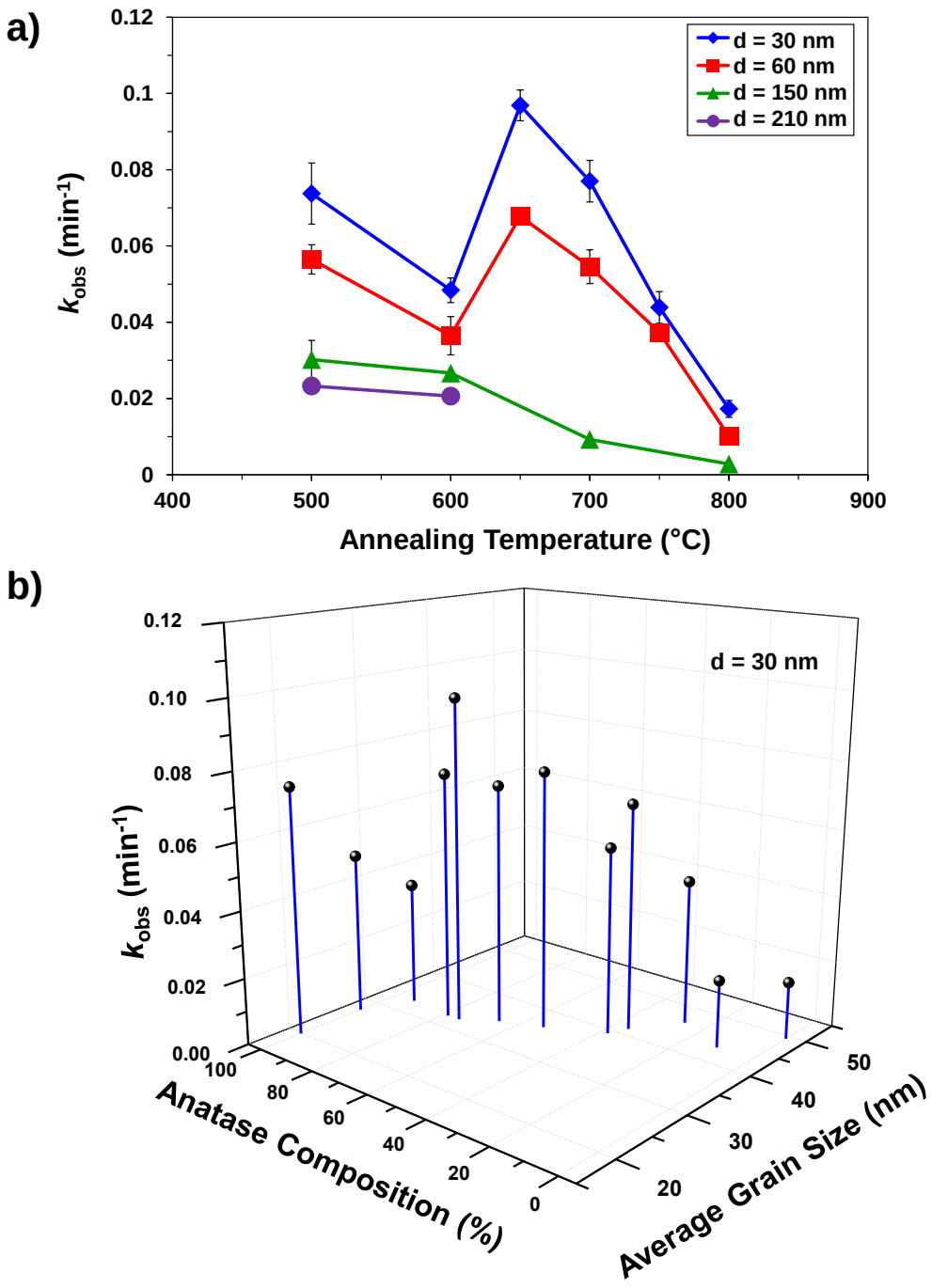

Figure 2-4. (a) Average k_{obs} values for phenol decay as a function of annealing temperature for TiO_2 nanofibers with different diameters. (b) Values of k_{obs} for phenol decay as a function of the average grain size and anatase composition for d = 30 nm TiO_2 nanofibers. Experimental conditions: pH 7, 0.1 g/L TiO_2 nanofiber loading, initial phenol concentration of 100 µM. Uncertainties represent one standard deviation from at least triplicate experiments [91].

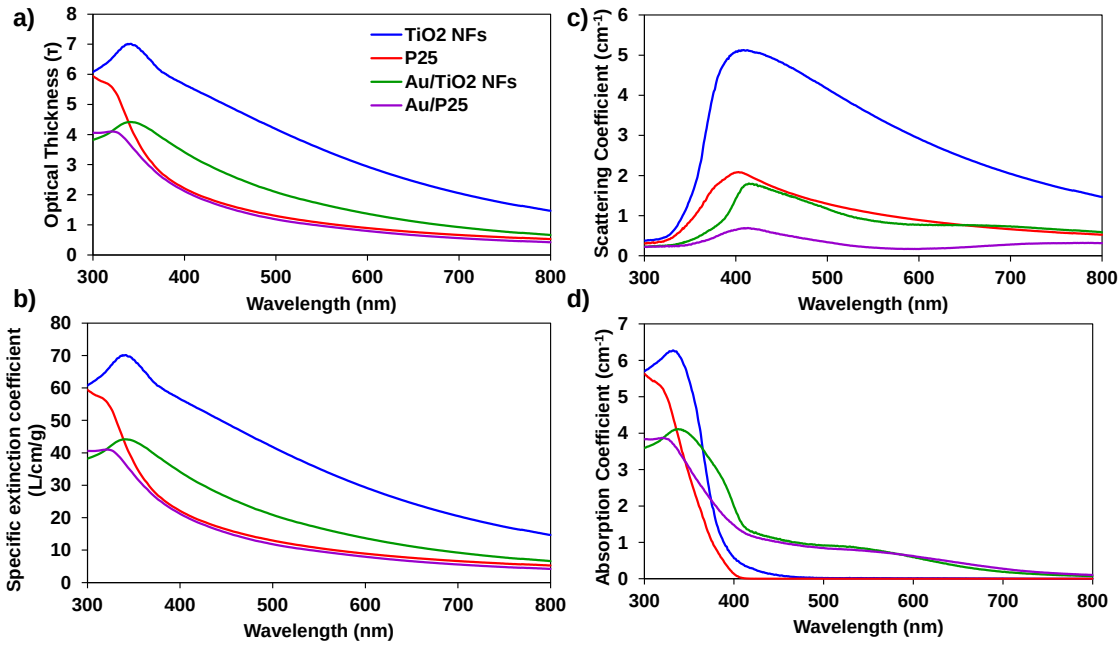

Figure 2-5. Optical characterization of photocatalyst suspensions (0.1 g/L). Values of (a) optical thickness, (b) specific extinction coefficient, (c) scattering coefficient and (d) absorption coefficient are shown as a function of wavelength and were calculated as described.

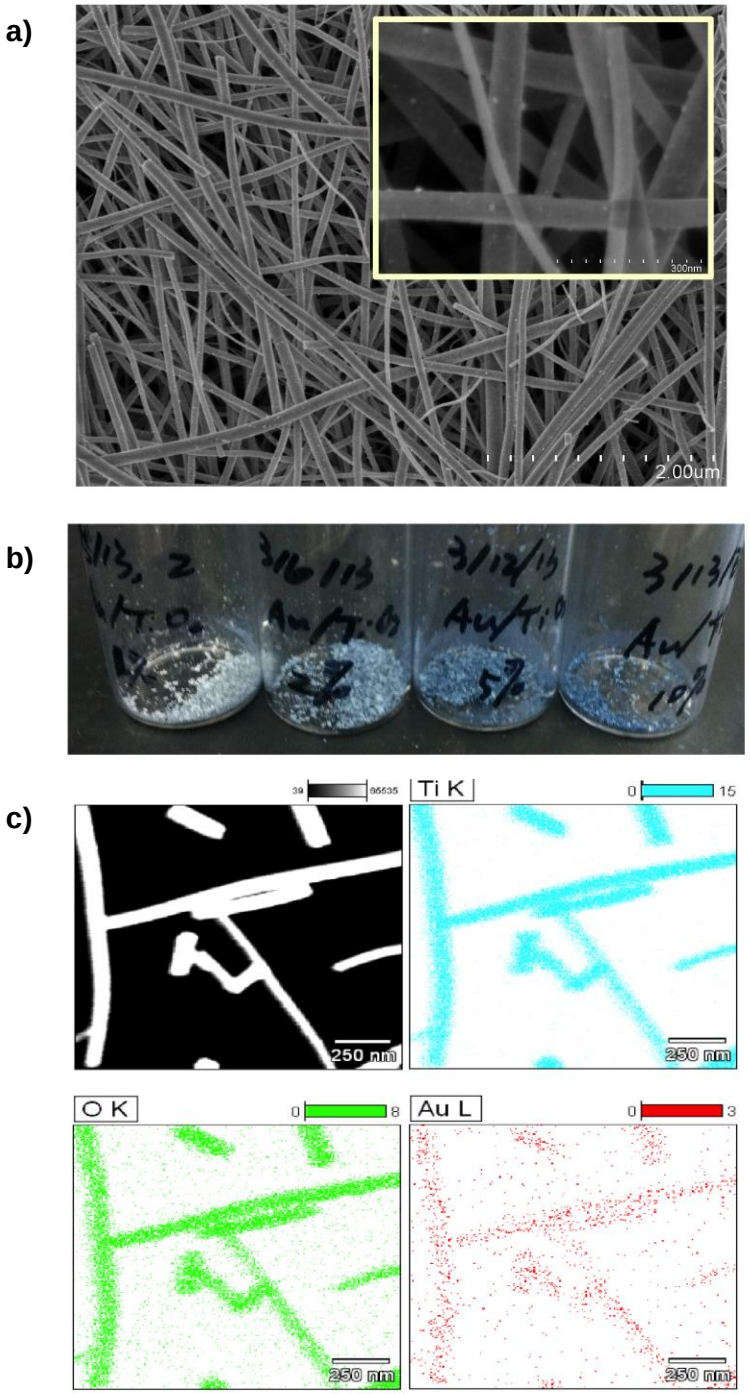

Figure 2-6. (a) SEM images and (b) photographs of Au/TiO_2 composites prepared via a one-pot electrospinning synthesis. In (a), the Au loading of the composite is 10 wt.% (relative to the mass of TiO_2). Photographs in (b) show increasing Au loading (left to right) from 1% to 10% by weight, which coincided with the development of a blue hue to the particles at high Au loadings. (c) Elemental mapping of the 5% Au/TiO_2 composite shows the relatively uniform distribution of Au integrated into the nanofibers.

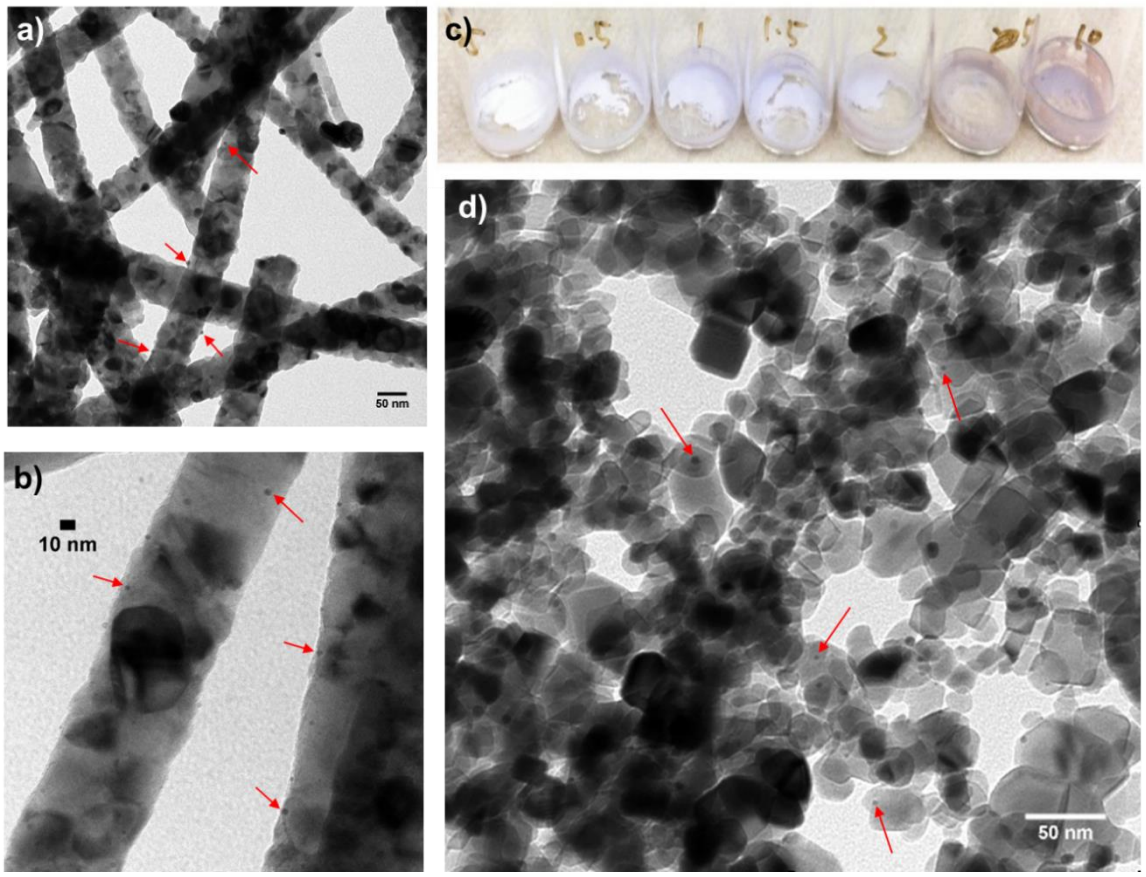

Figure 2-7. (a and b) TEM images of Au/TiO_2 nanofiber composites prepared via reductive deposition of Au(III) with urea. Images correspond to a nominal Au loading 1.5 wt.% (assuming complete Au deposition), which was the composite formulation with optimal performance in reactivity studies (c) Photograph of surface Au/TiO_2 composites, showing increasing Au loading from 0.5 to 10% by weight, which corresponded with a shift in the color of the composites from white (low Au) to pink or purple (high Au). (d) Also shown for comparison are TEM images of Au/P25 modified by an analogous surface deposition method. Arrows in all TEM images indicate locations of Au nanoparticles, roughly 3 nm in diameter.

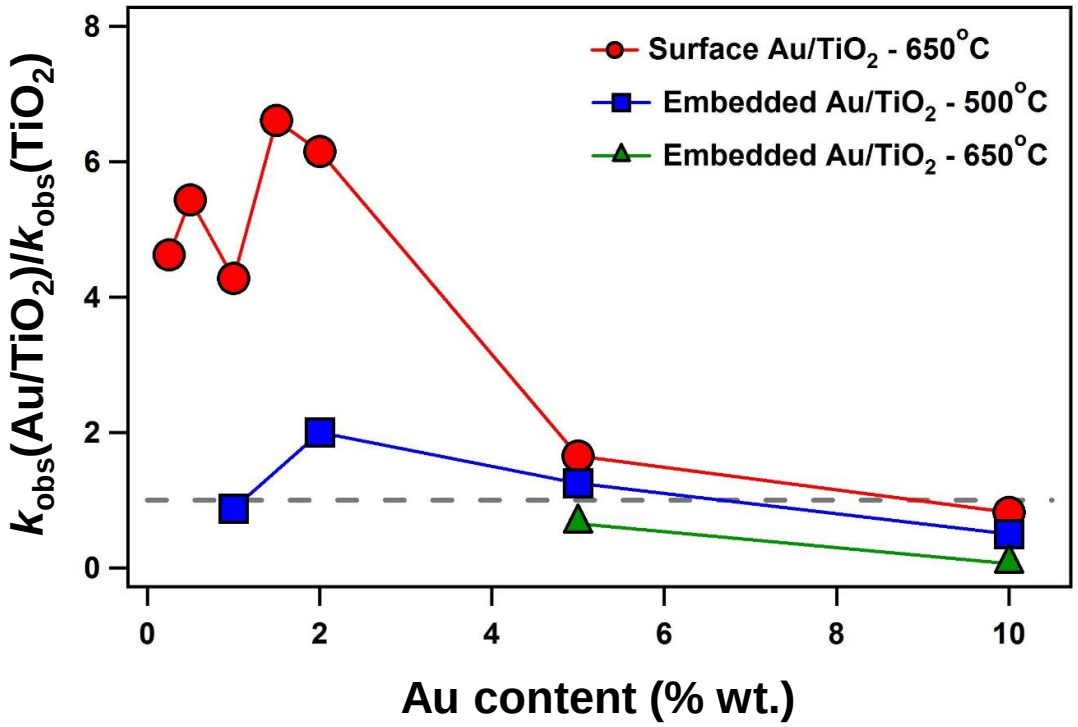

Figure 2-8. Reactivity of embedded Au/TiO_2 nanofibers (annealed at either 500 or 650 °C) and surface-integrated Au/TiO_2 nanofibers as a function of Au loading (wt.%). Values of k_{obs} for phenol decay in each composite nanofiber system have been normalized to the k_{obs} value measured with unmodified TiO_2 nanofibers. The dashed line indicates a value of 1, where Au modified and unmodified TiO_2 nanofibers exhibit identical reactivity.

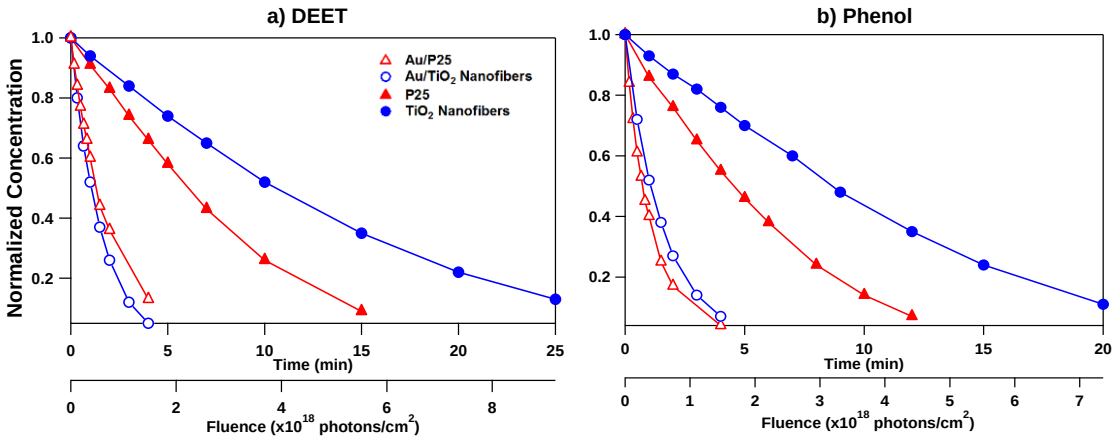

Figure 2-9. Representative concentration profiles for the reaction of irradiated photocatalyst suspensions with (a) DEET and (b) phenol shown as a function of time and fluence. Values of k_{obs} obtained from exponential decay model fits to this data are provided in **Table 1**. Experimental conditions: pH 7, 0.1 g/L photocatalyst, 20 μM initial concentration of DEET and phenol.

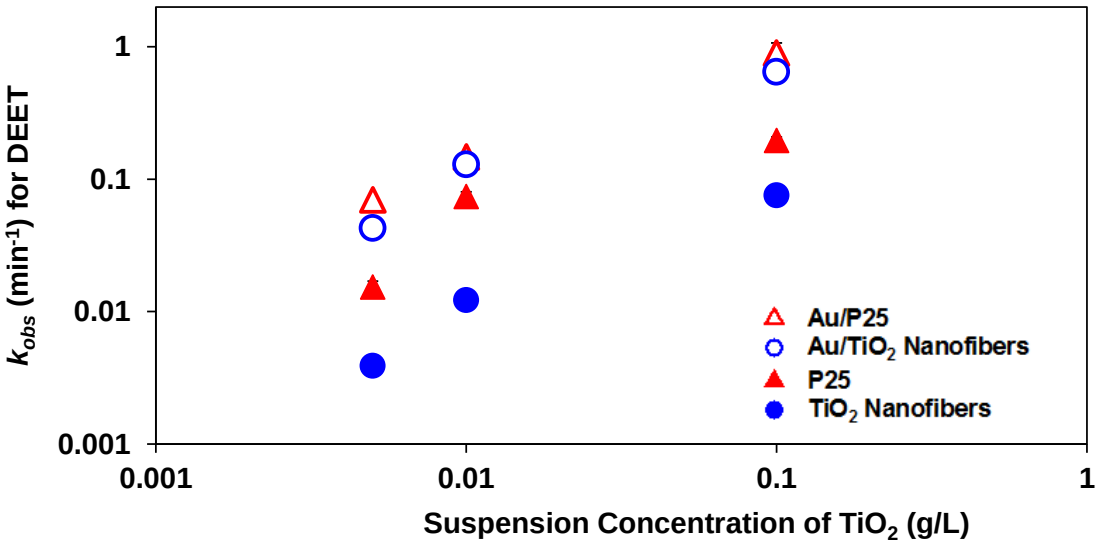

Figure 2-10. Relative reactivity of TiO_2 photocatalysts as a function of solid loading. While the majority of experiments were conducted at 0.1 g/L, these results show that the reported photocatalytic reactivity trend is consistent across all loadings considered. These values of k_{obs} are tabulated in **Table 2**. Experimental conditions: pH 7, 0.005-0.1 g/L photocatalyst, 20 μM of initial DEET.

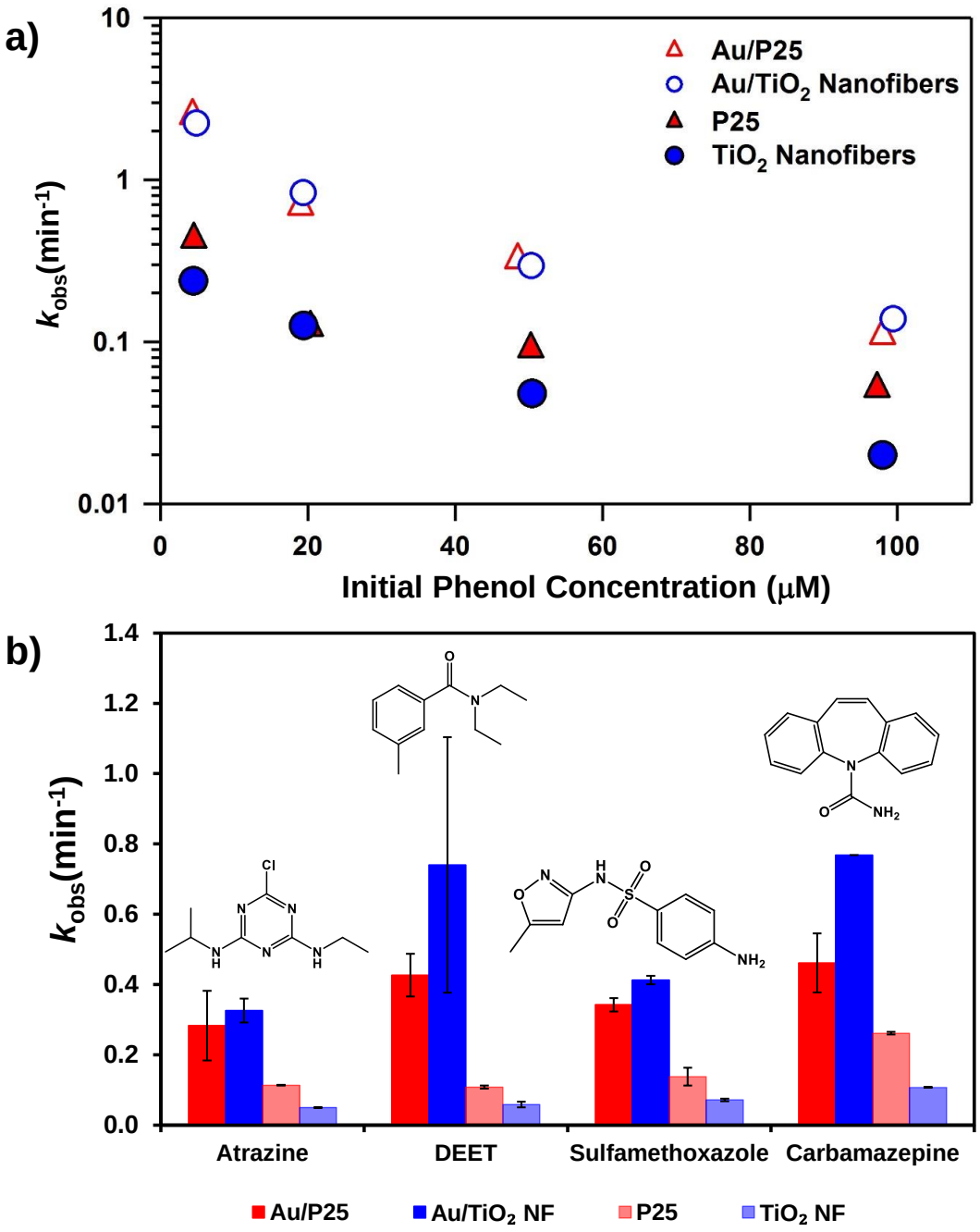

Figure 2-11. (a) Values of k_{obs} as a function of initial concentration for phenol and (b) k_{obs} values for photocatalytic degradation of atrazine, DEET, sulfamethoxazole, and carbamazepine (initially 20 μM) in irradiated suspensions of Au/P25, Au/TiO_2 nanofibers, P25, and TiO_2 nanofibers. Experimental conditions: pH 7, 0.1 g/L photocatalyst. Uncertainties represent one standard deviation from at least triplicate experiments.

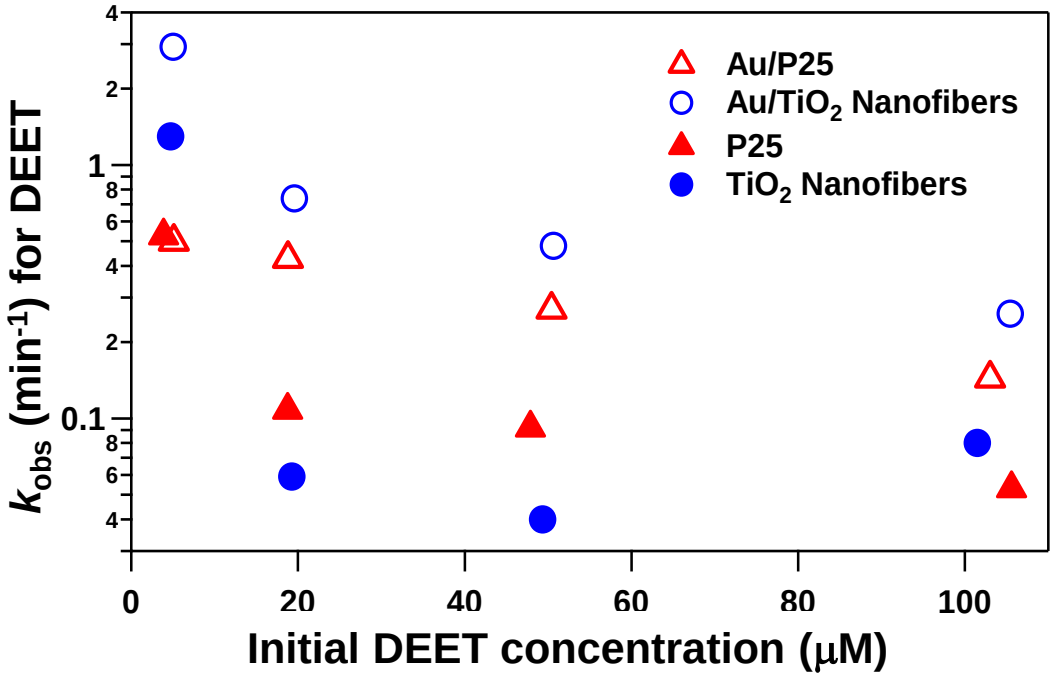

Figure 2-12. Values of k_{obs} as a function of initial DEET concentration. These concentration-dependent trends are analogous to those reported for phenol. Experimental conditions: pH 7, 0.1 g/L photocatalyst, 5-100 μM of initial DEET.

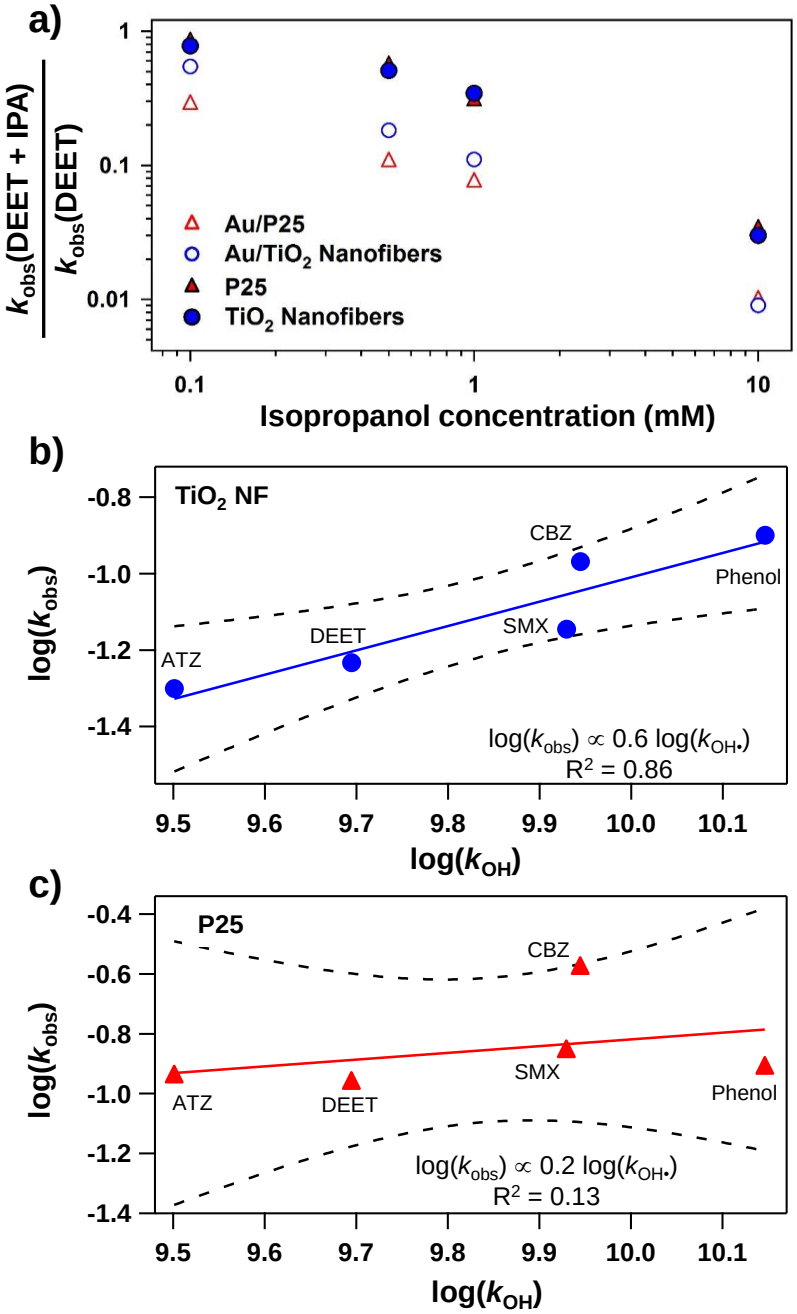

Figure 2-13. (a) Fractional inhibition of DEET transformation as a function of the IPA concentration added to photocatalyst suspensions. Reactivity cross correlations for irradiated suspensions (0.1 g/L) of (b) TiO_2 nanofibers and (c) P25, in which values of k_{obs} values for atrazine (ATZ), DEET, sulfamethoxazole (SMX), carbamazepine (CBZ), and phenol degradation are plotted as a function of reported rate coefficients for the reaction of each species with hydroxyl radical (k_{OH} values). Best fit linear regressions (solid line) and 95% confidence intervals (dashed lines) are provided.

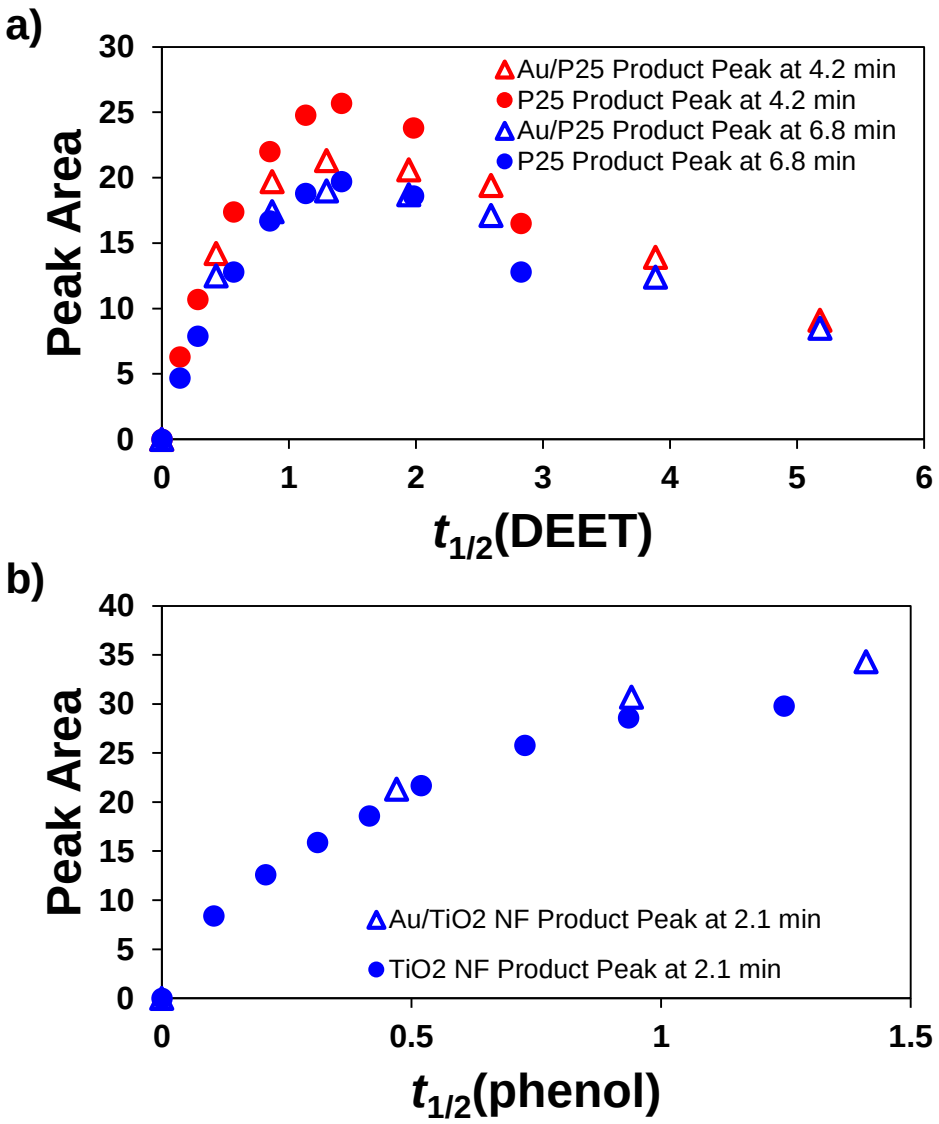

Figure 2-14. Comparison of product yields for (a) DEET and (b) phenol in unmodified and Au-modified TiO_2 systems. Major products (identified by reverse phase HPLC retention time and prioritized by the magnitude of their response using a diode array detector at 223 and 254 nm) are shown as a function of half-lives ($t_{1/2}$ values) for the parent species. For the major products shown, as well as minor products also detected (data not shown), no obvious differences in product relative yields were observed across different photocatalyst formulations, consistent with similar product formation pathways occurring in all systems.

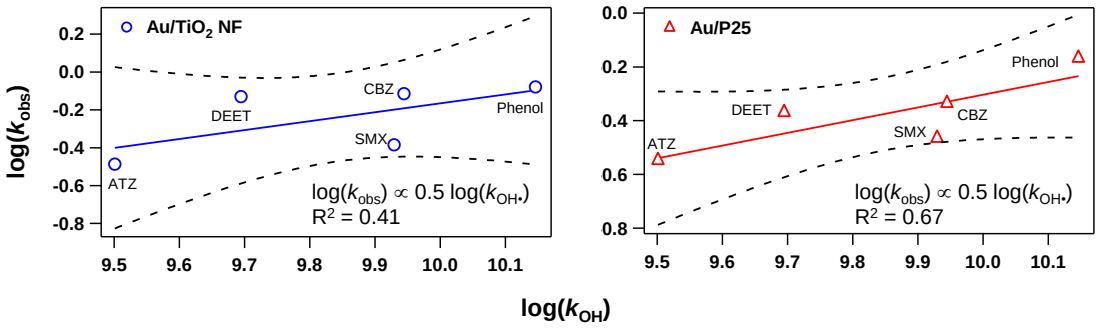

Figure 2-15. Reactivity cross correlations comparing k_{obs} values measured in 1.5 wt.% Au/TiO_2 nanofibers and 1.5 wt.% Au/P25 systems to published second-order rate coefficients for the reaction of our micropollutant suite with hydroxyl radical (k_{OH}), the presumptive oxidizing agent in irradiated TiO_2 systems. Data points, which are shown on a log-log scale, correspond to results obtained with atrazine (ATZ), DEET, sulfamethoxazole (SMX), carbamazepine (CBZ), and phenol as labeled. Solid lines represent best fits from linear regression analysis, for which the slope and correlation coefficient (R^2 value) are provided. Dashed lines represent 95% confidence bands associated with this regression analysis, where statistical analysis was performed in the software package Igor Pro (Wavemetrics). Please note that y-axes are presented on different scales. Experimental conditions: 0.1 g/L photocatalyst, pH 7, initial organic target concentration of 20 μM.

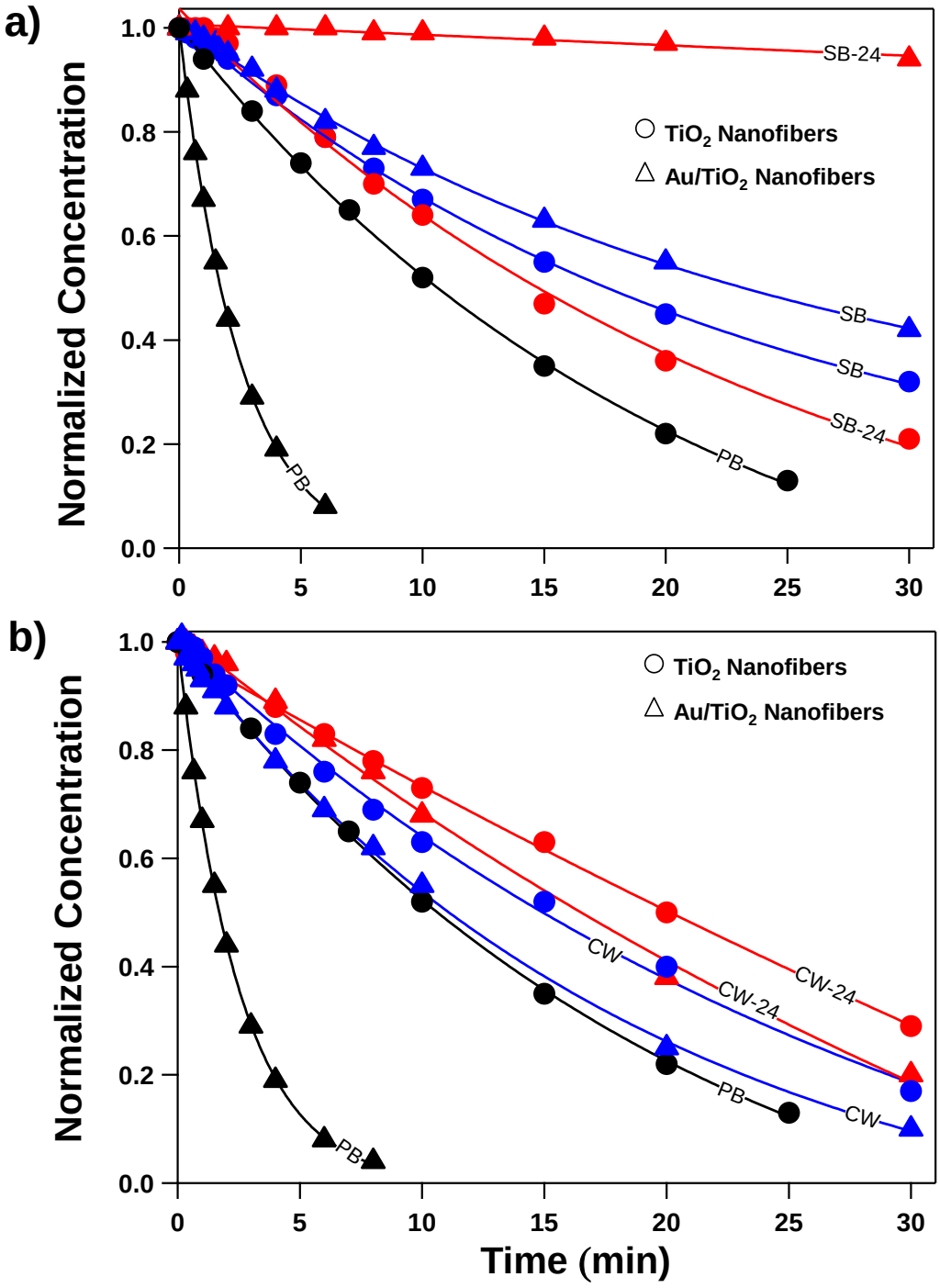

Figure 2-16. Normalized concentration versus time profiles for DEET (20 μM) transformation by electrospun TiO_2 nanofibers (circles) and 1.5 wt.% Au/TiO_2 nanofibers (triangles) in (a) effluent from the UIWTP sedimentation basin (SB) and (b) UIWTP clearwell effluent (CW). Data collected in model phosphate buffer systems (PB; shown in black) are also provided for comparison, as are data collected in each water sample either immediately (blue) or after 24 h of aging (red).

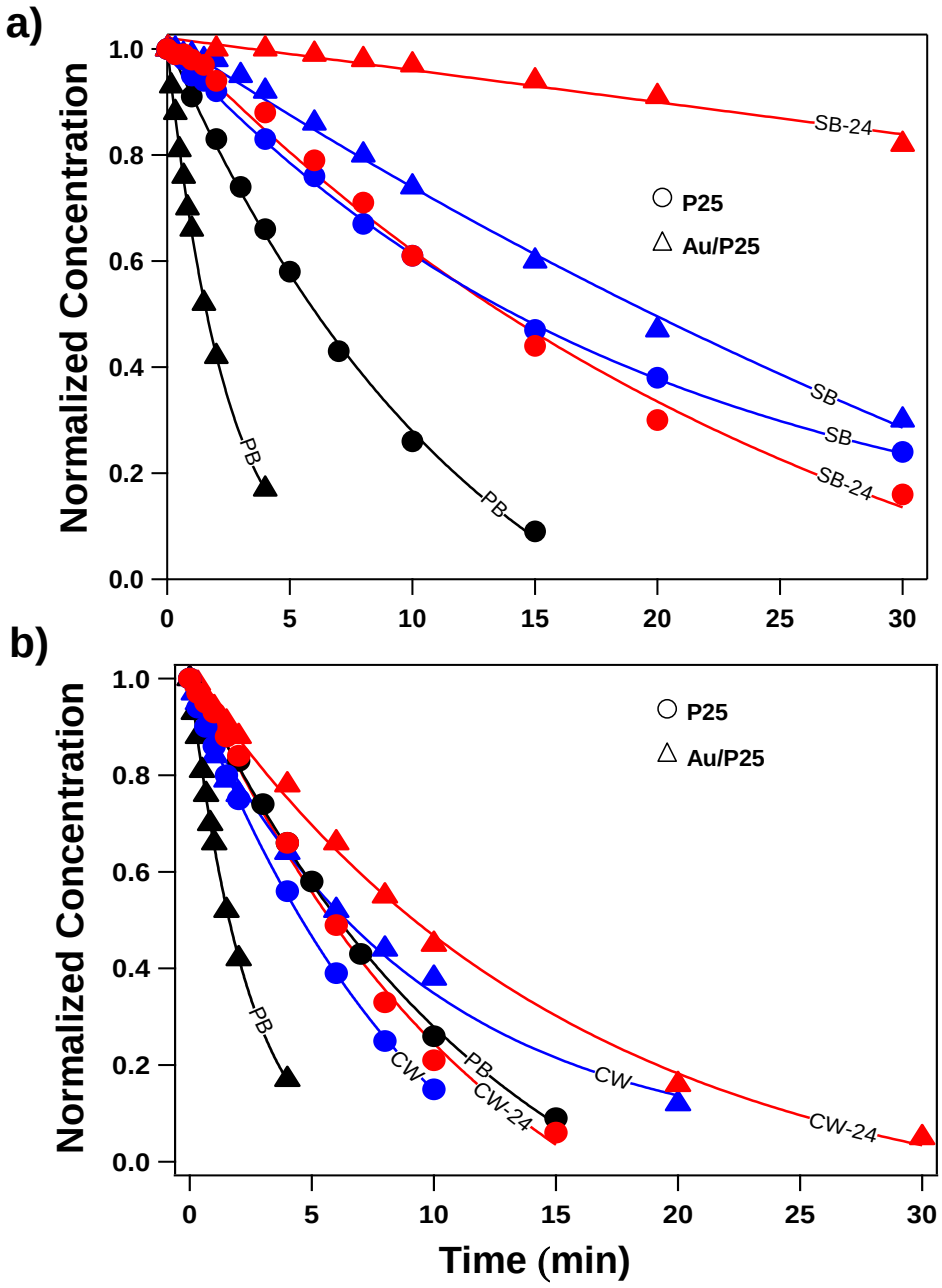

Figure 2-17: Normalized concentration profiles for DEET (20 µM) during reactivity studies with suspensions (0.1 g/L) of P25 (circles) and 1.5 wt.% Au/P25 (triangles) in (a) effluent from the UIWTP sedimentation basin (SB) and (b) clearwell effluent (CW) from the UIWTP. For comparison, data collected in model water systems (i.e., phosphate buffer; PB) are shown (in black). In each matrix, data is provided for reactivity studies conducted immediately upon suspension preparation (in blue) and after 24 h of aging of photocatalysts in each solution (in red). Relative reactivity and time-dependent reactivity trends observed for P25 and Au/P25 mirror those reported for electrospun TiO_2 nanofibers.

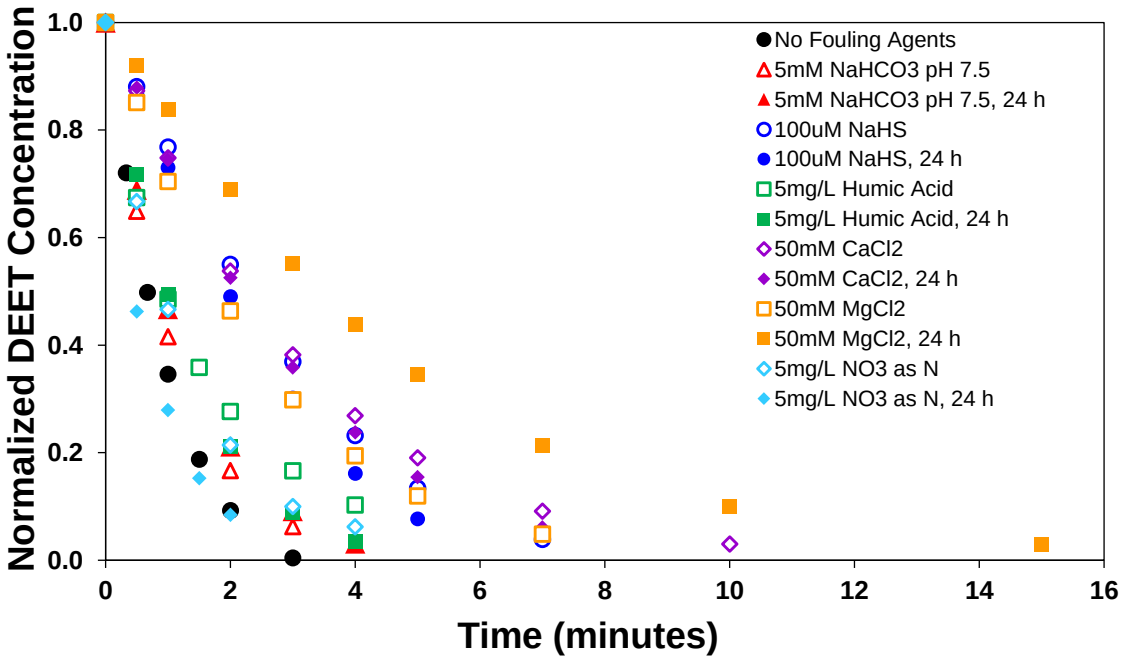

Figure 2-18. DEET decay in Au/P25 systems as a function of different model water constituents. As indicated in the key, data are shown both for suspensions (0.1 g/L) reacted immediately upon assembly as well as after suspension aging (while mixing) for 24 h. Experiments were conducted at pH 7 unless otherwise indicated in the key. Results are shown for the maximum concentration of each constituent that was explored herein.

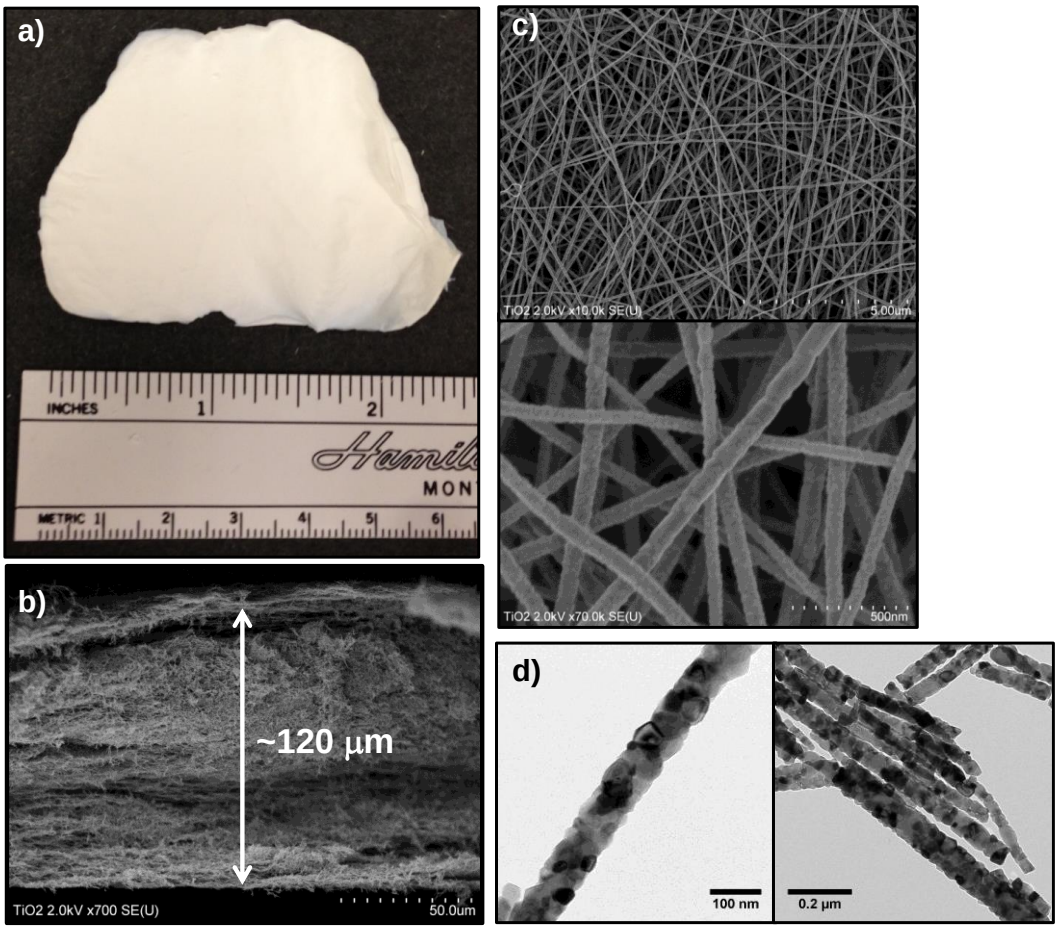

Figure 2-19. Representative images of a network or mat of TiO_2 nanofibers synthesized by electrospinning according to the standard protocol for 60 nm fibers. To increase the strength of the mat, it was synthesized by electrospinning for 22 h. The result is a nanofiber mat (a) roughly 2 in. by 2 in. and (b) approximately 120 μm in thickness based upon cross-sectional SEM analysis. Additional (c) SEM images of the mat and (d) TEM images taken of dispersed nanofibers (via sonication) are also shown.

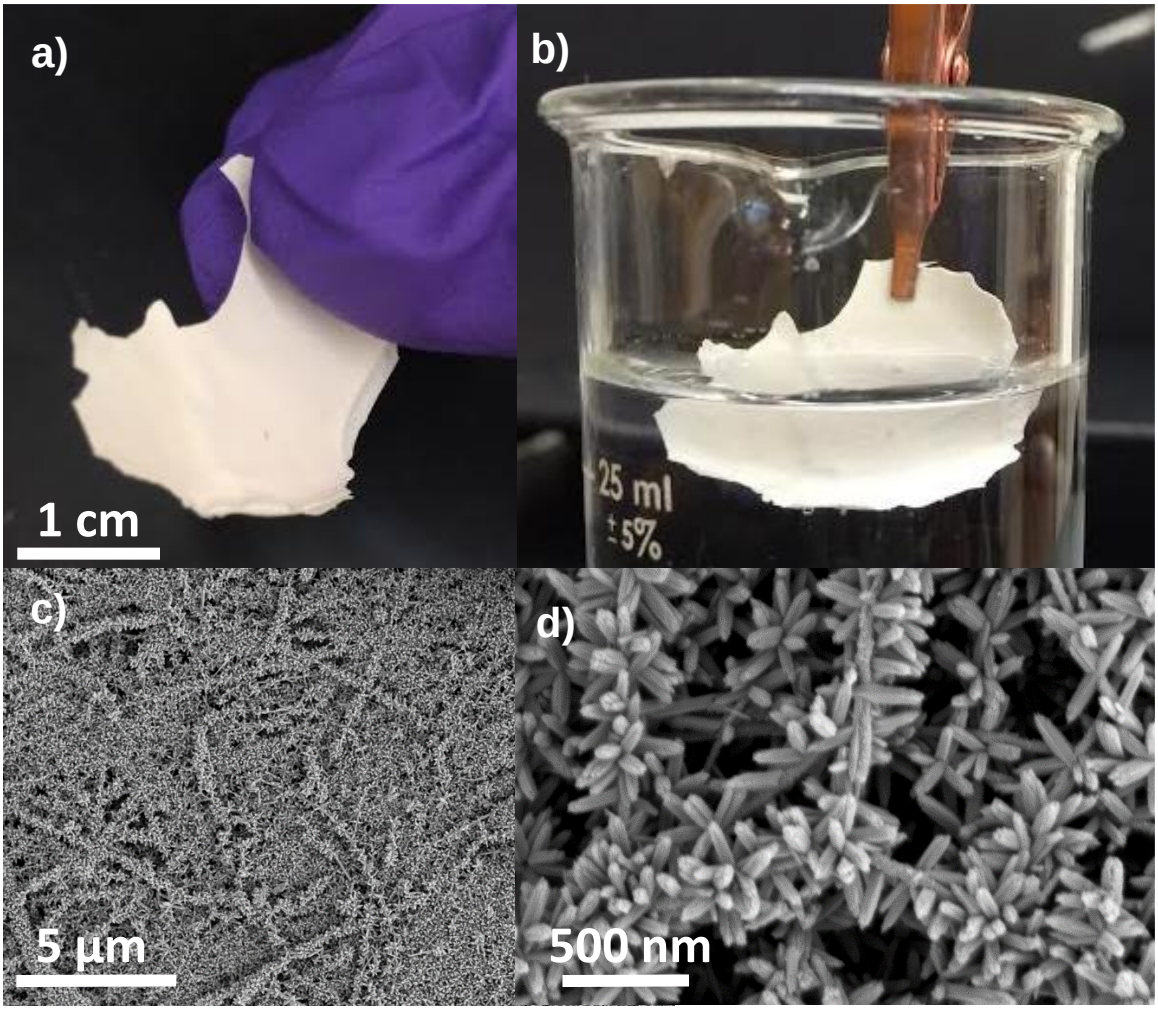

Figure 2-20. (a and b) Representative images of a TiO_2 nanofiber mat, in which mat shown in **Figure 2-19** was hydrothermally treated. This hydrothermal treatment involved placing the mat in a well-mixed solution of 30 mL of hydrochloric acid (Fisher Scientific), 30 mL of DI water, and 4 mL of titanium (IV) butoxide (Sigma Aldrich, 97%) and heating in a steel autoclave at 150 °C for 4 h [162]. This hydrothermal treatment produces a mat that is easier to handle and manipulate. As shown in SEM images (c and d), this treatment results in growth of rutile TiO_2 nanocrystals oriented perpendicular to the nanofiber to produce unique flower- or starburst-like surface structures. Notably, these hydrothermally treated mats are considerably stronger than non-hydrothermally processed mats, which we believe is due to the interlocking nature of the surface crystals that produces a more cohesive nanofiber network.

CHAPTER 3: PERFORMANCE COMPARISON OF HEMATITE - POLYMER COMPOSITE AND CORE-SHELL NANOFIBERS AS POINT-OF-USE FILTRATION PLATFORMS FOR METAL SEQUESTRATION

3.1. Abstract

Point-of-use water treatment technologies can help mitigate risks associated with drinking water quality, particularly for metals (and metalloids) that can originate in distribution systems (e.g., hexavalent chromium, lead, copper) and are naturally occurring in groundwater accessed by private wells (e.g., arsenic). Here, polyacrylonitrile (PAN) nanofiber composites with embedded hematite (α-Fe_2O_3) nanoparticles are synthesized via a single-pot electrospinning synthesis, while core-shell nanofibers were prepared via subsequent hydrothermal growth of Fe_2O_3 nanostructures on these electrospun composites. Properties of composite nanofibers were controlled using electrospinning synthesis variables (e.g., size and loading of embedded α-Fe_2O_3 nanoparticles), whereas core-shell structures were also tailored via hydrothermal treatment conditions (e.g., soluble iron concentration and duration). Although uptake of Cu(II), Pb(II), Cr(VI), and As(V) was largely invariant across the core-shell variables explored, metal uptake on composites increased with embedded α-Fe_2O_3 loading. Both materials exhibited maximum surface-area normalized capacities for our metal and metalloid suite that were comparable to α-Fe_2O_3 nanoparticle dispersions and exceeded that of commercial iron oxide based sorbents. Further, both nanofibers sorbents exhibited superior performance across a range of environmentally relevant pH values (6.0 to 8.0). Notably, while metal uptake was roughly comparable between the composite and core-shell nanofibers in batch (i.e., no flow) sorption experiments, core-shell structures, with a majority of α-Fe_2O_3 available as external

surface area, exhibited longer operation run times (i.e., larger volumes of water treated) prior to breakthrough in flow-through (i.e., dead end) microfiltration systems, where metal/metalloid uptake is likely kinetically (rather than thermodynamically) limited. Core-shell nanofiber filters also retained much of the durability and flexibility exhibited by composites, ideal for handling and application as filtration membranes. Additional tests with authentic groundwater samples demonstrated the ability of the core-shell nanofiber filters to remove simultaneously both As and suspended solids, illustrating their promise as a next-generation, nano-enabled technology for point-of-use water treatment.

3.2. Introduction

Water security amid increasing stressors on quantity and quality represents a challenge in many communities, especially those that are small, rural, and/or resource-limited in the United States and abroad. For drinking water quality, recent events illustrate that many communities continue to struggle with contamination from heavy metals and metalloids including (i) high levels of lead (Pb) found in drinking water in Flint, Michigan [28]; (ii) detection of arsenic (As) in ~50% of groundwater wells in the state of Iowa, with 8% exceeding the EPA maximum contaminant level (MCL) [21], and recent estimates of As levels above the MCL in many of the groundwater wells in the Central Valley of California [22]; and (iii) the detection of hexavalent chromium [Cr(VI)] in the tap water of 31 (of 35) cities across the United States [163]. Improving safety and reliability of water supplies in these communities will require technologies that are deployable across a range of scales ranging from point-of-use (POU) and point-of-entry (POE) applications to integration in conventional treatment [47]. Simultaneously, these technologies must be affordable, robust, and sustainable so they can also be of value to small water systems (i.e.,

systems that serve 10,000 people or less [164]) that often struggle to comply with federal regulations for drinking water quality due to limited financial and technological resources [47,48].

Engineered nanomaterials have vast potential for water treatment as a result of their high surface area-to-volume ratios, which allows all of their reactive surface area to be external and thus accessible to solution with limited mass transfer resistance during application [58]. In particular, this makes them ideal as adsorbents for pollutant removal [60,61,76], where they may represent improvements over more traditional, commercial adsorbents accepted for water treatment [e.g., granular activated carbon (GAC), Evoqua Granular Ferric Hydroxide (GFH®)] that have relatively large application footprints (e.g., bed filtration) and consist primarily of internal surface area. With nanotechnology, a treatment device with a small footprint and a minimal amount of material has the potential to exhibit enhanced reactivity relative to larger, bulk materials [60].

Iron oxides, and specifically hematite (α-Fe_2O_3), are earth abundant, making them inexpensive and readily available for treatment applications while also minimizing risks associated with their use [165]. Iron oxides also have favorable physicochemical properties for water treatment, namely surfaces with a point of zero charge near pH 7 that makes them useful as sorbents toward both cationic and anionic targets [166]. As a result, GFH® has become a widely used commercial adsorbent, predominantly for As removal as a U.S. EPA Best Available Technology (BAT) [167–170], while also being extensively evaluated as an adsorbent for a number of other metals, including antimony, copper, and chromium [167,171]. Iron oxide performance in this and other applications could likely be improved by exploiting the large reactive surface area of nanomaterials, but their use is not without

problems – aggregation, release, and difficulty with scale-up inhibit the application of nanomaterials in water treatment [71,72]. Thus, a platform that stabilizes nanoscale iron oxides without completely compromising available surface area is requisite for generating higher capacity, nano-enabled adsorbents in water treatment.

In this study, we use electrospinning, a novel and scalable route for synthesis of nanofibers [80,81,172], to produce various polyacrylonitrile (PAN)/hematite (α-Fe_2O_3) composite nanofibers for use as reactive filtration media (i.e., for simultaneous particle removal and metal sequestration). Via a single-pot electrospinning synthesis, we prepare traditional PAN nanofiber composites with embedded α-Fe_2O_3 nanoparticles. We also develop a subsequent hydrothermal treatment step to further process these more traditional composites into novel PAN/α-Fe_2O_3 core-shell nanofibers. Properties of these composite nanofibers obtained from microscopy and surface area analysis were then correlated with standard metrics of their sorption of common metal and metalloid pollutants encountered in drinking water including copper, lead, chromate, and arsenate. In batch systems, rates and extent of nanofiber uptake were examined across a range of metal and metalloid concentrations and mixtures, as well as pH values. Ultimately, the performance of traditional (i.e., nanoparticle embedded) and core-shell polymer nanofibers are compared and benchmarked versus commercially available GFH® to establish potential benefits of reactive filtration technologies using high surface area nanofiber sorbent networks.

Novelty in our work is derived not only from the synthesis and performance comparison of iron oxide-polymer composites and core-shell structures, but also complementary material strength testing to illustrate the robust nature and durability of these nanofiber networks during point-of-use water treatment. Indeed, while many studies

have established the reactivity of stand-alone metal oxide nanofibers, inorganic (e.g., iron oxide) nanofibers are often brittle and lack the material strength to make them practical in treatment applications [91,173]. More recently, while cohesive iron oxide-polymer composites have been fabricated, demonstrations of their reactivity have been limited to highly idealized systems (e.g., targeting dye removal) [174] that provide little insight into their performance toward more traditional pollutant targets (e.g., metals and metalloids) for conventional iron oxide sorbent materials. Accordingly, composite and core-shell materials optimized for both reactivity and material strength are also tested in a flow-through filtration system, including tests with authentic groundwater samples, for simultaneous removal of metals/metalloids and suspended particles or turbidity. Beyond demonstrating their potential in point-of-use water treatment, performance results in flow-through systems deviated from the behavior expected based upon results from thermodynamically controlled batch sorption systems. Thus, outcomes of reactive filtration studies, where metal/metalloid uptake is kinetically limited, highlight the advantages of core-shell nanofiber composites, for which iron oxide reactive surface area is more easily accessible to solution than nanofiber composites with embedded α–Fe_2O_3 nanoparticles.

3.3. Experimental methods

3.3.1. Reagents

All chemicals were reagent grade or better and used as received. The synthesis of α-Fe_2O_3-doped PAN nanofibers required polyacrylonitrile (PAN, Aldrich, MW 150,000), N,N-dimethylformamide (DMF, BDH, 99.8%), and 10 nm α-Fe_2O_3 (hereafter Fe_2O_3) nanoparticles synthesized using ferric nitrate nonahydrate ($Fe(NO_3)_3 \cdot 9H_2O$, Sigma-Aldrich, ≥98%). Ferric chloride heptahydrate ($FeCl_3 \cdot 6H_2O$, Sigma-Aldrich, 97%) and L-

arginine (Sigma, ≥98.5%) were used to prepare nanofibers hydrothermally coated with Fe_2O_3. Hydrochloric acid (HCl, Fisher Sci., Certified ACS Plus), sulfuric acid (H_2SO_4, Fisher Sci., Certified ACS Plus), hydroxylamine hydrochloride (Aldrich, 99%), 1,10-phenanthroline (Aldrich, ≥99%), ammonium acetate (Sigma-Alrich, ≥97%), glacial acetic acid (RPI, ≥99.7%) and ferrous ammonium sulfate (Fisher Sci., ≥99.9%) were used for acid digestion and colorimetric analysis of nanofiber iron content. HCl and sodium hydroxide (NaOH, Fisher Sci., Certified ACS) were used to clean hydrothermally treated nanofiber filters, while NaOH and nitric acid (HNO_3, Fisher Sci., Certified ACS Plus) were used in regeneration of spent nanofiber filters.

Buffer solutions prepared from either 10 mM MES hydrate (Sigma, ≥99.5%) adjusted to pH 6 and 6.5 or 10 mM HEPES (RPI, ≥99.9%) adjusted to pH 7 and 8 were used in adsorption experiments. Evoqua Granular Ferric Hydroxide (GFH®) was used as a commercially available iron-based sorbent for treatment efficiency comparisons. Potassium chromate (Sigma-Aldrich, ≥99.0%), sodium arsenate dibasic heptahydrate (Sigma, ≥98.0%), copper chloride dihydrate (Sigma-Alrich, ≥99.0%), and lead nitrate (Fisher Sci.) were used as pollutants in adsorption studies. Samples were treated with HNO_3 prior to analysis. Standards of 10 ppm and 100 ppm for hexavalent chromium (Cr(VI)), arsenic (As), copper (Cu), and lead (Pb) (Inorganic Ventures) were used in calibration of the inductively coupled plasma optical emission spectrometer (ICP-OES, Perkin Elmer Optima 7000 DV). Colorimetric analysis of chromate samples involved sulfuric acid (H_2SO_4, Fisher Sci., Certified ACS Plus), 1,5-diphenylcarbazide (Sigma-Aldrich, ACS reagent), and acetone (Fisher Sci., HPLC grade). All solutions were prepared in deionized (DI) water (Millipore, Milli-Q).

3.3.2. Synthesis of PAN/Fe_2O_3 composites and PAN/Fe_2O_3@Fe_2O_3 core-shell nanofiber filters

Electrospun PAN nanofibers with embedded Fe_2O_3 nanoparticles (hereafter PAN/Fe_2O_3) were prepared by electrospinning a PAN precursor solution containing 10 nm or 40 nm Fe_2O_3 nanoparticles that were synthesized as described elsewhere [175]. Briefly, various amounts of 10 or 40 nm Fe_2O_3 particles (from 8-50 wt.% relative to PAN) were suspended in 3.5 mL DMF, and sonicated for 5 h. Next, 0.3 g PAN was added and the solution was thermally mixed for 2 h at 60°C. The sol gel was allowed to cool to room temperature and then electrospun with a flow rate of 0.5 mL/h, 18 kV/10 cm, and 23G needle. After 6 h, the electrospinning process was stopped and the mat was peeled off the grounded collector. The system used for electrospinning was previously described (see Chapter 2).

To generate core-shell structures (hereafter PAN/Fe_2O_3@Fe_2O_3), these PAN/Fe_2O_3 nanofibers were then hydrothermally treated. A piece of PAN/Fe_2O_3 mat (~6 cm x 10 cm) was placed in a 150 mL equimolar solution (up to 0.14 M) of $FeCl_3 \cdot 6H_2O$ and L-arginine held in a plastic container that was then loosely covered and heated at 95°C for up to 12 h [176]. After treatment, mats were rinsed with deionized (DI) water, 0.1 M HCl, 0.1 M NaOH, and sonicated in DI water for 1.5 h to ensure the removal of extraneous material not firmly affixed to the surface.

3.3.3. Nanofiber filter characterization

Nanofiber filters were characterized to determine their physical and chemical properties. Materials were examined using scanning electron microscopy (SEM), X-ray diffraction (XRD), N_2-BET analysis, acid digestion, X-ray photoelectron spectroscopy (XPS), and a load-displacement cell.

Nanofiber diameter and extent of hydrothermal coating were examined with a Hitachi S-4800 scanning electron microscope (SEM), described in previous work [177]. Samples were prepared for SEM by mounting pieces of nanofiber mats approximately 0.5 cm by 0.5 cm on Al stubs with carbon tape. Samples were sputter-coated with Au prior to imaging. SEM imaging of n = 300 nanofibers (using images from 3 batches of a specified material) provided measurements used to create histograms of nanofiber diameter size, as well as determine average nanofiber diameters with standard deviation. X-ray diffraction (XRD, Rigaku MiniFlexII, cobalt X-ray source) was used to confirm the phase of nanoparticles and nanofiber coatings as hematite. Samples were prepared for XRD by placing a 1 cm by 1 cm piece of nanofiber mat on a slide with 0.2 mm well depth. Samples were analyzed from 20° to 80° for the Bragg angle with an interval of 0.02°. Specific surface area of the materials was determined via N_2-BET analysis (Quantachrome Nova 4200e) after outgassing samples at 40°C for 6 h prior to analysis.

Speciation of Pb(II) sorbed to the surface of PAN/Fe_2O_3@Fe_2O_3 was analyzed with a Kratos Axis Ultra X-ray photoelectron spectroscopy (XPS) system equipped with a monochromatic Al Kα X-ray source. For XPS analysis, approximately 0.5 cm by 0.5 cm of PAN/Fe_2O_3@Fe_2O_3 from a Pb(II) isotherm experiment (air dried for 24 h) was placed on a sample holder using carbon tape. XPS was used to collect full spectrum survey scans, as well as to examine O 1s, C 1s, N 1s, Fe 2p, and Pb 4f regions. The mechanical strength of nanofibers and nanofiber mats was evaluated via stress-strain curves developed using a load-displacement cell following the protocols in our group's previous work [177].

To determine iron content of materials, known masses of nanofiber mats were digested in 20 mL of 5 M HCl overnight. 40 µL of the acid was then diluted with 960 µL

of water and mixed with 30 µL of 10 g/L hydroxylamine solution to reduce Fe(III) to Fe(II). After the addition of 200 µL of 1 g/L 1,10-phenanthroline and 200 µL of 100 g/L ammonium acetate buffer, samples were allowed to sit for 20 minutes and subsequently analyzed colorimetrically at 510 nm with a UV-visible light spectrophotometer (Genesys 10uv) with calibration standards prepared using ferrous ammonium sulfate [178].

3.3.4. Batch sorption experiments

Pieces of nanofiber mats were reacted in batch with As(V), Cu(II), Cr(VI), and Pb(II) to assess their reactivity. Experiments with As(V), Cr(VI), and Cu(II) were conducted in 20 mL glass vials sealed with butyl rubber septa. Experiments with Pb(II) were conducted in 15 mL plastic centrifuge tubes, as Pb(II) sorbed significantly to glass. Approximately 5 mg of material (typically a 0.5 cm x 0.5 cm mat of nanofibers) was placed in 10 mL of appropriate buffer solution (10 mM MES or HEPES). Isotherm, kinetics, and pH edge batch experiments were initiated by spiking these solutions with As(V), Cr(VI), Cu(II), and Pb(II).

For isotherm experiments, reactors were spiked with concentrations ranging from 0.3 to 200 mg/L of metal or metalloid using potassium chromate, sodium arsenate dibasic heptahydrate, copper chloride dihydrate, and lead nitrate. Isotherm experiments were conducted at pH 6 to ensure solubility of metals/metalloids up to relatively high concentrations (especially with Cu, for which $Cu(OH)_2(s)$ dominates as a species above pH 7) necessary to achieve monolayer sorption. At this pH, As(V) was predominantly $H_2AsO_4^-$ (hereafter simply referred to as AsO_4^{3-}), Cr(VI) was predominantly $HCrO_4^-$ (hereafter simply referred to as CrO_4^{2-}), Cu(II) was predominantly Cu^{2+}, and Pb(II) was predominantly Pb^{2+}. For pH edge experiments, 10 mM MES adjusted to pH 6, 10 mM MES

adjusted to pH 6.5, 10 mM HEPES adjusted to pH 7, and 10 mM HEPES adjusted to pH 8 were used and spiked with 7.4 mg/L arsenate (AsO_4^{3-}), 6.7 mg/L chromate (CrO_4^{2-}), 3 mg/L Pb^{2+}, or 0.6 mg/L Cu^{2+}, with the exception that Cu^{2+} experiments were not conducted at pH 8 due to its limited solubility. Regarding metal speciation across these pH values, $H_2AsO_4^-$ was the dominant form below pH 6.8, above which $HAsO_4^{2-}$ became dominant. For Cr, $HCrO_4^-$ was the main form of Cr below pH 6.5, above which CrO_4^{2-} represented the major species. Cu^{2+} was the dominant form of Cu(II) from pH 6 to pH 7. Pb^{2+} was the main form of Pb(II) present below pH 7.2, above which $PbOH^+$ prevailed. Competitive sorption of metals/metalloids was also examined across these pH values by spiking reactors with mixtures of two pollutants, 7.4 mg/L AsO_4^{3-} and 6.7 mg/L CrO_4^{2-}, 7.4 mg/L AsO_4^{3-} and 0.6 mg/L Cu^{2+}, and 0.6 mg/L Cu^{2+} and 3 mg/L Pb^{2+}.

After assembly of batch experimental systems, vials were placed on a rotator (Cole-Parmer Roto-Torque) for 24 hours, after which 5 mL samples were taken, acidified to 2% HNO_3, and filtered with 0.45µm nylon filters for analysis by ICP-OES. Kinetics experiments were carried out using 10 mM MES buffer adjusted to pH 6 spiked with 7.4 mg/L AsO_4^{3-}, 6.7 mg/L CrO_4^{2-}, 3 mg/L Pb^{2+}, or 0.6 mg/L Cu^{2+}. Multiple reactors with each metal/metalloid were placed on a rotator and sampled at different times to quantify sorbed masses up to 24 hours. These 5 mL samples were acidified and filtered for analysis.

Sorbed masses of metals and metalloids were quantified by subtracting dissolved concentrations measured in reactor samples from known initial concentration and multiplying by the volume of solution in the reactor. Initial rates for sorption kinetics were determined by linear fits of normalized concentration of metals/metalloids over time before uptake of sorbates began to plateau as equilibrium was reached (typically around 1 hour).

For all experiments, controls were completed with buffer and metal/metalloid in the absence of any nanomaterial; sorption of As(V), Cr(VI), and Cu(II) on the glass vials and rubber septa and Pb(II) on the plastic tubes was negligible.

3.3.5. Simulated point-of-use treatment in flow-through filtration systems

For flow-through filtration experiments, nanofiber filters were placed in a 47 mm filter holder (Millipore) connected to a peristaltic pump (Masterflex). Buffer solutions at pH 6 containing either 100 ppb As(V) and Cr(VI) or 300 ppb Pb(II) were pumped through the system with a flux of 1,060 $L/m^2/h$, as determined by measuring water volume collected into a graduated cylinder after 1 minute of filtration and dividing by the 0.0011 m^2 filtration area. A schematic of the flow-through setup is provided in **Figure 3-1**. During operation, 5 mL samples were taken every 5 minutes, acidified, and filtered for analysis. Reversibility and regeneration of the filters in flow-through was examined by subsequently passing either 2 L of 10 mM MES buffer at pH 6, 1 L of 0.05 M NaOH followed by 1 L of pH 6 10 mM MES (for As, Cr experiments), or 1 L of 0.1 M HNO_3 followed by 1 L of pH 6 10 mM MES [for Pb(II) experiments] across the filter. Once again, samples of the regenerant solution were collected, acidified, filtered, and analyzed to establish recovery of the bound metal/metalloid contaminants.

To further assess the use of nanofiber filter materials in point-of-use treatment applications, composite nanofiber filters were also tested in flow-through filtration experiments with authentic groundwater samples containing As collected from private wells in Mason City and Clear Lake, Iowa. The raw groundwater from both locations had turbidity of 22 NTU, pH of 8.5, and As concentrations ranging from 100 to 120 ppb. Additional Mason City groundwater quality characteristics are provided in **Table 3-1**.

3.3.6. Dissolved metals analysis

Samples from adsorption experiments were analyzed with inductively coupled plasma optical emission spectrometry (ICP-OES, PerkinElmer Optima 7000 DV). The ICP-OES was calibrated with standards for As(V), Cu(II), Cr(VI), and Pb(II) preceding analysis of samples. In addition, a limited number of Cr(VI) samples were also analyzed colorimetrically using the diphenylcarbazide method [179]; for 100 ppb Cr, 1 mL of sample containing Cr(VI) was placed in a plastic cuvette and acidified with 40 uL 5 N H_2SO_4. Then, 40 uL of diphenylcarbazide solution (5 mg/L in acetone) was added and the solution was mixed with a micropipette. Color was allowed to develop for 30 minutes before measuring absorbance with a UV-vis spectrophotometer at a detection wavelength of 540 nm. Above 100 ppb Cr(VI), 0.5 mL of sample was diluted with 0.5 mL DI prior to acidification and addition of diphenylcarbazide.

3.4. Results and Discussion

3.4.1. Nanofiber characterization and material strength testing

Figure 3-2 shows SEM images, nanofiber diameter distributions, and specific surface areas for unamended PAN, the embedded PAN/Fe_2O_3 composite, and the hydrothermally treated core-shell PAN/Fe_2O_3@Fe_2O_3. The PAN/Fe_2O_3 composite shown contained 33 wt.% 10 nm Fe_2O_3 nanoparticles (relative to PAN) in the electrospinning sol-gel, while the core-shell PAN/Fe_2O_3@Fe_2O_3 was synthesized by hydrothermally treating this same PAN/Fe_2O_3 composite for 12 h in a solution of 0.14 M $FeCl_3 \cdot 6H_2O$ and L-arginine.

XRD confirmed that the phase of nanoparticles embedded in PAN remained as hematite throughout synthesis, while the hydrothermal coating on PAN/Fe_2O_3 was also

hematite (**Figure 3-3**). Further, histograms of nanofiber diameters revealed that the inclusion of Fe_2O_3 at 33 wt.% caused the average nanofiber diameter to increase from 180 (±30) nm to 240 (±40) nm. Although hydrothermal treatment resulted in clear growth of particulate nanostructures on the surface of PAN/Fe_2O_3 nanofibers, PAN/Fe_2O_3@Fe_2O_3 materials did not exhibit any significant increase in average diameter [250 (± 50) nm]. Also, despite differences in nanofiber diameter, thickness of the mats was relatively consistent at ~0.5 mm for PAN, PAN/Fe_2O_3, and PAN/Fe_2O_3@Fe_2O_3, as determined with SEM. We also characterized the iron content of all sorbent materials due to its presumed role as the active sorbent phase in all materials. Both the composite and the core-shell structures contained less total iron than commercial GFH®, with ~20% and 50% total Fe by mass, respectively. For comparison, GFH® consists of ~70% Fe by mass.

Measurements of nanofiber mat specific surface area suggest that despite exhibiting larger average diameters, Fe_2O_3-containing materials exhibit greater specific surface area than the unmodified PAN. We attribute this to the high surface area of the hematite nanoparticles (~80 m^2/g) integrated into the PAN, which SEM images show impart some degree of surface roughness to the nanofiber mat. However, variations in the mass loading of Fe_2O_3 nanoparticles in PAN (up to 50 wt.% relative to PAN) did not impact specific surface area measured with BET. In contrast, the extensive growth of nanostructures on the surface of the core-shell material increased nanofiber specific surface area by two-fold, from ~15 m^2/g for all hematite loadings within PAN/Fe_2O_3 to 30 m^2/g for PAN/Fe_2O_3@Fe_2O_3.

As an important practical consideration, hydrothermal treatment of PAN/Fe_2O_3 did not eliminate the flexibility or wettability of the mat despite extensive surface coating with

Fe_2O_3. Mats could be bent and rolled (**Figure 3-2**), which should help facilitate their application in reactor platforms (e.g., spiral-wound membrane filters) that optimize their treatment capacity. Failure loads for PAN/Fe_2O_3, and PAN/Fe_2O_3@Fe_2O_3 were statistically equivalent at 0.27 (±0.06) and 0.22 (±0.03) N, respectively (where values represent mean and standard deviations of at least 3 measurements), suggesting additional hydrothermal processing exerted no adverse effect on nanofiber mat strength, although these values were less than that measured for unamended PAN [0.40 (± 0.10) N]. With the considerable addition of 33 wt.% Fe_2O_3, the embedded nanoparticles and nanoparticle aggregates likely serve as areas that concentrate stress and cause failure at lower loads relative to unamended PAN, as has been reported elsewhere [180,181]. Further, inclusion of Fe_2O_3 nanoparticles produced wider nanofibers, and the Young's modulus of electrospun nanofibers has often been found to increase with decreasing diameter because the level of molecular orientation in the nanofibers increases [182,183].

3.4.2. Optimization of PAN/Fe_2O_3 composites and PAN/Fe_2O_3@Fe_2O_3 core-shell structures for metal uptake

For all nanofiber sorbents, equilibrium was typically achieved after 12 hours, with adsorption isotherms exhibiting clear plateaus consistent with a maximum uptake equivalent to one monolayer (**Figures 3-5 to 3-8**). Accordingly, the Langmuir adsorption isotherm was used to model all metal/metalloid uptake (equation 3-1):

$$q = \frac{K_L q_{max} C_e}{1 + K_L C_e} \qquad (3\text{-}1)$$

where q is the mass of contaminant adsorbed per unit mass or specific surface area of adsorbent (mg/g or mg/m^2); K_L is the Langmuir coefficient; q_{max} is the amount of adsorption at one monolayer; and C_e is the concentration of the contaminant in solution at

equilibrium [184]. Although adsorption described by the Langmuir model is assumed to be reversible, we note that sorption here proved only partially reversible (to be described in further detail below).

Langmuir model fit parameters (i.e., K_L and q_{max} values) were determined and the corresponding best-fit isotherms are shown on all data presented in corresponding **Figures 3-5 to 3-8** (as solid lines). Because a goal of this study was to assess the performance of different nanofiber composite formulations (e.g., metal/metalloid uptake as a function of embedded Fe_2O_3 loading), these Langmuir model fit parameters were used as a basis for material comparison. A priority was initially placed on maximizing material capacity, thus q_{max} values (both per unit mass and surface area of sorbent) were originally the focus of nanofiber optimization efforts.

For development of composite PAN/Fe_2O_3 nanofibers, we first evaluated how the size of the embedded hematite nanoparticles influenced uptake of CrO_4^{2-} (**Figure 3-4**). PAN containing 20 wt.% of either 10 nm or 40 nm Fe_2O_3 exhibited identical sorption capacities, with q_{max} values in each case of ~0.6 mg CrO_4^{2-}/g. Because of its smaller primary particle size, 10 nm Fe_2O_3 exhibits greater specific surface area than 40 nm Fe_2O_3, but is prone to aggregate more extensively than 40 nm Fe_2O_3 [185]. This, in turn, could limit the amount of surface Fe_2O_3 exposed in electrospun PAN/Fe_2O_3 composites and cause comparable reactivity between composites made with 10 nm and 40 nm Fe_2O_3.

Next, the influence of Fe_2O_3 nanoparticle loading (up to 50 wt.% 10 nm Fe_2O_3) on CrO_4^{2-} and Pb^{2+} adsorption isotherms was evaluated at pH 6 (**Figure 3-5**). Without Fe_2O_3, PAN nanofibers demonstrated some, albeit limited, sorption of Pb^{2+}, although they did not sorb any CrO_4^{2-}. The small amount of Pb^{2+} sorption is presumably due to the electron rich

nitrile (-C≡N) groups present within the PAN structure, which may represent a viable complexation site for cationic metal targets. Increasing 10 nm Fe_2O_3 loading within PAN generally increased uptake of both CrO_4^{2-} and Pb^{2+}, with q_{max} values increasing monotonically from 0.1 to 3 mg CrO_4^{2-}/g and 3 to 11 mg Pb^{2+}/g, respectively, across the Fe_2O_3 loadings considered (8-50 wt.% relative to PAN) (**Figure 3-5**). From model fit q_{max} values, uptake of Pb^{2+} was far more sensitive to inclusion of Fe_2O_3, increasing ~0.3 mg Pb^{2+}/g sorbent for every unit wt.% increase in Fe_2O_3 (R^2 = 0.99) (compared to ~0.1 mg CrO_4^{2-}/g sorbent, R^2 = 0.99). Increasing Fe_2O_3 loading also improved the affinity of PAN/Fe_2O_3 for CrO_4^{2-}, with K_L values increasing for CrO_4^{2-} (0.7 to 3 L/mg). K_L values were relatively constant for Pb^{2+} (from 0.1-0.2 L/mg), representative of consistent affinity for Pb^{2+} though the number of sorption sites increases. Nevertheless, observed increases in q_{max} and K_L values imply that Fe_2O_3 nanoparticles exposed at the composite-water interface represent the dominant sorbent species in embedded composite systems, with the amount of near-surface Fe_2O_3 increasing proportionally with the bulk Fe_2O_3 content.

For development of core-shell PAN/Fe_2O_3@Fe_2O_3 nanofibers, various Fe_2O_3 nanoparticle sizes (10 and 40 nm) and loadings (20 wt.% to 33 wt.%), hydrothermal solution concentrations (0.07 M to 0.14 M $FeCl_3 \cdot 6H_2O$ and L-arginine), and hydrothermal treatment times (1-12 h) were studied. However, across this matrix of synthetic conditions, all core-shell materials were effectively comparable in performance, as assessed by CrO_4^{2-} sorption isotherms (**Figure 3-6**). We attribute these materials' consistent performance to the relatively high loading of embedded Fe_2O_3 nanoparticles, which produced an abundance of uniformly distributed nucleation sites on the PAN surface for additional deposition and growth of Fe_2O_3 nanostructures during hydrothermal coating. In

combination with a high dissolved iron content in the hydrothermal solution and adequate hydrothermal processing times, this allowed for a uniform coating (or shell) of Fe_2O_3 on the PAN (core) nanofibers, and in turn reactive, external surface area for CrO_4^{2-} uptake that was essentially invariant across the synthesis conditions explored.

Accordingly, further improvement in the performance of core-shell nanofibers will most likely have to come via other means to enhance the external reactive surface area of these nanofibers. For example, one approach would be to develop core-shell composites from nanofibers with smaller diameters. Preliminarily, core-shell nanofibers produced from narrower diameter PAN/Fe_2O_3 were explored by first electrospinning PAN/33 wt.% Fe_2O_3 at low relative humidity (~10% RH) and subsequently coating these composites hydrothermally with Fe_2O_3. The result were core-shell nanofibers with an average diameter of 160 ± 40 nm, roughly 100 nm less than those shown in **Figure 3-6**. However, the resulting q_{max} value was the same for these narrower diameter materials, suggesting that gains in reactive surface area via decreasing diameter may be negligible relative to the surface area increase afforded by the Fe_2O_3 coating growth hydrothermally.

3.4.3. Performance comparison of PAN/Fe_2O_3 and PAN/Fe_2O_3@Fe_2O_3 to traditional iron oxide sorbents

3.4.3.1. Sorption isotherms

At pH 6, adsorption isotherms for AsO_4^{3-}, CrO_4^{2-}, Cu^{2+}, and Pb^{2+} are shown in **Figures 3-7 and 3-8** for PAN/Fe_2O_3 (33 wt.% of Fe_2O_3 relative to PAN), PAN/Fe_2O_3@Fe_2O_3, and GFH®. Also provided for comparison is the sorption capacity for each metal/metalloid measured in well-mixed dispersions of 10 nm Fe_2O_3 nanoparticles. In **Figures 3-7 and 3-8**, sorbed metal/metalloid concentrations are reported after

normalization to: (a) sorbent surface area (mg/m^2), (b) sorbent mass (mg/g), and (c) available Fe in each sorbent material (mg/g Fe).

Across all metals considered, notable outcomes from adsorption isotherms are that PAN/Fe_2O_3@Fe_2O_3 (i) outperforms PAN/Fe_2O_3 and commercial GFH® on the basis of available surface area (in most cases by nearly two-fold); and (ii) achieves surface-area-normalized sorption capacities equivalent to dispersions of 10 nm Fe_2O_3 nanoparticles (**Figure 3-7a,d and Figure 3-8a,d**). Furthermore, at pH 6 PAN/Fe_2O_3@Fe_2O_3 and 10 nm Fe_2O_3 nanoparticles generally exhibit greater sorption capacities for cationic species (Cu^{2+} and Pb^{2+}), while GFH® is a more effective sorbent for oxyanions (AsO_4^{3-} and CrO_4^{2-}) than cations (**Table 3-1**). These trends are most obvious when comparing sorbed metal/metalloid concentrations per unit mass of sorbent and per unit mass of available Fe in each material (**Figure 3-7b-c,e-f and Figure 3-8b-c,e-f**). This suggests our synthetic Fe_2O_3 surfaces, both nanoparticle suspensions and composite nanofibers, possess lower points of zero charge (pzc) than GFH®, producing a larger number of neutral or negatively charged sites (e.g., >Fe-OH and >Fe-O^-) at pH 6 for binding cations [186]. Indeed, we anticipated that GFH®, which consists of poorly crystalline akaganeite (β-FeOOH) [187], would adsorb anions better than cations at near-neutral pH because it is widely marketed for As removal [167]. Beyond its surface charge, the extensive internal surface area of GFH® (290 m^2/g from N_2-BET) also promotes its substantial uptake of oxyanions, particularly in these closed batch systems where sufficient equilibrium times minimize diffusion limitations in metal uptake.

It is worth noting that on a per mass basis (either of total sorbent mass or available Fe mass), GFH® represents a superior sorbent for anions, its intended target. For cations,

on the other hand, mass-normalized metal uptake on GFH® is essentially equivalent to composite nanofibers. Interestingly, on the basis of available Fe mass, values of q_{max} with PAN/Fe_2O_3@Fe_2O_3 are ~1.3 times that of PAN/Fe_2O_3, suggesting that embedding Fe_2O_3 nanoparticles into PAN results in the loss of a small amount of surface sites for sorption, as would be expected.

Finally, for our composite materials, it is worth considering whether they behave in a manner analogous to the components from which they were assembled. As a first line of comparison, the relative q_{max} values for CrO_4^{2-}, AsO_4^{3-}, Cu^{2+}, and Pb^{2+} at pH 6 are 1:1.5:3.3:4.4 for the suspension of 10 nm Fe_2O_3, a trend in maximum uptake that reasonably matches that observed for PAN/Fe_2O_3 (1:1.4:2.6:4.2). This indicates that the process of embedding the Fe_2O_3 nanoparticles in the PAN nanofiber matrix has little influence on their surface chemistry and propensity to bind metals/metalloids. For PAN/Fe_2O_3@Fe_2O_3, although the same qualitative trend in metal uptake was observed, some quantitative difference was observed (1:1.1:2.2:3.5) suggesting that the nature of the hematite coating on the core-shell structures is distinct (i.e., different types and abundance of crystal faces and surface sites) from that of the 10 nm nanoparticles. Nevertheless, both hematite-based composites follow trends in adsorption capacity previously reported for hematite with this metal/metalloid suite (AsO_4^{3-}, CrO_4^{2-}, Cu^{2+}, and Pb^{2+} [188–191]), suggesting that established mechanisms for their uptake on hematite (e.g., surface complexation) are also occurring in nanofiber composite systems [190–193]. This is especially promising for predicting performance and application targets for such composite Fe_2O_3 nanofibers from the plethora of existing studies on the application of nanoparticulate Fe_2O_3 as sorbents [194–200].

3.4.3.2. Sorption rates

Equilibrium of oxyanions (AsO_4^{3-} and CrO_4^{2-}) with PAN/Fe_2O_3 was achieved after ~1 h, while equilibrium with PAN/Fe_2O_3@Fe_2O_3 was reached after ~2 h (**Figure 3-9a,b**). For uptake of cations (Cu^{2+} and Pb^{2+}), PAN/Fe_2O_3 was first to achieve equilibrium after ~2 h, whereas PAN/Fe_2O_3@Fe_2O_3 reached equilibrium after 5 h for Cu^{2+} and between 5 and 12 h for Pb^{2+} (**Figure 3-9c,d**). In comparison, GFH® had reached ~50% uptake of all metals within 2 to 4 hours, and equilibrium was typically attained over 12 to 24 hours.

For filtration applications, the initial rate of sorption may be a better performance metric for material comparisons because such platforms will have very short contact times between the sorbent and influent water. With their greater amount of external reactive surface area, initial rates (i.e., within the first 2 h) of metal sorption on PAN/Fe_2O_3@Fe_2O_3 and PAN/Fe_2O_3 were either comparable to or greater than those observed for GFH® (**Figure 3-9)**. Among the nanofiber composites, PAN/Fe_2O_3 and core-shell PAN/Fe_2O_3@Fe_2O_3 exhibited equivalent initial sorption rates of uptake for all metals/metalloids. Such relatively fast initial rates of metal/metalloid sorption on PAN/Fe_2O_3 and PAN/Fe_2O_3@Fe_2O_3 reveal promise for their potential application in a high flux, reactive filtration platform.

3.4.3.3. Sorption pH edge experiments

pH-dependent sorption was assessed from pH 6 to 8 at relatively low concentrations of metals/metalloids compared to those used in isotherms (7.4 mg/L AsO_4^{3-}, 6.7 mg/L CrO_4^{2-}, 0.6 mg/L Cu^{2+}, and 3 mg/L Pb^{2+}). Results are shown in **Figure 3-10** for oxyanions and **Figure 3-11** for cations, where once again sorbed metal/metalloid concentrations are reported after normalization to: (a) sorbent surface area (mg/m^2), (b) sorbent mass (mg/g),

and (c) available Fe in each sorbent material (mg/g Fe). Data for GFH® and a suspension of 10 nm hematite nanoparticles are shown for comparison, as are data for unamended PAN, which showed limited uptake in some instances (i.e., mostly Pb^{2+}).

For AsO_4^{3-}, sorption by PAN/Fe_2O_3, PAN/Fe_2O_3@Fe_2O_3, and GFH® decreased with increasing pH, while sorption by 10 nm Fe_2O_3 remained largely unchanged across the pH range. The decrease in uptake is most notable for PAN/Fe_2O_3, for which sorbed AsO_4^{3-} concentrations halved from pH 6 to pH 8. As with isotherms, PAN/Fe_2O_3@Fe_2O_3 bound the most AsO_4^{3-} per unit surface area at these experimental conditions, and it was also generally a superior adsorbent relative to PAN/Fe_2O_3 when sorbed AsO_4^{3-} concentrations were normalized by total sorbent mass and the mass of available Fe. Per unit mass of sorbent and available Fe, GFH® and 10 nm hematite suspensions remained better sorbent materials across the pH range. These relative trends in pH-dependent performance for our different iron-based sorbent materials for AsO_4^{3-} appear generalizable toward other (oxy)anions, with comparable results obtained for sorption of CrO_4^{2-}.

For cations, sorption of Cu^{2+} on PAN, PAN/Fe_2O_3, PAN/Fe_2O_3@Fe_2O_3 and GFH® increased modestly (typically by no more than two-fold) from pH 6 to pH 7, while sorbed Cu^{2+} concentrations were constant over this pH range in suspensions of 10 nm Fe_2O_3. In contrast, Pb^{2+} uptake as a function of pH varied somewhat for the different materials. For example, Pb^{2+} uptake was relatively low on PAN from pH 6-7, but increased nearly four-fold at pH 8 to yield surface-area normalized concentrations of sorbed Pb^{2+} that rivaled nanofiber composites. For PAN/Fe_2O_3, a maximum in Pb^{2+} uptake occurred at pH 6.5, almost two-fold higher than that measured at pH 6. Notably, PAN/Fe_2O_3, the embedded composite, exhibited the greatest degree of Pb^{2+} uptake per unit surface area under the

conditions used in pH edge experiments. This behavior was mirrored by GFH®, which also exhibited maximum Pb^{2+} uptake at pH 6.5. In contrast, uptake of Pb^{2+} on PAN/Fe_2O_3@Fe_2O_3 decreased monotonically, albeit only slightly, across pH 6 to 8, while sorption on 10 nm Fe_2O_3 was once again relatively insensitive to pH.

Because GFH® generally exhibited weaker performance toward cations, composite nanofibers not only exhibited greater adsorption per unit surface area, but were equivalent to or better than GFH® (as well as suspended 10 nm Fe_2O_3) on the basis of total sorbent mass and available Fe across all pH values. In fact, at the metal concentrations used in pH-edge experiments (lower than those in isotherms) PAN/Fe_2O_3 adsorbed comparable or more metal cations on a surface area basis than PAN/Fe_2O_3@Fe_2O_3, despite its greater external reactive surface area. We propose the better performance of embedded rather than core-shell Fe_2O_3 composites may be the result of synergies between electron rich nitrile groups adjacent to Fe_2O_3 surfaces sites at the composite-water interface. In support of such a hypothesis, we note that unlike isotherms, pH dependent trends in sorption for PAN/Fe_2O_3 were distinct from those of 10 nm hematite, suggesting that the embedded nanoparticles behave uniquely relative to their dispersed counterparts, at least at the low metal concentrations explored for pH edge development.

Generally, however, the pH-dependent behavior of AsO_4^{3-}, CrO_4^{2-}, and Cu^{2+} in systems with PAN/Fe_2O_3 and PAN/Fe_2O_3@Fe_2O_3 is consistent with that previously observed with these metals in more traditional iron oxide sorbent systems [188–190,201,202]. For Pb^{2+}, however, a clear increase in adsorption is often reported with increasing pH on iron oxides [203,204], behavior that was not pronounced on our composites. Again, this may relate to the ability of PAN to bind Pb^{2+}, particularly at higher

pH, providing further evidence that Fe_2O_3 immobilized in or on PAN nanofibers may exhibit distinct reactivity from unsupported hematite under some circumstances.

Finally, for composites, results from these pH-edge experiments imply that electrostatics is the primary driver for uptake. For example, the extent of adsorption of AsO_4^{3-} is expected to decrease with increasing pH due to deprotonation of $H_2AsO_4^-$ to $HAsO_4^{2-}$ when system pH is equal to pK_{a2} (= 6.8) while the hematite surface becomes more negatively charged with increasing pH values (and thus repelling oxyanions) [205,206]. Similarly, the decrease in CrO_4^{2-} adsorption with increasing pH can be attributed to $HCrO_4^-$ deprotonation to CrO_4^{2-} at pH = pK_{a2} of 6.5 [189,207]. This is also the case for cations. For pH values below 7, Cu^{2+} dominates Cu(II) speciation [208], but the hematite surface becomes progressively more negative in charge and thus more favorable for cation adsorption [186]. Likewise, as pH shifts from 6 to 8 the dominant Pb(II) species shifts from Pb^{2+} to less positive complexes with diminished attraction to a negative surface, including $PbOH^+$ at pH 7.2 and $PbCO_3$(aq) (from carbonate available from the atmosphere) [13,29,209,210].

3.4.3.4. Competitive sorption studies

Competition effects in metal/metalloid mixtures was also evaluated across a range of pH from 6.0 to 8.0. Simultaneous uptake of Cu^{2+} with Pb^{2+} (cation-cation) and AsO_4^{3-} with Cu^{2+} (oxyanion-cation) did not significantly differ from uptake of the individual species across the pH range, although Cu^{2+} uptake generally increased on PAN/Fe_2O_3, PAN/Fe_2O_3@Fe_2O_3, and GFH® in the presence of AsO_4^{3-} at pH 6 (**Figure 3-12**). As might be expected, AsO_4^{3-} and Cu^{2+} sorb at different surface sites, and the co-occurrence of bound AsO_4^{3-} has previously been shown to increase Cu^{2+} sorption by making the iron oxide

surface charge more negative [211]. However, because this enhancement of Cu^{2+} uptake was not observed in suspensions of 10 nm Fe_2O_3, this behavior may be attributable to favorable interactions between PAN nitrile groups adjacent to Fe_2O_3 surfaces. Additionally, sorbed Cu^{2+} and Pb^{2+} have been suggested to precipitate on the surface of Fe_2O_3 as oxides or hydroxides at pH values above 6.0, a mechanism of removal that would limit competitive inhibition observed when surface adsorption dominates at lower pH values [212]. Surface precipitation of Pb^{2+} at high concentrations (200 mg/L initial Pb) was supported by XPS analysis, in which peaks were associated with lead oxides; however, we do not expect this mechanism to be relevant in pH edge systems with the lower concentration (3 mg/L) of Pb(II) studied.

For mixtures of AsO_4^{3-} and CrO_4^{2-}, sorption of AsO_4^{3-} was largely the unaffected (**Figure 3-13a**) but uptake of CrO_4^{2-} decreased considerably for all materials across the pH range (**Figure 3-13b**). GFH®, which exhibited two- to three- fold inhibition of CrO_4^{2-} uptake in the presence of AsO_4^{3-}, was least affected by oxyanion interspecies competition. For PAN/Fe_2O_3, uptake was generally decreased three- to four-fold, which was comparable to the extent of inhibition observed in suspensions of 10 nm Fe_2O_3. PAN/Fe_2O_3@Fe_2O_3 exhibited five-fold less uptake of CrO_4^{2-} in the presence of AsO_4^{3-}. Previous studies have shown AsO_4^{3-} and CrO_4^{2-} to compete directly for surface sites on iron oxide, with AsO_4^{3-} prevailing in equilibrium systems [211]. Thus, while subject to interspecies competition when applied to metal/metalloid mixtures, the susceptibility of Fe_2O_3 nanofiber composites is very much in line with expectations for more traditional iron oxide-based sorbents.

3.4.4. Reactive filtration studies with simulated and authentic groundwater

In equilibrium batch (closed) systems, core-shell PAN/Fe_2O_3@Fe_2O_3 typically performed slightly better than embedded composite PAN/Fe_2O_3 in regard to sorption capacities. There were even instances (e.g., Pb^{2+} uptake) where PAN/Fe_2O_3 out performed core-shell PAN/Fe_2O_3@Fe_2O_3 despite the greater degree of external, reactive surface area in the core-shell configuration. From the perspective of material processing and technology scale-up, PAN/Fe_2O_3 is also more advantageous because it is prepared in a single synthesis step (i.e., a single-pot synthesis). In contrast, PAN/Fe_2O_3@Fe_2O_3 requires electrospinning with an additional, subsequent synthesis step via hydrothermal treatment.

Both types of Fe_2O_3 nanofiber composites were next assessed in flow-through, reactive filtration experiments to determine their viability in point-of-use water treatment applications. A filter consisting of 100 mg of PAN/Fe_2O_3 (1.4 m^2 available surface area) was evaluated at pH 6 (with 10 mM MES buffer) against an influent of 100 ppb As(V) (i.e., 10 times the EPA MCL) and 100 ppb Cr(VI) (i.e., equal to the EPA MCL). Both AsO_4^{3-} and CrO_4^{2-} were immediately detectable in effluent, with effluent concentrations ~80% and 60% of influent, respectively, after the first 100 mL of water treated (**Figure 3-14**). Similarly, upon exposure to 300 ppb Pb(II) (i.e., 20 times the EPA action level), Pb^{2+} was detectable at ~60% of influent within the first 100 mL (**Figure 3-14**).

Similar evaluation of a 100 mg filter (2.8 m^2 available surface area) of core-shell PAN/Fe_2O_3@Fe_2O_3 was also conducted at pH 6 (10 mM MES) with both an influent mixture of 100 ppb As(V) and 100 ppb Cr(VI), as well as a separate trial with an influent of 300 ppb Pb(II). Metal removal was much improved in this system, with AsO_4^{3-} below detection limits (~10 μg As/L) for the first 1,500 mL, while CrO_4^{2-} was below detection limits (~6 μg Cr/L) for the first 700 mL (**Figure 3-14**) of testing. For Pb, effluent Pb^{2+}

exceeded detection limits (~10 μg Pb/L) after 400 mL (**Figure 3-14**). Thus, although the performance of PAN/Fe_2O_3 composites compared reasonably to core-shell materials in closed batch systems, metal uptake in flow-through appears considerably more dependent on Fe_2O_3 surface area being easily accessible. Thus, for the short contact times anticipated during reactive filtration applications (less than 1 s), core-shell PAN/Fe_2O_3@Fe_2O_3 appears the most viable composite for application because of its external hematite shell.

Unexpectedly, AsO_4^{3-} did not adversely impact uptake of CrO_4^{2-} in flow-through, as breakthrough curves for solutions with only CrO_4^{2-} were comparable to that seen in **Figure 3-14** for the oxyanion mixed influent. Thus, factors influencing competitive sorption between oxyanions must be different in flow-through systems, where contact time is much shorter (kinetically limited sorption to the most reactive and available binding sites) than in batch equilibrium systems. Notably, the levels of sorption achieved after exposure to 4 L of 100 ppb As/100 ppb Cr mixed influent (i.e., 5.3 mg AsO_4^{3-}/g and 1.5 mg CrO_4^{2-}/g) were lower, for chromate considerably, than the sorption capacities measured in batch isotherms (9.3 and 8.7 mg/g, respectively). Further, while effluent AsO_4^{3-} did not ever reach influent concentration during the 4 L experiment, effluent CrO_4^{2-} matched influent concentrations after treatment of 1,500 mL. Thus, it appears the majority of the sites available for CrO_4^{2-} sorption at equilibrium (i.e., in batch) were inaccessible in the kinetically limited regime imposed by flow-through filtration.

The influence of filter mass on uptake was also assessed using Pb^{2+}. The volume treated before detection of Pb^{2+} was doubled by doubling the amount of PAN/Fe_2O_3@Fe_2O_3 used, with detection of Pb^{2+} occurring after 900 mL with 200 mg PAN/Fe_2O_3@Fe_2O_3 (5.7 m^2 available surface area) in flow-through (**Figure 3-15c**). The

level of uptake reached during this flow-through was 3.9 mg Pb^{2+}/g, much less than the sorption capacity determined in batch isotherms (31 mg/g), though the filter was unsaturated because effluent Pb^{2+} never reached the concentration of the influent.

Given the more promising viability of PAN/Fe_2O_3@Fe_2O_3, regeneration (i.e., sorption reversibility) was explored in this flow-through platform. Both AsO_4^{3-} and CrO_4^{2-} sorption proved partially reversible, as 20% of the sorbed AsO_4^{3-} and 15% of the sorbed CrO_4^{2-} were released into the effluent when clean buffer (pH 6, 10 mM MES) was passed through the filter after completion of the flow-through experiment (after 4L of influent was applied) (**Figure 3-15a,b**). Pb^{2+} sorption was also partially reversible, as 15% of sorbed Pb^{2+} was released into effluent when clean buffer passed through the filter (**Figure 3-15c**). Consistent with this lack of bound metal release, additional trials after spent filter regeneration with clean buffer showed near immediate detection of the metals/metalloid in the process effluent, suggesting the majority of binding sites remained filled despite the buffer wash. That the majority of oxyanion and cation mass remains bound during treatment with clean (i.e., metal-free) influent is encouraging, as a spent filter will not likely become a significant pollutant source in the event the quality of influent improves.

More aggressive regenerative treatments were also explored as a means to achieve complete regeneration of spent filters, thereby enabling reuse and extending technology longevity. Specifically, we found that treatment with 1 L of 0.05 M NaOH was able to significantly regenerate filter activity toward both AsO_4^{3-} and CrO_4^{2-}. Alkaline regeneration, which has previously proven effective for iron oxides with bound As(V) and Cr(VI) [205,213,214], resulted in the removal of 85% of sorbed AsO_4^{3-} and 60% of sorbed CrO_4^{2-} (**Figure 3-15a,b**). Further, subsequent tests with our metal-containing test influent

revealed performance of the alkaline regenerated filter was close to that of the new, pristine filter material. Meanwhile, treatment with 1 L of 0.1 M HNO_3 was able to slightly regenerate the filter toward Pb^{2+}. Acid regeneration, previously reported to regenerate iron oxides with bound Pb(II) [215,216], removed 50% of sorbed Pb^{2+}. This acid regeneration partially restored performance of the filter (**Figure 3-15c**).

Finally, PAN/Fe_2O_3@Fe_2O_3 was evaluated in flow-through for removal of As from contaminated groundwater samples collected from small drinking water systems in Iowa. Although As was not immediately detectable in the treated effluent for groundwater samples, performance was poorer than observed in idealized buffer system (10 mM MES at pH 6). In Mason City groundwater, As was detectable in effluent after ~1.2 L of treatment, while As in Clear Lake groundwater was detectable much more rapidly, after only ~400 mL were treated (**Figure 3-16a**). For Clear Lake groundwater samples, the breakthrough curve noticeably plateaued at a concentration roughly 80% of the influent. This can be attributed to a pseudo-steady state condition dependent on pH and influent As concentration [217], where a steady rate of uptake for a portion of As is fast relative to flow through the filter after initial breakthrough [218]. Ultimately, this would be a multi-step breakthrough curve with an eventual plateau occurring at effluent concentrations equivalent to influent over greater volumes of water treatment.

Due to the higher pH of both groundwater samples relative to our model systems (groundwater pH of 8.5 versus pH 6 buffer), we expected As to break through earlier in groundwater samples when using the same amount of filter material; at pH 8.5, the surface of the PAN/Fe_2O_3@Fe_2O_3 becomes more negative and less attractive to oxyanions like AsO_4^{3-}, as observed from pH edge experiments. We suspect that the extensive differences

in As breakthrough for the two groundwater samples indicate that co-solutes [e.g., carbonate (CO_3^{2-}) and phosphate (PO_4^{3-})] likely interfere with As uptake on PAN/Fe_2O_3@Fe_2O_3, as has been reported elsewhere [219,220]. In such instances, we anticipate that the mass of PAN/Fe_2O_3@Fe_2O_3 filter could be increased to increase sorption of metals/metalloids in complex water matrices and overcome inhibition from co-solutes present in such samples.

Finally, a major component of the groundwater samples was particulate matter, presumably arising from colloidal iron, which caused initial turbidity in the water samples of 22 NTU. This provided an ideal scenario to test for concurrent removal of As and particulate matter using composite nanofibers as a reactive filtration technology. Indeed, the filters simultaneously achieved turbidity removal concurrent with As sorption, lowering effluent turbidity to 0.2 NTU and removing ~20 mg of suspended solids from both samples (**Figure 3-16b**). This left a visible layer of solids on top of the filters after flow-through experiments.

3.5. Conclusion

While existing technologies utilize iron oxides for sorption of metals/metalloids (e.g., GFH® for As removal), such technologies have larger footprints (i.e., packed bed with depth for filtration) and, as larger systems, require some operational knowledge. Implementation of nanotechnology using well-studied chemical mechanisms (i.e., binding of metals/metalloids onto iron oxide surfaces) can decrease the scale of systems required to treat water by increasing the amount of reactive surface area without increasing the volume and mass of filtration materials needed. Nanotechnology can deliver upon its promise of enhanced reactivity in water treatment applications if suitably harnessed in

cohesive platforms appropriate for filtration. Current studies on nanomaterials have focused on either reactivity of iron oxide suspensions, which are impractical for water treatment, or material synthesis of cohesive platforms, uncoupled with performance demonstration that shows applicability in water treatment.

This study demonstrates the promise, as well as areas for future optimization, of two cohesive platforms for metal sequestration in water treatment applications – PAN/Fe_2O_3 and core-shell PAN/Fe_2O_3@Fe_2O_3 nanofiber filters. The electrospinning process allowed the facile synthesis of a flexible, stable nanofiber network, while hydrothermal treatment achieved a coating of Fe_2O_3 nanostructures increasing the reactive iron oxide surface area available to adsorb metals from solution. PAN/Fe_2O_3 and PAN/Fe_2O_3@Fe_2O_3 adsorbed significant amounts of AsO_4^{3-}, CrO_4^{2-}, Cu^{2+}, and Pb^{2+} across a range of initial concentrations and pH values. Adsorption capacities were comparable to those of 10 nm Fe_2O_3 nanoparticles, so two materials have been created that likely utilize the studied mechanisms of uptake of nanoparticulate hematite while bound in a cohesive platform. PAN/Fe_2O_3 and PAN/Fe_2O_3@Fe_2O_3 also employed rapid kinetics relative to GFH®, which demonstrated promise for use as membrane filters with short contact times for treatment. Although both materials performed well in batch systems that reached thermodynamic equilibrium, core-shell PAN/Fe_2O_3@Fe_2O_3 outperformed PAN/Fe_2O_3 in flow-through filtration with As(V), Cr(VI), and Pb(II) making it the ideal choice for POU or POE water treatment, in which rapid kinetics play a key role. PAN/Fe_2O_3@Fe_2O_3 also achieved simultaneous As and suspended solids removal in groundwater samples, and thus is applicable in real water systems. Furthermore, the PAN/Fe_2O_3@Fe_2O_3 nanofiber filter – a flexible sheet of nanofibers, even after hydrothermal treatment – is a robust candidate as

a filtration technology, as supported by strength testing. The small footprint of this membrane filter would allow it to be deployed in POU and POE scenarios (e.g., by individual groundwater well users in rural areas) where larger technologies (e.g., a packed bed of GFH) cannot be easily utilized, particularly for Pb and As removal.

While this study balanced material strength with reactivity, with the knowledge gained here further strides can be made in making the cohesive nanofiber platform more reactive, scalable, and deployable for POU and POE water treatment applications. First, decreasing average nanofiber diameter by changing electrospinning parameters would likely improve performance in flow-through filtration. Despite decreases in nanofiber diameter having little impact on sorption capacity for Cr(VI), we have demonstrated that properties determined at equilibrium are not necessarily representative of properties exhibited in a kinetically limited regime (i.e., membrane filtration). Decreasing nanofiber diameter and increasing specific surface area could vastly improve rapid uptake of metals/metalloids. Regarding scalability, although electrospinning has been demonstrated on an industrial scale, industrial-scaled electrospinning with hydrothermal synthesis post-processing is not prevalent. The hydrothermal synthesis utilized herein for Fe_2O_3 coating of nanofibers is ideal for scalability because it does not require high pressure (i.e., above 1 atm) nor high temperature (i.e., above 100 °C). In addition, the durability of PAN/Fe_2O_3@Fe_2O_3 means it could be easily integrated and deployed in household faucet filters and water bottle filters. Future work, centered on improving reactivity (without adding synthesis steps) while producing filters at-scale and in forms that can be used in current water treatment process designs, would help bring this nano-enabled iron oxide

technology into the hands of consumers who face the challenge of metal/metalloid contamination in drinking water.

Table 3-1. Water quality characteristics for groundwater from Mason City, Iowa.

Parameter	
Source	Lime Creek Aquifer
Well depth	60 feet
Dissolved oxygen	<0.13 mg/L
Ammonia N	0.5 mg/L as N
Chloride	16 mg/L
Sulfate	13 mg/L
Nitrate N	Non-detect
Dissolved organic carbon	1.2 mg/L
Total alkalinity	280 mg/L
Total dissolved solids	320 mg/L
Arsenic	0.11 mg/L (95 ug/L As(V))
Calcium	70 mg/L
Iron	1.5 mg/L
Magnesium	23 mg/L
Sodium	13 mg/L

Table 3-2. Langmuir coefficients (K_L, in L/mg) and maximum adsorption capacities (q_{max}, in mg/m^2 sorbent, mg/g sorbent, and mg g/Fe in sorbent) for PAN/Fe_2O_3@Fe_2O_3, PAN/Fe_2O_3, and GFH® for AsO_4^{3-}, Cu^{2+}, CrO_4^{2-}, and Pb^{2+} at pH 6. Maximum adsorption capacities are also given for 10 nm Fe_2O_3 nanoparticles.

Material	q_{max} units	AsO_4^{3-}		Cu^{2+}		CrO_4^{-2}		Pb^{2+}	
		K_L (L/mg)	q_{max}	K_L (L/mg)	q_{max}	K_L (L/mg)	q_{max}	K_L (L/mg)	q_{max}
PAN/ Fe_2O_3@ Fe_2O_3	mg/m^2		0.33 ± 0.02		0.67 ± 0.04		0.31 ± 0.01		1.1 ± 0.1
	mg/g	2.6 ± 1.5	9.3 ± 0.5	0.10 ± 0.02	19 ± 1	0.94 ± 0.11	8.7 ± 0.2	0.18 ± 0.056	31 ± 2
	mg/g Fe		17 ± 1		35 ± 2		16 ± 0		57 ± 4
PAN/ Fe_2O_3	mg/m^2		0.19 ± 0.01		0.37 ± 0.04		0.14 ± 0.01		0.59 ± 0.04
	mg/g	2.0 ± 1.0	2.7 ± 0.1	0.086 ± 0.023	5.2 ± 0.5	4.4 ± 3.7	2.0 ± 0.2	0.16 ± 0.05	8.3 ± 0.5
	mg/g Fe		13 ± 1		26 ± 3		10 ± 1		42 ± 3
GFH®	mg/m^2		0.25 ± 0.02		0.067 ± 0.006		0.19 ± 0.01		0.25 ± 0.04
	mg/g	0.17 ± 0.07	71 ± 6	0.067 ± 0.018	19 ± 2	0.34 ± 0.10	53 ± 4	0.018 ± 0.006	70 ± 12
	mg/g Fe		110 ± 10		31 ± 3		86 ± 6		110 ± 20
10 nm Fe_2O_3	mg/m^2		0.28 ± 0.09		0.63 ± 0.25		0.19 ± 0.05		0.84 ± 0.23
	mg/g		22 ± 7		49 ± 20		15 ± 4		66 ± 18
	mg/g Fe		31 ± 10		70 ± 28		21 ± 5		94 ± 25

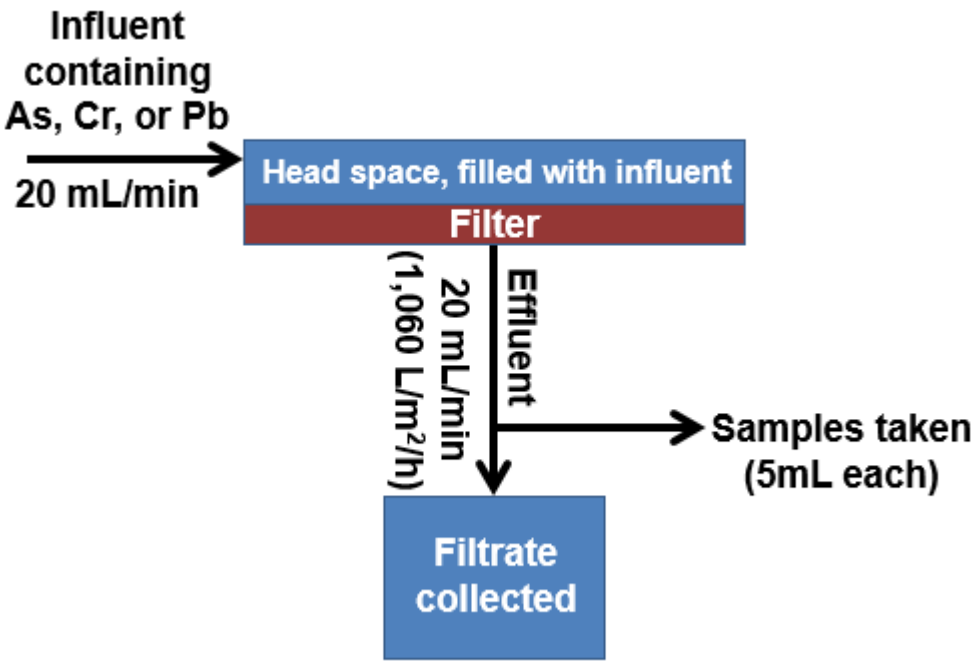

Figure 3-1. Schematic of the dead-end filtration system used to test nanofiber filters in flow-through. As the filter holder had been modified so that it could be used for cross-flow or dead-end filtration, influent was pumped into the system on a side inlet of a Millipore 47 mm filter holder at a sufficiently high flow rate (20 mL/min) to ensure influent contact with the entire filter. Influent passed through the filter and was collected, with 5 mL samples taken periodically from the filter outlet for analysis.

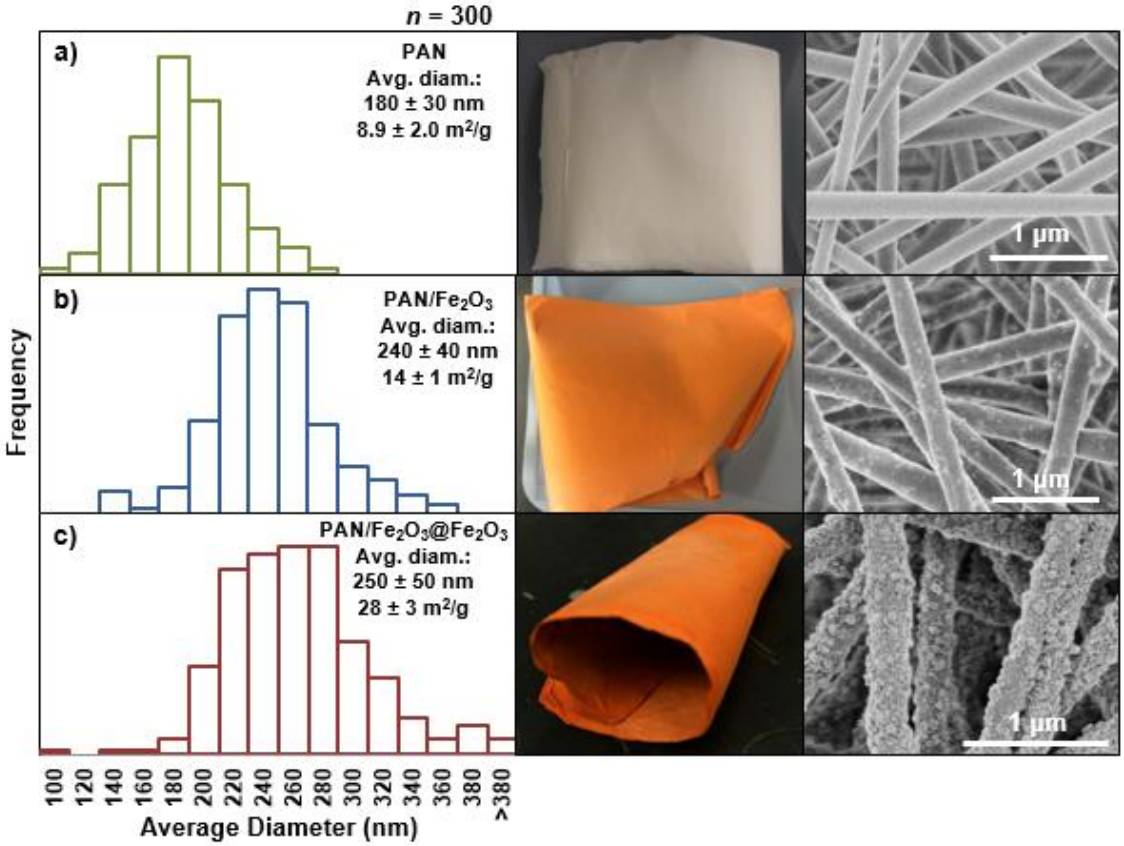

Figure 3-2. Size distribution histograms for (a) PAN, (b) PAN/Fe_2O_3, and (c) PAN/Fe_2O_3@Fe_2O_3 nanofibers, with corresponding images of the mats and SEM images of the nanofiber mats. Average nanofiber diameters and measured surface areas from BET with standard deviation are given for each material.

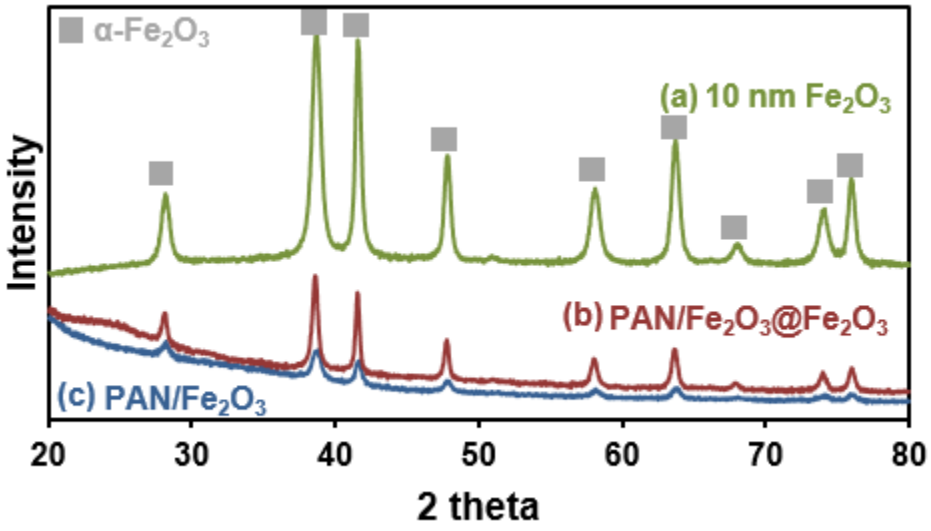

Figure 3-3. X-ray diffraction (XRD) spectra for (a) 10 nm Fe_2O_3 nanoparticles in green, (b) PAN/Fe_2O_3@Fe_2O_3 in red, and (c) PAN/Fe_2O_3 in blue. Peaks are consistent with d-spacings for hematite, indicated with grey squares.

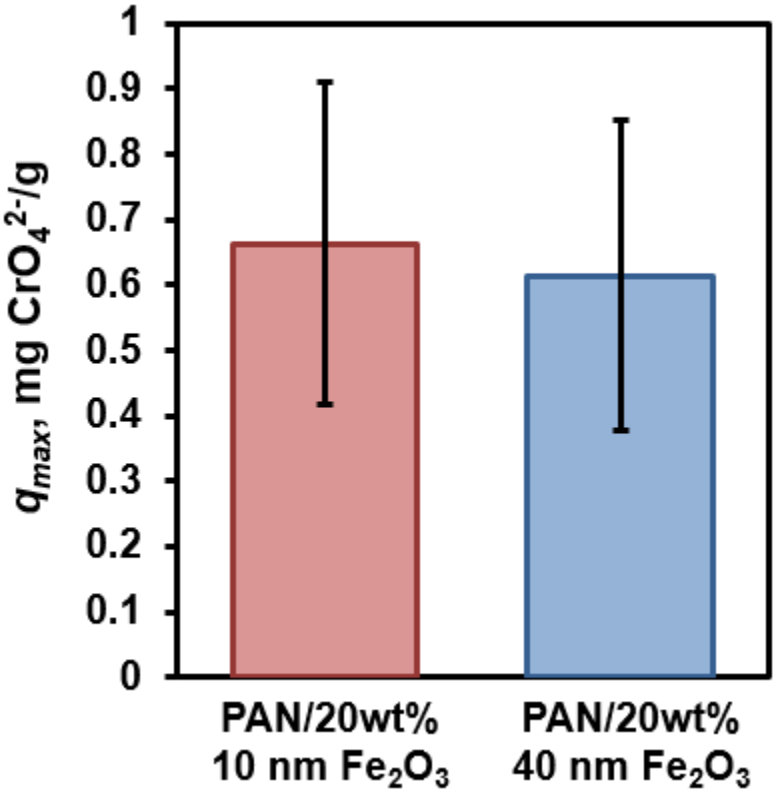

Figure 3-4. Sorption capacities for CrO_4^{2-} for as-electrospun PAN/20 wt.% 10 nm Fe_2O_3 and PAN/20 wt.% 40 nm Fe_2O_3.

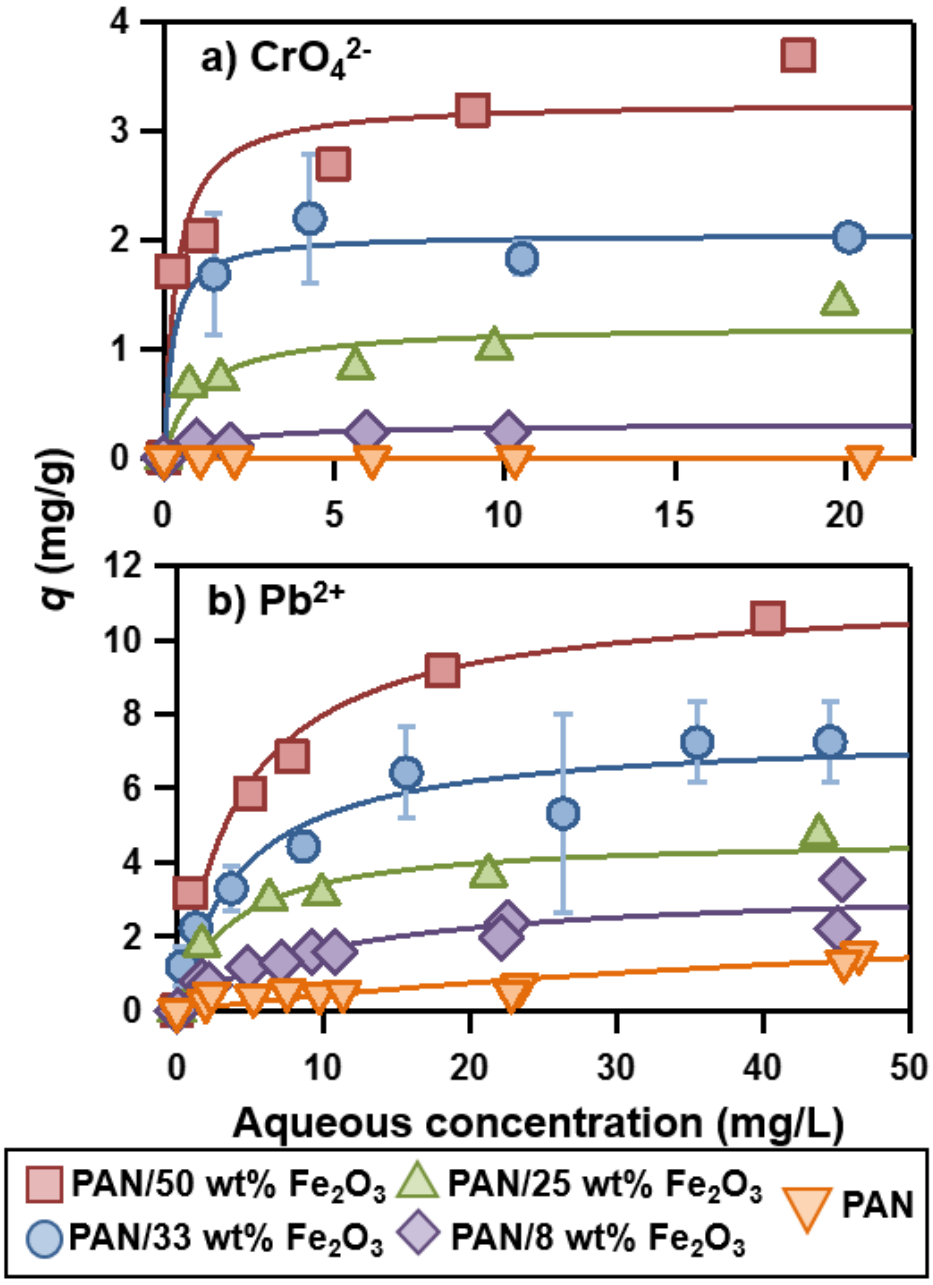

Figure 3-5. Adsorption isotherms for PAN/Fe_2O_3 with different mass loadings of Fe_2O_3 for (a) CrO_4^{2-} and (b) Pb^{2+}. Experiments were conducted in pH 6 10 mM MES buffer. Isotherms are given in terms of mass adsorbed per mass of adsorbent (mg/g), and lines are Langmuir model fits. Results demonstrate that higher loadings of Fe_2O_3 correspond with increased uptake of metals. PAN alone adsorbs some Pb^{2+} but does not adsorb any CrO_4^{2-}.

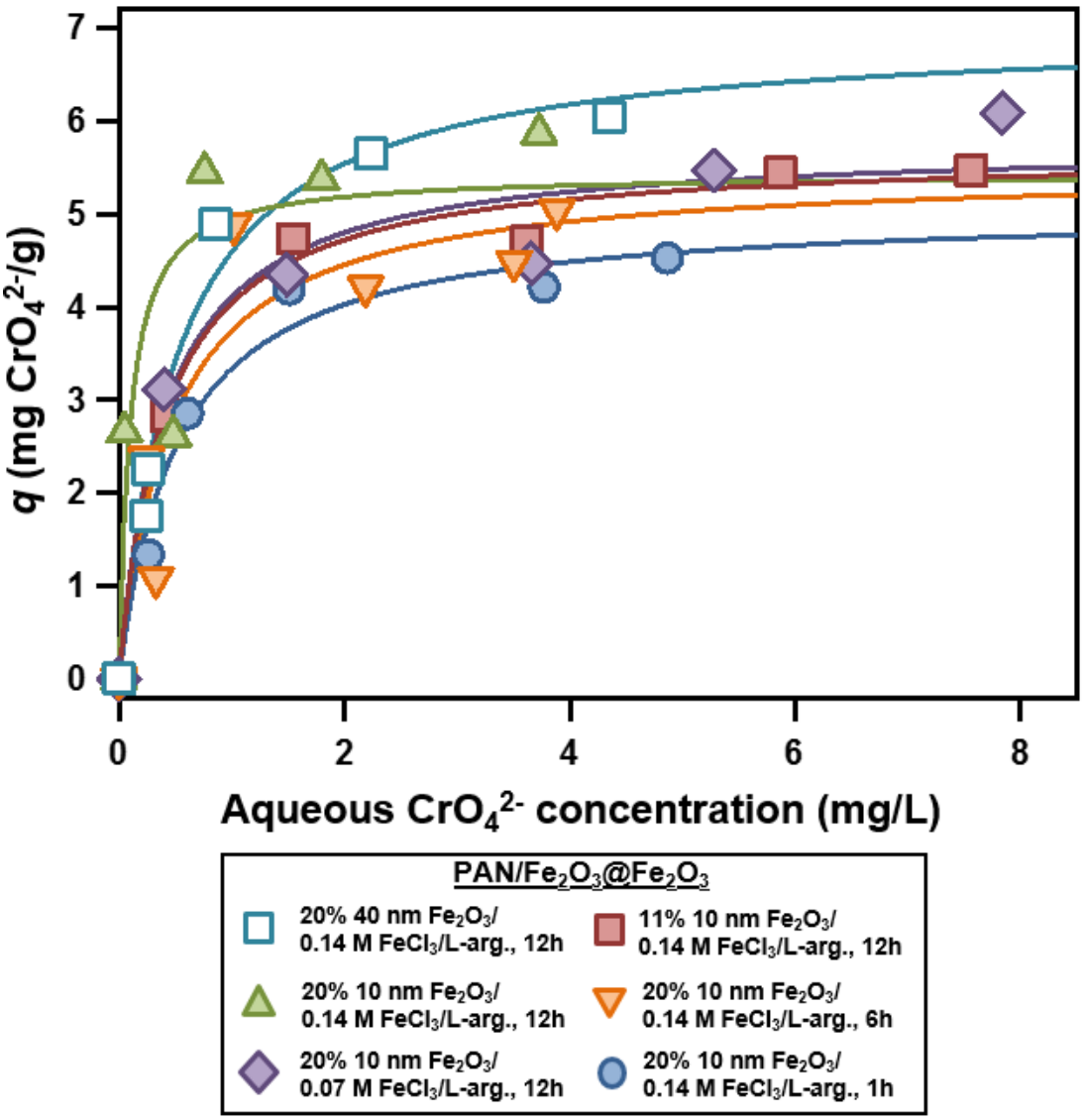

Figure 3-6. Adsorption isotherms for CrO_4^{2-} for core-shell PAN/Fe_2O_3@Fe_2O_3 with various sizes Fe_2O_3 in electrospun nanofibers, wt.% of Fe_2O_3 in electrospun nanofibers, concentrations of hydrothermal solutions, and hydrothermal treatment durations. Experiments were conducted in pH 6 10 mM MES buffer.

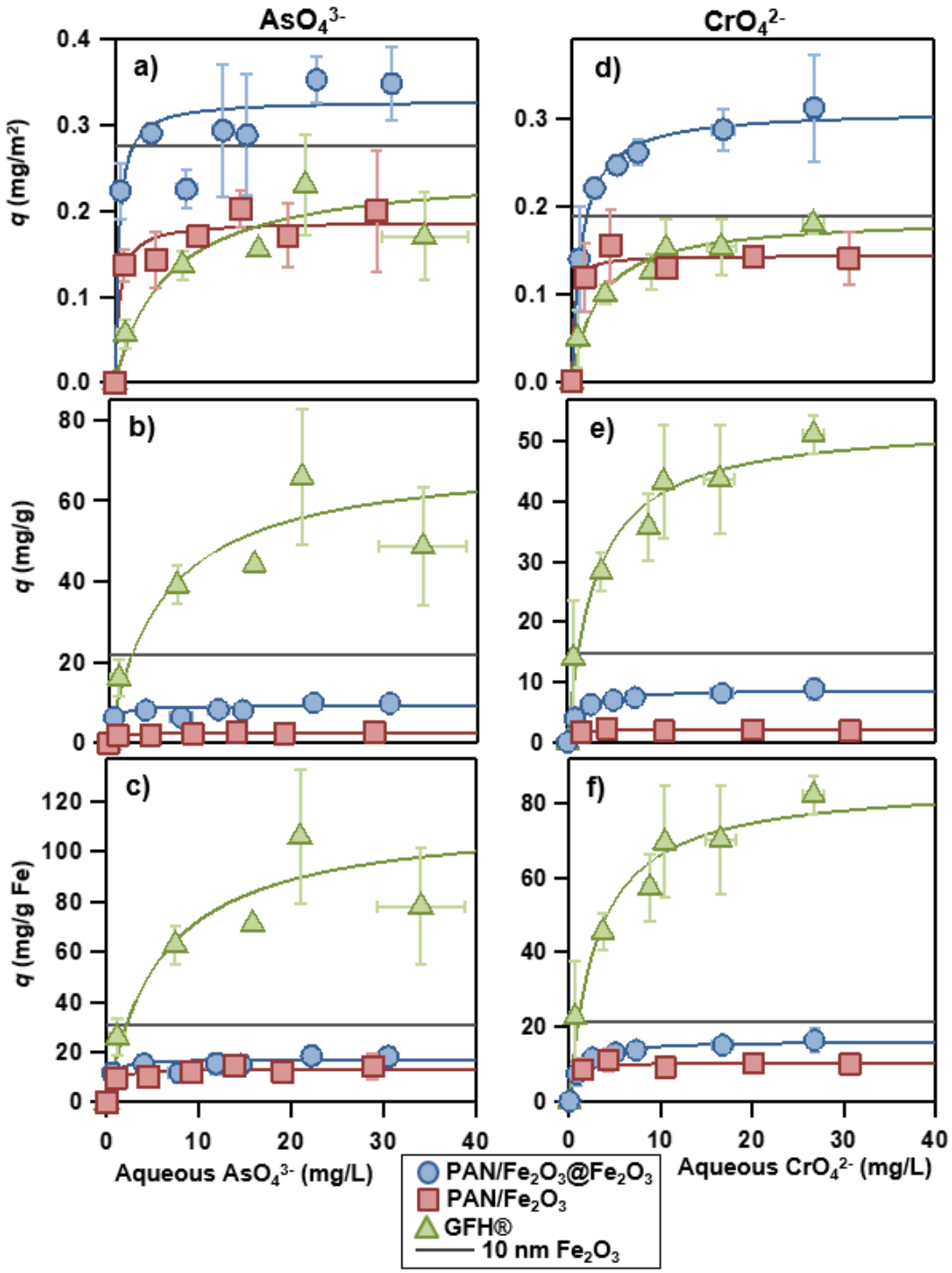

Figure 3-7. Adsorption isotherms for PAN/Fe_2O_3@Fe_2O_3 in blue, PAN/Fe_2O_3 in red, and GFH® in green for uptake of (a,b,c) AsO_4^{3-} and (c,d,e) CrO_4^{2-}. Maximum adsorption capacities for 10 nm Fe_2O_3 nanoparticles are given by the grey lines. Experiments were conducted in batch with 5 mg of sorbent and 10 mL of 10 mM MES buffer at pH 6 with the appropriate concentration of metal/metalloid. Isotherms are given in terms of mass adsorbed per surface area of adsorbent (m^2), mass of sorbent (g), and mass Fe in sorbent (g Fe); lines are Langmuir model fits.

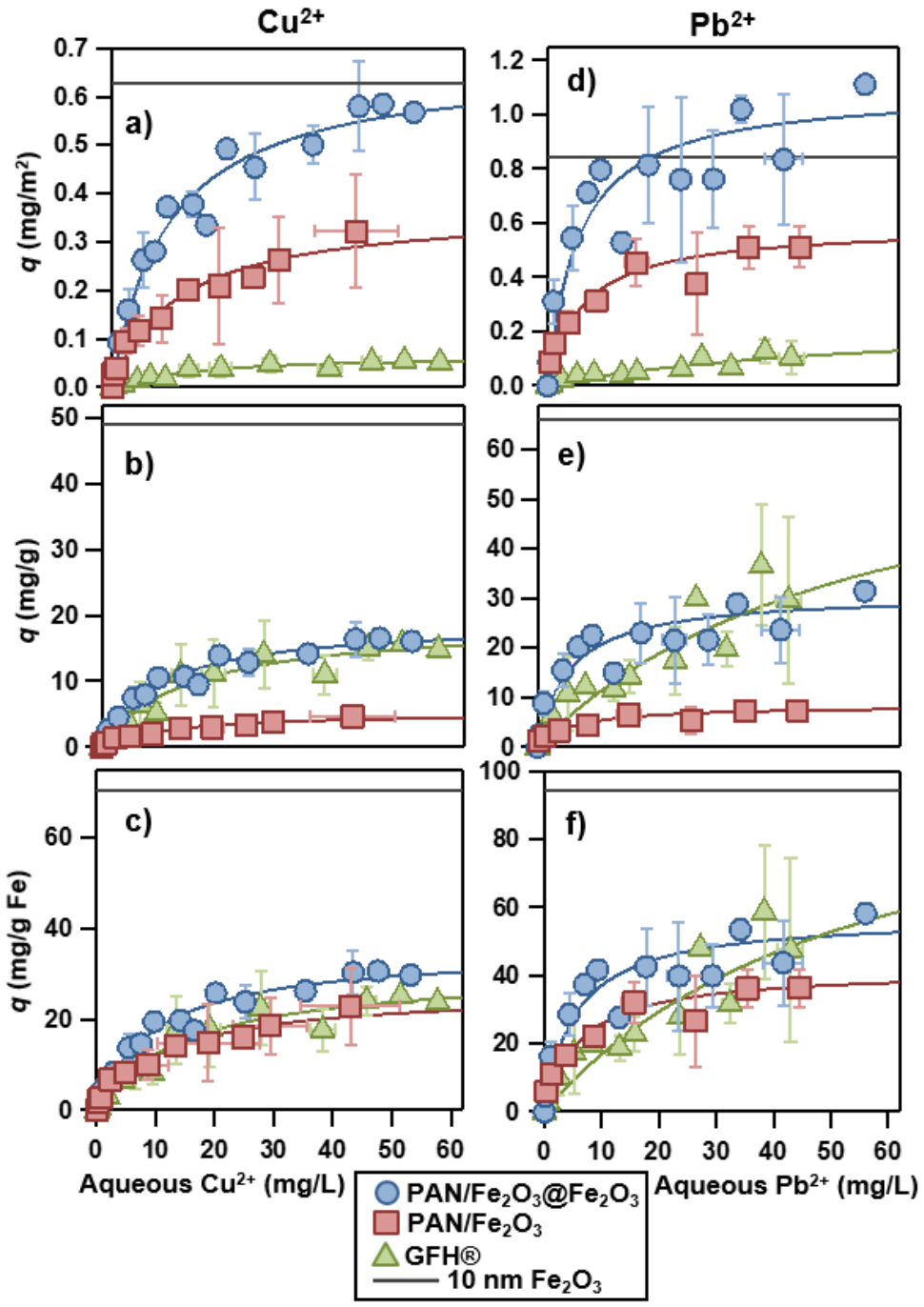

Figure 3-8. Adsorption isotherms for PAN/Fe_2O_3@Fe_2O_3 in blue, PAN/Fe_2O_3 in red, and GFH® in green for uptake of (a,b,c) Cu^{2+} and (c,d,e) Pb^{2+}. Maximum adsorption capacities for 10 nm Fe_2O_3 nanoparticles are given by the grey lines. Experiments were conducted in batch with 5 mg of sorbent and 10 mL of 10 mM MES buffer at pH 6 with the appropriate concentration of metal/metalloid. Isotherms are given in terms of mass adsorbed per surface area of adsorbent (m^2), mass of sorbent (g), and mass Fe in sorbent (g Fe); lines are Langmuir model fits.

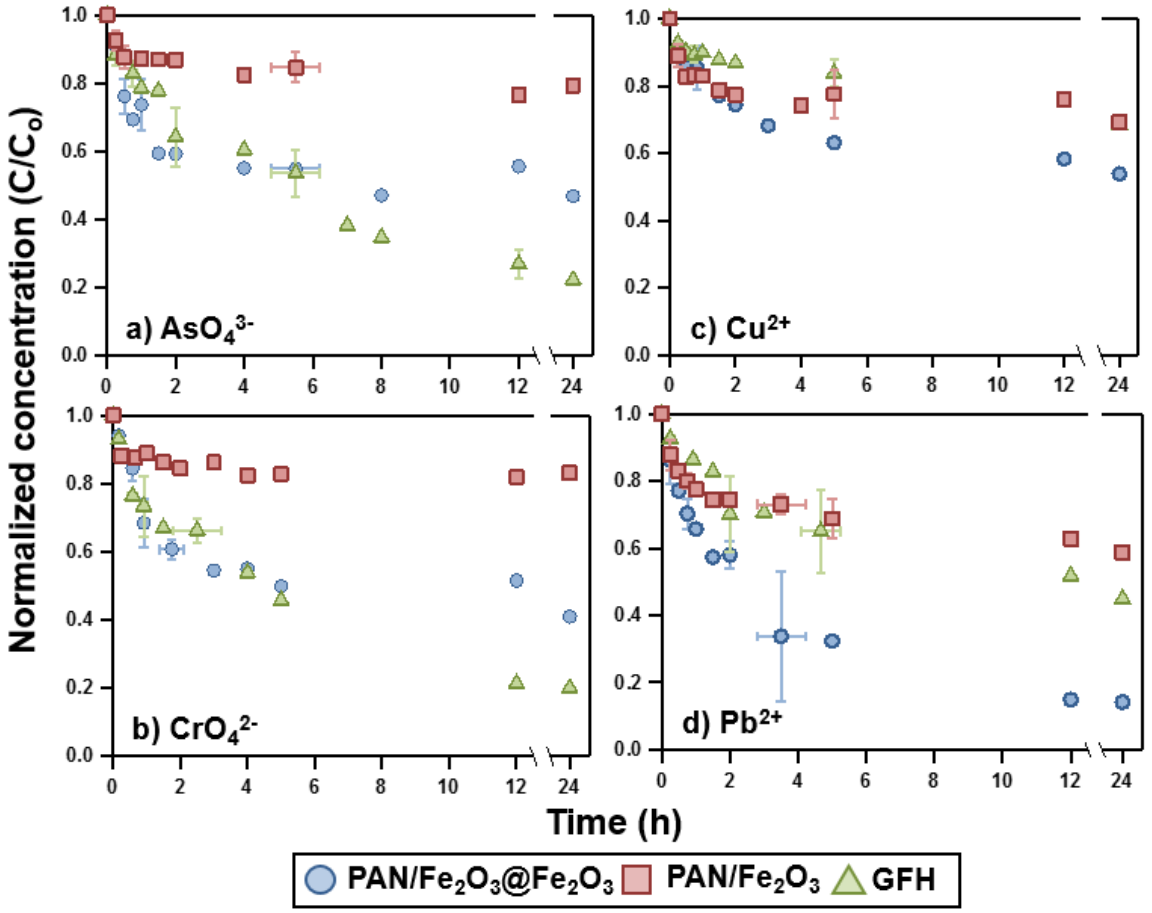

Figure 3-9. Sorption kinetics for PAN/Fe_2O_3@Fe_2O_3 in blue, PAN/Fe_2O_3 in red, and GFH® in green for (a) AsO_4^{3-}, (b) CrO_4^{2-}, (c) Cu^{2+}, and (d) Pb^{2+}. Normalized concentrations of cations or oxyanions are shown as a function of time. Experiments were conducted in batch with 5 mg of sorbent and 10 mL of 10 mM MES buffer at pH 6 with 7.4 mg/L AsO_4^{3-}, 6.7 mg/L CrO_4^{2-}, 3.0 mg/L Pb^{2+}, or 0.6 mg/L Cu^{2+}.

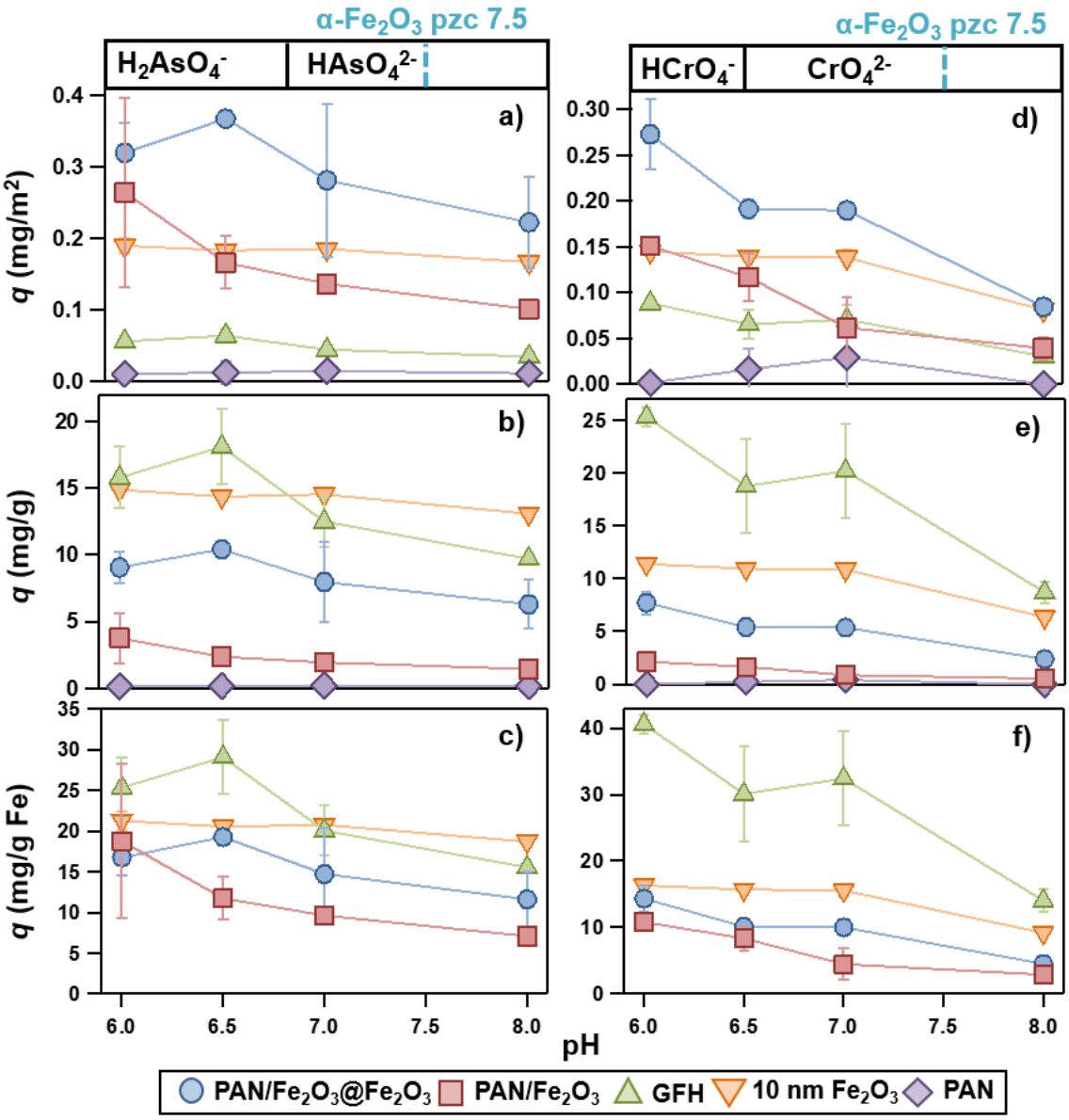

Figure 3-10. Sorption pH edge experiments shown for 7.4 mg/L AsO_4^{3-} (a-c) and 6.7 mg/L CrO_4^{2-} (d-f). Uptake (q) is given on a surface area basis (a,d), mass sorbent basis (b,e), and mass Fe basis (c,f). Speciation of metals/metalloids is given at the top, along with the typical pzc of Fe_2O_3.

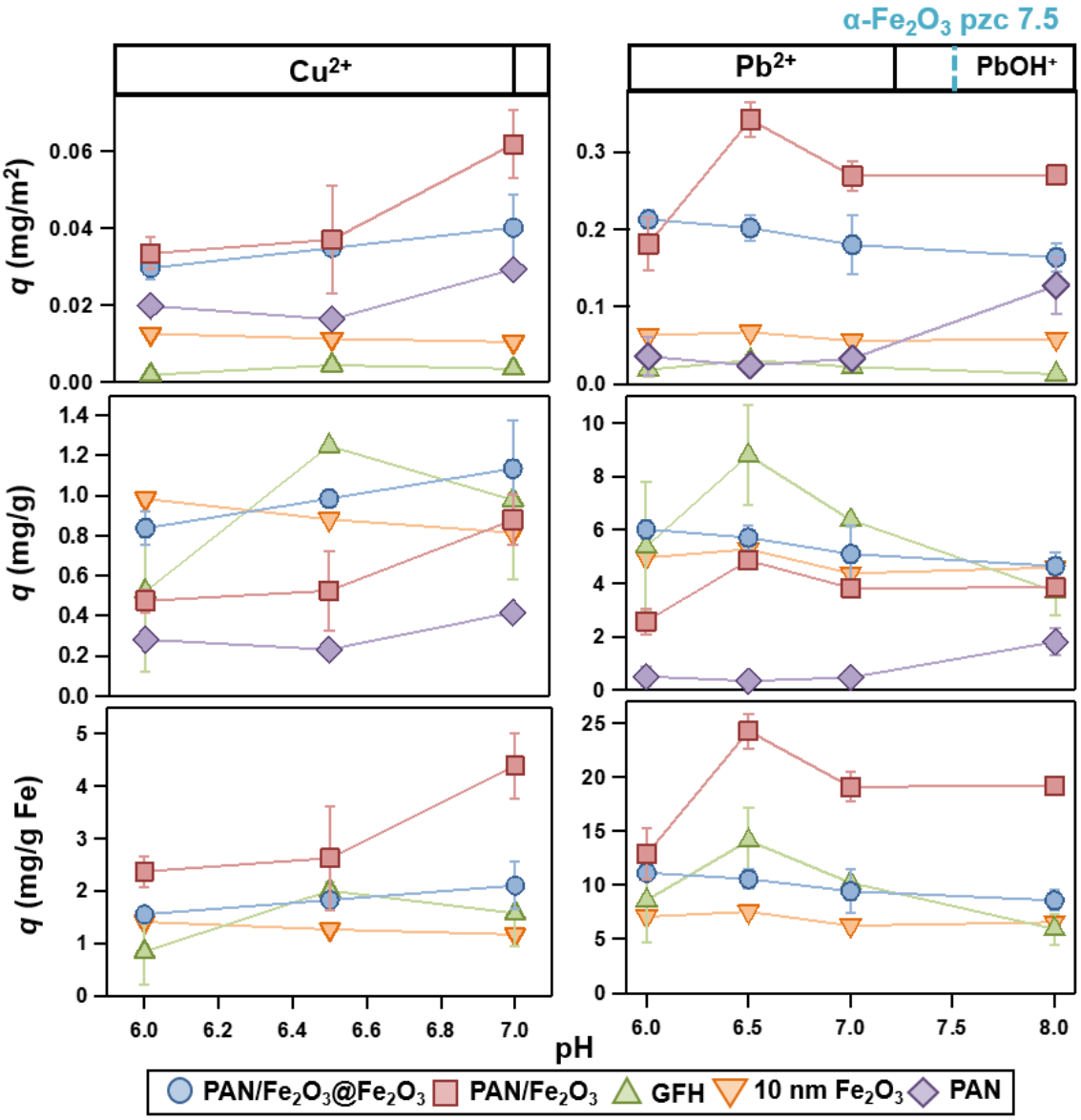

Figure 3-11. Sorption pH edge experiments shown for 0.6 mg/L Cu^{2+} (a-c) and Pb^{2+} (d-f). Uptake (*q*) is given on a surface area basis (a,d), mass sorbent basis (b,e), and mass Fe basis (c,f). Speciation of metals is given at the top, along with the typical pzc of Fe_2O_3.

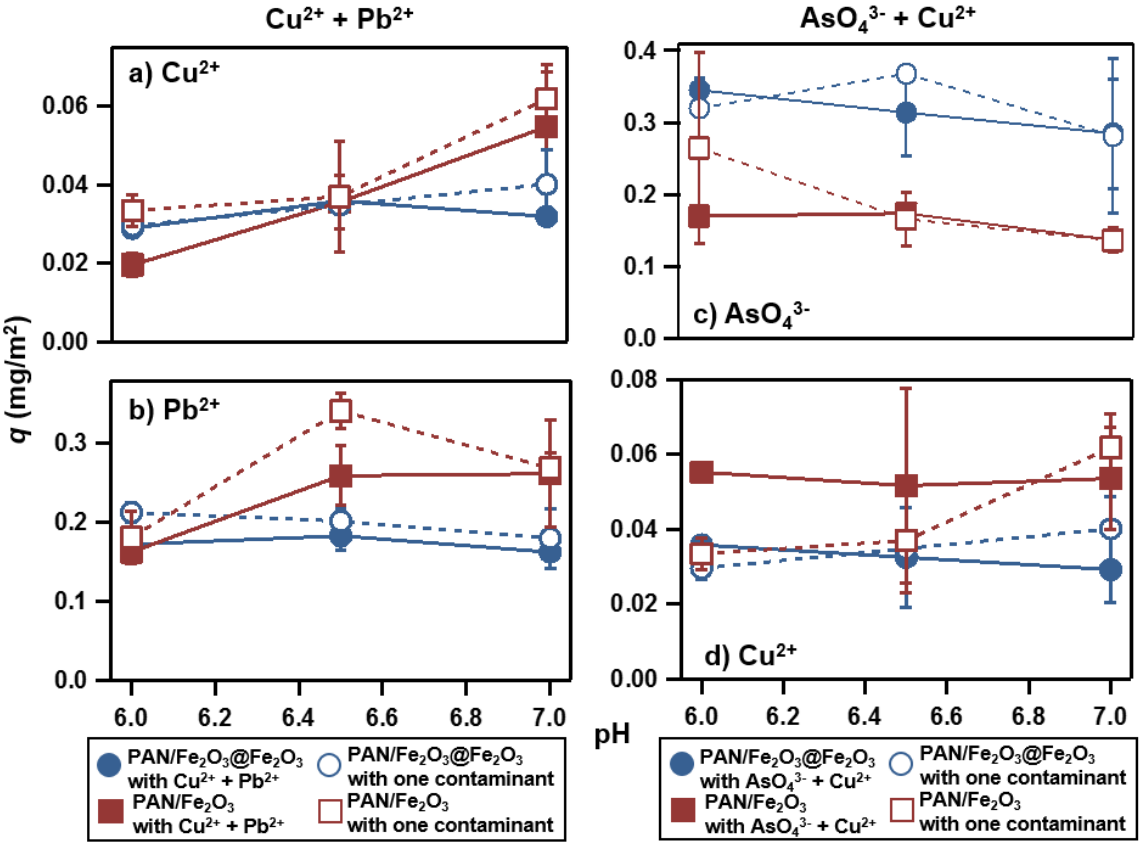

Figure 3-12. Sorption pH edges for PAN/Fe_2O_3@Fe_2O_3 in blue and PAN/Fe_2O_3 in red for (a) 0.6 mg/L Cu^{2+}, (b) 3.0 mg/L Pb^{2+} and (c) 7.4 mg/L AsO_4^{3-}, (d) 0.6 mg/L Cu^{2+} with additonal contaminants present. Open symbols and dashed lines show pH edges with the single contaminant, while closed symbols and solid lines show pH edges with competitive sorption. Experiments were conducted in batch with 5 mg of sorbent and 10 mL of of 10 mM MES buffer for pH 6 and 6.5 and 10 mM HEPES buffer for pH 7. pH edges are given in terms of mass adsorbed per surface area of adsorbent.

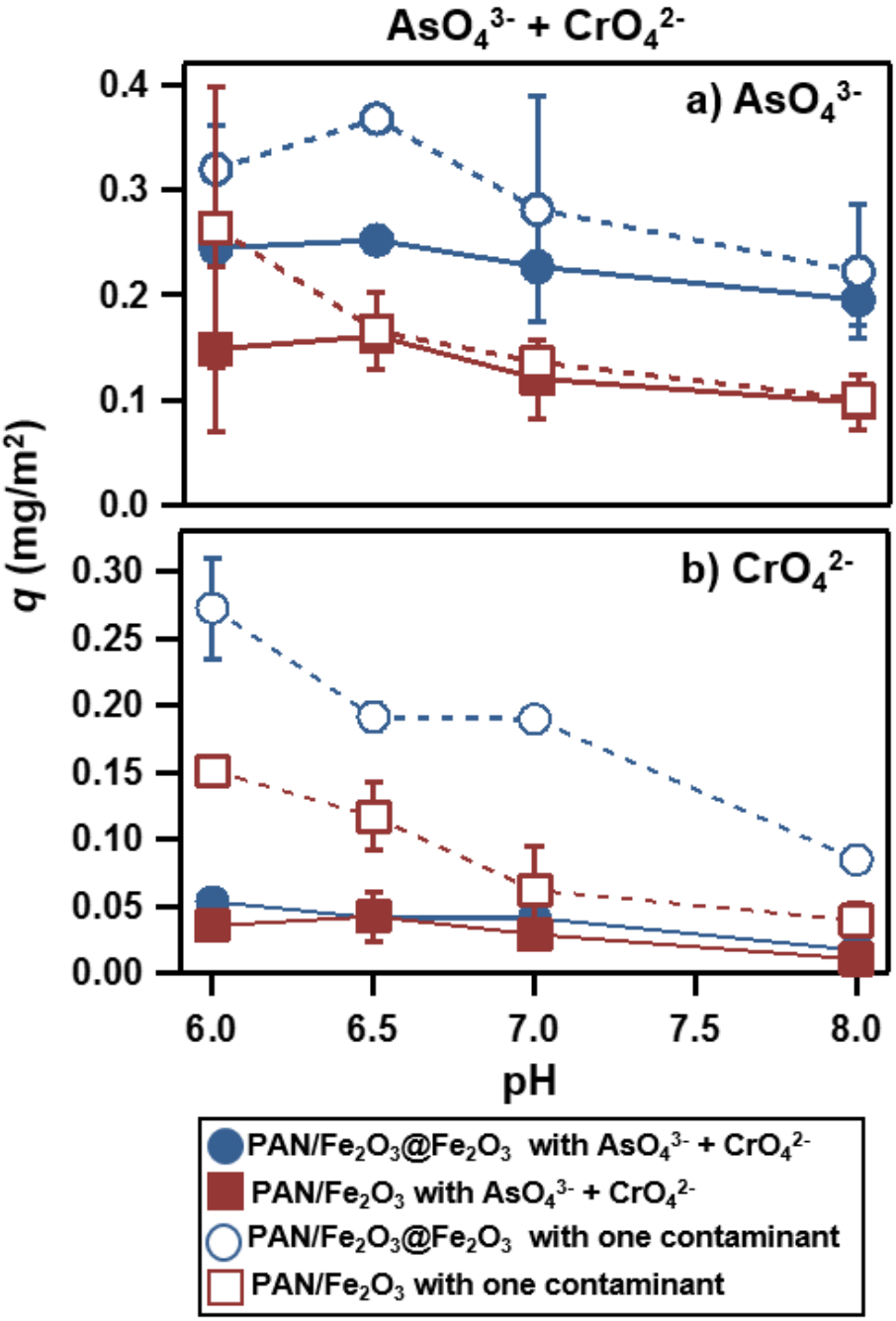

Figure 3-13. Adsorption pH edges for PAN/Fe_2O_3@Fe_2O_3 in blue and PAN/Fe_2O_3 in red for (a) 7.4 mg/L AsO_4^{3-} and (b) 6.7 mg/L CrO_4^{2-}. Open symbols and dashed lines show pH edges with the single contaminant (AsO_4^{3-} or CrO_4^{2-} present), while closed symbols and solid lines show pH edges with competitive sorption (AsO_4^{3-} and CrO_4^{2-} both present). Experiments were conducted in batch with 5 mg of sorbent and 10 mL of of 10 mM MES buffer for pH 6 and 6.5 and 10 mM HEPES buffer for pH 7 and 8. pH edges are given in terms of mass adsorbed per surface area of adsorbent.

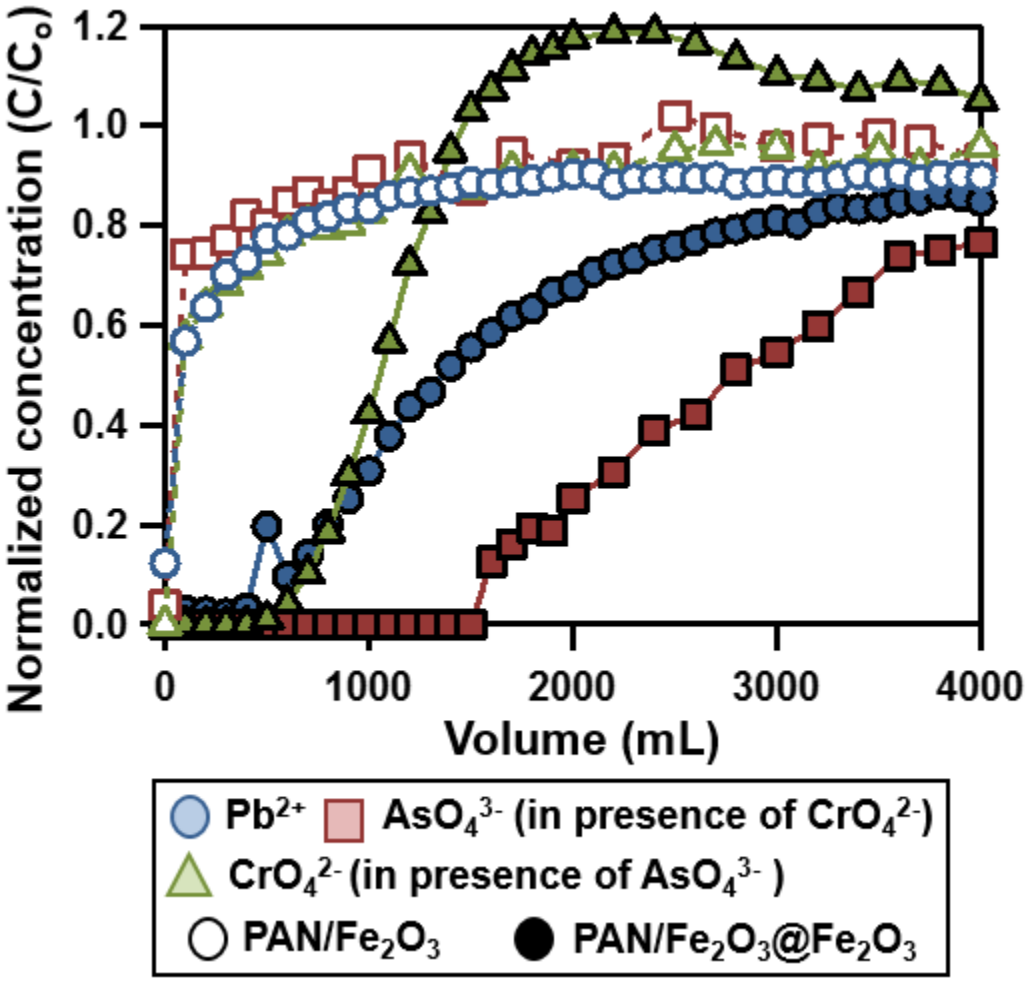

Figure 3-14. Breakthrough curves for PAN/Fe_2O_3 (open symbols) and PAN/Fe_2O_3@Fe_2O_3 (closed symbols) for 100 ppb As(V) [with Cr(VI) present] in red, 100 ppb Cr(VI) [with As(V) present] in green, and 300 ppb Pb(II) in blue. For all filtration experiments, ~100 mg of material was used. Metal/metalloid solutions were prepared in 10 mM MES buffer adjusted to pH 6.

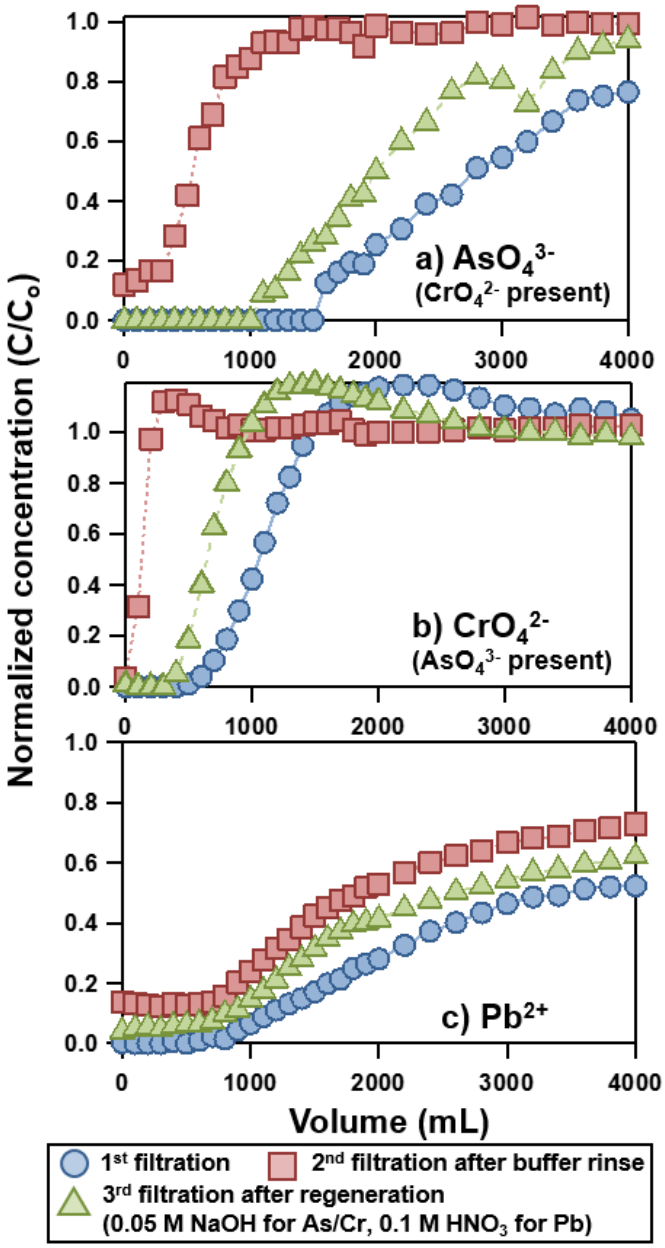

Figure 3-15. Breakthrough curves with regeneration from flow-through filtration with PAN/Fe_2O_3@Fe_2O_3 for (a) 100 ppb As(V) (with Cr(VI) present), (b) 100 ppb Cr(VI) (with As(V) present), and (c) 300 ppb Pb(II). For the As(V)/Cr(VI) flow-through in (a) and (b), ~100 mg of PAN/Fe_2O_3@Fe_2O_3 was used. After the first filtration (shown in blue), the filter was rinsed with clean buffer, and after the second filtration (shown in red), the filter was regenerated with 0.05 M NaOH followed by clean buffer. For Pb(II) flow-through in (c), ~200 mg of PAN/Fe_2O_3@Fe_2O_3 was used. After the first filtration, the filter was rinsed with clean buffer, and after the second filtration, the filter was regenerated with 0.1 M HNO_3 followed by clean buffer. All influent solutions, with the exception of 0.05 M NaOH and 0.1 M HNO_3, were prepared in 10 mM MES buffer at pH 6.

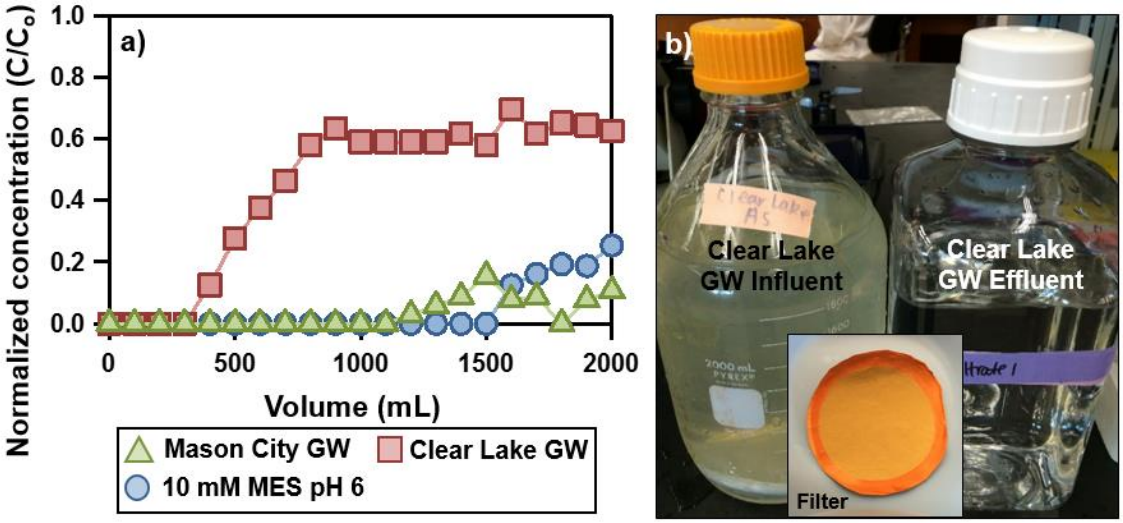

Figure 3-16. (a) Breakthrough curves from flow-through filtration with ~100 mg PAN/Fe_2O_3@Fe_2O_3 for Mason City groundwater (shown in green) with influent 103 ppb As and Clear Lake groundwater (shown in red) with influent 112 ppb As (with breakthrough of 100 ppb As in 10 mM MES buffer at pH 6 shown in blue for comparison). (b) Clear Lake groundwater influent and effluent, with turbidities of 22 NTU prior to filtration and 0.2 NTU after filtration, respectively. The inset shows the filter with a layer of solids after the flow-through experiment.

CHAPTER 4: TITANIUM DIOXIDE/CARBON COMPOSITE NANOFIBER FILTERS FOR PHOTOCATALYTIC DEGRADATION OF EMERGING ORGANIC CONTAMINANTS

4.1. Abstract

The recalcitrance of some emerging organic contaminants in water supplies necessitates highly effective point-of-use water treatment technologies, such as those that use highly reactive, non-specific hydroxyl radical in advanced oxidation processes (AOPs). Here, polyacrylonitrile (PAN) nanofibers with embedded TiO_2 nanoparticles are synthesized via electrospinning and subsequently stabilized and carbonized to produce carbon/TiO_2 (C/TiO_2) nanofiber composites. Reactivity of nanofiber composites is optimized toward atrazine, an organic micropollutant, by varying mass loading of TiO_2, adding phthalic acid (PTA) to electrospinning sol gels, and testing Aeroxide® P25 versus 5 nm anatase TiO_2 nanoparticles in composites. High bulk and surface TiO_2 concentrations in and on nanofibers correspond with enhanced reactivity, while PTA makes it possible to electrospin high P25 loadings (~80% wt.%). Most notably, C/TiO_2 composites up to 63 wt.% TiO_2 remain flexible and are easily handled during filtration experiments. Filtration variables are further optimized by assessing nanofiber filters of different thicknesses and evaluating micropollutant removal efficiencies achieved with low fluxes (in the microfiltration range) to high fluxes for dead-end and cross-flow filtration water treatment applications. The effectiveness of nanofiber composites is also tested in UV light (> 250 nm) versus simulated sunlight (> 305 nm). Optimal C/TiO_2 composites, consisting of ~30 mg of material with 0.3 mm thickness, were tested for removal of a suite of emerging organic contaminants, including benzotriazole, carbamazepine, DEET, metoprolol, and sulfamethoxazole. We find that the initial reaction rate for these emerging pollutants in

irradiated filtration systems scales with the second order rate coefficient for their reaction with hydroxyl radical (k_{OH}), implying that photocatalytic production of hydroxyl radical drives pollutant transformation. Ultimately, we believe the materials synthesized and assessed herein represent next-generation, chemically reactive filtration technologies with photocatalytic activity and material strength necessary for nanomaterial-enabled water treatment technologies.

4.2. Introduction

The use of titanium dioxide (TiO_2) as a photocatalyst for advanced oxidation processes (AOPs) remains heavily studied in recent years [221–223] despite barriers to practical implementation in water treatment [59,71]. Commercially available as a nanoparticle catalyst (i.e., commercial "gold standard" Aeroxide® P25) that is challenging to deploy at water treatment scale, a focus of many researchers, including herein, has been to develop larger assemblies of nanoparticles that can be applied more responsibly. For example, we have synthesized and assessed the performance of pure TiO_2 nanofibers, demonstrating that such materials can achieve reactivity comparable or even exceeding more traditional TiO_2 nanoparticles (see Chapter 2). However, our previous efforts fell short in that the bulk, three-dimensional nanofiber mat was not mechanically stable enough to withstand handling and application in its intended platform, a photoactive filtration network for simultaneous chemical oxidation (via photocatalytic hydroxyl radical production) and filtration. Indeed, even recent attempts to develop TiO_2 nanofiber structures specifically designed to exhibit some enhanced strength and durability [89] remain relatively brittle when compared with polymeric and carbon nanofibers. While our earlier efforts developed insight on how best to optimize TiO_2 reactivity by tuning

nanofiber diameter, crystalline phase, and co-catalyst (e.g., Au nanoparticle) loading, focus must shift to designing TiO_2 nanofiber networks able to withstand both the physical (e.g., durability) and chemical (e.g., fouling) challenges of their practical application in water treatment.

To develop a cohesive electrospun platform that balanced material strength and reactivity, recent studies have explored the immobilization of TiO_2 nanoparticles on or within polymeric electrospun nanofibers [e.g., cellulose or polyacrylonitrile (PAN)]. Several synthesis approaches are common, including (i) direct addition of TiO_2 nanoparticles or nanorods into electrospinning precursor solutions [224–226]; (ii) incorporation of Ti-containing compounds (e.g., titanium tetraisopropoxide) into electrospinning precursor solutions with post-processing to form *in situ* TiO_2 nanoparticles [227–230]; and (iii) hydrothermal treatment of previously fabricated nanofibers for TiO_2 surface deposition [231–234]. Many of these have been fabricated for applications beyond water treatment, including air purification [233,235,236] and oil-water separation [234]. Of those most relevant to technology development for water treatment, most have focused on treatment targets (e.g., dyes) of limited relevance to the current challenges of water treatment providers [226,231]. Notably, PVDF nanofibers electrosprayed with TiO_2 nanoparticles have been demonstrated for oxidation of bisphenol A, 4-chlorophenol, and cimetidine [237]. However, the multiple synthesis steps required and concern over stability of surface deposited TiO_2 (as opposed to TiO_2 integrated into nanofibers) limit viability for water treatment. Further, PVDF as a membrane material is relatively hydrophobic and can limit flux and require high pressure to drive filtration. Ti/PAN nanofibers treated hydrothermally to grow TiO_2 in situ have been demonstrated for oxidation of phenol, a

model hydroxyl radical probe compound [230]. PAN likely scavenged some of the hydroxyl radical species, reducing treatment efficiency, and no other transformations of organic micropollutants were evaluated [230]. In addition, although PVDF can withstand the oxidative species generated by TiO_2/UV, many polymers, including PAN, are not resistant to oxidation [238].

Carbon is likely a more promising material for a TiO_2 composite; it can withstand the oxidative environment created by TiO_2/UV and it may also function as sorbent that can surface concentrate organic targets for subsequent degradation by photogenerated hydroxyl radicals likely to be most concentrated at the composite surface. Nevertheless, development and performance assessments of carbon/TiO_2 nanofiber composites remain sparse and have thus far primarily centered on hydrothermal growth or solvothermal synthesis of TiO_2 nanostructures on pre-fabricated electrospun carbon nanofibers [239,240]. These syntheses demand post-processing of electrospun and stabilized/carbonized nanofibers, which adds to the complexity and time required for making materials. Further, carbon nanofibers generally suffer from being as brittle and low in material strength as most, pure inorganic nanofibers do (e.g., our previous TiO_2 nanofibers from Chapter 2), which leaves their viability as reactive filtration platforms for water treatment in question. Indeed, reactivity studies with carbon/TiO_2 reactivity have been conducted in batch suspensions after breaking up (i.e., dispersing) the carbon/TiO_2 nanofibers, thereby neglecting any consideration of material strength during composite development [239,240]. It is worth nothing, that as with polymer composites, most of this work has also failed to demonstrate nanofiber performance in conditions representative of water treatment, often focusing on

photocatalytic removal of dyes (e.g., methylene blue, methyl orange, and acid red) at relatively high (5-15 mg/L) concentrations [239,240].

Currently, no study has developed a TiO_2-based nanofiber composite via an electrospinning synthesis that (i) is simplified (e.g., single-pot); (ii) ensures material strength, durability and flexibility; and (iii) enables photocatalytic reactivity in a flow through platform able to target persistent organic micropollutants most relevant to modern challenges in drinking water treatment. Herein, we use a single-pot electrospinning method to produce polyacrylonitrile (PAN) nanofibers with embedded Aeroxide® P25 nanoparticles (as a commercially available TiO_2 photocatalyst), where subsequent stabilization/carbonization is used to convert PAN into a flexible and photochemically active carbon/titanium dioxide (C/TiO_2) composite. Specifically, using this approach, we demonstrate the ability to electrospin PAN/TiO_2 composites with up to 80 wt% TiO_2 relative to PAN (with aid of an organic acid dispersant, phthalic acid), producing a nanofiber framework mostly comprised of TiO_2 but that still retains some strength and flexibility derived from its PAN (and ultimately carbon) backbone.

For a suite of systematically tailored C/TiO_2 composites, we assessed and optimized the material properties most influential on material robustness, as well as photocatalytic activity toward atrazine, a widely applied organic herbicide and ubiquitous micropollutant in drinking water. Composite variables explored included (i) mass loading of TiO_2; (ii) concentration of phthalic acid incorporated into electrospinning precursor solutions; and (iii) the type and size of TiO_2 nanoparticles (e.g., mixed-phase Aeroxide® P25 with ~21 nm diameter versus 5 nm anatase TiO_2 nanoparticles). All reactivity studies toward atrazine were conducted in a cross-flow UV (micro)filtration apparatus, and thus

we also explored how process flow rate and the thickness of the photoactive composite nanofiber network (tailored by the volume of electrospinning precursor used in fabrication) influenced atrazine removal efficiencies. Ultimately, the performance of the optimal C/TiO_2 composite was also tested toward a suite of commonly detected, persistent organic micropollutants, including benzotriazole, carbamazepine, DEET, metoprolol, and sulfamethoxazole. Novelty in this work is derived from the prioritization of C/TiO_2 flexibility and stability alongside reactivity, and the testing of optimized C/TiO_2 toward organic micropollutants that currently challenge conventional water and wastewater treatment systems.

4.3. Experimental methods

4.3.1. Reagents

All chemicals were reagent grade or better and used as received. The synthesis of the C/TiO_2 nanofibers involved *N,N*-dimethylformamide (DMF) (BDH, 99.8%), polyacrylonitrile (PAN) (Aldrich, MW 150,000), Aeroxide® P25 (Acros Organics), 5 nm anatase TiO_2 nanoparticles (U.S. Research Nanomaterials, Inc., 99.5%), and phthalic acid (PTA) (Sigma Aldrich, 99.5+%). 5 mM potassium phosphate monobasic (Fisher Scientific, 99.3%) with pH adjusted to 7 was the buffer used in all photochemical experiments. Atrazine (Fluka, 99.1%), 1H-benzotriazole (Alfa Aesar, 99%), carbamazepine (Sigma-Aldrich, 98+%), *N,N*-Diethyl-meta-toluamide (DEET) (Sigma-Aldrich, 97.6%), metoprolol tartrate (LKT Laboratories, 98+%), and sulfamethoxazole (Sigma-Aldrich, 99+%) were used as organic micropollutants in photochemical filtration studies. The eluents for HPLC analyses of micropollutants contained potassium phosphate monobasic (Fisher Scientific, 99.3%), acetonitrile (Fisher Scientific, 99.9%), and methanol (Fisher

Scientific, 99.9%). All solutions were prepared in deionized (DI) water (Millipore, Milli-Q).

4.3.2. Sol gel preparation for electrospinning

Nanofibers were prepared to assess the impact of TiO_2 nanoparticle size, phase composition, and mass loading in carbon nanofibers (CNFs), as well as the impact of phthalic acid (PTA; both as a dispersant for TiO_2 in sol gels and to introduce nanofiber porosity) [177] on C/TiO_2 composite flexibility and reactivity. Accordingly, polyacrylonitrile (PAN) nanofibers containing PTA and seeded with TiO_2 nanoparticles were electrospun, stabilized, and carbonized to obtain carbon/TiO_2 composite nanofiber filters. Either 5 nm TiO_2 (anatase) or Aeroxide® P25 (~75%:25% anatase: rutile; ~21 nm in diameter) nanoparticles were suspended in DMF (from 1 to 7 mL) with either no PTA or 2.5 wt.% PTA (relative to total sol gel mass) and sonicated for 5 h. PAN (8 wt.% relative to DMF) was added and dissolved by thermally mixing the solution at 60 °C for 2 h. For assessment of mass loading of P25 on reactivity, 15 to 80 wt.% P25 was added to sol gels along with 2.5 wt.% PTA. To evaluate the effect of PTA, sol gels with either 50 wt.% P25 or 50 wt.% 5 nm TiO_2 were prepared both free of PTA and with 2.5 wt.% PTA. These sol gels were also used to compare the effect of TiO_2 nanoparticle size and phase on composite reactivity.

4.3.3. Synthesis of carbon/TiO_2 composites

After cooling to room temperature following thermal mixing, prepared sol gels were electrospun with a 23G needle and 15 kV/10 cm with a flow rate of 0.5 mL/h using the previously described system (Chapter 2). The electrospinning process was ceased after 6 h, and the mat was peeled off the Al foil-coated grounded collector. Electrospun

PAN/TiO_2 nanofibers were then stabilized at 250 °C in air for 2.5 h and carbonized at 450 °C in nitrogen (N_2) for 1 h in a tube furnace (MTI OTF 1200x) (with ramp rate of 5°C/min). After stabilization and carbonization, nanofiber mats were cut into circles with diameter of 47 mm for use in reactive filtration experiments.

4.3.4. Nanofiber filter characterization

C/TiO_2 nanofiber composites were characterized to ascertain their chemical and physical properties. Nanofiber diameter, TiO_2 distribution, and porosity were investigated with a Hitachi S-4800 scanning electron microscope (SEM) [91]. To prepare for SEM, approximately 0.5 cm by 0.5 cm pieces of nanofiber mats were placed on carbon tape on Al sample stubs and subsequently sputter-coated with Au to reduce charging while imaging. To prepare samples for cross-sectional imaging using SEM, 0.5 cm by 0.5 cm pieces of nanofiber mats were sandwiched between pieces of cardboard with carbon tape for support, with the cardboard holding the samples subsequently carbon taped to Al stubs. The phase of TiO_2 nanoparticles was confirmed with X-ray diffraction (XRD, Rigaku MiniFlexII, Co X-ray source). For XRD, a ~0.5 cm by 0.5 cm piece of nanofiber mat was taped to a glass slide with 0.2 mm well depth and analyzed from 20°C to 80°C for Bragg angle. N_2-BET analysis (Quantachrome Nova 4200e) was used to determine surface area of nanofiber composites after outgassing samples at 60°C for 6 h prior to measurement. Relative abundance of Ti on the surface of nanofibers was analyzed with a Kratos Axis Ultra X-ray photoelectron spectroscopy (XPS) system equipped with a monochromatic Al Kα X-ray source. For XPS analysis, approximately 0.5 cm by 0.5 cm of C/TiO_2 was placed on a sample holder using carbon tape. XPS was used to collect full spectrum survey scans, as well as to examine O 1s, C 1s, N 1s, and Ti 2p regions.

4.3.5. Preparation of organic micropollutant stock solutions

Saturated stock solutions of 110 µM (24 mg/L) atrazine, 125 µM (30 mg/L) carbamazepine, and 1 mM (253 mg/L) sulfamethoxazole were prepared in DI water by adding each constituent to a level above the solubility limit in water, stirring overnight, and using vacuum filtration with 0.22 µm nitrocellulose filters (Millipore) for removal of any residual, undissolved solids. 10 mM stock solutions of atrazine, carbamazepine, and sulfamethoxazole were also prepared in methanol for use in making calibration curve standards. Because of their higher solubility in water, stock solutions of benzotriazole, DEET, and metoprolol were prepared directly in DI water (at 10 mM, 1 mM, and 10 mM, respectively).

4.3.6. Optimization in cross-flow filtration system

Composite performance was assessed in a custom-built cross-flow filtration apparatus with integrated quartz window to allow UV irradiation during operation. A 47 mm diameter nanofiber filter was supported with a 0.22 µm PVDF filter (Durapore) and placed into a Millipore filter holder modified with a 38 mm diameter quartz window (**Figure 4-1**). 500 mL of test solutions were prepared for flow-through experiments using 5 mM phosphate buffer adjusted to pH 7 spiked with 0.14 µM (30 ppb) atrazine or 0.5 µM of atrazine, benzotriazole, carbamazepine, DEET, metoprolol, or sulfamethoxazole. Solution was pumped across and through the filter at equal rates, from 5 mL/min across and 5 mL/min through (270 $L/m^2/h$ flux) up to 50 mL/min across and 50 mL/min through (2,700 L/m^2 flux) the filter, with all solution returned to the magnetically stirred reservoir. A schematic of the cross-flow filtration system is shown in **Figure 4-1**. The solution was circulated through the system for 1 h in darkness to allow any sorption of the target analyte

on the filter to reach equilibrium. After 1 h, the quartz window was exposed to UV light from an Hg(Xe) arc lamp (Newport, 200W) with a 250 nm cut-on long-pass filter (Asahi Spectra) or a 305 nm cut-on long-pass filter (for minimal experiments). Cross-flow filtration experiments with UV light were executed for up to 3 h, during which 0.5 mL samples were taken periodically from the reservoir, retentate (i.e, the cross-flow effluent), and permeate (i.e., through-flow effluent). For these experiments, permeate was returned to the reservoir for recirculation along with the retentate. UV control experiments were also conducted, in which the system was operated and sampled without a C/TiO_2 filter to quantify phototransformation of atrazine, benzotriazole, carbamazepine, DEET, metoprolol, and sulfamethoxazole by UV light alone.

4.3.7. Sample analysis

Samples were analyzed via high performance liquid chromatography with diode array detector (HPLC-DAD, Agilent 1100 Series). The 0.5 mL samples were placed in 2 mL amber autosampler vials that were crimp sealed prior to analysis. All HPLC methods were adapted from previous work [91,177]. Briefly, atrazine samples were analyzed at 223 nm with an eluent of 50% acetonitrile/50% DI water at 1 mL/min for 6 min per sample. For benzotriazole samples, an eluent of 40% methanol/60% 5mM phosphate buffer at pH 7 was used at 1 mL/min for 7 min per sample, with analysis at 268 nm. Carbamazepine samples were analyzed at 213 nm with an eluent of 45% acetonitrile/55% DI water at 1 mL/min for 6 min per sample. For DEET samples, an eluent of 40% acetonitrile/60% 5mM phosphate buffer, all adjusted to pH 3, was used at 1 mL/min for 9 min per sample, with analysis at 220 nm. Metoprolol samples were analyzed at 223 nm with an eluent of 22% acetonitrile/78% 5mM phosphate buffer at pH 5. For sulfamethoxazole samples, an eluent

of 30% methanol/70% 5mM phosphate buffer at pH 5 was used at 1 mL/min for 9 min per sample, with analysis at 268 nm. Samples were analyzed using an Agilent ZORBAX Eclipse Plus C18 column. For all HPLC methods, injection volumes of 100 µL of each sample were used to ensure detection of low levels (ppb) of micropollutants.

4.4. Results and Discussion

4.4.1. Composite nanofiber characterization

4.4.1.1. Mass loadings of TiO_2

Figure 4-2 shows SEM images of and histograms for C/P25 composites with 0 wt.% up to 63 wt.% P25 (relative to PAN), denoted as C-(wt.%) hereafter (e.g., C-15 for C/15 wt.% P25). We note that each sol gel also contained 2.5 wt.% PTA (to be discussed in further detail below). Histograms of nanofiber diameter distribution reveal that increasing the mass loading of P25 in PAN/TiO_2 nanofibers (from 0 to 63 wt.%) generally increased the average nanofiber diameter of C/TiO_2. From 0 to 63 wt.% P25 relative to PAN, average nanofiber diameter increased from 200 ± 40 nm to 360 ± 80 nm, with the largest increase (~100 nm) occurring from 33 wt.% to 50 wt.% P25 (**Figure 4-3a**). However, below 33 wt.%, the average diameters were roughly constant, suggesting there is a critical mass of P25 at which the composite deviates from the typical morphology of carbon nanofibers.

SEM images revealed considerable differences in surface morphology of the nanofibers as P25 loading increased. Below C-33 (see **Figure 4-2a to 4-2c**), the nanofibers appear to be predominantly carbon containing isolated aggregates of P25 nanoparticles (~400 nm in diameter), the number of which increases with P25 loading. Above C-33, not only are more aggregates of P25 observed on the surface of nanofibers, but also isolated

P25 nanoparticles. This causes the nanofiber surfaces to become visibly rougher. We believe this transition from (primarily) isolated P25 aggregates in carbon nanofibers to more evenly distributed P25 aggregates and particles contributes to the increase in diameter observed for these composites, perhaps due to repulsive electrostatic interactions between the surfaces of P25 nanoparticles once embedded in PAN. Indeed, distance between nanofiber layers is increased by the inclusion of high wt.% P25, as nanofiber mats with more P25 seemed more voluminous and less dense after electrospinning.

We note that the highest loading of P25 that could be electrospun was 80 wt.% relative to PAN, and the resulting C-80 nanofibers are shown in **Figure 4-3b and 4-3c**. These nanofibers exhibited the most dramatic increase in diameter, with most diameters measuring at ~1 μm (although a sufficient sample size for a complete histogram of nanofiber diameter was not collected at this time). Notably, during imaging of C-80 samples, a substantial distance between nanofiber layers in the nonwoven mat was apparent, consistent with features resulting from unfavorable electrostatic interactions between nanofibers arising from the extensive amount of embedded P25. However, while composites with up to 67 wt.% P25 remained moderately flexible, higher P25 loadings (75 and 80 wt.% P25) were especially brittle, chalky, and more susceptible to breakage while handling. Thus, they were not extensively utilized in subsequent flow-through reactivity studies, as a result of concerns over their durability and potential to leach loosely bound P25 into the finished water supply.

In terms of P25 distribution in composites, XPS indicated a mere 0.3 atomic % (at.%) Ti on the surface of C-15 nanofibers. Surface TiO_2 increased, albeit non-linearly, with increasing P25 content (**Figure 4-4a**). Specifically, rather modest increases were

observed up to 50 wt.%, while a more marked increase in surface Ti was observed above 63 wt%. For example, surface Ti more than doubled (from ~4 to ~9 at.% Ti) over only a ~20% increase in P25 content for C-63 and C-80 nanofibers. Thus, low with P25 loadings, it appears the majority of P25 is embedded within the bulk of the carbon nanofibers, and only above a critical loading of 63 wt.% P25 can more proportional increases in surface Ti be achieved.

Increases in P25 content also yielded composites with greater specific surface area, as measured by N_2 BET isotherms (**Figure 4-4b**). While carbon nanofibers without P25 (i.e., C-0) had rather low specific surface area (5 m^2/g), the addition of P25 produced a linear increase in surface area for composites from 33 to 80 wt.%. Thus, despite the increase in nanofiber diameter observed for these composites, the roughness imparted by the accumulation of P25 on the nanofiber surface yields considerable increases in composite surface area. Indeed, at the highest loadings investigated (C-80), as much as a 10-fold increase in surface area (to 50 m^2/g) relative to C-0 was observed, a value roughly equivalent to the specific surface area of P25 nanoparticles.

Finally, we note that XRD confirmed that the phase of embedded TiO_2 nanoparticles was not altered during synthesis. **Figure 4-5** compares diffraction patterns for P25 nanoparticles and 5 nm TiO_2 nanoparticles to that of their composites. Patterns for P25 indicate a mixed phase consisting of both 75% anatase and 25% rutile, as expected for this widely studied, commercially available photocatalyst. In contrast, XRD results with 5 nm TiO_2 particles are indicative of pure anatase, while also showing the line broadening expected for smaller primary particle sizes (materials prepared from these 5 nm particles are discussed in greater detail below). In composites, the XRD patterns were consistent

with those obtained with the different TiO_2 starting materials. Thus, electrospinning, and most importantly carbonization, did not change the phase of TiO_2 in nanofibers. Because mixed phases like P25 are typically observed to be most reactive as photocatalysts, this phase conservation holds important implications for the reactivity of P25-based composites.

4.4.1.2. Inclusion of phthalic acid

The inclusion of 2.5 wt.% PTA increased the average nanofiber diameter of C-50 from 180 ± 40 nm to 310 ± 60 nm (**Figure 4-6a and 4-6b)**, presumably due to the increase in precursor solution viscosity arising from its inclusion in the sol gel, as has been previously observed [177]. In addition to this effect on diameter, comparison of SEM images of C-50 with and without PTA suggest that PTA also introduces pores into the composite (**Figures 4-6c and 4-6d**), a phenomenon resulting from its volatilization during carbonization and noted to increase not only surface area but also flexibility of CNFs and CNF composites [177,241].

Unexpectedly, however, SEM images also suggest that PTA improves the distribution of P25 nanoparticles in the nanofibers, while the introduced macroporosity also appears to be most concentrated near the P25 particles and their aggregates. In support of its stabilizing effect in P25 suspensions, we note that higher mass loadings of P25, most notably C-80, could only be fabricated via electrospinning when PTA was present at 2.5 wt.%, whereas such high mass loadings without PTA produced an unstable precursor solution that could not be electrospun. Indeed, sedimentation studies conducted with P25 nanoparticles suspended in DMF illustrate that inclusion of PTA results in a more stable sol gel suspension (**Figure 4-7**). Specifically, 4 h after suspension preparation P25 began

to settle out of solution when PTA was not present, and by 24 h the majority of P25 had settled out of the suspension. In contrast, P25 remained well-dispersed in DMF when PTA was present, resulting in a stable suspension throughout the 24 h observation period.

We propose, therefore, that PTA, an aromatic dicarboxylic acid, sorbs to the P25 surface in suspension, thereby functioning as a stabilizing ligand in DMF. In water, PTA is known to bind as a bidentate complex on TiO_2 [242], and we presume a similar complex forms in polar DMF. Further, we believe the ability of PTA to complex the P25 particle surface promotes the localization of macroporosity near the embedded P25 particles in the nanofiber composites. Indeed, most pores observed in SEM images (see **Figure 4-6d**) are located near regions of the nanofibers where P25 is clearly concentrated. Despite this effect, C-67 both with and without PTA had ~6 at.% Ti on the nanofiber surface, indicating that the abundance of TiO_2 available in the sol gel results in decent surface coverage on electrospun nanofibers with or without PTA as a dispersant.

4.4.1.3. Composites prepared with 5 nm anatase TiO_2 nanoparticles

In contrast with larger P25 particles, C/TiO_2 nanofiber composites prepared from 5 nm anatase TiO_2 nanoparticles were affected differently by the inclusion of PTA in sol gel. As shown in **Figure 4-8**, the surface morphology of C/50% 5 nm anatase TiO_2 with and without 2.5% PTA were comparable, with those nanofibers prepared with PTA showing virtually no introduced macroporosity in the nanofiber, though PTA did increase the nanofiber diameter (as seen with P25 composites) from 150 ± 50 nm to 230 ± 60 nm. Further, in comparing 50 wt.% TiO_2 composites prepared from 5 nm anatase or P25, TiO_2 exhibited a lower surface abundance in nanofibers prepared from 5 nm nanoparticles (~1 at.% surface Ti from XPS) relative to those prepared from P25 (~2 at.% surface Ti from

XPS). This is likely the result of the greater aggregation state of the 5 nm particles, which limits their ability to more uniformly distribute themselves on the nanofiber surface. Sedimentation studies supported this, as 5 nm anatase TiO_2 nanoparticles aggregated and settled out of DMF more rapidly than P25 nanoparticles (**Figure 4-9**).

4.4.2. Optimization of C/TiO_2 composite nanofiber filters for chemical oxidation of organic contaminants in cross-flow filtration systems.

4.4.2.1. Optimization of photocatalytic composite material properties

Initial reaction rate coefficients (initial k_{obs} values) were determined from the normalized atrazine concentration (i.e., concentration at some time *t* divided by the initial concentration or C_t/C_0) in the reservoir of the cross-flow filtration system (see **Figure 4-1**) assuming a pseudo-first order degradation process. Over time, the reservoir concentration of atrazine approximated exponential decay in all experimental systems (**Figure 4-10**), as was also observed for decay of atrazine (and other micropollutants) in closed (i.e., no flow) batch systems with P25 (in Chapter 2). This was the case both in UV only controls (i.e., no C/TiO_2 composite filter) and in systems with C/TiO_2 filters across the range of P25 mass loadings investigated. We note that all materials were allowed to equilibrate under flow in the absence of UV light for 1 h to allow for any loss of atrazine via sorption to the composite filter layer. In these systems, we observed ~10% of atrazine sorbs to the filters, although no additional atrazine loss via sorption occurred beyond 1 h. Moreover, UV light alone (i.e., in the absence of C/TiO_2 composites) photolyzed ~40% of atrazine over 3 h (the standard time period utilized in reactive filtration experiments). Thus, initial k_{obs} values reported for C/TiO_2 composite systems have been corrected to account for atrazine loss to direct UV photolysis.

For irradiated composite filters, increasing the loading of P25 from 15 to 80 wt.% correspondingly increased the reactivity of C/TiO_2 nanofibers toward atrazine upon exposure to UV light (**Figure 4-10**). Initial k_{obs} values increased from 0.004 to 0.013 min^{-1} over this range, corresponding to half-lives from 1-3 h. Assuming a steady-state concentration of hydroxyl radical ($[OH^{\bullet}]_{ss}$) on the surface of the irradiated filter, these coefficients correspond to between 1×10^{-12} to 4×10^{-12} M. These values were estimated from our measured initial value of $k_{obs} = k_{OH}[OH^{\bullet}]_{ss}$, where k_{OH} is the reported second order rate constant for atrazine oxidation by hydroxyl radical ($3.17x10^9$ M^{-1} s^{-1}) [243].

Generally, initial k_{obs} values increased with P25 content, expressed both as bulk P25 concentration (wt.%) and surface Ti concentration (at.%) from XPS (**Figure 4-11**). This is consistent with the larger abundance of P25 in the composite nanofibers being able to produce a greater concentration of hydroxyl radical (and possibly other reactive oxygen species known to be produced during P25 irradiation) at the nanofiber filter surface. However, these correlations are rather weak, which may indicate that other physical and/or chemical factors may influence atrazine degradation in these systems. For example, as P25 loading increases, so too does nanofiber diameter, which will influence the nominal pore size of the filter layer and potentially the degree of interaction between atrazine and the photocatalytic nanofiber surface.

Based on the moderate reactivity, ease of fabrication, and strength of C-50, this material was selected to evaluate the influence of other synthetic variables on composite performance. For example, as shown in **Figure 4-10**, the inclusion of PTA in C/TiO_2 had no impact on reactivity, while the use of 5 nm anatase TiO_2 in place of P25 rendered C/TiO_2 unreactive as a photocatalyst, with degradation of atrazine on par with the UV control

(without TiO_2 material present). Complementary experiments conducted in batch compared the reactivity of 5 nm anatase particles to P25, showing that under UV irradiation P25 is roughly 3-fold more reactive than the anatase particles (**Figure 4-12**). This inherent difference in reactivity relates to mixed phase TiO_2 (anatase and rutile) being recognized as a superior photocatalyst than either pure rutile or pure anatase because of an electron trapping mechanism associated with the mixed phases [129,244]. Nevertheless, from these batch results, we would anticipate some level of performance enhancement in composites prepared from 5 nm anatase particles. We assume that the lack of reactivity in these composites may reflect the greater extent of aggregation (and thus, lower degree of surface availability) observed for 5 nm particles relative to P25 upon integration into nanofiber composites.

4.4.2.2. Optimization of photocatalytic filtration parameters

Various flow rates in cross-flow filtration were assessed to determine optimal conditions for achieving and analyzing removal of organic micropollutants (**Figure 4-13**). Operating in cross-flow mode, samples were collected over time of the reservoir, retentate, and permeate. This sampling regime not only allowed us to assess C-50 filter performance in a recirculating cross-flow configure (by monitoring reservoir concentration over time), but also its performance during dead-end filtration applications by comparing the difference between the reservoir and permeate concentrations at each sampling point (where this difference represents the extent of atrazine removal in a single pass through the irradiated filter).

Although the relatively rapid flow rates of 50 mL/min across the filter and 50 mL/min through the filter achieved the fastest decrease in atrazine concentration in the

reservoir (non-detect after 1.5 h), this configuration relied on high filter throughput with relatively low reduction of atrazine in the permeate (initial k_{obs} of 0.03 min^{-1} for filter permeate). In comparison, with flow rates of 10 mL/min across the filter and 10 mL/min through the filter, the reservoir concentration of atrazine reduced more gradually over time (non-detect after 3 h) due to less volume being passed through the filter in the same time period. However, filter permeate immediately exhibited much lower concentrations of atrazine (initial k_{obs} of 0.1 min^{-1}), achieving ~80% atrazine transformation in a single pass through the irradiated filter.

In fact, focusing solely on the extent of removal in a single pass (from the difference between reservoir and permeate concentration at each sampling time), we see that the maximum atrazine removal the can be achieved in a single pass decreases considerably at higher flow rates (i.e., higher values of permeate flux) (**Figure 4-14**). This is not unexpected, as the contact time between the atrazine solution and the irradiated C-50 filter layer is greatest at lower values of flux. Thus, low flow rates that can achieve high removal in a single pass would be ideal in dead-end filtration applications of photoactive composites, while high flow rates with greater loss in the reservoir over time would be optimal in a recirculating cross-flow system. We note that to continue assessing reactivity from both cross-flow and dead-end filtration standpoints, all additional experiments were conducted using the relatively low flow rates 10 mL/min across the filter and 10 mL/min through the filter.

To minimize the amount of nanofiber mass required for efficient micropollutant removal, we also explored the performance of C-50 nanofiber filters with half (~300 μm) and three-times (1800 μm) the thickness of our standard recipe for composite filter

fabrication (i.e., that used during optimization; ~600 μm). Filters with cross-sectional widths of 290 ± 20, 600 ± 40, and 1,800 ± 200 μm (determined by SEM) all exhibited comparable reactivity toward atrazine (**Figure 4-15**), with initial k_{obs} value estimated from reservoir atrazine concentrations of ~0.012 min^{-1}. This suggests that the photic zone (i.e., the depth of the composite filter layer exposed to light) is likely less than ~300 μm, such that any increases in filter thickness beyond this depth provide little additional performance benefit. While attempts were made to explore the performance of even thinner nanofiber filter layers, preparations of composites with cross-sections less than ~300 μm could not be effectively prepared via electrospinning because the material was too thin to be removed from the collector without damaging it. Due to its efficacy and the minimal amount of materials needed to prepare filters 300 μm thick (which corresponds to only ~30 mg of composite), this formulation was used in all subsequent flow-through studies.

Finally, all experiments thus far have been conducted with irradiation from high energy UV light, which provides the maximum degree of overlap with the bandgap of TiO_2. To minimize the energy needed for photocatalytic applications of composite filters, additional tests compared material performance during irradiation with simulated sunlight (with wavelengths greater than 305 nm using a long-pass, cut-on filter at this value). **Figure 4-16** compares the time-dependent removal of atrazine in a single filter pass (from the difference in reservoir and permeate concentration) for C-50 filters under UV and simulated sunlight. Notably, under both UV and simulated solar irradiation, removal in a single pass through the C-50 filter layer increases with time. The timescales of our experiments should be sufficient to achieve steady-state hydroxyl radical production during irradiation. Instead, the time-dependent removal likely reflects a near-constant level of $OH^{\bullet}$

radical being produced at the irradiated filter surface, while the concentration of atrazine decreases over time in the filter influent. Thus, during operation, the ratio of $[OH^{\bullet}]_{ss}/[atrazine]_{influent}$ increases, which in turn allows the extent of removal in a single pass to increase over time.

4.4.3. Demonstration of optimized nanofiber filters with different micropollutants

C-50 nanofiber filters with 300 μm thickness (electrospun with 2.5 wt% PTA) were assessed in cross-flow filtration using flow rates of 10 mL/min across and 10 mL/min through the filter for photochemical oxidation of 0.5 μM atrazine, benzotriazole, carbamazepine, DEET, metoprolol, and sulfamethoxazole. Normalized concentration profiles of each pollutant in the reservoir, retentate, and permeate, along with UV controls (without C-50 present), are shown in **Figure 4-17**. After equilibration for 1 h to allow for sorption, ~10% of atrazine and ~15% of DEET sorbed to filters, while benzotriazole, carbamazepine, metoprolol, and sulfamethoxazole did not measurably sorb. Sulfamethoxazole was susceptible to direct photolysis, degrading by 80% over 3 h with exposure to UV light alone. Direct UV photolysis occurred to a lesser extent for atrazine, benzotriazole, DEET, and metoprolol (~40%, 20%, 20%, and 15%, respectively, over a 3 h period), while carbamazepine was recalcitrant.

In the presence of C-50, the permeate had considerably reduced concentrations of each micropollutant as compared to the reservoir and retentate early in the flow-through experiments (**Figure 4-17**). The notable decrease in sulfamethoxazole in retentate as compared to the reservoir was due to the impact of photolysis on concentration within the quartz filtration cell. Overall, the micropollutant suite exhibited half-lives ranging from 45

min to 1 h in the recirculating flow through system, based on trends in reservoir concentration over time.

Using the difference at each sampling point between retentate and permeate, **Figure 4-18a** illustrates the time-dependent (or concentration dependent) removal of each micropollutant in a single pass through the UV-irradiated C-50 filter. In this configuration, the C-50 filter is promising, with all micropollutants exhibiting increasing removal through the filter over time. All micropollutants appear to achieve steady-state removal after ~30 minutes of operation, which represents the maximum removal of each compound in a single pass through the irradiated filter (**Figure 4-18b**). These maximum removal range from 60-80% removal across the analyte suite, and we assume the removal in this regime is limited by the transport of the micropollutant to the near surface region of the irradiated C-50 filter where hydroxyl radical concentrations are greatest.

Trends in the removal of our micropollutant suite do, in fact, support a role for hydroxyl radical in micropollutant removal. Specifically, in comparing initial k_{obs} for micropollutants based on reservoir concentrations, k_{obs} increases linearly with reported second-order rate constants for the oxidation of each micropollutant with hydroxyl radical (i.e., k_{OH} values) (**Figure 4-19**). The lone exception is sulfamethoxazole, which deviates considerably from the correlation with the other micropollutants, presumably due to its extensive direct UV photolysis. Notably, the dependence of k_{obs} on k_{OH} is decidedly not first order [i.e., $\log(k_{obs}) \propto 0.2 \times \log(k_{OH})$], consistent with a similar correlation observed for P25 reactivity toward organic micropollutants in batch systems (see Chapter 2). This likely implies that reaction with hydroxyl radical is not entirely rate-limiting, and that other steps

in the reaction sequence (e.g., micropollutant surface adsorption or product desorption) also influence the overall rate of transformation.

4.5. Conclusion

This study describes the optimization and demonstration of photochemically reactive TiO_2/carbon nanofibers that offer a robust, stand-alone filter platform for use in POU and POE water treatment applications. Electrospinning enabled a simple, single-pot synthesis of these composites, while stabilization and carbonization converted PAN (susceptible to oxidative stress) to a more resistant carbon. C/TiO_2 nanofiber filter reactivity could be enhanced by increasing TiO_2 mass loading in nanofibers (ultimately enabled by inclusion of PTA in electrospinning precursor solutions) and using P25 as opposed to 5 nm anatase TiO_2 nanoparticles. Reactivity was also assessed from cross-flow and dead-end filtration considerations, and it was determined that high flow rates are well-suited for cross-flow filtration while low flow rates work well for dead-end filtration (in which organic micropollutants need to be removed during first pass through a filter). Additionally, filters consisting of 30 mg mass with 0.3 mm thickness performed equivalently to filters of more mass/greater thickness. C/TiO_2 materials were less reactive under simulated sunlight (>305 nm light) as compared to UV (>250 nm light), but still exhibited considerable organic micropollutant removal. Finally, observed initial rate coefficients for atrazine, benzotriazole, carbamazepine, DEET, and metoprolol had a small correlation with second order rate coefficients (k_{OH}) for the micropollutants, while sulfamethoxazole proved an outlier because it underwent extensive direct photolysis. Ultimately, these C/TiO_2 composite nanofiber filters effectively combine the reactivity of

TiO_2 with the durability of flexible carbon nanofibers, providing a stable platform for the exploitation of TiO_2 with UV as an AOP for water treatment applications.

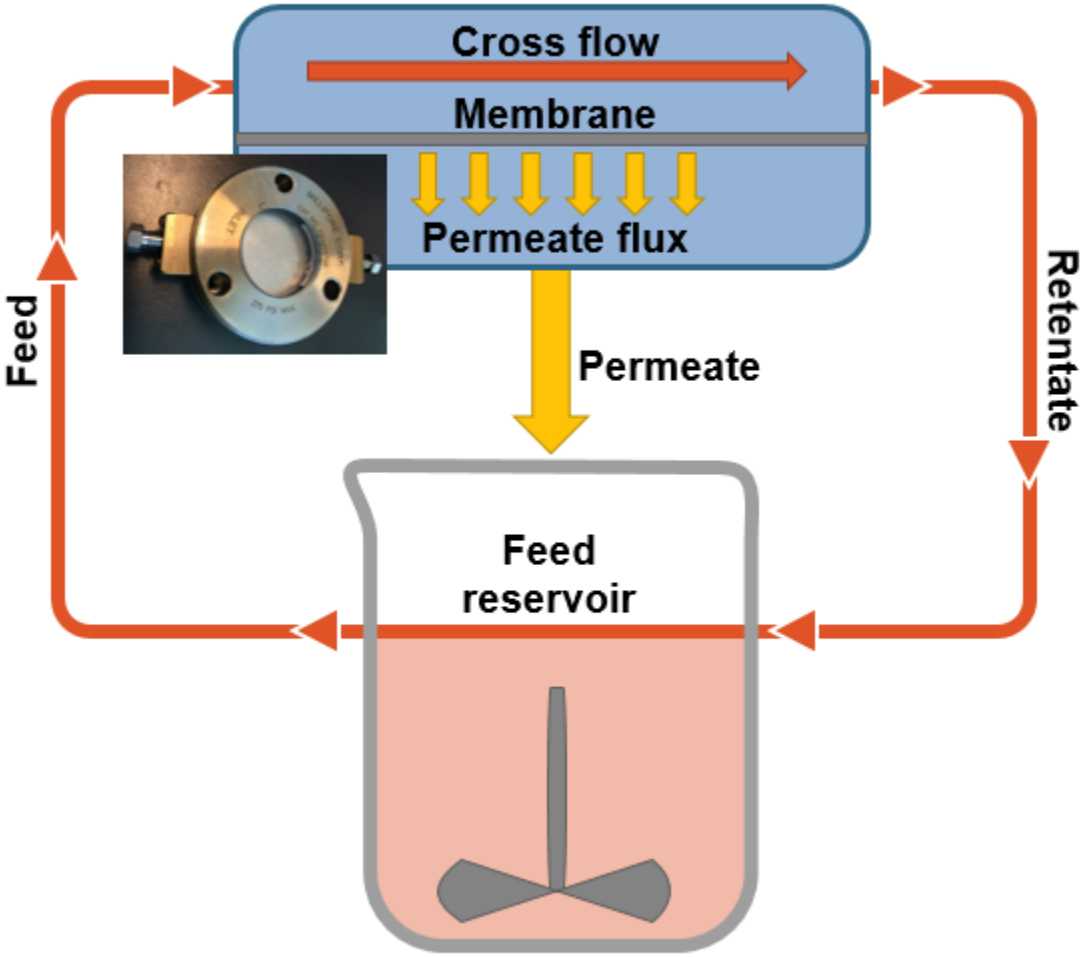

Figure 4-1. A schematic of the cross-flow filtration system used to test C/TiO2 nanofibers in this study. The inset by the cross-flow membrane shows the Millipore filter holder modified with a quartz window and side inlet/outlet to allow for cross-flow filtration with exposure to UV light. Both retentate (cross-flow) and permeate (flow through the filter) were returned to the feed reservoir. Periodic samples were taken of permeate, retentate, and the reservoir during filtration experiments.

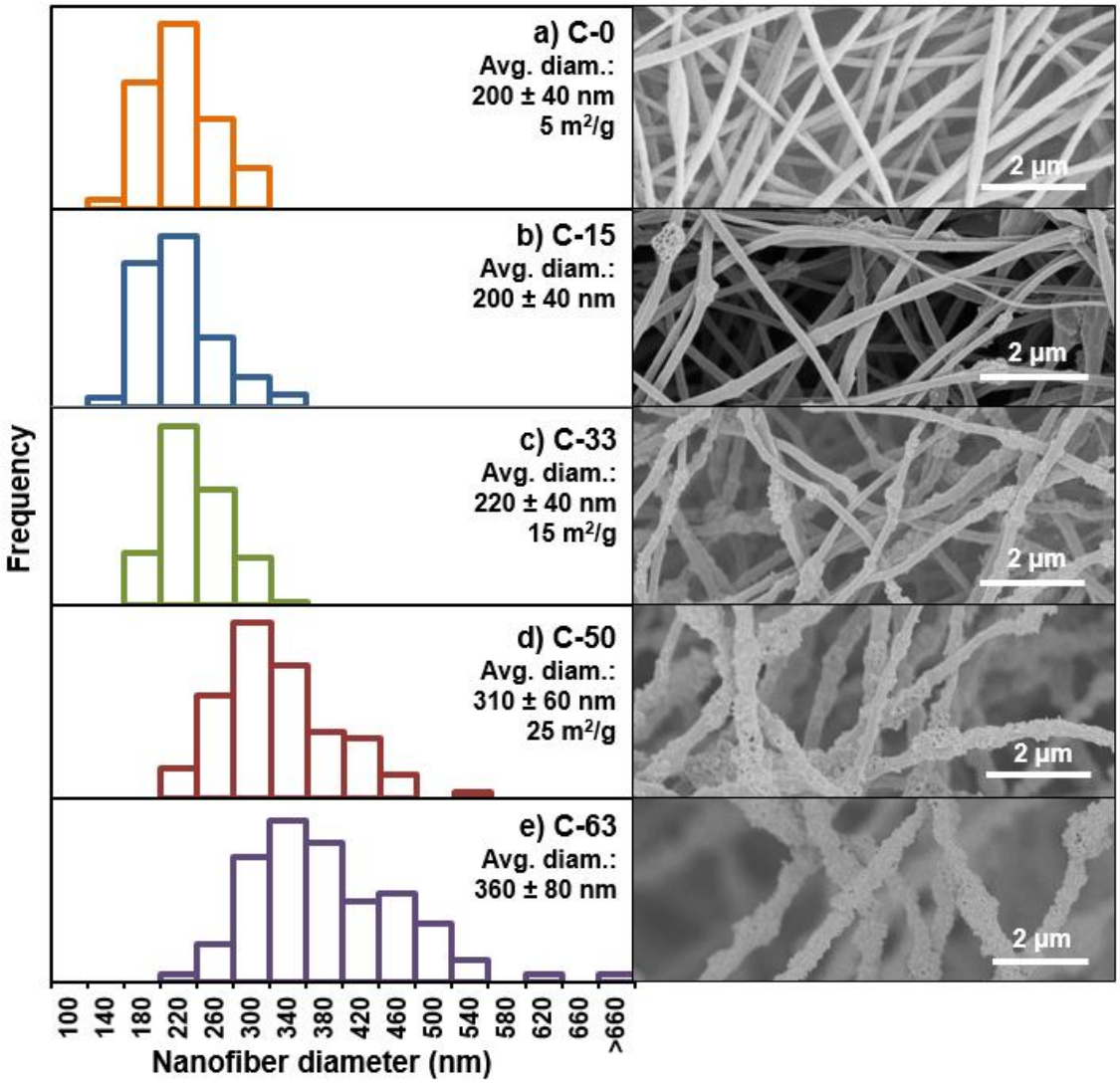

Figure 4-2. Histograms and associated SEM images for (a) C-0 (0 wt.% P25), (b) C-15, (c) C-33, (d) C-50, and (e) C-63 nanofiber composites. All electrospun sol gels contained 2.5 wt.% PTA. As mass loading of P25 in the nanofibers increased, nanofibers transitioned from smooth carbon nanofibers, to rough nanofibers with visible TiO_2 aggregates and increased surface area.

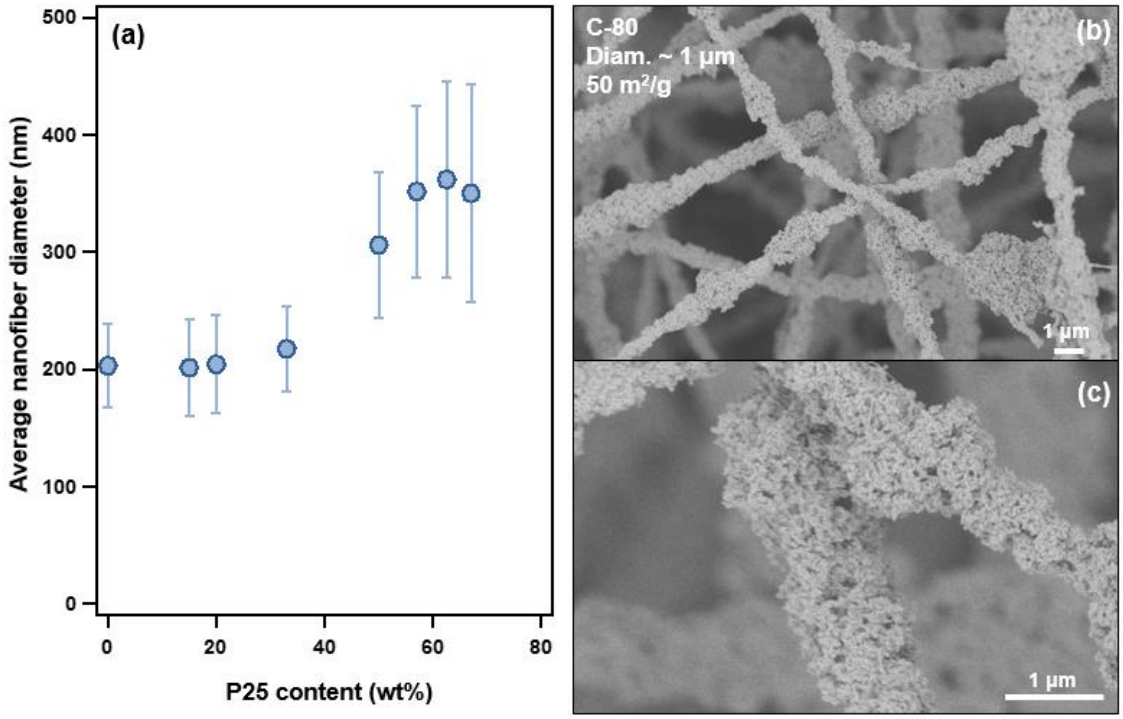

Figure 4-3. (a) Average nanofiber diameter is shown as a function of P25 content (wt. %) in C/TiO_2 nanofibers. (b and c) SEM images of C-80 which show nanofiber diameters of ~1 µm and extensive surface coverage with P25 nanoparticles.

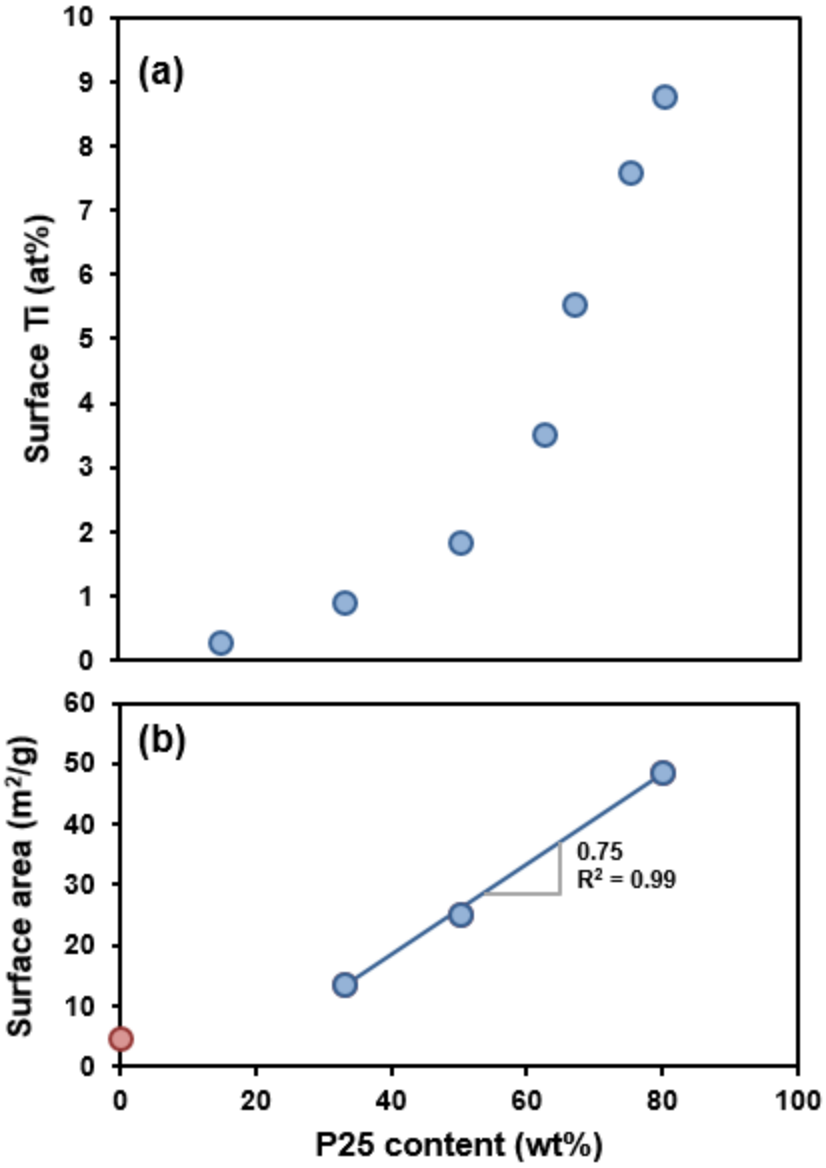

Figure 4-4. (a) Surface at.% Ti (determined via XPS) and (b) surface area of C/TiO_2 nanofiber composites as functions of P25 content in nanofibers. Above 63 wt.% P25, increases in P25 corresponded with sharp increase in surface Ti. Surface area increased linearly between 33 wt.% P25 and 80 wt.% mass loadings in nanofibers.

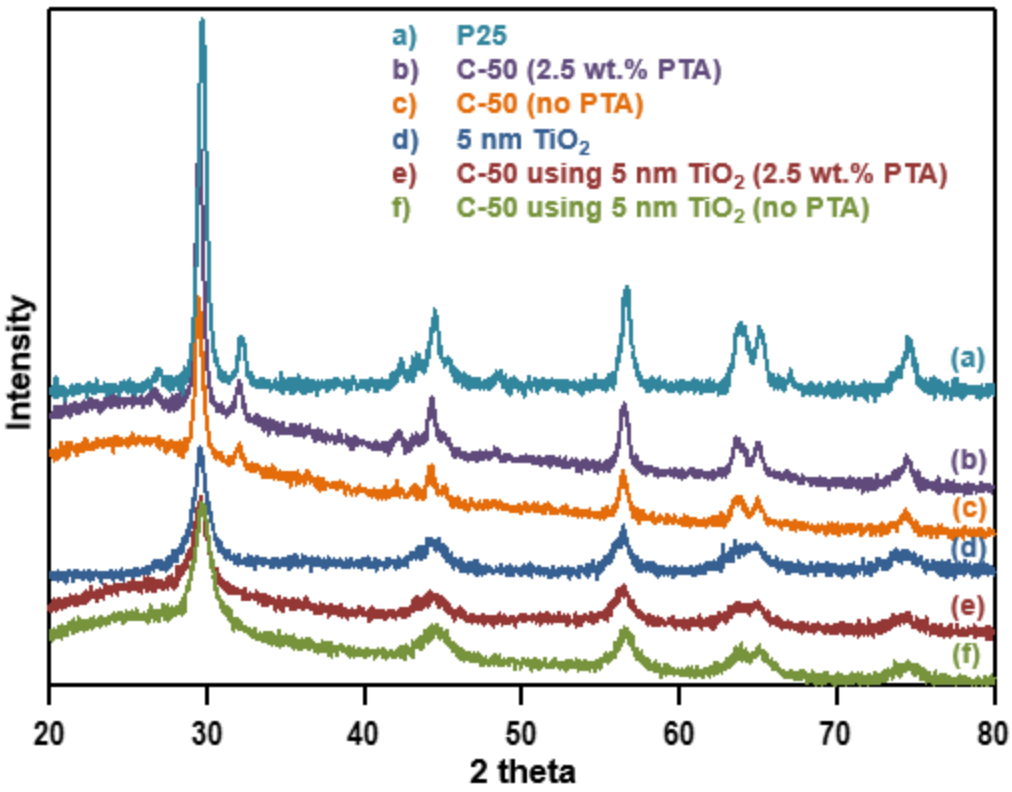

Figure 4-5. X-ray diffraction spectra for (a) P25 nanoparticles, (b) C-50 with 2.5 wt.% PTA, (c) C-50 (without PTA), (d) 5 nm anatase TiO_2 nanoparticles, (e) C-50 using 5 nm TiO_2 with 2.5 wt.% PTA, and (f) C-50 using 5 nm TiO_2 (without PTA). Electrospinning and stabilizing/carbonizing composites did not change the resultant XRD spectra of TiO_2 nanoparticles.

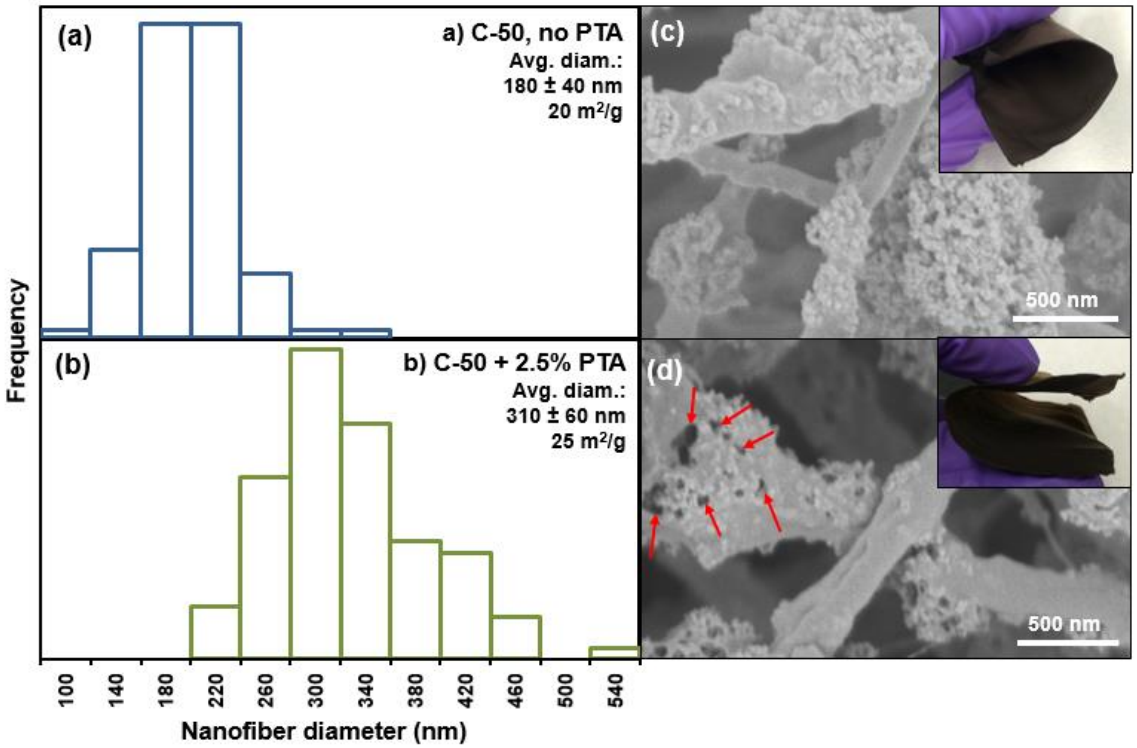

Figure 4-6. Histograms, SEM images, and digital images of (a,c) C-50 without PTA and (b,c) C-50 with 2.5 wt.% PTA. Pores introduced into nanofibers via PTA inclusion are indicated with red arrows in (d). Both materials remained flexible after stabilization/carbonization (c,d).

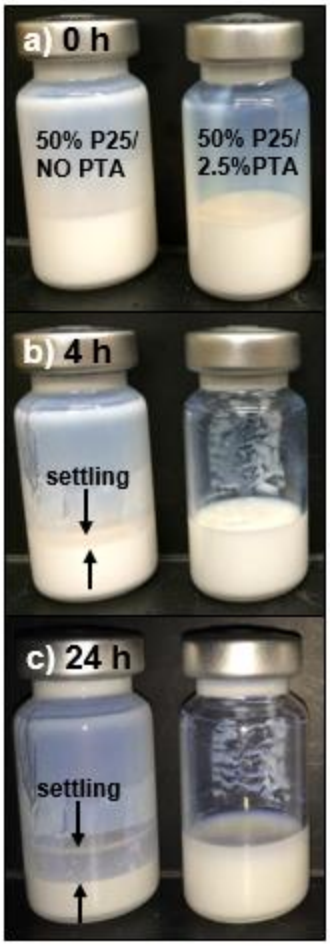

Figure 4-7. Electrospinning sol gels containing 50 wt.% P25 (relative to PAN that would be added) in DMF without PTA (left) and with 2.5 wt.% PTA (relative to final sol gel mass) after (a) initial preparation and 5 h of sonication (0 h), (b) 4 h, and (c) 24 h. P25 began to settle out, as indicated with arrows, after (b) 4 h and (c) 24 h without PTA present.

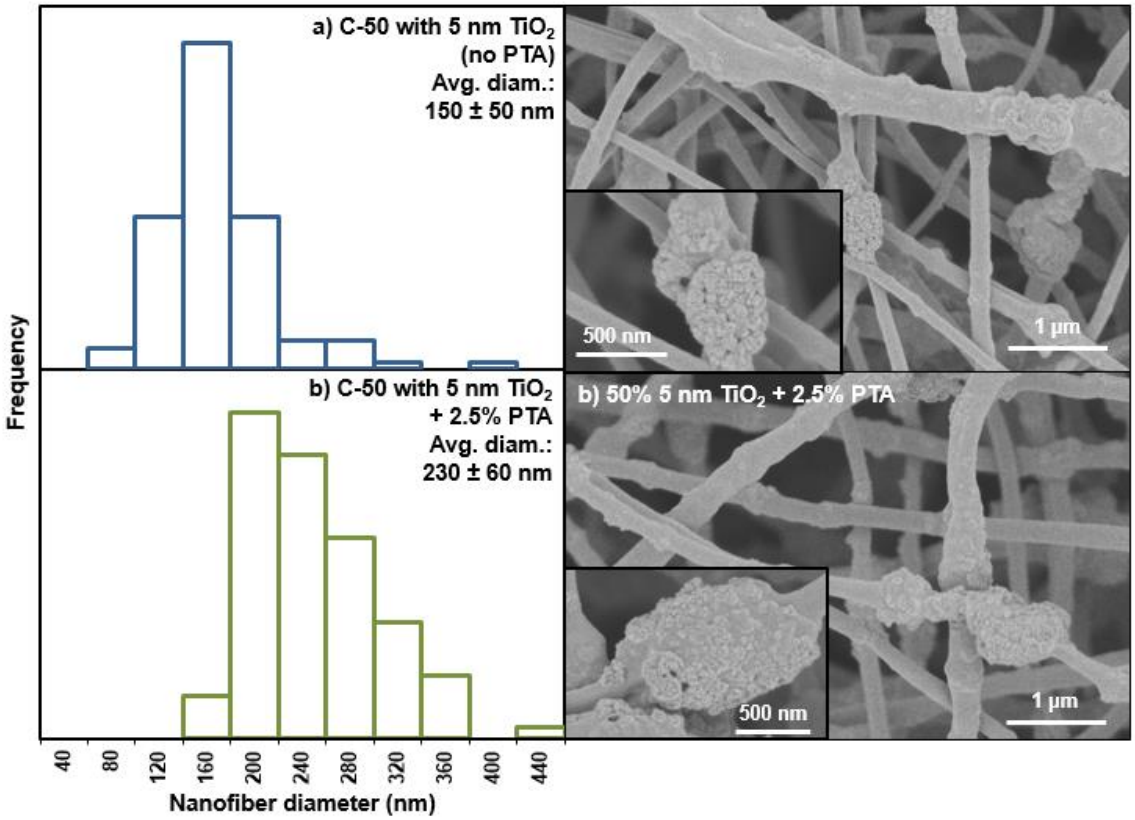

Figure 4-8. Histograms and associated SEM images of (a) C-50 using 5 nm anatase TiO_2 nanoparticles without PTA and (b) C-50 using 5 nm anatase TiO_2 nanoparticles with 2.5 wt.% PTA. SEM insets show aggregates of 5 nm TiO_2 in the composite nanofibers.

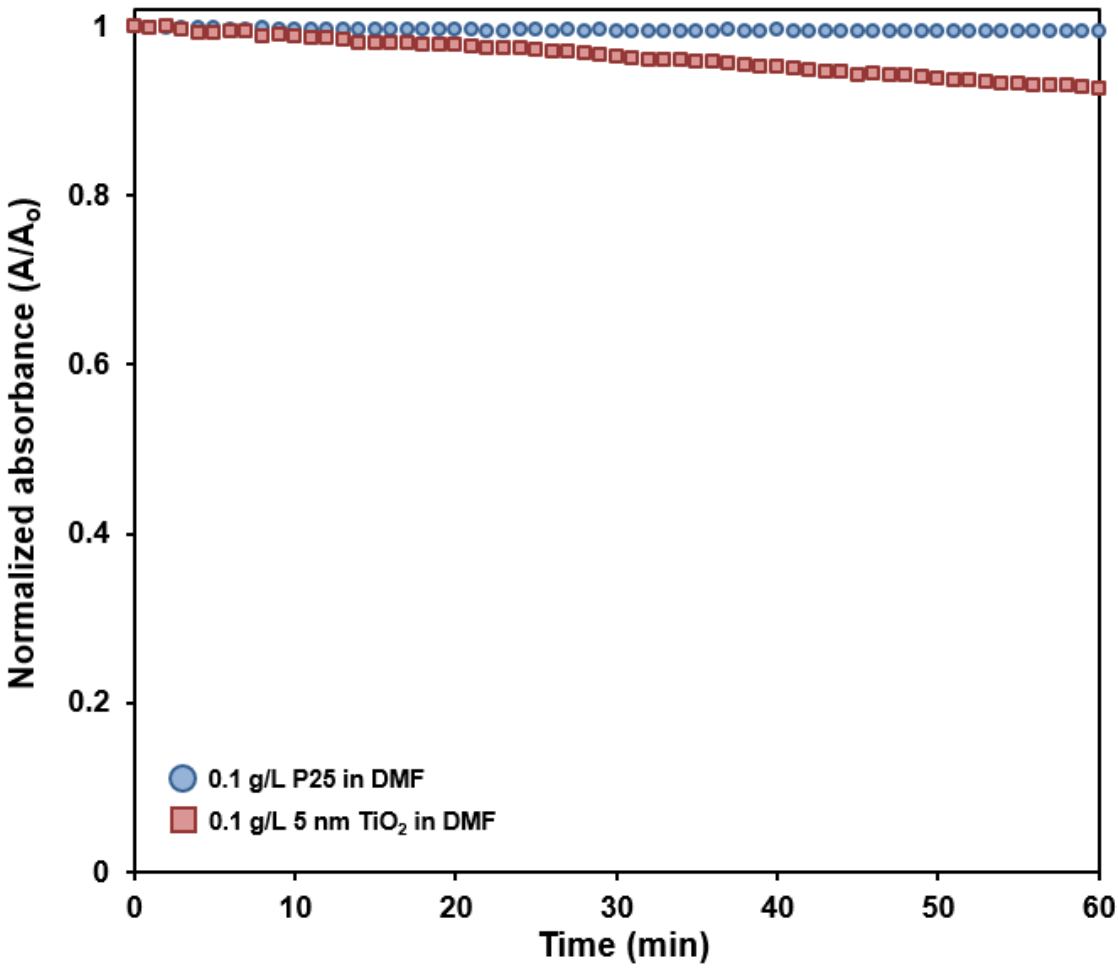

Figure 4-9. Sedimentation studies showing normailized absorbance versus time for 0.1 g/L P25 in DFM in blue and 0.1 g/L 5 nm anatase TiO_2 in DFM in red.

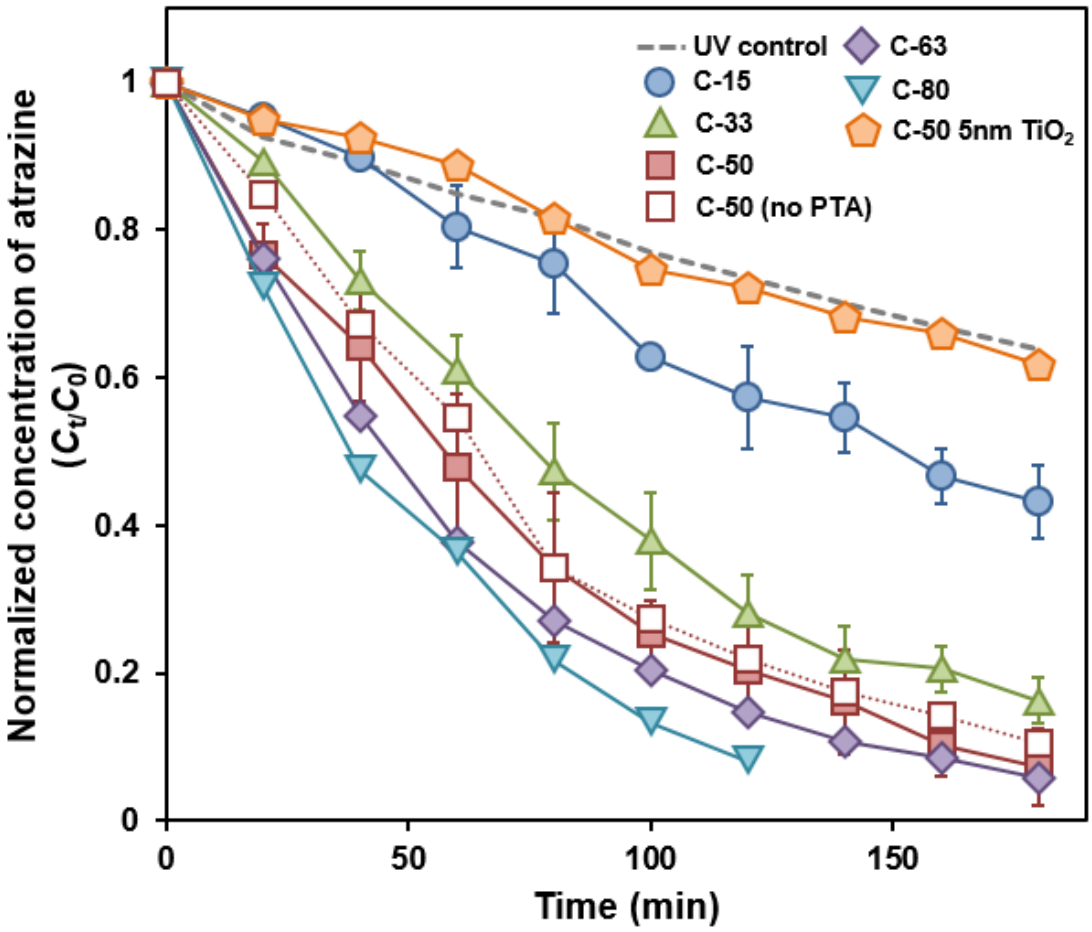

Figure 4-10. Curves showing phototransformation of 30 ppb atrazine over time for C/TiO_2 nanofiber composites with different mass loadings of P25 (15 to 80 wt.%), with and without PTA, and with 5 nm TiO_2 nanoparticles used in place of P25. A UV control (conducted without TiO_2 material) is shown with the grey dashed line.

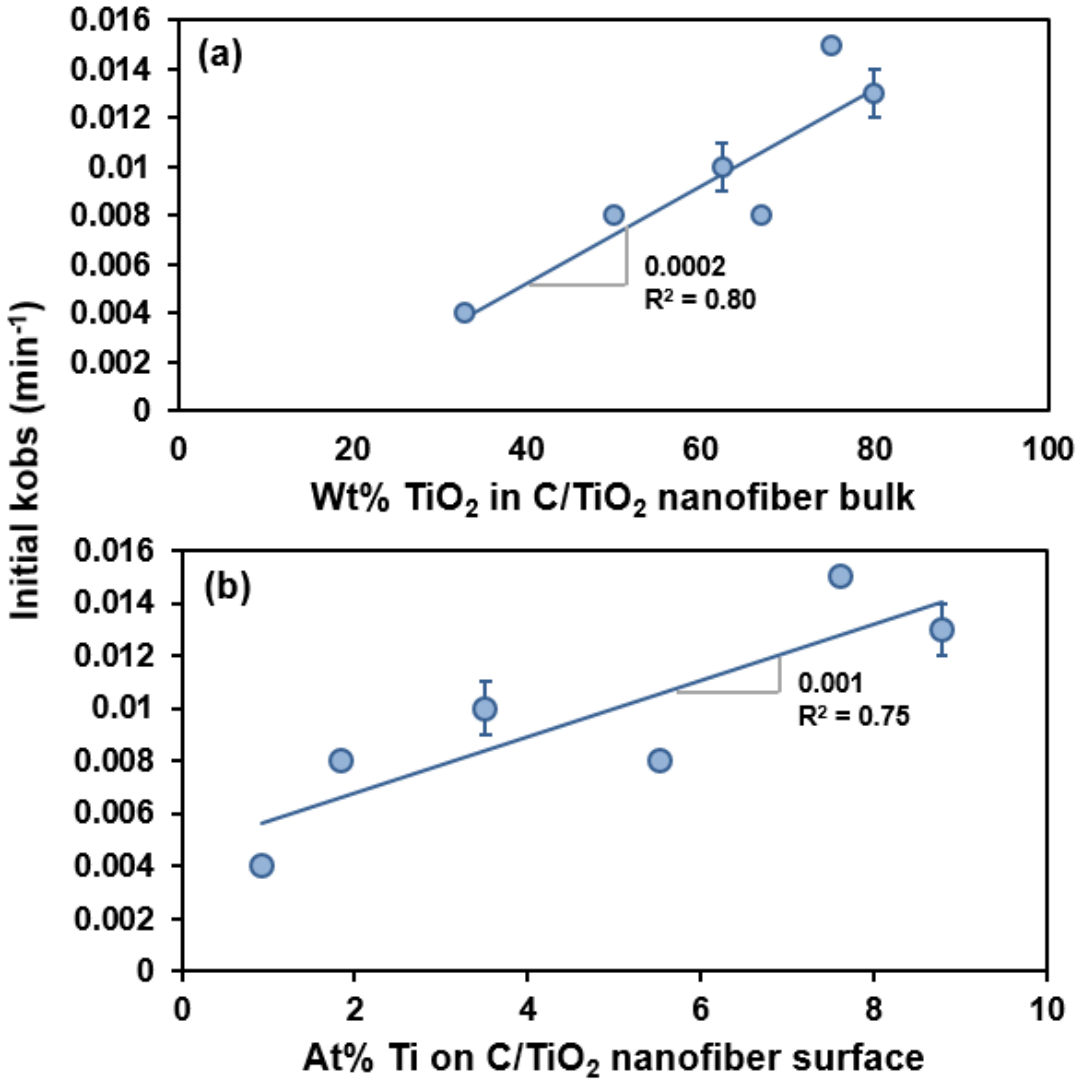

Figure 4-11. Initial k_{obs} for C/TiO_2 composites as a function of different amounts (a) bulk TiO_2 and (b) resultant surface Ti abundance for nanofibers. Rate coefficients correspondingly increased with increasing bulk and surface TiO_2.

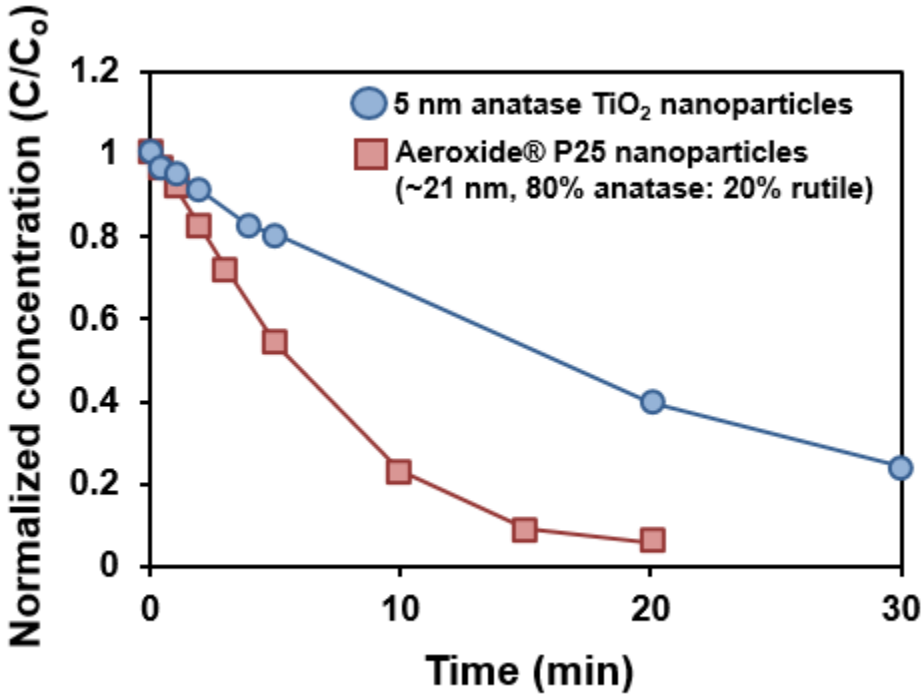

Figure 4-12. Normalized concentration of 75 μM atrazine over time when reacted in batch suspensions containing 0.1 g/L P25 (shown in red) and 0.1 g/L 5 nm anatase TiO_2 (shown in blue) under UV light with wavelengths greater than and equal to 250 nm.

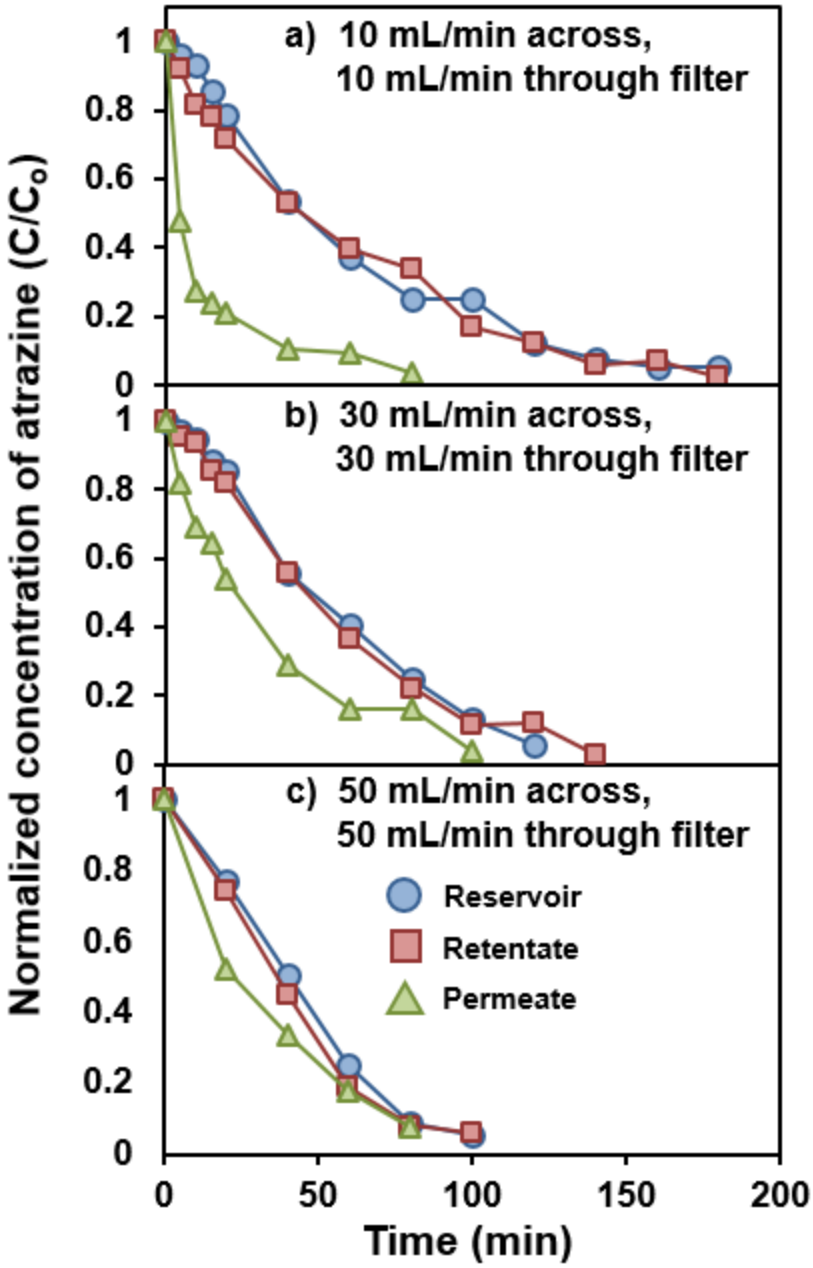

Figure 4-13. Normalized concentration of atrazine (with initial 30 ppb concentration) over time in cross-flow filtration reservoir, retentate, and permeate for (a) 10 mL/min retentate and permeate flow rates, (b) 30 mL/min retentate and permeate flow rates, and (c) 50 mL/min retentate and permeate flow rates. Although more removal is achieved overall with high flow rates (c), low flow rates correspond with more removal of influent to the filter [as measured by permeate concentrations (a)].

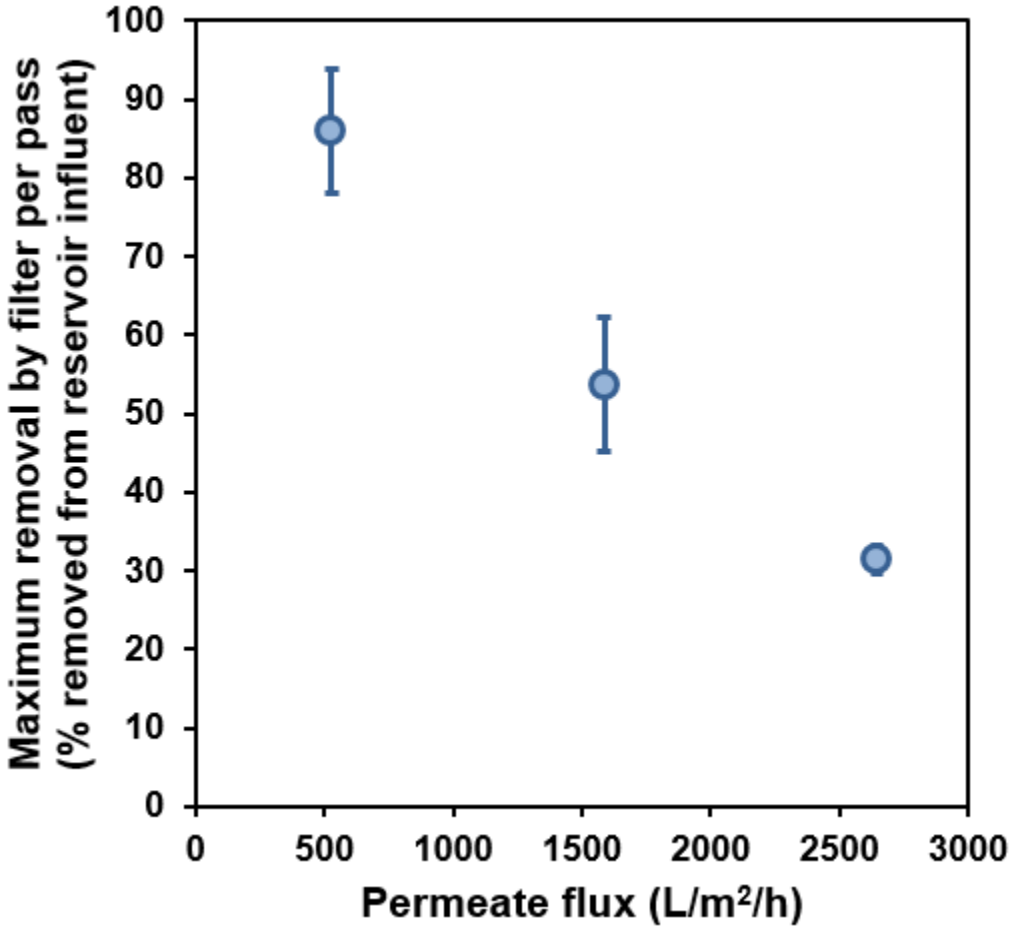

Figure 4-14. Maximum removal of atrazine by filter pass (measured by differences in concentration between filter influent and permeate) across permeate fluxes. Only 530 $L/m^2/h$, the leftmost point with the highest maximum removal, falls within the range of microfiltration.

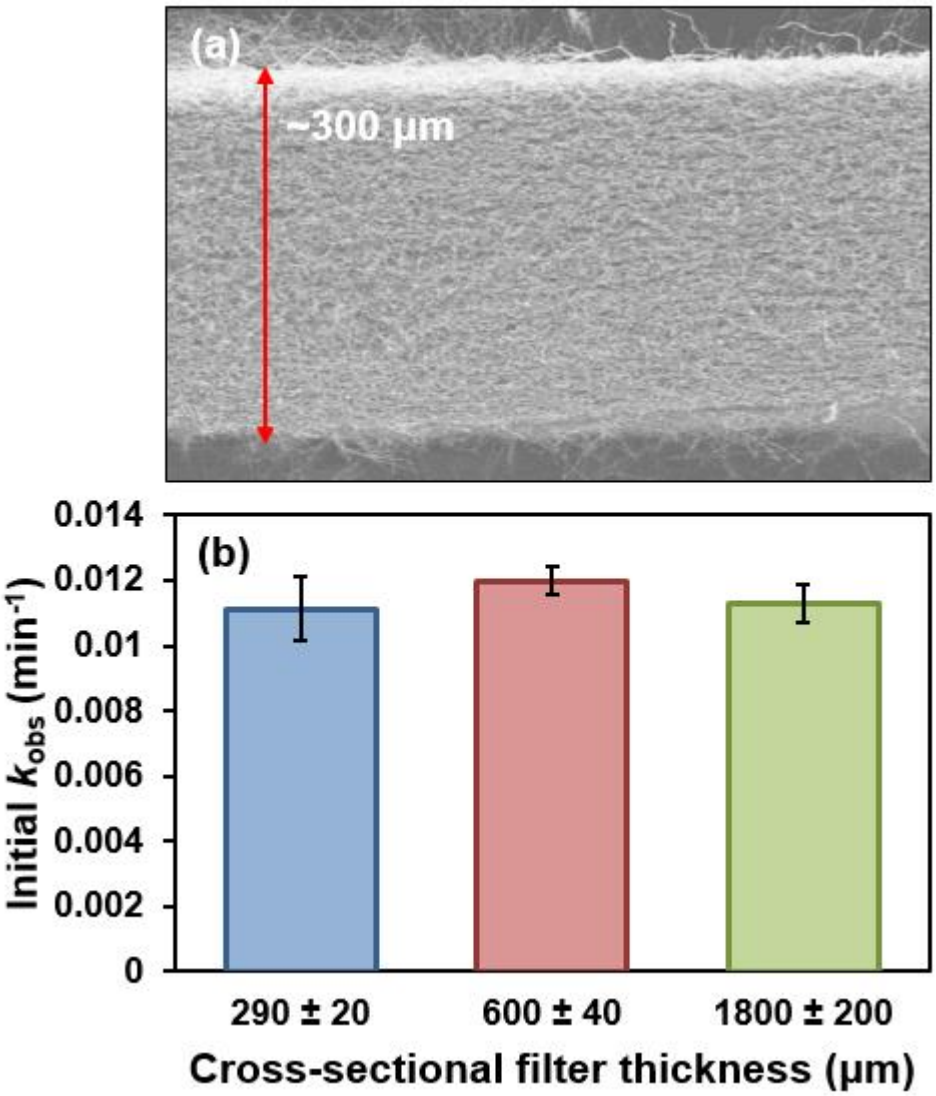

Figure 4-15. (a) SEM image of the cross-section of ~300 µm thick C-50 nanofiber filter. (b) Initial reaction rate coefficients (k_{obs}) as a function of cross-sectional filter thickness for C-50. Greater filter thicknesses corresponded with more mass.

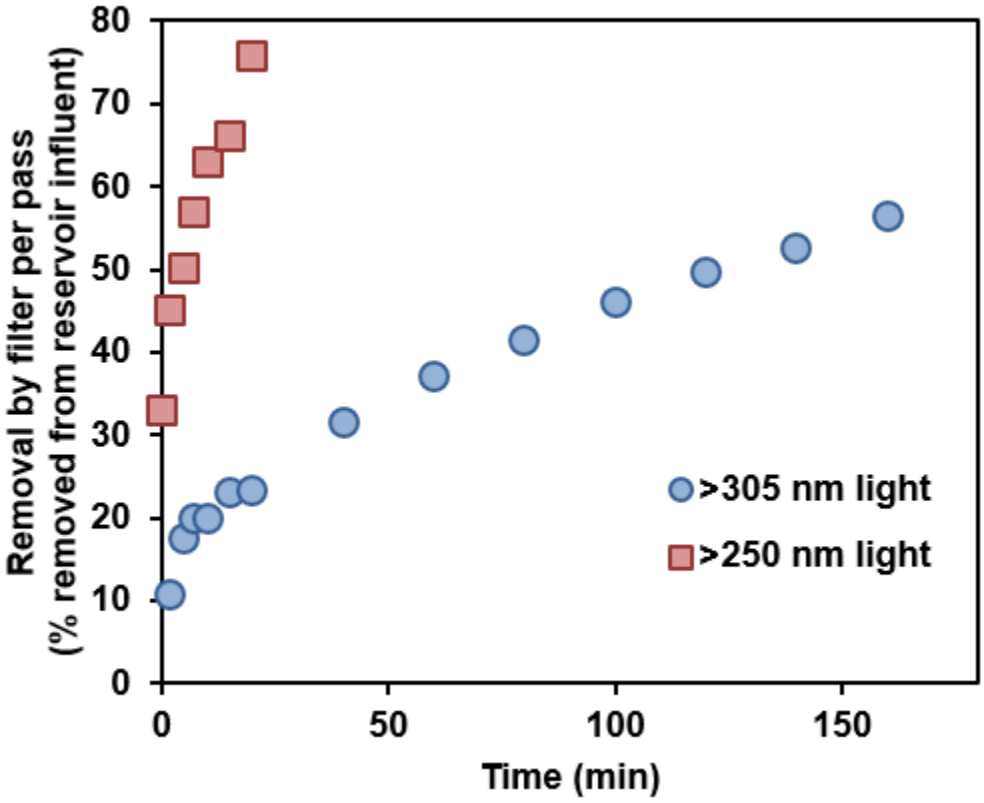

Figure 4-16. Removal by filter pass (as measured by differences in atrazine concentration between filter influent and permeate) over time for experiments conducted with simulated sunlight [UV light greater than 305 nm in length (in blue)] and UV light greater than 250 nm in length (in red). The use of UV light with smaller wavelengths resulted in more rapid removal, though notable removal (20-50%) was still achieved with simulated sunlight (> 305 nm light).

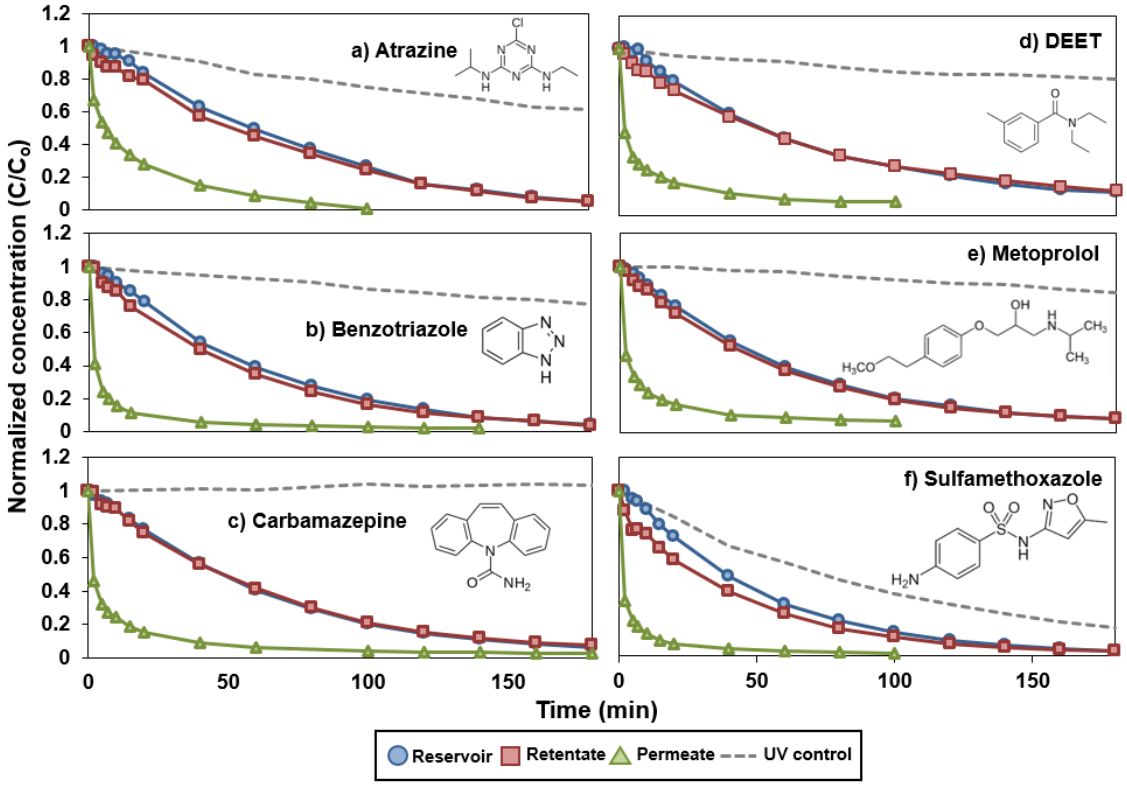

Figure 4-17. Normalized concentration chemical contaminants over time in cross-flow filtration reservoir, retentate, and permeate with initial 0.5 μM (a) atrazine, (b) benzotriazole, (c) carbamazepine, (d) DEET, (e) metoprolol, and (f) sulfamethoxazole. UV controls, conducted without TiO_2 material present, are shown by grey dashed lines.

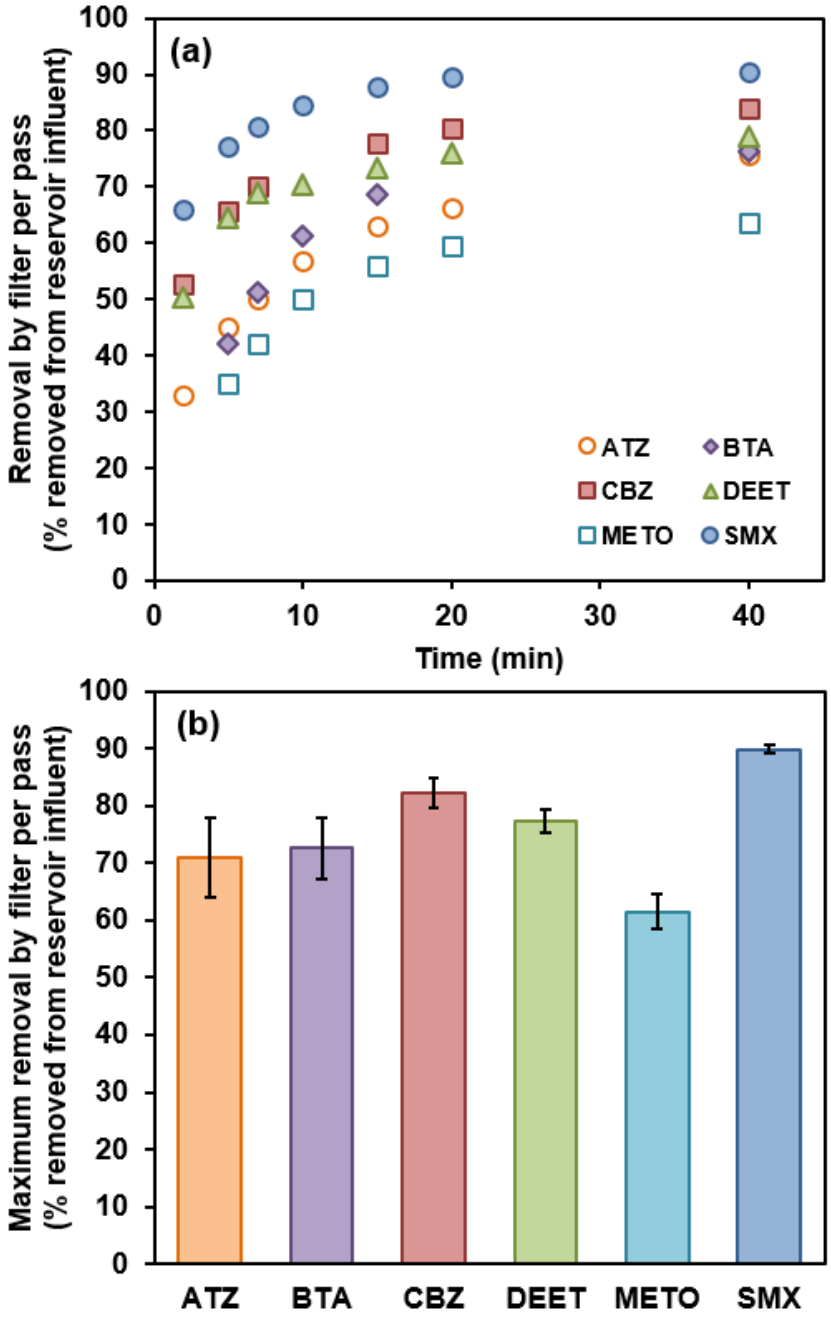

Figure 4-18. (a) Removal by filter per pass (as measured by differences in contaminant concentration in filter influent and permeate) over time for atrazine (ATZ), benzotriazole (BTA), carbamazepine (CBZ), DEET, metoprolol (METO), and sulfamethoxazole (SMX). (b) Maximum removal achieved per filter pass, calculated by averaging removals at 20 and 40 minutes from (a).

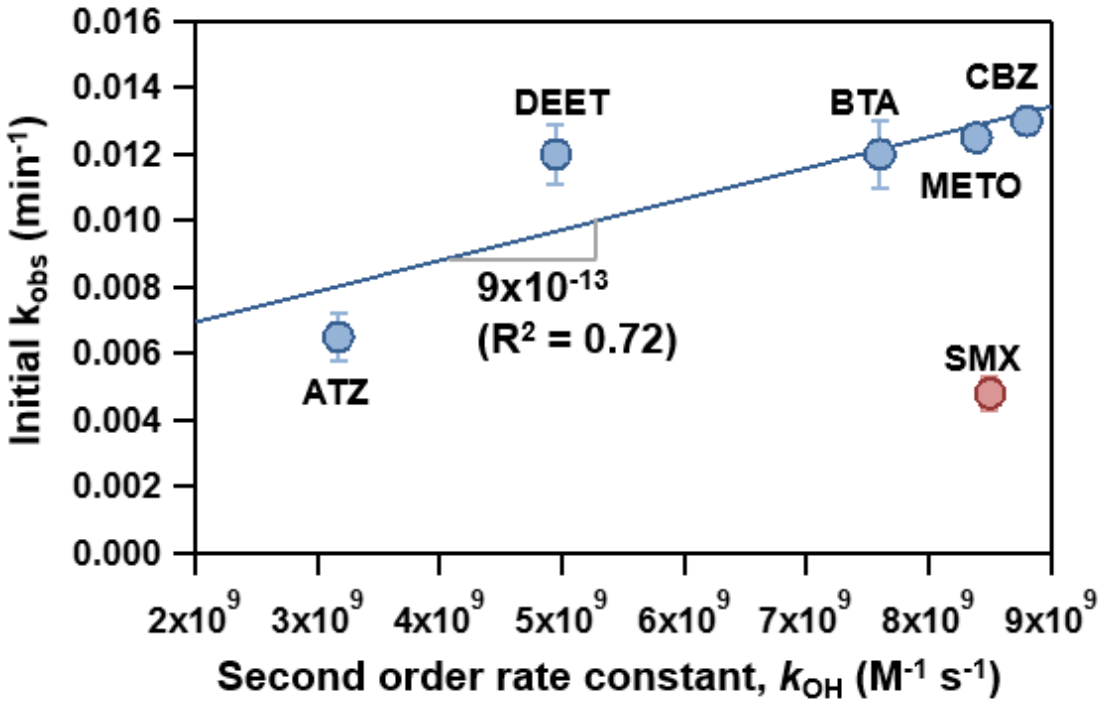

Figure 4-19. Initial reaction rate coefficients for atrazine (ATZ), benzotriazole (BTA), carbamazepine (CBZ), DEET, metoprolol (METO), and sulfamethoxazole (SMX) as a function of their known second order rate constants for hydroxyl radical. Notably, all k_{obs} values showed a linear dependence on k_{OH} except for sulfamethoxazole, which was greatly impacted by direct UV photolysis during filtration experiments.

CHAPTER 5: CONCLUSIONS

Collectively, this work balanced optimization of nanomaterial reactivity, which has historically been the exclusive focus in research studies, with optimization of nanomaterial strength to develop nano-enabled filters for POU and POE water treatment applications. While electrospun nanofibers are highly tunable and can be used to target specific water pollutants, without ensuring their cohesiveness as a filtration platform, they are impractical and will not deliver on their promise as water treatment technologies. Ultimately, we believe this work establishes the commercial viability of chemically active nanofiber filters for removal of inorganic and organic water pollutants.

In this study, each research chapter built upon the previous one. First, TiO_2 nanofibers were optimized for reactivity toward a suite of organic micropollutants in a variety of water qualities in Chapter 2. However, these nanofibers were brittle and ultimately impractical for use in filters for POU/POE water treatment. This issue was immediately considered and addressed for materials developed in Chapter 3. Fe_2O_3 nanofiber sorbents were synthesized (utilizing PAN) with concerted effort focused on maintaining material cohesiveness, flexibility, and strength. We succeeded in making a material, easily manipulated and used in flow-through filtration, almost completely covered in reactive Fe_2O_3 surfaces for uptake of inorganic (e.g., As, Pb) contaminants. Finally, we applied lessons from Chapter 2 and Chapter 3 in synthesizing C/TiO_2 composites that were both reactive and flexible/strong in Chapter 4. The result was development of nanofibers with substantial surface TiO_2 and corresponding reactivity toward a suite of EOCs.

5.1. Enhanced photocatalytic reactivity of gold/titanium dioxide nanofiber composites

Although photocatalysis with TiO_2 has been studied for decades [62], we sought to optimize TiO_2 nanofiber reactivity by tuning electrospinning and post-processing parameters during TiO_2 synthesis. We established that like Aeroxide® P25, TiO_2 nanofibers obtain optimal reactivity with a mixed-phase composition of 75% anatase and 25% rutile. Consistent with hypotheses, narrower nanofiber diameters resulted in greater surface area-to-volume ratios and thus enhanced reactivity. Further, we determined that surface-deposited Au at relatively low amounts relative to TiO_2 (i.e., 1.5 wt.%) increased reactivity, while Au embedded in nanofibers did not impact reactivity. Finally, we assessed nanoparticulate and nanofiber catalysts in batch for reactivity toward a suite of emerging organic contaminants (e.g., DEET, sulfamethoxazole) and across different water qualities (e.g., sedimentation basin effluent). No previous study had taken the same holistic approach toward electrospun TiO_2 optimization, both mechanistically tuning parameters to optimize reactivity while maintaining relevance to real-world water treatment through testing with various contaminants and in samples of different water qualities.

Significantly, this work established that TiO_2 nanofibers behave analogously to TiO_2 nanoparticles. This means that the substantial body of work related to nanoparticulate photocatalysts does relate to the TiO_2 nanofibers developed herein. This also allows for TiO_2 nanotechnology to push application of materials, without needing to complete wholly new mechanistic studies for every formulation of TiO_2 synthesized.

Additionally, while Au was demonstrated as an effective catalyst on TiO_2 surfaces, it proved highly susceptible to fouling in real-water matrices that shut down reactivity of TiO_2 altogether. Thus, noble metal catalysts must be employed carefully, and although they

can optimize reactivity in clean matrices, they may have unintended, negative consequences in practical applications.

5.2. Metal sequestration via iron oxide/polymer nanofiber filters

After the development of extremely reactive yet brittle nanofibers in Chapter 2, we focused our efforts on making reactive, durable materials that could withstand application as filters in water treatment. We optimized both polymer-Fe_2O_3 composite nanofibers and core-shell polymer-Fe_2O_3 composite nanofibers coated with additional Fe_2O_3 nanostructures to increase surface area and sites for metal/metalloid uptake from water. Both materials were flexible and able to sorb measurable amounts of As, Cu, Cr(VI), and Pb, making both candidates for water filtration applications. Additionally, in mixed metal/metalloid solutions, As(V) outcompeted Cr(VI) for surface sites on nanofiber materials, behaving comparably to GFH® and Fe_2O_3 nanoparticle suspensions. Ultimately, both composite and core-shell (coated) nanofiber materials performed equivalently in batch experiments across a range of metal/metalloid concentrations and pH values and outperformed commercial GFH® on a surface area basis.

However, the core-shell nanofiber filters exhibited substantially more uptake of As(V), Cr(VI), and Pb(II) in flow-through filtration, demonstrating that behavior in batch experiments is not necessarily indicative of behavior in kinetically limited regimes encountered in water treatment. Furthermore, core-shell nanofibers were also capable of simultaneous removal of As and suspended solids when tested in flow-through filtration with groundwater samples naturally containing more than 100 ppb As and 22 NTU turbidity. Thus, these core-shell nanofiber filters are well-suited for treatment of complex water matrices.

An additional outcome was the reinforcement that polymer/iron oxide composites react in aqueous solutions similarly to traditional (i.e., nanoparticulate) iron oxide sorbents. Polymeric iron oxide nanofiber composites sorbed similar amounts of cations and oxyanions as Fe_2O_3 in suspension on a surface area basis. Once again, this means the numerous studies on binding of metals/metalloids to iron oxides in suspension can be used to gain insight into reactivity of these nanofiber composites.

5.3. Photocatalytic oxidation of organics via titanium dioxide/carbon nanofiber filters

Moving forward from Chapters 2 and 3, our goal had been to develop a filter utilizing immobilized TiO_2 in a cohesive platform that retained reactivity and minimized barriers to using it in photochemically reactive water filtration. TiO_2 nanoparticulate suspensions, though impractical, will always be the most reactive form of the photocatalysts in water; development of a cohesive, reactive filter platform requires balancing material strength and flexibility with reactivity. Thus, we endeavored to use carbon nanofibers, analogously to how we had employed polymer nanofibers in Chapter 3, to provide structural integrity to carbon/TiO_2 composite nanofibers. All filters are cohesive mats, able to be tested in cross-flow filtration, which is a vast improvement from the batch experiments executed in Chapter 2.

Tuning various synthesis parameters, as we had in Chapter 2, enabled us to optimize reactivity of flexible carbon/TiO_2 nanofibers. First, mass loading of TiO_2 in electrospun nanofibers directly impacted the amount of surface TiO_2, and thus reactivity, of composites. The inclusion of PTA in electrospinning precursor solutions enabled high (80 wt.% relative to PAN) loadings of TiO_2 to be electrospun, though these materials in turn proved more brittle and susceptible to breakage while loading into and unloading from the

filter holder. PTA also introduced pores associated with TiO_2 aggregates in the nanoparticles, which may have use in other applications of C/TiO_2, but did not impact reactivity in our system. Finally, P25 proved more reactive as a nanofiber additive than 5 nm anatase TiO_2 nanoparticles, which mirrored reactivity observed in batch experiments.

Regarding filtration parameters, the amount of material could be minimized without loss of reactivity, as 30 mg carbon/TiO_2 nanofiber filters were as reactive as filters with more mass. Flow rates during filtration could also be decreased to achieve higher levels of removal from influent into the filter (a benefit for dead-end filtration applications), while increased flow rates were associated with more removal in our cross-flow filtration system due to high volumes passing through the filter during short time periods. Removal of micropollutants was likewise achieved with UV light and with simulated sunlight (> 305 nm).

Ultimately, carbon/TiO_2 nanofiber filters exhibited reactivity toward a suite of emerging organic contaminants, supporting their applicability for use as an AOP with UV light. The observed initial rates in flow-through filtration correlated with second order rate coefficients for the chemicals, showing potential for reactivity toward other EOCs to be predicted based on published k_{OH} values. Furthermore, all materials remained intact and flexible, even after use in filtration experiments. Material strength and reactivity were elegantly balanced in these C/TiO_2 composite nanofiber filters.

5.4. Future research

Our study has made great strides in navigating practical considerations while developing nanotechnologies for POU and POE water treatment devices. However, additional research is required to understand the mechanisms that make the materials

effective as chemically active filters. Future work should aim to bridge the gap between bench-scale research and pilot-scale/prototype demonstration that can bring about actual use of these technologies in water treatment. Additionally, methods used in this study can be applied in syntheses of other materials that would be effective for water treatment; materials in this study can also be applied in environmental contexts beyond water treatment.

5.4.1. Mechanistic studies with nanofiber filters

Deeper understanding of the binding mechanisms of metals/metalloids on polymeric iron oxide nanofiber composite filters synthesized herein would enable prediction of filter behavior and thus application in a broader range of water qualities. For example, X-ray photoelectron spectroscopy (XPS), Fourier transform infrared (FTIR) spectroscopy, and synchrotron-based X-ray absorption near edge structure (XANES) analysis have been used to elucidate that sorption can occur by ion exchange between As(V) and Cr(VI) species and hydroxyl groups on flowerlike α-Fe_2O_3 structures [245]. Extended X-ray absorption fine structure (EXAFS) spectroscopy has also been used in modeling surface complexation of Cu(II) on iron oxide surfaces and in turn predicting uptake on iron oxides across a range of pH values [246]. Such studies with PAN/Fe_2O_3 composites would help determine how the structure of Fe_2O_3 coatings on the nanofibers impacts the nature (and efficacy) of metal/metalloid uptake.

Likewise, a more in-depth study of photochemical oxidation of EOCs by C/TiO_2 composites with UV light (as an AOP) could further link reactivity to hydroxyl radical concentrations and other system parameters, thus enabling prediction of reactivity toward certain micropollutants. Analysis of transformation products of EOCs (e.g., with HPLC or LC-MS) would provide insight into the extent of oxidation of organics [247,248].

Experiments probing inhibition of C/TiO_2 also facilitate better understanding of how it degrades organic micropollutants.

Studies of the combined reactivity of core-shell PAN/Fe_2O_3@Fe_2O_3 and C/TiO_2 nanofiber composites would provide insight into synergies achieved through multi-functionality. With a C/TiO_2 layer on top, exposed to UV light, followed by a polymeric iron oxide layer, it is expected that C/TiO_2 would oxidize As(III) to As(V) and thus make As less mobile [19] and more likely to sorb on Fe_2O_3.

Future work should also focus on the stability of nanoparticles and coatings used in the synthesized TiO_2 and Fe_2O_3 nanofiber composite filters. Such studies should analyze fate and transport of the nanostructures and potential leaching of ions (e.g., Fe^{3+}) in batch and filtration systems. Especially with the C-80 composite (80 wt.% P25) synthesized in Chapter 4 of this work, which had a surface area comparable to that of P25 nanoparticles, some TiO_2 is likely loosely bound to the nanofiber surfaces and susceptible to release during cross-flow filtration.

5.4.2. Practical demonstration of nanofiber filters

While carbon/TiO_2 composites were demonstrated for removal of various EOCs, based on previous studies [55] these materials should also be capable of providing some drinking water disinfection. Assessment of bacteria and virus inactivation by C/TiO_2 with UV in comparison with UV light alone would provide insight into disinfection achieved in UV/TiO_2 AOPs and add value to use of the composite filters. Like much work with TiO_2 nanomaterials, a majority of experiments are conducted in batch systems (e.g., inactivation of *E. coli* in a Petrie dish) [249,250]. We suggest that disinfection studies conducted in flow-through filtration would be most representative of conditions in water treatment.

C/TiO_2 nanofiber filters should also be assessed in more challenging water samples. For example, work should follow that completed in Chapter 2 with pure TiO_2 nanofibers, and push testing of C/TiO_2 in surface water samples. Studies could evaluate anti-fouling properties of C/TiO_2 under UV light, propensity of filters to foul after considerable aging (especially in the absence of UV light), and changes in flux over time as a result of influent water quality. Additionally, C/TiO_2 could be assessed for removal of taste and odor compounds, which are commonly encountered in surface water sources.

5.4.3. Scale-up of nanofiber filters

While we have employed bench-scale systems to synthesize nanofiber filters, for these technologies to be truly applicable in the field of water treatment, synthesis would need to be demonstrated as scalable for increased and consistent production of these materials. This is certainly achievable, as electrospinning has been demonstrated on an industrial scale [251]. Likewise, the hydrothermal process used herein to achieve Fe_2O_3 coatings would be well-suited for scaling up, as it was at ambient pressure and relatively low temperature (less than 100 °C). Tube furnace processes used to convert polymer to carbon also utilized relatively low temperatures (250 °C and 450 °C), well within parameters used for industrial nanomaterial syntheses. With industrial collaboration, increased production of these materials could be demonstrated and negate any concerns about scalability.

Scaling up the syntheses processes would enable the production and subsequent testing of nanofiber filter prototypes for POU/POE water treatment applications. Further, development and demonstration of a pilot-scale membrane filtration unit could enable demonstration of this nanotechnology as a viable treatment option for small public water systems (PWS). All electrospun materials in this work were hydrophilic, and thus could

pass water with gravity filtration or with low applied pressures. This characteristic would enable the treatment of relatively large volumes of water (as compared to POU/POE treatment) processed by small PWS, even with several layers of nanofiber filters deployed in series.

5.4.4. Use of methods herein for material development and expansion of applications

Methods herein could be utilized to synthesize similar materials for other environmental applications beyond water treatment. C/TiO_2 composites would be especially relevant for air pollution control and gas phase catalysis, with TiO_2 already commercially used for air purification [252]. In addition, the macroporosity of C/TiO_2 nanofiber mats synthesized with PTA would be ideal for photocatalytic reactions in air, in which porosity increases reaction sites available [253]. These sites, inaccessible in water in this study (likely due to diffusion limitations), are accessible in gas phase applications. Methods from Chapter 2 and Chapter 4 could also be combined to develop carbon nanofibers containing Au/TiO_2 composites; Au/TiO_2 is a well-studied catalyst for gas-phase oxidation reactions [254–257].

Methods in this study could also be used to synthesize different materials that would be effective for water treatment processes. For example, while we focused on Fe_2O_3 for metal/metalloid uptake, similar syntheses could be used to make alumina/aluminum oxide nanofiber composites for fluoride removal [258,259]. Likewise, iron-based sorbents could be similarly synthesized using a number of other iron oxides (e.g., goethite, magnetite) that sorb water pollutants.

5.4.5. Economic and life-cycle assessments of nanofiber filters

To ensure composite nanofiber filters can be truly viable in commercial water treatment devices, economic analyses and life-cycle assessments (LCAs) for the materials synthesized in this study would be invaluable in evaluating these nanotechnologies for real-world application. While some LCAs (assessing benefits and environmental impacts of new technologies) exist for electrospun nanofibers [260,261], current literature is sparse and lacking a framework for assessing electrospun nanofibers produced on different scales [262]. Furthermore, economic analyses based on bench-scale electrospinning would differ greatly from that for scaled-up electrospinning. Thus, economic analyses and LCAs must appropriately account for product development at a smaller scale than would eventually be used for manufacturing nanofiber filters for these technologies to be fairly judged on commercial viability.

LITERATURE CITED

1. Sauvé S, Desrosiers M. A review of what is an emerging contaminant. Chem Cent J. 2014;8(1):15.
2. Schwarzenbach RP, Escher BI, Fenner K, Hofstetter TB, Johnson CA, von Gunten U, et al. The Challenge of Micropollutants in Aquatic Systems. Science. 2006;313(5790):1072–7.
3. Pal A, Gin KY-H, Lin AY-C, Reinhard M. Impacts of emerging organic contaminants on freshwater resources: Review of recent occurrences, sources, fate and effects. Sci Total Environ. 2010 Nov 15;408(24):6062–9.
4. Petrie B, Barden R, Kasprzyk-Hordern B. A review on emerging contaminants in wastewaters and the environment: Current knowledge, understudied areas and recommendations for future monitoring. Water Res. 2015 Apr;72:3–27.
5. Richardson SD, Kimura SY. Water Analysis: Emerging Contaminants and Current Issues. Anal Chem. 2016 Jan 5;88(1):546–82.
6. Ahmed H, Häder D-P. A fast algal bioassay for assessment of copper toxicity in water using Euglena gracilis. J Appl Phycol. 2010 Dec;22(6):785–92.
7. Dang F, Wang W-X, Rainbow PS. Unifying Prolonged Copper Exposure, Accumulation, and Toxicity from Food and Water in a Marine Fish. Environ Sci Technol. 2012 Mar 20;46(6):3465–71.
8. Hughes MF. Arsenic toxicity and potential mechanisms of action. Toxicol Lett. 2002 Jul;133(1):1–16.
9. Hughes MF, Beck BD, Chen Y, Lewis AS, Thomas DJ. Arsenic Exposure and Toxicology: A Historical Perspective. Toxicol Sci. 2011 Oct 1;123(2):305–32.
10. Focazio MJ, Welch AH, Watkins SA, Helsel DR, Horn MA. A retrospective analysis on the occurrence of arsenic in ground-water resources of the United States and limitations in drinking-water-supply characterizations.
11. Tam YS, Elefsiniotis P. Corrosion control in water supply systems: Effect of pH, alkalinity, and orthophosphate on lead and copper leaching from brass plumbing. J Environ Sci Health Part A. 2009 Sep 17;44(12):1251–60.
12. Tong S, Schirnding YE von, Prapamontol T. Environmental lead exposure: a public health problem of global dimensions. Bull World Health Organ. 2000;78:1068–77.
13. Schock MR. Response of lead solubility to dissolved carbonate in drinking water. J Am Water Works Assoc. 1980;72(12):695–704.
14. Pellerin C, Booker SM. Reflections on hexavalent chromium: health hazards of an industrial heavyweight. Environ Health Perspect. 2000 Sep;108(9):A402–7.
15. Costa M. Potential hazards of hexavalent chromate in our drinking water. Toxicol Appl Pharmacol. 2003 Apr;188(1):1–5.

16. McNeill LS, McLean JE, Parks JL, Edwards M. Hexavalent chromium review, part 2: Chemistry, occurrence, and treatment. J - Am Water Works Assoc. 2012 Jul 2;104:E395–405.

17. Technical Fact Sheet: Final Rule for Arsenic in Drinking Water [Internet]. US Environmental Protection Agency; 2001 [cited 2016 Jul 9]. Available from: http://nepis.epa.gov/Exe/ZyPdf.cgi?Dockey=20001XXE.txt

18. Davis MA, Higgins J, Li Z, Gilbert-Diamond D, Baker ER, Das A, et al. Preliminary analysis of in utero low-level arsenic exposure and fetal growth using biometric measurements extracted from fetal ultrasound reports. Environ Health. 2015;14(1):12.

19. Kersten M. Geochemistry of Priority Pollutants in Anoxic Sludges: Cadmium, Arsenic, Methyl Mercury, and Chlorinated Organics. In: Salomons W, Förstner U, editors. Chemistry and Biology of Solid Waste: Dredged Material and Mine Tailings [Internet]. Berlin, Heidelberg: Springer Berlin Heidelberg; 1988. p. 170–213. Available from: http://dx.doi.org/10.1007/978-3-642-72924-9_8

20. Merian E, Clarkson TW. Metals and their compounds in the environment: occurrence, analysis, and biological relevance [Internet]. VCH; 1991. Available from: https://books.google.com/books?id=uELxAAAAMAAJ

21. Center for Health Effects of Environmental Contamination. Iowa Statewide Rural Well Water Survey Phase 2 (SWRL2): Results and Analysis. University of Iowa; 2009.

22. Ayotte JD, Nolan BT, Gronberg JA. Predicting Arsenic in Drinking Water Wells of the Central Valley, California. Environ Sci Technol. 2016 Jul 19;50(14):7555–63.

23. First Drinking Water Standard for Hexavalent Chromium Now FInal [Internet]. California Department of Public Health. 2014 [cited 2016 Jul 9]. Available from: https://www.cdph.ca.gov/Pages/NR14-053.aspx

24. Kendig M, Jeanjaquet S, Addison R, Waldrop J. Role of hexavalent chromium in the inhibition of corrosion of aluminum alloys. Surf Coat Technol. 2001 May;140(1):58–66.

25. Sutton R. Chromium-6 in U.S. Tap Water [Internet]. Environmental Working Group; 2010 Dec. Available from: http://static.ewg.org/reports/2010/chrome6/chrome6_report_2.pdf?_ga=1.214127188.239193962.1451936612

26. Lead and Copper Rule [Internet]. EPA. 2016 [cited 2016 Jul 30]. Available from: https://www.epa.gov/dwreginfo/lead-and-copper-rule

27. Edwards M, Triantafyllidou S, Best D. Elevated Blood Lead in Young Children Due to Lead-Contaminated Drinking Water: Washington, DC, 2001−2004. Environ Sci Technol. 2009 Mar;43(5):1618–23.

28. Hanna-Attisha M, LaChance J, Sadler RC, Champney Schnepp A. Elevated Blood Lead Levels in Children Associated With the Flint Drinking Water Crisis: A

Spatial Analysis of Risk and Public Health Response. Am J Public Health. 2015 Dec 21;e1–8.

29. Perera WN, Hefter G, Sipos PM. An Investigation of the Lead(II)−Hydroxide System. Inorg Chem. 2001 Jul;40(16):3974–8.

30. Stern BR. Essentiality and Toxicity in Copper Health Risk Assessment: Overview, Update and Regulatory Considerations. J Toxicol Environ Health A. 2010 Jan 20;73(2–3):114–27.

31. Regulatory Determination 3 [Internet]. EPA. 2016 [cited 2016 Jul 30]. Available from: https://www.epa.gov/ccl/regulatory-determination-3

32. Kärrman A, Elgh-Dalgren K, Lafossas C, Møskeland T. Environmental levels and distribution of structural isomers of perfluoroalkyl acids after aqueous fire-fighting foam (AFFF) contamination. Environ Chem. 2011;8(4):372–80.

33. Moody CA, Hebert GN, Strauss SH, Field JA. Occurrence and persistence of perfluorooctanesulfonate and other perfluorinated surfactants in groundwater at a fire-training area at Wurtsmith Air Force Base, Michigan, USA. J Env Monit. 2003;5(2):341–5.

34. Groundwater Information Sheet: N-Nitrosodimethylamine (NDMA) [Internet]. State Water Resources Control Board, Division of Water Quality, GAMA Program; 2015 [cited 2016 Jul 30]. Available from: http://www.waterboards.ca.gov/gama/docs/ndma.pdf

35. Carson R, Darling L, Darling L. Silent spring. Boston; Cambridge, Mass.: Houghton Mifflin ; Riverside Press; 1962.

36. Oulton RL, Kohn T, Cwiertny DM. Pharmaceuticals and personal care products in effluent matrices: A survey of transformation and removal during wastewater treatment and implications for wastewater management. J Environ Monit. 2010;12(11):1956.

37. Leung HW, Jin L, Wei S, Tsui MMP, Zhou B, Jiao L, et al. Pharmaceuticals in Tap Water: Human Health Risk Assessment and Proposed Monitoring Framework in China. Environ Health Perspect. 2013 May 10;121(7):839–46.

38. Fick J, Söderström H, Lindberg RH, Phan C, Tysklind M, Larsson DGJ. CONTAMINATION OF SURFACE, GROUND, AND DRINKING WATER FROM PHARMACEUTICAL PRODUCTION. Environ Toxicol Chem. 2009;28(12):2522.

39. Basic Information on the CCL and Regulatory Determination [Internet]. EPA. 2016 [cited 2016 Jul 30]. Available from: https://www.epa.gov/ccl/basic-information-ccl-and-regulatory-determination

40. Esplugas S, Bila DM, Krause LGT, Dezotti M. Ozonation and advanced oxidation technologies to remove endocrine disrupting chemicals (EDCs) and pharmaceuticals and personal care products (PPCPs) in water effluents. J Hazard Mater. 2007 Nov;149(3):631–42.

41. Imai S, Koyama J, Fujii K. Effects of 17β-estradiol on the reproduction of Java-medaka (Oryzias javanicus), a new test fish species. 4th Int Conf Mar Pollut Ecotoxicology4th Int Conf Mar Pollut Ecotoxicol. 2005;51(8–12):708–14.

42. Ankley GT, Jensen KM, Makynen EA, Kahl MD, Korte JJ, Hornung MW, et al. Effects of the androgenic growth promoter 17-β-trenbolone on fecundity and reproductive endocrinology of the fathead minnow. Environ Toxicol Chem. 2003;22(6):1350–60.

43. Pisa LW, Amaral-Rogers V, Belzunces LP, Bonmatin JM, Downs CA, Goulson D, et al. Effects of neonicotinoids and fipronil on non-target invertebrates. Environ Sci Pollut Res. 2015;22(1):68–102.

44. Hladik ML, Kolpin DW. First national-scale reconnaissance of neonicotinoid insecticides in streams across the USA. Environ Chem. 2016;13(1):12–20.

45. Hladik ML, Kolpin DW, Kuivila KM. Widespread occurrence of neonicotinoid insecticides in streams in a high corn and soybean producing region, {USA}. Environ Pollut. 2014;193:189–96.

46. Sivey JD, Lehmler H-J, Salice CJ, Ricko AN, Cwiertny DM. Environmental Fate and Effects of Dichloroacetamide Herbicide Safeners: “Inert” yet Biologically Active Agrochemical Ingredients. Environ Sci Technol Lett. 2015 Oct 13;2(10):260–9.

47. National Research Council (U.S.). Safe water from every tap: improving water service to small communities. Washington, D.C: National Academy Press; 1997. 218 p.

48. U.S. Environmental Protection Agency. Much effort and resources needed to help small drinking water systems overcome challenges [electronic resource] : evaluation report. [Washington, D.C.]: United States Environmental Protection Agency, Office of Inspector General; 2006.

49. How EPA Regulates Drinking Water Contaminants [Internet]. US Environmental Protection Agency. 2016 [cited 2016 Jul 9]. Available from: https://www.epa.gov/dwregdev/how-epa-regulates-drinking-water-contaminants

50. State Library of Iowa. Iowa Quick Facts [Internet]. State Data Center of Iowa. [cited 2011 Aug 15]. Available from: www.iowadatacenter.org/quickfacts

51. Cain TG, Kolpin DW, Vargo JD, Wichman MD. Occurrence of antibiotics, pharmaceuticals and sterols at select surface and wastewater sites in Iowa. Retrieved US Geol Serv Web Site. 2005;

52. The Cadmus Group, Inc. Point-of-Use or Point-of-Entry Treatment Options for Small Drinking Water Systems. Arlington, VA: EPA; 2006 Apr.

53. Parsons S. Advanced oxidation processes for water and wastewater treatment. IWA publishing; 2004.

54. Dodd MC, Kohler H-PE, von Gunten U. Oxidation of Antibacterial Compounds by Ozone and Hydroxyl Radical: Elimination of Biological Activity during Aqueous Ozonation Processes. Environ Sci Technol. 2009 Apr;43(7):2498–504.

55. Cho M, Chung H, Choi W, Yoon J. Linear correlation between inactivation of E. coli and OH radical concentration in TiO2 photocatalytic disinfection. Water Res. 2004 Feb;38(4):1069–77.

56. Li L, Quinlivan PA, Knappe DRU. Effects of activated carbon surface chemistry and pore structure on the adsorption of organic contaminants from aqueous solution. Carbon. 2002;40(12):2085–100.

57. Jusoh A, Su Shiung L, Ali N, Noor MJMM. EuroMed 2006A simulation study of the removal efficiency of granular activated carbon on cadmium and lead. Desalination. 2007 Feb 5;206(1):9–16.

58. National Science Foundation. National Nanotechnology and Its Implementation Plan. 2000.

59. Wiesner MR, Lowry GV, Alvarez P, Dionysiou D, Biswas P. Assessing the risks of manufactured nanomaterials. Environ Sci Technol. 2006;40(14):4336–45.

60. Masciangioli T, Zhang W-X. Environmental technologies at the nanoscale: potential and pitfalls. Environ Sci Technol. 2003 Mar 1;37(5):102A–108A.

61. Diallo M, Street A, Sustich R, Duncan J, Savage N. Nanotechnology Applications for Clean Water: Solutions for Improving Water Quality. William Andrew; 2009.

62. Hoffmann MR, Martin ST, Choi W, Bahnemann DW. Environmental Applications of Semiconductor Photocatalysis. Chem Rev. 1995 Jan 1;95(1):69–96.

63. Di Paola A, Bellardita M, Ceccato R, Palmisano L, Parrino F. Highly Active Photocatalytic TiO2 Powders Obtained by Thermohydrolysis of TiCl4 in Water. J Phys Chem C. 2009 Jul 30;113(34):15166–74.

64. Han C, Pelaez M, Likodimos V, Kontos AG, Falaras P, O'Shea K, et al. Innovative visible light-activated sulfur doped TiO2 films for water treatment. Appl Catal B Environ. 2011 Aug 31;107(1–2):77–87.

65. Avisar D, Horovitz I, Lozzi L, Ruggieri F, Baker M, Abel M-L, et al. Impact of water quality on removal of carbamazepine in natural waters by N-doped TiO2 photo-catalytic thin film surfaces. J Hazard Mater. 2013 Jan 15;244–245(0):463–71.

66. Wang X, Choi J, Mitchell DRG, Truong YB, Kyratzis IL, Caruso RA. Enhanced Photocatalytic Activity: Macroporous Electrospun Mats of Mesoporous Au/TiO2 Nanofibers. ChemCatChem. 2013;5(9):2646–2654.

67. Žabová H, Církva V. Microwave photocatalysis III. Transition metal ion-doped TiO2 thin films on mercury electrodeless discharge lamps: preparation, characterization and their effect on the photocatalytic degradation of mono-chloroacetic acid and Rhodamine B. J Chem Technol Biotechnol. 2009;84(11):1624–1630.

68. Zhang X, Du AJ, Lee P, Sun DD, Leckie JO. TiO2 nanowire membrane for concurrent filtration and photocatalytic oxidation of humic acid in water. J Membr Sci. 2008 Apr 10;313(1–2):44–51.

69. Bahnemann D. Photocatalytic water treatment: solar energy applications. Photocatalysis. 2004 Nov;77(5):445–59.

70. Linley S, Leshuk T, Gu FX. Magnetically Separable Water Treatment Technologies and their Role in Future Advanced Water Treatment: A Patent Review. CLEAN – Soil Air Water. 2013;41(12):1152–1156.

71. Zhang Y, Chen Y, Westerhoff P, Hristovski K, Crittenden JC. Stability of commercial metal oxide nanoparticles in water. Water Res. 2008 Apr;42(8–9):2204–12.

72. Keller AA, Wang H, Zhou D, Lenihan HS, Cherr G, Cardinale BJ, et al. Stability and Aggregation of Metal Oxide Nanoparticles in Natural Aqueous Matrices. Environ Sci Technol. 2010 Feb 12;44(6):1962–7.

73. Federici G, Shaw BJ, Handy RD. Toxicity of titanium dioxide nanoparticles to rainbow trout (Oncorhynchus mykiss): Gill injury, oxidative stress, and other physiological effects. Aquat Toxicol. 2007 Oct 30;84(4):415–30.

74. Burns R, Crittenden J, Hand D, Selzer V, Sutter L, Salman S. Effect of Inorganic Ions in Heterogeneous Photocatalysis of TCE. J Environ Eng. 1999 Jan 1;125(1):77–85.

75. Gimenez J, Martinez M, Depablo J, Rovira M, Duro L. Arsenic sorption onto natural hematite, magnetite, and goethite. J Hazard Mater. 2007 Mar 22;141(3):575–80.

76. Hua M, Zhang S, Pan B, Zhang W, Lv L, Zhang Q. Heavy metal removal from water/wastewater by nanosized metal oxides: A review. Nanotechnologies Treat Water Air Soil. 2012 Apr 15;211–212(0):317–31.

77. Breeuwsma A, Lyklema J. Physical and chemical adsorption of ions in the electrical double layer on hematite (α-Fe2O3). Kendall Award Symp 163rd Am Chem Soc Meet. 1973 May;43(2):437–48.

78. Lücking F, Köser H, Jank M, Ritter A. Iron powder, graphite and activated carbon as catalysts for the oxidation of 4-chlorophenol with hydrogen peroxide in aqueous solution. Water Res. 1998 Sep;32(9):2607–14.

79. Dai Y, Liu W, Formo E, Sun Y, Xia Y. Ceramic nanofibers fabricated by electrospinning and their applications in catalysis, environmental science, and energy technology. Polym Adv Technol. 2011;22(3):326–38.

80. Ramakrishna S, Fujihara K, Teo W-E, Lim T-C, Ma Z. An introduction to electrospinning and nanofibers. Vol. 90. World Scientific; 2005.

81. Thavasi V, Singh G, Ramakrishna S. Electrospun nanofibers in energy and environmental applications. Energy Environ Sci. 2008;1(2):205–21.

82. Ramakrishna S, Jose R, Archana PS, Nair AS, Balamurugan R, Venugopal J, et al. Science and engineering of electrospun nanofibers for advances in clean energy, water filtration, and regenerative medicine. J Mater Sci. 2010;45(23):6283–312.

83. Bjorge D, Daels N, De Vrieze S, Dejans P, Van Camp T, Audenaert W, et al. Initial testing of electrospun nanofibre filters in water filtration applications. Water SA. 2010;36(1):151–6.

84. Homaeigohar SS, Buhr K, Ebert K. Polyethersulfone electrospun nanofibrous composite membrane for liquid filtration. J Membr Sci. 2010;365(1):68–77.

85. Daels N, De Vrieze S, Decostere B, Dejans P, Dumoulin A, De Clerck K, et al. The use of electrospun flat sheet nanofibre membranes in MBR applications. Desalination. 2010;257(1):170–6.

86. Botes M, Eugene Cloete T. The potential of nanofibers and nanobiocides in water purification. Crit Rev Microbiol. 2010;36(1):68–81.

87. Bai H, Zan X, Juay J, Sun DD. Hierarchical heteroarchitectures functionalized membrane for high efficient water purification. J Membr Sci. 2015 Feb 1;475(0):245–51.

88. Gao P, Tai MH, Sun DD. Hierarchical TiO2/V2O5 Multifunctional Membrane for Water Purification. ChemPlusChem. 2013;78(12):1475–1482.

89. Sun C, Wang N, Zhou S, Hu X, Zhou S, Chen P. Preparation of self-supporting hierarchical nanostructured anatase/rutile composite TiO2 film. Chem Commun. 2008;(28):3293–5.

90. Chen M, Zhang F, Oh W. Synthesis, characterization, and photocatalytic analysis of CNT/TiO2 composites derived from MWCNTs and titanium sources. New Carbon Mater. 2009 Jun;24(2):159–66.

91. Nalbandian MJ, Greenstein KE, Shuai D, Zhang M, Choa Y-H, Parkin GF, et al. Tailored Synthesis of Photoactive TiO $_2$ Nanofibers and Au/TiO $_2$ Nanofiber Composites: Structure and Reactivity Optimization for Water Treatment Applications. Environ Sci Technol. 2015 Feb 3;49(3):1654–63.

92. Qu X, Brame J, Li Q, Alvarez PJJ. Nanotechnology for a safe and sustainable water supply: enabling integrated water treatment and reuse. Acc Chem Res. 2013 Mar 19;46(3):834–43.

93. Qu X, Alvarez PJJ, Li Q. Applications of nanotechnology in water and wastewater treatment. Water Res. 2013 Aug 1;47(12):3931–46.

94. Munter R. Advanced Oxidation Processes - Current Status and Prospects. Proc Est Acad Sci Chem. 2001;20(2):59–80.

95. Gaya UI, Abdullah AH. Heterogeneous photocatalytic degradation of organic contaminants over titanium dioxide: A review of fundamentals, progress and problems. J Photochem Photobiol C Photochem Rev. 2008 Mar;9(1):1–12.

96. Choi H, Sofranko a. C, Dionysiou DD. Nanocrystalline TiO_2 Photocatalytic Membranes with a Hierarchical Mesoporous Multilayer Structure: Synthesis, Characterization, and Multifunction. Adv Funct Mater. 2006 May 19;16(8):1067–74.

97. Choi H, Stathatos E, Dionysiou DD. Photocatalytic TiO_2 films and membranes for the development of efficient wastewater treatment and reuse systems. Desalination. 2007 Jan;202(1–3):199–206.

98. Ruppert G, Bauer R. UV-O_3, UV-H_2O_2, UV-TiO_2 and the photo-Fenton reaction - comparison of advanced oxidation processes for wastewater treatment. Chemosphere. 1994;28(8):1447–54.

99. Gaya UI. Heterogeneous Photocatalysis Using Inorganic Semiconductor Solids. Berlin: Springer; 2013.

100. Motegh M, van Ommen JR, Appel PW, Kreutzer MT. Scale-Up Study of a Multiphase Photocatalytic Reactor - Degradation of Cyanide in Water over TiO_2. Environ Sci Technol. 2014;48:1574–81.

101. Servos MR. Nanotechnology for Water Treatment and Purification. Berlin: Springer; 2014.

102. Wiesner MR, Lowry G V., Alvarez P, Dionysiou D, Biswas P. Assessing the risks of manufactured nanomaterials. Environ Sci Technol. 2006;40:4336–45.

103. Gardea-Torresdey JL, Rico CM, White JC. Trophic transfer, transformation, and impact of engineered nanomaterials in terrestrial environments. Environ Sci Technol. 2014 Mar 4;48(5):2526–640.

104. Andon FT, Fadeel B, Torres F. Programmed Cell Death: Molecular Mechanisms and Implications for Safety Assessment of Nanomaterials. Acc Chem Res. 2013;46(3):733–42.

105. Powers CM, Bale AS, Kraft AD, Makris SL, Trecki J, Cowden J, et al. Developmental neurotoxicity of engineered nanomaterials: identifying research needs to support human health risk assessment. Toxicol Sci. 2013 Aug;134(2):225–42.

106. Kiser M a, Westerhoff P, Benn T, Wang Y, Pérez-Rivera J, Hristovski K. Titanium nanomaterial removal and release from wastewater treatment plants. Environ Sci Technol. 2009 Sep 1;43(17):6757–63.

107. Chong MN, Jin B, Chow CWK, Saint C. Recent developments in photocatalytic water treatment technology: A review. Water Res. 2010 May;44(10):2997–3027.

108. Zhang Y, Chen Y, Westerhoff P, Hristovski K, Crittenden JC. Stability of commercial metal oxide nanoparticles in water. Water Res. 2008 Apr;42(8–9):2204–12.

109. Keller A a, Wang H, Zhou D, Lenihan HS, Cherr G, Cardinale BJ, et al. Stability and aggregation of metal oxide nanoparticles in natural aqueous matrices. Environ Sci Technol. 2010 Mar 15;44(6):1962–7.

110. Thiruvenkatachari R, Ouk Kwon T, Shik Moon I. Application of Slurry Type Photocatalytic Oxidation-Submerged Hollow Fiber Microfiltration Hybrid System for the Degradation of Bisphenol A (BPA). Sep Sci Technol. 2005 Oct;40(14):2871–88.

111. Carbonaro S, Sugihara MN, Strathmann TJ. Continuous-flow photocatalytic treatment of pharmaceutical micropollutants: Activity, inhibition, and deactivation of TiO_2 photocatalysts in wastewater effluent. Appl Catal B Environ. 2013 Jan;129:1–12.

112. Li D, Xia Y. Fabrication of Titania Nanofibers by Electrospinning. Nano Lett. 2003 Apr;3(4):555–60.

113. Choi SK, Kim S, Lim SK, Park H. Photocatalytic Comparison of TiO_2 Nanoparticles and Electrospun TiO_2 Nanofibers: Effects of Mesoporosity and Interparticle Charge Transfer. J Phys Chem C. 2010;114:16475–80.

114. Thavasi V, Singh G, Ramakrishna S. Electrospun nanofibers in energy and environmental applications. Energy Environ Sci. 2008;1(2):205–21.

115. Wang X, Choi J, Mitchell DRG, Truong YB, Kyratzis IL, Caruso RA. Enhanced Photocatalytic Activity: Macroporous Electrospun Mats of Mesoporous Au/TiO_2 Nanofibers. ChemCatChem. 2013;5(9):2646–2654.

116. Zhang X, Xu S, Han G. Fabrication and photocatalytic activity of TiO_2 nanofiber membrane. Mater Lett. 2009 Aug;63(21):1761–3.

117. Gao P, Tai MH, Sun DD. Hierarchical TiO_2 /V_2O_5 Multifunctional Membrane for Water Purification. ChemPlusChem. 2013 Dec 4;78(12):1475–82.

118. Lee J-S, Lee Y-I, Song H, Jang D-H, Choa Y-H. Synthesis and characterization of TiO_2 nanowires with controlled porosity and microstructure using electrospinning method. Curr Appl Phys. 2011 Jan;11(1):S210–4.

119. Mowbray DJ, Martinez JI, Thygesen KS, Jacobsen KW. Stability and Electronic Properties of TiO_2 Nanostructures With and Without B and N Doping. J Phys Chem C. 2009;113(28):12301–8.

120. Doh SJ, Kim C, Lee SG, Lee SJ, Kim H. Development of photocatalytic TiO_2 nanofibers by electrospinning and its application to degradation of dye pollutants. J Hazard Mater. 2008 Jun 15;154(1–3):118–27.

121. Peng X, Santulli AC, Sutter E, Wong SS. Fabrication and enhanced photocatalytic activity of inorganic core–shell nanofibers produced by coaxial electrospinning. Chem Sci. 2012;3:1262–672.

122. Zhang X, Thavasi V, Mhaisalkar SG, Ramakrishna S. Novel hollow mesoporous 1D TiO_2 nanofibers as photovoltaic and photocatalytic materials. Nanoscale. 2012 Mar 7;4:1707–16.

123. Du P, Song L, Xiong J, Cao H. Photocatalytic degradation of Rhodamine B using electrospun TiO_2 and ZnO nanofibers: a comparative study. J Mater Sci. 2013 Aug 17;48(24):8386–92.

124. Zhang P, Shao C, Zhang Z, Zhang M, Mu J, Guo Z, et al. Core/shell nanofibers of TiO_2@carbon embedded by Ag nanoparticles with enhanced visible photocatalytic activity. J Mater Chem. 2011;21:17746–53.

125. Ohtani B, Prieto-Mahaney OO, Li D, Abe R. What is Degussa (Evonik) P25? Crystalline composition analysis, reconstruction from isolated pure particles and photocatalytic activity test. J Photochem Photobiol Chem. 2010 Dec;216(2–3):179–82.

126. Hirakawa T, Kamat P V. Charge separation and catalytic activity of Ag@TiO_2 core-shell composite clusters under UV-irradiation. J Am Chem Soc. 2005 Mar 23;127(11):3928–34.

127. Kochuveedu ST, Kim D-P, Kim DH. Surface-Plasmon-Induced Visible Light Photocatalytic Activity of TiO_2 Nanospheres Decorated by Au Nanoparticles with Controlled Configuration. J Phys Chem C. 2012;116:2500–6.

128. Wang H, Faria JL, Dong S, Chang Y. Mesoporous Au/TiO_2 composites preparation, characterization, and photocatalytic properties. Mater Sci Eng B. 2012 Jun;177(11):913–9.

129. Hurum DC, Agrios AG, Gray KA, Rajh T, Thurnauer MC. Explaining the Enhanced Photocatalytic Activity of Degussa P25 Mixed-Phase TiO_2 Using EPR. J Phys Chem B. 2003;107:4545–9.

130. Ding Z, Lu GQ, Greenfield PF. Role of the Crystallite Phase of TiO_2 in Heterogeneous Photocatalysis for Phenol Oxidation in Water. 2000;4815–20.

131. Wold A. Photocatalytic Properties of TiO_2. Chem Mater. 1993;5:280–3.

132. Nam SH, Shim H-S, Kim Y-S, Dar MA, Kim JG, Kim WB. Ag or Au Nanoparticle-Embedded One-Dimensional Composite TiO_2 Nanofibers Prepared via Electrospinning for Use in Lithium-Ion Batteries. ACS Appl Mater Interfaces. 2010 Jul 28;2(7):2046–52.

133. Zanella R, Delannoy L, Louis C. Mechanism of deposition of gold precursors onto TiO_2 during the preparation by cation adsorption and deposition–precipitation with NaOH and urea. Appl Catal Gen. 2005 Sep;291(1–2):62–72.

134. Hosseini SN, Borghei SM, Vossoughi M, Taghavinia N. Immobilization of TiO_2 on perlite granules for photocatalytic degradation of phenol. Appl Catal B Environ. 2007 Jun;74(1–2):53–62.

135. Liu T, Liu Y, Zhang Z, Li F, Li X. Comparison of Aqueous Photoreactions with TiO_2 in its Hydrosol Solution and Powdery Suspension for Light Utilization. Ind Eng Chem Res. 2011;50:7841–8.

136. Motegh M, Cen J, Appel PW, van Ommen JR, Kreutzer MT. Photocatalytic-reactor efficiencies and simplified expressions to assess their relevance in kinetic experiments. Chem Eng J. 2012 Oct;207–208:607–15.

137. Cabrera MI, Alfano OM, Cassano AE. Absorption and Scattering Coefficients of Titanium Dioxide Particulate Suspensions in Water. J Phys Chem. 1996;100:20043–50.

138. Verdugo EM, Krause C, Genskow K, Han Y, Baltrusaitis J, Mattes TE, et al. N-functionalized carbon nanotubes as a source and precursor of N-

nitrosodimethylamine: implications for environmental fate, transport, and toxicity. Environ Sci Technol. 2014 Aug 19;48(16):9279–87.

139. Baltrusaitis J, Usher CR, Grassian VH. Reactions of sulfur dioxide on calcium carbonate single crystal and particle surfaces at the adsorbed water carbonate interface. Phys Chem Chem Phys. 2007 Jun 21;9(23):3011–24.

140. Qu S, Kolodziej EP, Cwiertny DM. Phototransformation rates and mechanisms for synthetic hormone growth promoters used in animal agriculture. Environ Sci Technol. 2012 Dec 18;46(24):13202–11.

141. Newport Corporation. Optical Radiation Terminology and Units [Internet]. 2015. Available from: <http://www.newport.com/Optical-Radiation-Terminology-and-Units/381842/1033/content.aspx>

142. Oulton RL, Kohn T, Cwiertny DM. Pharmaceuticals and personal care products in effluent matrices: A survey of transformation and removal during wastewater treatment and implications for wastewater management. J Environ Monit. 2010 Nov;12(11):1956–78.

143. Araña J, Doña-Rodríguez JM, Portillo-Carrizo D, Fernández-Rodríguez C, Pérez-Peña J, González Díaz O, et al. Photocatalytic degradation of phenolic compounds with new TiO_2 catalysts. Appl Catal B Environ. 2010 Oct 11;100(1–2):346–54.

144. Newcombe D. A, Crowley DE. Bioremediation of atrazine-contaminated soil by repeated applications of atrazine-degrading bacteria. Appl Microbiol Biotechnol. 1999 Jun;51(6):877–82.

145. Borisover M, Sela M, Chefetz B. Enhancement effect of water associated with natural organic matter (NOM) on organic compound-NOM interactions: a case study with carbamazepine. Chemosphere. 2011 Mar;82(10):1454–60.

146. Kaur R, Pal B. Size and shape dependent attachments of Au nanostructures to TiO_2 for optimum reactivity of Au–TiO_2 photocatalysis. J Mol Catal Chem. 2012 Mar;355:39–43.

147. Yu K, Lee G. Decomposition of gas-phase toluene by the combination of ozone and photocatalytic oxidation process (TiO_2/UV, TiO_2/UV/O_3, and UV/O_3). Appl Catal B Environ. 2007 Aug 29;75(1–2):29–38.

148. Tôrres AR, Azevedo EB, Resende NS, Dezotti M. A comparison between bulk and supported TiO_2 photocatalysts in the degradation of formic acid. Braz J Chem Eng. 2007;24(2):185–92.

149. Sopyan I, Hafizah N, Jamal P. Immobilization of TiO_2 with cement : Photocatalytic degradation of phenol and its kinetic studies. Indian J Chem Technol. 2011;18:263–70.

150. Chen D, Ray AK. Photocatalytic kinetics of phenol and its derivatives over UV irradiated TiO_2. Appl Catal B Environ. 1999;23:143–57.

151. Ghosh SK, Pal T. Interparticle coupling effect on the surface plasmon resonance of gold nanoparticles: from theory to applications. Chem Rev. 2007 Nov;107(11):4797–862.

152. Mock JJ, Hill RT, Degiron A, Zauscher S, Chilkoti A, Smith DR. Distance-dependent plasmon resonant coupling between a gold nanoparticle and gold film. Nano Lett. 2008 Aug;8(8):2245–52.

153. Fleger Y, Rosenbluh M. Surface Plasmons and Surface Enhanced Raman Spectra of Aggregated and Alloyed Gold-Silver Nanoparticles. Res Lett Opt. 2009;2009:1–5.

154. Lu S-Y, Wu D, Wang Q-L, Yan J, Buekens AG, Cen K-F. Photocatalytic decomposition on nano-TiO_2: destruction of chloroaromatic compounds. Chemosphere. 2011 Feb;82(9):1215–24.

155. Paramasivam I, Macak JM, Schmuki P. Photocatalytic activity of TiO_2 nanotube layers loaded with Ag and Au nanoparticles. Electrochem Commun. 2008 Jan;10(1):71–5.

156. Arabatzis IM, Stergiopoulos T, Andreeva D, Kitova S, Neophytides SG, Falaras P. Characterization and photocatalytic activity of Au/TiO_2 thin films for azo-dye degradation. J Catal. 2003 Nov 15;220(1):127–35.

157. Kohn T, Arnold WA, Roberts AL. Reactivity of substituted benzotrichlorides toward granular Iron, Cr(II), and an Iron(II) porphyrin: A correlation analysis. Environ Sci Technol. 2006 Jul 1;40(13):4253–60.

158. Cwiertny DM, Arnold WA, Kohn T, Rodenburg LA, Roberts AL. Reactivity of alkyl polyhalides toward granular iron: development of QSARs and reactivity cross correlations for reductive dehalogenation. Environ Sci Technol. 2010 Oct 15;44(20):7928–36.

159. Huber MM, Canonica S, Park G-Y, von Gunten U. Oxidation of pharmaceuticals during ozonation and advanced oxidation processes. Environ Sci Technol. 2003 Mar 1;37(5):1016–24.

160. De AK, Chaudhuri B, Bhattacharjee S, Dutta BK. Estimation of $^{\cdot}OH$ radical reaction rate constants for phenol and chlorinated phenols using UV/H_2O_2 photo-oxidation. J Hazard Mater B. 1999 Jan 1;64(1):91–104.

161. Cooper WJ, Snyder SA, Mezyk SP, Peller JR, Nickelsen MG. Reaction Rates and Mechanisms of Advanced Oxidation Processes (AOPs) for Water Reuse. Alexandria: WateResue Foundation; 2010.

162. Sun C, Wang N, Zhou S, Hu X, Zhou S, Chen P. Preparation of self-supporting hierarchical nanostructured anatase/rutile composite TiO_2 film. Chem Commun. 2008 Jul 28;(28):3293–5.

163. Sutton R, Group EW. Chromium-6 in US tap water. Environmental Working Group; 2010.

164. U.S. EPA. Learn about Small Drinking Water Systems [Internet]. U.S. EPA; 2015. Available from: http://www.epa.gov/dwcapacity/learn-about-small-drinking-water-systems

165. Cornell RM, Schwertmann U. The iron oxides: structure, properties, reactions, occurrences, and uses. 2nd, completely and extended ed ed. Weinheim: Wiley-VCH; 2003. 664 p.

166. Kosmulski M. pH-dependent surface charging and points of zero charge. IV. Update and new approach. J Colloid Interface Sci. 2009 Sep;337(2):439–48.

167. Evoqua Water Technologies. GFH Granular Ferric Hydroxide Media [Internet]. Evoqua Water Technologies; 2014. Available from: http://www.evoqua.com/en/brands/IPS/productinformationlibrary/ESGFHDS.pdf

168. Evoqua Water Technologies. GFH Media Removes Arsenic in Arizona Water Supply [Internet]. Evoqua Water Technologies; 2014. Available from: http://www.evoqua.com/en/brands/IPS/productinformationlibrary/ES-AZGFH-CS.pdf

169. Evoqua Delivers Temporary Arsenic Treatment System for Bucks County Water Authority. Evoqua Delivers Temporary Arsenic Treatment System for Bucks County Water Authority [Internet]. Evoqua Water Technologies; 2014. Available from: http://www.evoqua.com/en/brands/IPS/productinformationlibrary/ESSOLEPP.pdf

170. American Gypsum Purchases Arsenic Removal System to Treat On-Site Well. American Gypsum Purchases Arsenic Removal System to Treat On-Site Well [Internet]. Evoqua Water Technologies; 2014. Available from: http://www.evoqua.com/en/brands/IPS/productinformationlibrary/ESAMERICANPP.pdf

171. Genç-Fuhrman H, Mikkelsen PS, Ledin A. Simultaneous removal of As, Cd, Cr, Cu, Ni and Zn from stormwater: Experimental comparison of 11 different sorbents. Water Res. 2007 Feb;41(3):591–602.

172. Ramakrishna S, Fujihara K, Teo W-E, Yong T, Ma Z, Ramaseshan R. Electrospun nanofibers: solving global issues. Mater Today. 2006 Mar;9(3):40–50.

173. Nalbandian MJ, Zhang M, Sanchez J, Choa Y-H, Nam J, Cwiertny DM, et al. Synthesis and optimization of Fe2O3 nanofibers for chromate adsorption from contaminated water sources. Chemosphere. 2016 Feb;144:975–81.

174. Patel S, Hota G. Iron oxide nanoparticle-immobilized PAN nanofibers: synthesis and adsorption studies. RSC Adv. 2016;6(19):15402–14.

175. Schwertmann U, Cornell RM. Iron oxides in the laboratory: preparation and characterization. 2nd completely rev. and extended ed. Weinheim ; New York: Wiley-VCH; 2000. 188 p.

176. Bora DK, Braun A, Erni R, Fortunato G, Graule T, Constable EC. Hydrothermal Treatment of a Hematite Film Leads to Highly Oriented Faceted Nanostructures with Enhanced Photocurrents. Chem Mater. 2011 Apr 26;23(8):2051–61.

177. Peter KT, Vargo JD, Rupasinghe TP, De Jesus A, Tivanski AV, Sander EA, et al. Synthesis, Optimization, and Performance Demonstration of Electrospun Carbon

Nanofiber–Carbon Nanotube Composite Sorbents for Point-of-Use Water Treatment. ACS Appl Mater Interfaces. 2016 May 11;8(18):11431–40.

178. Smith GF, McCurdy WH, Diehl H. The colorimetric determination of iron in raw and treated municipal water supplies by use of 4:7-diphenyl-1:10-phenanthroline. Analyst. 1952;77(917):418–22.

179. Test Methods for Evaluating Solid Waste, Physical/Chemical Methods, Method 7196A: Chromium, Hexavalent (Colorimetric) [Internet]. U.S. EPA; 1992. Available from: http://www3.epa.gov/epawaste/hazard/testmethods/sw846/pdfs/7196a.pdf

180. Wetzel B, Haupert F, Qiu Zhang M. Epoxy nanocomposites with high mechanical and tribological performance. Compos Sci Technol. 2003 Nov;63(14):2055–67.

181. Augustine R, Kalarikkal N, Thomas S. Electrospun PCL membranes incorporated with biosynthesized silver nanoparticles as antibacterial wound dressings. Appl Nanosci. 2016 Mar;6(3):337–44.

182. Pai C-L, Boyce MC, Rutledge GC. Mechanical properties of individual electrospun PA 6(3)T fibers and their variation with fiber diameter. Polymer. 2011 May;52(10):2295–301.

183. Yao J, Bastiaansen C, Peijs T. High Strength and High Modulus Electrospun Nanofibers. Fibers. 2014 Apr 30;2(2):158–86.

184. Lakshmipathiraj P, Narasimhan B, Prabhakar S, Bhaskarraju G. Adsorption of arsenate on synthetic goethite from aqueous solutions. J Hazard Mater. 2006 Aug 21;136(2):281–7.

185. Lanzl C. Size-dependent reactivity of hematite nanoparticles: environmental implications of dissolution mechanisms and aggregation [Internet]. University of Iowa; 2013 [cited 2016 Jul 29]. Available from: http://ir.uiowa.edu/cgi/viewcontent.cgi?article=4686&context=etd

186. Filipek LH, Society of Economic Geologists, editors. The environmental geochemistry of mineral deposits. Pt. B: Case studies and research topics. Chelsea, Mich.: Soc. of Economic Geologists; 1999. 373 p. (Reviews in economic geology).

187. Chen W, Zou J, Jang M, Cannon FS, Dempsey BA. Arsenic Removal by Tailored Activated Carbon at Ambient pH. Water Research Foundation; 2009.

188. Singh DB, Prasad G, Rupainwar DC. Adsorption technique for the treatment of As(V)-rich effluents. Colloids Surf Physicochem Eng Asp. 1996 Jun;111(1–2):49–56.

189. Ajouyed O, Hurel C, Ammari M, Allal LB, Marmier N. Sorption of Cr(VI) onto natural iron and aluminum (oxy)hydroxides: Effects of pH, ionic strength and initial concentration. J Hazard Mater. 2010 Feb;174(1–3):616–22.

190. Peacock CL, Sherman DM. Copper(II) sorption onto goethite, hematite and lepidocrocite: a surface complexation model based on ab initio molecular geometries and EXAFS spectroscopy. Geochim Cosmochim Acta. 2004 Jun;68(12):2623–37.

191. Bargar JR, Brown GE, Parks GA. Surface complexation of Pb(II) at oxide-water interfaces: II. XAFS and bond-valence determination of mononuclear Pb(II) sorption products and surface functional groups on iron oxides. Geochim Cosmochim Acta. 1997 Jul;61(13):2639–52.

192. Yin S, Ellis DE. DFT studies of Cr(VI) complex adsorption on hydroxylated hematite () surfaces. Surf Sci. 2009 Feb 15;603(4):736–46.

193. Catalano JG, Park C, Fenter P, Zhang Z. Simultaneous inner- and outer-sphere arsenate adsorption on corundum and hematite. Geochim Cosmochim Acta. 2008 Apr 15;72(8):1986–2004.

194. Jeon B-H, Dempsey BA, Burgos WD, Royer RA. Sorption kinetics of Fe(II), Zn(II), Co(II), Ni(II), Cd(II), and Fe(II)/Me(II) onto hematite. Water Res. 2003 Oct;37(17):4135–42.

195. Davis AP, Bhatnagar V. Adsorption of cadmium and humic acid onto hematite. Chemosphere. 1995 Jan;30(2):243–56.

196. Shuibo X, Chun Z, Xinghuo Z, Jing Y, Xiaojian Z, Jingsong W. Removal of uranium (VI) from aqueous solution by adsorption of hematite. Radioecol Stud Sel Pap Present Int Symp ONIN-SITU Nucl Metrol TOOL Radioecol INSINUME 2006. 2009 Feb;100(2):162–6.

197. Rose AW, Bianchi-Mosquera GC. Adsorption of Cu, Pb, Zn, Co, Ni, and Ag on goethite and hematite; a control on metal mobilization from red beds into stratiform copper deposits. Econ Geol. 1993 Aug 1;88(5):1226–36.

198. Li W, Zhang S, Jiang W, Shan X. Effect of phosphate on the adsorption of Cu and Cd on natural hematite. Chemosphere. 2006 May;63(8):1235–41.

199. Lenhart JJ, Honeyman BD. Uranium(VI) sorption to hematite in the presence of humic acid. Geochim Cosmochim Acta. 1999 Oct;63(19–20):2891–901.

200. Osseo-Asare K, Fuerstenau DW. Adsorption phenomena in hydrometallurgy, 1 The uptake of copper, nickel and cobalt by oxide adsorbents in aqueous ammoniacal solutions. Int J Miner Process. 1979 Oct;6(2):85–104.

201. Mamindy-Pajany Y, Hurel C, Marmier N, Roméo M. Arsenic adsorption onto hematite and goethite. Comptes Rendus Chim. 2009 Aug;12(8):876–81.

202. Giménez J, Martínez M, de Pablo J, Rovira M, Duro L. Arsenic sorption onto natural hematite, magnetite, and goethite. J Hazard Mater. 2007 Mar 22;141(3):575–80.

203. Shipley HJ, Engates KE, Grover VA. Removal of Pb(II), Cd(II), Cu(II), and Zn(II) by hematite nanoparticles: effect of sorbent concentration, pH, temperature, and exhaustion. Environ Sci Pollut Res. 2013 Mar;20(3):1727–36.

204. Barton LE, Grant KE, Kosel T, Quicksall AN, Maurice PA. Size-Dependent Pb Sorption to Nanohematite in the Presence and Absence of a Microbial Siderophore. Environ Sci Technol. 2011 Apr 15;45(8):3231–7.

205. Mohan D, Pittman CU. Arsenic removal from water/wastewater using adsorbents—A critical review. J Hazard Mater. 2007 Apr;142(1–2):1–53.

206. Martin M, Violante A, Ajmone-Marsan F, Barberis E. Surface Interactions of Arsenite and Arsenate on Soil Colloids. Soil Sci Soc Am J. 2014;78(1):157.

207. Campos V, Büchler PM. Removal of chromate from drinking water using powder carbon steel. Environ Geol. 2005 May;47(7):926–30.

208. Cuppett JD. Evaluation of Copper Speciation and Water Quality Factors That Affect Aqueous Copper Tasting Response. Chem Senses. 2006 Jun 26;31(7):689–97.

209. M. V, Villaescus I. The Chemistry Behind the Use of Agricultural Biomass as Sorbent for Toxic Metal Ions: pH Influence, Binding Groups, and Complexation Equilibria. In: Matovic MD, editor. Biomass - Detection, Production and Usage [Internet]. InTech; 2011 [cited 2016 Jan 8]. Available from: http://www.intechopen.com/books/biomass-detection-production-and-usage/the-chemistry-behind-the-use-of-agricultural-biomass-as-sorbent-for-toxic-metal-ions-ph-influence-bi

210. AWWA Research Foundation, DVGW-Technologiezentrum Wasser, editors. Internal corrosion of water distribution systems. 2nd ed. Denver, CO: The Foundation; 1996. 586 p. (Cooperative research report).

211. Khaodhiar S, Azizian MF, Osathaphan K, Nelson PO. Copper, Chromium, and Arsenic Adsorption and Equilibrium Modeling in An Iron-Oxide-Coated Sand, Background Electrolyte System. Water Air Soil Pollut. 2000;119(1):105–20.

212. Christl I, Kretzschmar R. Competitive sorption of copper and lead at the oxide-water interface: Implications for surface site density. Geochim Cosmochim Acta. 1999 Oct;63(19–20):2929–38.

213. Zhang W, Singh P, Paling E, Delides S. Arsenic removal from contaminated water by natural iron ores. Miner Eng. 2004 Apr;17(4):517–24.

214. Bailey RP, Bennett T, Benjamin MM. Sorption onto and Recovery of Cr(VI) Using Iron-Oxide-Coated Sand. Water Sci Technol. 1992 Sep 1;26(5–6):1239–44.

215. Lai CH, Chen CY. Removal of metal ions and humic acid from water by iron-coated filter media. Chemosphere. 2001 Aug;44(5):1177–84.

216. Theis TL, Iyer R, Ellis SK. Evaluating a New Granular Iron Oxide for Removing Lead From Drinking Water. J Am Water Works Assoc. 1992;84(7):101–5.

217. Hanna K, Martin S, Quilès F, Boily J-F. Sorption of Phthalic Acid at Goethite Surfaces under Flow-Through Conditions. Langmuir. 2014 Jun 17;30(23):6800–7.

218. Adeel Z, Luthy RG. Sorption and Transport Kinetics of a Nonionic Surfactant through an Aquifer Sediment. Environ Sci Technol. 1995 Apr;29(4):1032–42.

219. Luther S, Borgfeld N, Kim J, Parsons JG. Removal of arsenic from aqueous solution: A study of the effects of pH and interfering ions using iron oxide nanomaterials. Microchem J. 2012 Mar;101:30–6.

220. Jain A, Loeppert RH. Effect of Competing Anions on the Adsorption of Arsenate and Arsenite by Ferrihydrite. J Environ Qual. 2000;29(5):1422.

221. Nguyen AT, Juang R-S. Treatment of o-Cresol/4-chlorophenol binary mixtures in aqueous solutions by TiO2 photocatalysis under UV irradiation. Desalination Water Treat. 2016 Mar 27;57(15):6820–8.

222. Zhao Z, Wang Y, Xu J, Wang Y. Mesoporous Ag/TiO $_2$ nanocomposites with greatly enhanced photocatalytic performance towards degradation of methyl orange under visible light. RSC Adv. 2015;5(73):59297–305.

223. Eslami A, Amini MM, Yazdanbakhsh AR, Mohseni-Bandpei A, Safari AA, Asadi A. N,S co-doped TiO $_2$ nanoparticles and nanosheets in simulated solar light for photocatalytic degradation of non-steroidal anti-inflammatory drugs in water: a comparative study: photocatalytic degradation of non-steroidal anti-inflammatory drugs. J Chem Technol Biotechnol. 2015 Dec;n/a-n/a.

224. Im JS, Kim MI, Lee Y-S. Preparation of PAN-based electrospun nanofiber webs containing TiO2 for photocatalytic degradation. Mater Lett. 2008 Aug;62(21–22):3652–5.

225. Deniz AE, Celebioglu A, Kayaci F, Uyar T. Electrospun polymeric nanofibrous composites containing TiO2 short nanofibers. Mater Chem Phys. 2011 Oct;129(3):701–4.

226. Lombardi M, Palmero P, Sangermano M, Varesano A. Electrospun polyamide-6 membranes containing titanium dioxide as photocatalyst. Polym Int. 2011 Feb;60(2):234–9.

227. Hong Y, Li D, Zheng J, Zou G. Sol–gel growth of titania from electrospun polyacrylonitrile nanofibres. Nanotechnology. 2006 Apr 28;17(8):1986–93.

228. Mehrpouya F, Tavanai H, Morshed M, Ghiaci M. The formation of titanium dioxide crystallite nanoparticles during activation of PAN nanofibers containing titanium isopropoxide. J Nanoparticle Res [Internet]. 2012 Aug [cited 2016 Jul 22];14(8). Available from: http://link.springer.com/10.1007/s11051-012-1074-3

229. Meng X, Luo N, Cao S, Zhang S, Yang M, Hu X. In-situ growth of titania nanoparticles in electrospun polymer nanofibers at low temperature. Mater Lett. 2009 Jun;63(16):1401–3.

230. Su C, Tong Y, Zhang M, Zhang Y, Shao C. TiO2 nanoparticles immobilized on polyacrylonitrile nanofibers mats: a flexible and recyclable photocatalyst for phenol degradation. RSC Adv. 2013;3(20):7503.

231. Zhang H, Yang L. Immobilization of nanoparticle titanium dioxide membrane on polyamide fabric by low temperature hydrothermal method. Thin Solid Films. 2012 Jul;520(18):5922–7.

232. Abdal-hay A, Mousa HM, Khan A, Vanegas P, Lim JH. TiO2 nanorods coated onto nylon 6 nanofibers using hydrothermal treatment with improved mechanical properties. Colloids Surf Physicochem Eng Asp. 2014 Sep;457:275–81.

233. Szatmáry L, Šubrt J, Kalousek V, Mosinger J, Lang K. Low-temperature deposition of anatase on nanofiber materials for photocatalytic NOx removal. Catal Today. 2014 Jul;230:74–8.

234. the Nanyang Technological University, 50 Nanyang Avenue, Singapore 639798, Tai MH, Gao P, the Nanyang Technological University, 50 Nanyang Avenue, Singapore 639798, Tan BYL, the Nanyang Technological University, 50 Nanyang Avenue, Singapore 639798, et al. A Hierarchically-Nano Structured TiO2-Carbon Nanofibrous Membrane for Concurrent Gravity-Driven Oil-Water Separation. Int J Environ Sci Dev. 2015;6(8):590–5.

235. Kim S, Lim SK. Preparation of TiO2-embedded carbon nanofibers and their photocatalytic activity in the oxidation of gaseous acetaldehyde. Appl Catal B Environ. 2008 Oct;84(1–2):16–20.

236. Su C, Ran X, Hu J, Shao C. Photocatalytic Process of Simultaneous Desulfurization and Denitrification of Flue Gas by TiO 2 –Polyacrylonitrile Nanofibers. Environ Sci Technol. 2013 Oct 15;47(20):11562–8.

237. Ramasundaram S, Son A, Seid MG, Shim S, Lee SH, Chung YC, et al. Photocatalytic applications of paper-like poly(vinylidene fluoride)–titanium dioxide hybrids fabricated using a combination of electrospinning and electrospraying. J Hazard Mater. 2015 Mar;285:267–76.

238. Memetea LT, Billingham NC, Then ETH. Hydroperoxides in polyacrylonitrile and their role in carbon-fibre formation. Polym Degrad Stab. 1995 Jan 1;47(2):189–201.

239. Kim CH, Kim B-H, Yang KS. TiO2 nanoparticles loaded on graphene/carbon composite nanofibers by electrospinning for increased photocatalysis. Carbon. 2012 Jun;50(7):2472–81.

240. Gu Y, Li C, Bai J, Wang J, Ma T. One-step solvothermal synthesis of Au-TiO2 loaded electrospun carbon fibers to enhance photocatalytic activity. Vacuum. 2016 Aug;130:1–6.

241. Liu H, Cao C-Y, Wei F-F, Huang P-P, Sun Y-B, Jiang L, et al. Flexible macroporous carbon nanofiber film with high oil adsorption capacity. J Mater Chem A. 2014;2(10):3557.

242. Dobson KD, McQuillan AJ. In situ infrared spectroscopic analysis of the adsorption of aromatic carboxylic acids to TiO2, ZrO2, Al2O3, and Ta2O5 from aqueous solutions. Spectrochim Acta A Mol Biomol Spectrosc. 2000 Feb 15;56(3):557–65.

243. Cooper W, Snyder S, Mezyk S, Peller J, Nickelsen M. Reaction Rates and Mechanisms of Advanced Oxidation Processes (AOPs) for Water Reuse. 2010;

244. Scanlon DO, Dunnill CW, Buckeridge J, Shevlin S a, Logsdail AJ, Woodley SM, et al. Band alignment of rutile and anatase TiO_2. Nat Mater. 2013 Sep;12(9):798–801.

245. Cao C-Y, Qu J, Yan W-S, Zhu J-F, Wu Z-Y, Song W-G. Low-Cost Synthesis of Flowerlike α-Fe $_2$ O $_3$ Nanostructures for Heavy Metal Ion Removal: Adsorption Property and Mechanism. Langmuir. 2012 Mar 6;28(9):4573–9.

246. Peacock CL, Sherman DM. Copper(II) sorption onto goethite, hematite and lepidocrocite: a surface complexation model based on ab initio molecular geometries and EXAFS spectroscopy1. Geochim Cosmochim Acta. 2004 Jun 15;68(12):2623–37.

247. Rafqah S, Wong-Wah-Chung P, Nelieu S, Einhorn J, Sarakha M. Phototransformation of triclosan in the presence of TiO2 in aqueous suspension: Mechanistic approach. Appl Catal B Environ. 2006 Jun;66(1–2):119–25.

248. Mogyorósi K, Farkas A, Dékány I, Ilisz I, Dombi A. TiO $_2$ -Based Photocatalytic Degradation of 2-Chlorophenol Adsorbed on Hydrophobic Clay. Environ Sci Technol. 2002 Aug;36(16):3618–24.

249. Bogdan J, Zarzyńska J, Pławińska-Czarnak J. Comparison of Infectious Agents Susceptibility to Photocatalytic Effects of Nanosized Titanium and Zinc Oxides: A Practical Approach. Nanoscale Res Lett [Internet]. 2015 Dec [cited 2016 Aug 1];10(1). Available from: http://www.nanoscalereslett.com/content/10/1/309

250. Bonetta S, Bonetta S, Motta F, Strini A, Carraro E. Photocatalytic bacterial inactivation by TiO2-coated surfaces. AMB Express. 2013;3(1):59.

251. Persano L, Camposeo A, Tekmen C, Pisignano D. Industrial Upscaling of Electrospinning and Applications of Polymer Nanofibers: A Review. Macromol Mater Eng. 2013 May;298(5):504–20.

252. Fujishima A, Zhang X. Titanium dioxide photocatalysis: present situation and future approaches. Convers Photochimique Stock Lénergie Solaire2e PartiePhotochemical Convers Storage Sol EnergyPart II. 2006 May;9(5–6):750–60.

253. Taha AA, Li F. Porous WO $_3$ –carbon nanofibers: high-performance and recyclable visible light photocatalysis. Catal Sci Technol. 2014 Jul 10;4(10):3601–5.

254. Holz MC, Tolle K, Muhler M. Gas-phase oxidation of ethanol over Au/TiO2 catalysts to probe metal-support interactions. Catal Sci Technol. 2014;4(10):3495–504.

255. Daté M, Haruta M. Moisture Effect on CO Oxidation over Au/TiO2 Catalyst. J Catal. 2001 Jul;201(2):221–4.

256. Green IX, Tang W, Neurock M, Yates JT. Spectroscopic Observation of Dual Catalytic Sites During Oxidation of CO on a Au/TiO2 Catalyst. Science. 2011 Aug 5;333(6043):736–9.

257. Liu LM, McAllister B, Ye HQ, Hu P. Identifying an O $_2$ Supply Pathway in CO Oxidation on Au/TiO $_2$ (110): A Density Functional Theory Study on the Intrinsic Role of Water. J Am Chem Soc. 2006 Mar;128(12):4017–22.

258. Mahapatra A, Mishra BG, Hota G. Studies on Electrospun Alumina Nanofibers for the Removal of Chromium(VI) and Fluoride Toxic Ions from an Aqueous System. Ind Eng Chem Res. 2013 Jan 30;52(4):1554–61.

259. Tchomgui-Kamga E, Alonzo V, Nanseu-Njiki CP, Audebrand N, Ngameni E, Darchen A. Preparation and characterization of charcoals that contain dispersed aluminum oxide as adsorbents for removal of fluoride from drinking water. Carbon. 2010 Feb;48(2):333–43.

260. Abbasi SA. Exergetic Life Cycle Assessment of Electrospun Polyvinylidene Fluoride Nanofibers. University of South Florida; 2014.

261. Piccinno F, Hischier R, Seeger S, Som C. Life Cycle Assessment of a New Technology To Extract, Functionalize and Orient Cellulose Nanofibers from Food Waste. ACS Sustain Chem Eng. 2015 Jun;3(6):1047–55.

262. Simon B, Bachtin K, Kiliç A, Amor B, Weil M. Proposal of a framework for scale-up life cycle inventory: A case of nanofibers for lithium iron phosphate cathode applications: Cradle-to-Gate LCA of Nanofiber Li-ion Battery Cathodes. Integr Environ Assess Manag. 2016 Jul;12(3):465–77.